

## **Abstract**

Dissertation Title:                   MANIPULATION OF IONS, ELECTRONS,  
AND PHOTONS IN 2D MATERIALS BY ION  
INTERCALATION

**Jiayu Wan, Doctor of Philosophy, 2016**

Dissertation directed by:           Associate Professor Liangbing Hu, Department  
of Materials Science and Engineering

2D materials have attracted tremendous attention due to their unique physical and chemical properties since the discovery of graphene. Despite these intrinsic properties, various modification methods have been applied to 2D materials that yield even more exciting results. Among all modification methods, the intercalation of 2D materials provides the highest possible doping and/or phase change to the pristine 2D materials. This doping effect highly modifies 2D materials, with extraordinary electrical transport as well as optical, thermal, magnetic, and catalytic properties, which are advantageous for optoelectronics, superconductors, thermoelectronics, catalysis and energy storage applications. To study the property changes of 2D materials, we designed and built a planar nanobattery that allows electrochemical ion intercalation in 2D materials. More importantly, this planar nanobattery enables characterization of electrical, optical and structural properties of 2D materials *in situ* and real time upon ion intercalation. With this device, we successfully intercalated Li-ions into few layer graphene (FLG) and ultrathin graphite, heavily dopes the graphene to  $0.6 \times 10^{15} /\text{cm}^2$ , which simultaneously increased its conductivity and transmittance in the visible range. The intercalated  $\text{LiC}_6$  single crystallite achieved extraordinary optoelectronic properties, in which an eight-layered Li

intercalated FLG achieved transmittance of 91.7% (at 550 nm) and sheet resistance of 3 ohm/sq. We extend the research to obtain scalable, printable graphene based transparent conductors with ion intercalation. Surfactant free, printed reduced graphene oxide transparent conductor thin film with Na-ion intercalation is obtained with transmittance of 79% and sheet resistance of 300 ohm/sq (at 550 nm). The figure of merit is calculated as the best pure rGO based transparent conductors. We further improved the tunability of the reduced graphene oxide film by using two layers of CNT films to sandwich it. The tunable range of rGO film is demonstrated from 0.9  $\mu\text{m}$  to 10  $\mu\text{m}$  in wavelength. Other ions such as K-ion is also studied of its intercalation chemistry and optical properties in graphitic materials.

We also used the *in situ* characterization tools to understand the fundamental properties and improve the performance of battery electrode materials. We investigated the Na-ion interaction with rGO by *in situ* Transmission electron microscopy (TEM). For the first time, we observed reversible Na metal cluster (with diameter larger than 10 nm) deposition on rGO surface, which we evidenced with atom-resolved HRTEM image of Na metal and electron diffraction pattern. This discovery leads to a porous reduced graphene oxide sodium ion battery anode with record high reversible specific capacity around 450 mAh/g at 25mA/g, a high rate performance of 200 mAh/g at 250 mA/g, and stable cycling performance up to 750 cycles. In addition, direct observation of irreversible formation of  $\text{Na}_2\text{O}$  on rGO unveils the origin of commonly observed low 1<sup>st</sup> Columbic Efficiency of rGO containing electrodes. Another example for *in situ* characterization for battery electrode is using the planar nanobattery for 2D  $\text{MoS}_2$  crystallite. Planar nanobattery allows the intrinsic electrical conductivity measurement

with single crystalline 2D battery electrode upon ion intercalation and deintercalation process, which is lacking in conventional battery characterization techniques. We discovered that with a “rapid-charging” process at the first cycle, the lithiated MoS<sub>2</sub> undergoes a drastic resistance decrease, which in a regular lithiation process, the resistance always increases after lithiation at its final stage. This discovery leads to a 2-fold increase in specific capacity with with rapid first lithiated MoS<sub>2</sub> composite electrode material, compare with the regular first lithiated MoS<sub>2</sub> composite electrode material, at current density of 250 mA/g.

MANIPULATION OF IONS, ELECTRONS, PHOTONS IN 2D MATERIALS BY  
ION INTERCALATION

By

Jiayu Wan

Dissertation submitted to the Faculty of the Graduate School of the  
University of Maryland, College Park, in partial fulfillment  
of the requirements for the degree of  
Doctor of Philosophy  
2016

Advisory Committee:  
Associate Professor Liangbing Hu, Chair  
Professor Michael Fuhrer  
Professor Loudas Salamanca-riba  
Professor Chunsheng Wang  
Assistant Professor Yifei Mo

© Copyright by  
Jiayu Wan  
2016

## **Acknowledgements**

First and foremost, I would like to give my sincere thankfulness to my advisor, Dr. Liangbing Hu for giving me this opportunity to work with him in Bingnano group. I deeply appreciate his professional supervision to me throughout the five years. My success as a material science PhD is impossible without his guidance and support. He is and will still remain a role model in my life after graduation with his hardworking, dedicative, collaborative work style. I would also like to thank the committee members for their precious time and suggestions to my thesis.

I appreciate the previous postdoc, Dr. Wenzhong Bao, now a Professor at Fudan University in China. I still remember the days when we did overnight experiments together and the moments with breakthrough in the experiments. I am also grateful to the students I supervised and worked with in Bing group, Nick Weadock, Nich Feanza, Steven Lacey, Feng Gu, Dan Urban, Yue Xu, John Panagiotopoulos, Emily Hitz, Yanbing Wang, Lisha Xu, Yanan Chen, Dr. Fei Shen, Dr. Wei Luo, Dr. Colin Preston Dr. Hongli Zhu and Dr. Xiaogang Han. I thank all the Bing group members throughout the years for all the laughter we had together.

I would also like to thank my collaborators. Prof. Michael Fuhrer, Prof. Dennis Drew, Prof. Jeremy Munday, Prof. Jay Guo, Dr. Kang Xu, Dr. Yang Liu, Dr. Anmin Nie, Dr. Veronica Barone, and Mr. Burak Ozdemir who has been extremely supportive and patient to me in our collaborative projects.

At last, thank my mom Jiangnan Ren and my wife Haoting Cui. I cannot go this far without the two of you, and all my achievements are meaningful because of you.

# Table of Contents

<b>Acknowledgements</b> .....	ii
<b>List of Tables</b> .....	viii
<b>List of Figures</b> .....	ix
Chapter 1: Introduction.....	1
1.1 Introduction to 2D materials .....	1
1.1.1 What are 2D materials?.....	1
1.1.2 Preparation and growth of 2D materials .....	3
1.1.3 Modification of 2D materials.....	6
1.1.4 Intercalation of 2D materials .....	7
1.1.5 preparation of intercalated 2D materials.....	8
1.1.6 Current status of intercalation tuned 2D materials .....	10
1.2 Li-ion batteries and Na-ion batteries.....	27
1.2.1 Introduction to Li-ion batteries and Na-ion batteries.....	27
1.2.2 Layered materials for batteries.....	28
1.2.3 Current technology for <i>in situ</i> characterization of 2D battery materials upon intercalation.....	30
1.3 Objective of this research.....	32
1.3.1 Problem statement.....	32
1.3.2 Objective .....	33
Chapter 2: Design and build <i>in situ</i> planar battery for 2D materials intercalation .....	35
2.1 Introduction.....	35
2.2 Experimental .....	35

2.2.1 Planar battery for <i>in situ</i> optical studies.....	35
2.2.2 Planar nano battery for <i>in situ</i> electrical transport studies.....	38
Chapter 3: Li-ion intercalation in few layer graphene—approaching the limits of transparency and conductivity in graphitic materials .....	41
3.1 Introduction.....	41
3.2 <i>In situ</i> optical measurements and results .....	43
3.3 Drude and interband contribution of increased transmittance in intercalated ultrathin graphite.....	50
3.4 <i>in situ</i> measurement of electrical transport properties .....	54
3.5 transparent conductor performance of Li intercalated ultrathin graphene.....	57
3.6 Scalable application of Li intercalation with large area CVD graphene .....	60
3.7 Discussion and Summary.....	63
Chapter 4: Na-ion intercalation in large-scale, printed RGO network as high performance transparent conductors .....	66
4.1 Introduction.....	66
4.2 Electrochemical characterization of Na-ion intercalation in RGO thin film .....	69
4.3 Optical transmittance characterization of printed RGO film upon Na-ion intercalation.....	71
4.4 Performance of Na-ion intercalated RGO as transparent conductor .....	74
4.5 Air stability of Na-ion intercalated RGO transparent conductors .....	76
4.6 Summary .....	78
Chapter 5: In situ TEM study of Na-ion interaction with high performance RGO anodes .....	80

5.1 Introduction.....	80
5.2 preparation and characterization of rapid RGO Na-ion battery anode .....	82
5.3 In situ TEM characterization of Sodiation process with rapid RGO .....	86
5.4 Electrochemical performance of rapid RGO as Na-ion battery anode .....	92
5.5 Summary .....	95
Chapter 6: Electrochemical K-ion intercalation with graphite and RGO materials .....	97
6.1 Introduction.....	97
6.2 Electrochemical intercalation of K-ions in graphite electrodes .....	99
6.3 Electrochemical intercalation of K-ions in rGO electrodes .....	107
6.4 Conclusion .....	113
Chapter 7: Tunable broadband printed carbon transparent conductor by Li-ion and Na-ion intercalation.....	114
7.1 Introduction.....	114
7.2 Fabrication of large scale, printed CNT/rGO/CNT sandwich thin film .....	116
7.3 Reversible change of transmittance with intercalation/deintercalation .....	118
7.4 Optical modulation of CNT/rGO/CNT in Infrared region via ion intercalation...	122
7.5 DFT Calculation for broadband transmittance with intercalation .....	125
7.6 conclusion .....	132
Chapter 8: Li intercalation in MoS <sub>2</sub> with planar batteries—resistance change matters in battery electrodes .....	134
8.1 Introduction.....	134
8.2 Electrical measurement of MoS <sub>2</sub> upon lithiation by planar nano battery .....	136
8.3 In situ TEM characterization of MoS <sub>2</sub> upon Lithiation .....	140

8.4 In situ optical characterization of MoS <sub>2</sub> upon lithiation .....	144
8.5 Scalable application of MoS <sub>2</sub> electrode materials in Li ion batteries .....	146
8.5 Summary .....	149
Chapter 9: Li intercalation in 2D Si Nanowall array fabricated with nanoimprint lithiography .....	
9.1 Introduction.....	151
9.2 Fabrication and Characterization of Si nanowalls for LIBs.....	154
Figure 9.1 Outline of NIL process for Si nanowalls anode on an SS substrate (the SS substrate is not shown in this figure) .....	155
9.3 Electrochemical properties of Si nanowalls in Li half cell .....	157
9.4 Nanopore formation mechanism by modeling.....	162
9.5 Summary .....	166
Chapter 10: Conclusion.....	
10.1 Conclusion .....	167
10.2 Future Work .....	168
10.2.1 Improve the air stability of the ion intercalated film for optoelectronic devices .....	168
10.2.2 Investigate novel physical and chemical properties of a variety of 2D materials by intercalation.....	169
10.2.3 Real time and <i>in situ</i> investigate the properties of battery materials during ion insertion/desertion.....	170
Bibliography / References.....	171

## List of Tables

<b>Table 1.1</b> A summary of 2D materials, including graphene family, 2D chalcogenides and 2D oxides.....	3
<b>Table 1.2</b> Maximum (max) carrier density of 2D materials with different doping methods.....	11
<b>Table 5.1</b> Atomic percentage of carbon and oxygen from XPS analysis. (450 stands for rGO regular reduced at 450 °C, details in supplementary materials).....	84
<b>Table 10.1</b> Summary of intercalation in 2D layered materials, properties, and applications.....	168

## List of Figures

**Figure 1.1** (a) schematic of atomic structure of graphene (top view and side view), (b) calculated bandstructure of monolayer graphene, zoomed-in Dirac cone structure, (c-e) schematic atomic structure (top view and side view) of Boron Nitride, hexagonal and tetragonal metal dichalcogenide.....2

**Figure 1.2** Calculated bandstructure of bulk, 4-layers, bilayer and monolayer MoS<sub>2</sub>.....3

**Figure 1.3** Schematic illustration of tunable intercalation in 2D materials. Summary of the intercalation species, intercalation host (i.e. 2D materials), properties, and applications of intercalation tuned 2D materials.....8

**Figure 1.4** Electrical properties of FeCl<sub>3</sub>-intercalated FLG (a) SdH oscillations in  $R_{xx}(B)$  are recorded at temperatures of 2, 10, 20, and 40 K. Inset shows a schematic of an intercalated bilayer graphene device. (b) Atomic structural model of intercalated and unintercalated bilayer graphene domains. (c) Band diagrams of two domains exhibiting different electronic properties, especially chemical potential, carrier density, and band structures. (d) Longitudinal conductance as a function of magnetic field at different temperatures (curves shifted for clarity). (e) Schematic crystal structure of a 5L FeCl<sub>3</sub>-FLG in which the detailed structure was determined by electrical transport measurements.....12

**Figure 1.5** Electrical properties of tunable Li intercalation in MoS<sub>2</sub> (a) Extrapolation of the red lines yields contact resistances ( $R_c$ ) of 0.2 k $\Omega$ · $\mu\text{m}$  for 1T phase contacts at zero gate bias. Inset in (b) shows the percentage decrease in contact resistance with different gate voltages. An optical microscope image and device schematic are also shown as insets..... 13

**Figure 1.6** Electrical properties of Li-intercalated TaS<sub>2</sub> (a) Resistance  $R$  (normalized to its initial value  $R_0$ ) shown as a function of  $V_g$  for samples with varying thicknesses. The phase transition is manifested as the sudden drop in resistance by one-half. (b-d) Temperature-dependent resistances at fixed  $V_g$  for three sample thicknesses: 14 nm, 8 nm and 3.5 nm. The inset in each panel displays the gate-induced phase transition at 310 K. (e) Resistance and volumetric carrier density measured as a function of  $V_g$  at 10 K in the same 14-nm-thick sample shown in (b). (f-h) Doping–temperature phase diagrams of 1T-TaS<sub>2</sub> sheets in bulk, quasi-two-dimensional and two-dimensional regimes, respectively.....15

**Figure 1.7** Optical and photonic properties of zerovalent metal and organic intercalated 2D materials. (a) Schematic of Cu-intercalated  $\text{Bi}_2\text{Se}_3$ . Microscope image of  $\text{Bi}_2\text{Se}_3$  (b) before and (c) after Cu intercalation. (d) Band structure of Cu-intercalated  $\text{Bi}_2\text{Se}_3$ . Optical transmittance of  $\text{Bi}_2\text{Se}_3$  over the (e) visible and (f) near-infrared spectral range before and after Cu intercalation. Schematics of zerovalent metal intercalated  $\text{MoO}_3$ : (g) crystal structure and (h) band structure. (i) Digital images of the reversible intercalation of Co metal in  $\text{MoO}_3$ . (j-l) EELS and diffraction patterns of intercalated  $\text{Bi}_2\text{Se}_3$  with organic molecules.....17

**Figure 1.8** Thermoelectric properties of tunably intercalated  $\text{TiS}_2$  (a) High resolution TEM image of  $(\text{SnS})_{1.2}(\text{TiS}_2)_2$  along the [100] zone axis. The zoom-in image depicts the actual crystal structure of  $(\text{SnS})_{1.2}(\text{TiS}_2)_2$ , reconstructed from the area indicated in the HRTEM image. (b) Total thermal conductivities  $k$  and the electron component  $k_e$  of  $\text{TiS}_2$  and  $(\text{SnS})_{1.2}(\text{TiS}_2)_2$  in both the in-plane and cross-plane directions. (c)  $ZT$  values of  $\text{TiS}_2$  and  $(\text{SnS})_{1.2}(\text{TiS}_2)_2$  in both the in-plane and cross-plane directions. (d) The process to electrochemically intercalate a  $\text{TiS}_2$  single crystal to create a  $\text{TiS}_2[(\text{HA})_x(\text{H}_2\text{O})_y(\text{DMSO})_z]$  superlattice. (e) In-plane thermal conductivity vs. temperature. (f) In-plane thermoelectric figure of merit vs. temperature.....18

**Figure 1.9** Thermal properties of tunable Li intercalation in  $\text{LiCoO}_2$ . (a) Schematic of the *in situ* measurement cell consisting of ~500 nm  $\text{LiCoO}_2$ , 70 nm Al transducer and 100 nm  $\text{SiO}_2$  thermal isolation layer on a sapphire substrate. (b) TDTR data (open circles) and thermal conductivity fit (lines) for representative lithiated ( $x=1.0$ ) and delithiated ( $x=0.6$ )

Li<sub>x</sub>CoO<sub>2</sub>. (c) Thermal conductivity and potential as a function of lithium insertion. (d) The lithiation-dependent longitudinal elastic modulus of Li<sub>x</sub>CoO<sub>2</sub> calculated from the longitudinal speed of sound. In both (c) and (d), the data in red and blue corresponds to the delithiation process and the lithiation process, respectively.....20

**Figure 1.10** Magnetic properties of metal/molecule intercalated 2D materials. (a) Schematic crystal structure of trilayer FeCl<sub>3</sub>-FLG. (b) The measured weak localization contribution to the magneto-conductance (scatter points) and theoretical fits (solid line). (c) The temperature dependence of  $L_{\phi}$  for pristine graphene prepared by different methods. The values are compared to the estimated values of FeCl<sub>3</sub>-FLG. (d) The crystal structure of Fe<sub>0.25</sub>TaS<sub>2</sub>. (e) Measurement of magnetoresistance  $\Delta\rho/\rho_0$  for bulk and thin Fe<sub>0.28</sub>TaS<sub>2</sub> devices at selected temperatures for  $H \parallel c$  axis, and  $i \parallel ab$ -plane. (f) Comparison of  $H_S$  and  $\Delta\rho/\rho_0$  peak height values as a function of temperature for bulk (solid symbols) and thin 2D devices. The inset displays a typical bulk sample (left) and an exfoliated sample with metal contacts (right).....22

**Figure 1.11** Enhanced energy storage properties for tunable Li-intercalated MoS<sub>2</sub> (a) Digital image of a flexible 1T-MoS<sub>2</sub> electrode. (b) HRTEM image of 1T-MoS<sub>2</sub>. (c) Capacitance of 1T-MoS<sub>2</sub> electrodes in various solutions. (d) Schematic of MoS<sub>2</sub> intercalated with different solvated ions.....24

**Figure 1.12** Catalytic properties of tunable Li-intercalated MX<sub>2</sub> 2D materials (a) Schematic of WS<sub>2</sub> with 2H and 1T phases. TEM images of (b), (c) and diffraction pattern

of (d), (e) of WS<sub>2</sub> before and after Li intercalation. (f) Tafel plot of MoS<sub>2</sub> and WS<sub>2</sub> catalyst with different forms. (g) Electrochemical preparation of 1T-MoS<sub>2</sub> for water splitting. (h) Tafel plot of 1T-MoS<sub>2</sub> as a water splitting catalyst. (i) SEM image of the 1T-MoS<sub>2</sub> catalyst.....27

**Figure 1.13** Schematic of a standard Li-ion or Na-ion battery with liquid electrode.....28

**Figure 1.14** Voltage profile of Li intercalation in graphite, with different intercalations stages.....30

**Figure 1.15** (a) schematic of in situ TEM set up for lithium intercalation in GNR (b-d) Morphological evolution of a (de)lithiated GNR using *in situ* TEM.....32

**Figure 2.1** Fabrication process of planar device for optical measurements of 2D materials with ion intercalation.....36

**Figure 2.2** Schematic of optical transmittance measurement of 2D materials by intercalation, controlled with battery tester. Inset demonstrate the AFM image of FLG with metal electrode on glass substrate.....37

**Figure 2.3** Fabrication process of planar nanobattery for electrical transport measurements of 2D materials with ion intercalation.....39

**Figure 2.4** Process flow of ultrathin graphite transfer and cell encapsulation.....39

**Figure 2.5** Optical transmission images of devices with ultrathin graphite sheets transferred onto pre-fabricated Hall bar electrodes. The scale bar is 20  $\mu\text{m}$ .....40

**Figure 3.1** Photo images of FLG upon lithium intercalation at different stages taken by optical microscope. (a). pristine, (b).  $\text{LiC}_{36}$ , (c).  $\text{LiC}_{12}$ , (d).  $\text{LiC}_6$ , (e). atomic structure of  $\text{LiC}_6$  and (f). delithiated FLG.....43

**Figure 3.2** Raman spectrum of FLG intercalation at different stages (a) range from 1400-1700  $\text{cm}^{-1}$ , (b) range from 1200 to 3000  $\text{cm}^{-1}$ .....45

**Figure 3.3** (a) Optical transmittance (right) and electrochemical potential (left) vs. lithiation time are plotted. (b) Detail of voltage profile vs. time near the intercalation plateau. (c-g) Optical images of an ultrathin graphite sheet at different time points during intercalation as indicated in each panel, showing a clear lithiation front (red dashed line) between  $\text{LiC}_{36}$  (lighter contrast) and  $\text{LiC}_{72}$  (darker contrast). The ultrathin graphite sample is about 120 layers thick and the scale bar in (c) is 20  $\mu\text{m}$ . (h) Lithiated  $\text{LiC}_{36}$  area vs. time extracted from images such as (c-g).....47

**Figure 3.4** Wavelength-dependent optical transmittance of intercalated ultrathin graphite. (a-c). Transmittance as a function of wavelength for different thickness ultrathin graphite samples for pristine ultrathin graphite (a), LiC<sub>12</sub> (b), LiC<sub>6</sub> (c) stages. (d-e) Transmittance as a function of thickness plot for pristine ultrathin graphite, LiC<sub>12</sub>, and LiC<sub>6</sub> at wavelengths 550 nm (d) and 800 nm (e). Insets show transmittance at same wavelength over a larger range of thicknesses.....49

**Figure 3.5** (a) Schematic of doped graphene bandstructure illustrating suppression of optical transitions due to Pauli exclusion principle. (b-c) Modeled results for transmittance (b), and the real part of optical conductivity,  $\sigma_1/N\sigma_0$  (c) of pristine ultrathin graphite (dashed line) and intercalated LiC<sub>6</sub> (solid line). For the model we assume  $E_F = 1.5$  eV,  $n = 1.5$ ,  $T = 300$ K, and  $1/\tau = \gamma = 200$  cm<sup>-1</sup>. The red and black colors in (b) correspond to 8 and 83-layer ultrathin graphite sheets, respectively. Experimental data of 8 and 83-layer shown in (Figure 2.7c) are also plotted in (b) for comparison with the model, (d). Modeled result for the real part of dielectric constant  $\epsilon$  vs. photon energy.....50

**Figure 3.6** Transport measurement of Li intercalated ultrathin graphite sheets. (a) Resistivity vs. thickness for ultrathin graphite sheets with different thickness. Data for pristine (red) and two lithiated stages (LiC<sub>12</sub> and LiC<sub>6</sub> indicated as green and blue) are shown. Inset: An optical image of an ultrathin graphite device with Hall bar geometry before intercalation. The scale bar is 10  $\mu$ m. (b) Hall resistance of a 4-nm-thick pristine FLG sheet and its LiC<sub>12</sub> and LiC<sub>6</sub> states as a function of magnetic field. (c) Carrier density calculated from Hall measurement as a function of ultrathin graphite thickness.

(d) Temperature dependent sheet resistance for two ultrathin graphite samples. Blue, red and green colors indicate pristine,  $\text{LiC}_{12}$  and  $\text{LiC}_6$  stages, respectively.....56

**Figure 3.7** Optical transmittance vs. sheet resistance for two batches of devices. Solid data points are taken on the same device using a concurrent optical/electrical measurement setup.....58

**Figure 3.8** Optoelectronic properties of intercalated ultrathin graphite sheets and comparison with other materials. (a) Transmittance at 550 nm vs. sheet resistance for our  $\text{LiC}_6$  FLG, and other high-performance carbon-based transparent conducting materials  $\text{FeCl}_3$ -doped graphene<sup>15</sup>, acid-doped graphene<sup>9</sup>, and carbon nanotube (CNT) films<sup>37</sup>, as well as indium tin oxide (ITO)<sup>39</sup>. The red solid line is a fit with equation 3 with  $\sigma_{\text{dc}}/\sigma_{\text{opt}} = 920 \pm 100$ . (b) Figure of merit ( $\sigma_{\text{dc}}/\sigma_{\text{opt}}$ ) for various materials. A higher value for  $\sigma_{\text{dc}}/\sigma_{\text{opt}}$  leads to better performance in transparent conductor.....60

**Figure 3.9** Demonstration of encapsulated large-area transparent electrode (a-b) Photographs of 40- and 80-nm thick CVD grown thin graphite before and after full Li intercalation. (c) Corresponding transmittance spectra of the two devices before and after full intercalation, (d) Van de Pauw measurement of CVD ultrathin graphite, and (e)  $R_s$  of pristine graphite and  $\text{LiC}_6$  for three 40-nm-thick CVD graphite devices.....62

**Figure 3.10** (a-c) Stability of encapsulated CVD thin graphite device in air. (d-g), Decapsulated thick  $\text{LiC}_6$  is stable in glove box but unstable in air.....63

**Figure 4.1** (a) Schematic of Na-ion intercalation between two RGO sheets, enhancing simultaneously their optical transmittance and electrical conductivity. (b) Schematic of Na-ion intercalation in printed RGO network on transparent substrate. (c) AFM image of a printed RGO network. (d) Highly transparent and stable S-RGO film (confined in red dotted square) in air after one month.....68

**Figure 4.2** Electrochemical and XRD characterizations of Na-ion intercalation in RGO thin films. (a) Voltage profile of RGO film as positive electrode in coin cell. Inset is the schematic of RGO-Na coin cell (b) XRD of RGO film before, after Na intercalation, and plastic wrap as background.....70

**Figure 4.3** (a) A bottle of as prepared GO ink to be added with Zynol to tailor the surface energy for printing purpose. (b) Meyer rod coating of GO ink with excellent uniformity on glass substrate. (c) A two terminal, lateral device with RGO network as working electrode, Na metal as the counter electrode and 1M NaPF<sub>6</sub> in EC:DEC (1:1=v:v) as the electrolyte. (d) After Na ion intercalation, the RGO network becomes more transparent.....72

**Figure 4.4** Optical transmittance of a RGO network device before and after Na-ion intercalation. (a-b) show optical microscope (transmission mode) images of the same RGO network before and after sodiation. (c) Transmittance vs. thickness of RGO network before and after sodiation at 550 nm. The inset is the percentage of relative

increase in transmittance at 550 nm. (d) Transmittance vs. wavelength of the same RGO network before and after sodiation with a visible spectrum from 450 nm to 900 nm.....73

**Figure 4.5** (a) Four-point probe I-V measurement of a RGO network before and after sodiation. Insets are the schematic and photo images of four-probe measurement on RGO network. (b) Sheet resistance change of two different samples. (c) Transmittance vs. sheet resistance plots of S-RGO vs. reported RGO network transparent conductors. (d) FOM of network transparent electrodes, including exfoliated graphene, S-RGO and RGO.....75

**Figure 4.6** Stability in air of transparent conductor based on S-RGO network. Photo images of S-RGO in air after 0, 0.5, 2 and 3 hours. The scale bar (white) is 2 mm.....77

**Figure 5.1** Schematics of two types of GO reduction process (a) stacked GO sheet is (b) slowly thermal reduced and (c) rapidly reduced.....82

**Figure 5.2** Methods and characterization of GO and rapid-rGO. (a) A schematic image of rapid reduction process by Xexon lamp, (b) XRD patterns of GO film and rapid-rGO, (c) XPS spectra of GO film and rapid-rGO, (d) C 1s spectrum of rapid-rGO, SEM images of (e) dense GO film and (f) rapid-rGO, inset a higher magnification SEM image of rapid-rGO.....85

**Figure 5.3** *In situ* TEM study of the first sodiation of rGO. (a) Schematic of in situ TEM set-up (b) TEM image of Na/Na<sub>2</sub>O as counter electrode/solid electrolyte and rGO as working electrode before sodiation (b) after sodiation (d) Diffraction pattern of rGO before sodiation (e) after sodiation.....87

**Figure 5.4** (a) High angle annular dark field (HAADF) image of sodiated RGO (b-d) Elemental distribution of sodiated RGO mapped by Energy-dispersive X-ray (EDX)....88

**Figure 5.5** HRTEM images of sodiated rGO. (a) Low-mag HRTEM image recording the surface of the sodiated rGO. (b) High-mag HRTEM image taken from the blue box in the panel a. (c) 2x2x2 supercell for BCC Na metal. (d) High-mag HRTEM image taken from the green box in the panel a. (e) 2x2x2 supercell for FCC Na<sub>2</sub>O.....90

**Figure 5.6** HRTEM images recording the first desodiation process of rGO. (a) HRTEM image of material on rGO before desodiation. Inset shows atomic scale HRTEM image of a Na metal and the corresponding FFT pattern. (b) HRTEM image of material on rGO after desodiation. Inset of the panel (b) shows an SAED pattern of the totally desodiated rGO.....91

**Figure 5.7** Electrochemical performance of rapid-rGO as anode for SIBs: (a) potential profiles of rapid-rGO anode at 500 mA/g, 250 mA/g, 125 mA/g, 50 mA/g and 25 mA/g, (b) rate performance of rapid-rGO at above-mentioned current rates, (c) cycling performance of rapid-rGO.....93

**Figure 6.1** Schematic illustration of electrochemical intercalation of Li, Na, and K ions into graphite and reduced graphene oxide (RGO). Li and K ions can electrochemically intercalate into both graphite and RGO, while Na ions can only be electrochemically intercalated into RGO.....97

**Figure 6.2.** Electrochemical intercalation of K and Li ions into graphite at ambient temperature and pressure. (a) A schematic of graphite electrode/K metal within coin-cell. (b) Discharge/charge profiles vs. K (blue) and Li (black) at 5 mA/g for graphite electrode; the highlighted part in (b) is enlarged and shown in (c) for a graphite/K system and (d) for a graphite/Li system.....100

**Figure 6.3** DFT calculations. (a) Calculated potential profile for K ions intercalation into graphite for different staging scenarios. Blue line (Theory (a)) corresponds to an intercalation staging:  $KC_{24}$ (Stage III)  $\rightarrow$   $KC_{16}$  (Stage II)  $\rightarrow$   $KC_8$  (Stage I). Green dotted line (Theory (b)) corresponds to calculated values for the previously reported staging:  $KC_{24}$  (Stage II)  $\rightarrow$   $KC_8$  (Stage I). Red dotted line corresponds to the averaged experimental data shifted by 26 mAh/g to correct the capacity contribution from SEI formation. (b) Scheme of the different stages of K-intercalated graphite, K shown in blue and C in yellow.....103

**Figure 6.4** *Ex situ* measurements of  $KC_8$  and the rate performance of graphite electrode. (a) Photo images, (b) XRD patterns, and (c) Raman spectra of graphite electrodes before

and after electrochemical intercalation of K ions. (d) Discharge/charge profiles for graphite electrodes at various current densities.....105

**Figure 6.5** CV curves of graphite electrode in graphite/K cell.....106

**Figure 6.6** Characterizations of RGO film and electrochemical intercalation of K ions into RGO film. (a) XRD pattern, (b) Raman spectrum, (c) SEM image and (d) discharge/charge profiles for the first two cycles at 5 mA/g of RGO film.....108

**Figure 6.7.** *In situ* optical measurements of RGO film. (a) Schematic of K ions intercalation into a printed RGO film. (b, c) Photo and (d, e) optical microscope images of the RGO film before and after K ions intercalation.....110

**Figure 6.8** Calculated band structure of (a) graphite and (b)  $KC_8$  (Stage-I), where the arrow between K-H indicates the shift in the Fermi level with respect to graphite; (c)  $\epsilon_1$  and (d)  $\epsilon_2$  calculated within the RPA in the visible range for pristine graphite as well as K intercalated graphite.....111

**Figure 7.1** Failure mechanism of pure rGO thin film during lithiation/delithiation process (a) schematic of ion intercalated rGO film, (b) schematic of ion deintercalation in rGO film. (c) photo image of cracked pure rGO film after ion deintercalation.....116

**Figure 7.2** (a) Schematic of alkali ion intercalation in a CNT/rGO thin film. (b) Schematic of the CNT/rGO/CNT sandwich structure. Large scale printed CNT/rGO/CNT

film on PET substrate before Li-ion intercalation (c) and after Li-ion intercalation (d). (e) Typical transmittance change of carbon film before and after Li-ion intercalation for selected wavelengths of 550 nm (visible range) and 2 $\mu$ m (infrared range).....116

**Figure 7.3** (a) photo images and (b) microscope images of pristine, lithiated and delithiated CNT/rGO/CNT film. Reversible transmittance change at visible range (wavelengths of 450 nm, 550 nm, 750 nm). The length of scale bars in figure (a) and (b) are 1 cm and 50  $\mu$ m, respectively. Transmittance obtained in (c) pristine, lithiated, and delithiated CNT/rGO/CNT network and (d) pristine, sodiated, and desodiated CNT/RGO/CNT network.....118

**Figure 7.4** (a) Schematic of in situ Raman with planar battery of CNT/rGO/CNT thin film with ion intercalation and deintercalation process. Raman spectrum of (b) pristine, lithiated, delithiated and (c) pristine, sodiated and desodiated CNT/rGO/CNT thin film.....120

**Figure 7.5** (a) Schematic of IR transmission characterization with CNT/rGO/CNT film by IR camera. False color image of the CNT/rGO/CNT film before and after (b) Li ion intercalation and (c) Na ion intercalation. Transmission change of the CNT/rGO/CNT before and after (d) Li ion intercalation, inset a simplified schematic (e) Na ion intercalation, as a function of energy in the infrared range.....122

**Figure 7.6** Figure 7.6. (a) Top and side views of  $\text{LiC}_6$  structure; yellow and gray balls represent C and Li atoms, respectively. (b) Electronic structure of 6 layers of graphene using the optimized interlayer separation of 3.311 Å labelled as “Graphene (6)” and using an increased interlayer separation of 4.00 Å labelled as “Graphene\*\* (6)”. Transmission of (b) 6 and (c) 20 layers of graphene and  $\text{LiC}_6$ , and reflectance of (d) 6 layers and (e) 20 layers of graphene and  $\text{LiC}_6$ . All the results are obtained from the electronic structure of 6 layers, except “Graphene\* (20)” which is obtained by using the electronic structure of bulk graphite. “Graphene\*\* (20)” is obtained from the electronic structure of 6 layers of graphene with 4 Å of increased interlayer spacing instead of the LDA optimized value of 3.311 Å. Blue arrow in (e) and (f) denote the intraband transitions and interband transitions of the intercalated graphene.....124

**Figure 8.1** Li-MoS<sub>2</sub> microbattery. (a) Lattice structure of 2H-MoS<sub>2</sub>. (b) Schematic of MoS<sub>2</sub>-Li microbattery. (c), (d) Optical images of large area uniform MoS<sub>2</sub> crystals on glass substrates at 550 nm wavelength under transmission mode; both scale bars are 50 μm. (e) AFM image of MoS<sub>2</sub> crystal in (c). (f) Line trace of AFM image along dashed line in (e). (g) Photograph of microbattery. (h) Micrograph of electrode area with MoS<sub>2</sub>.....136

**Figure 8.2** Electronic transport measurement. (a) Resistance vs. time of MoS<sub>2</sub> flake undergoing electrochemical lithiation at constant current. Insets show a schematic of the microbattery setup for *in situ* resistance measurement (upper right), and optical images of lithiated MoS<sub>2</sub> at stages I, II, and III, from left to right. (b) Resistance vs. time for a

MoS<sub>2</sub> crystal after electrically shorting the microbattery. Insets show a schematic of the microbattery for *in situ* resistance measurement during shorting, and a log-log plot of the resistance vs. time. (c) Resistance vs. thickness phase diagram of shorted MoS<sub>2</sub> crystals; red circles show resistance of pristine MoS<sub>2</sub>, black diamonds show resistance after shorting of microbattery. (d) Schematic showing discontinuous Mo particles imbedded in Li<sub>2</sub>S matrix resulting from slow lithiation in thick MoS<sub>2</sub>. (e) Schematic showing percolative Mo nanoparticle network imbedded in Li<sub>2</sub>S matrix resulting from fast lithiation in thick MoS<sub>2</sub>. (f) Schematic of discontinuous Mo particle network imbedded in Li<sub>2</sub>S matrix resulting from fast lithiation in thin MoS<sub>2</sub> crystallite..... 139

**Figure 8.3** *In situ* TEM of MoS<sub>2</sub> lithiation. (a) Schematic illustration of *in situ* TEM microbattery setup. (b) Pristine MoS<sub>2</sub> nanoflake attached on Au substrate. (c) Electron diffraction pattern of pristine MoS<sub>2</sub>, the spots circled by red correspond to the 2H crystal structure of MoS<sub>2</sub>. (d) HRTEM of the MoS<sub>2</sub> flake showing lattice constant of 0.27 nm. (e) TEM of final product after full lithiation. (f) Electron diffraction pattern of final product. Rings in the diffraction pattern correspond to randomly oriented crystallites; the corresponding crystal indices for Mo and Li<sub>2</sub>S are indicated in the legend. (g) HRTEM image of the final product.....142

**Figure 8.4** Transmission electron micrographs of MoS<sub>2</sub> and Li<sub>x</sub>O/Li electrode (a) before and (b) after lithiation of MoS<sub>2</sub>.....143

**Figure 8.5** *In situ* optical transmittance measurement. (a) Schematic of *in situ* optical transmittance measurement of MoS<sub>2</sub> lithiation. (b-d) Optical images of a MoS<sub>2</sub> flake at 2.8 V, 0.9 V and 0.05 V. (e) Transmittance of MoS<sub>2</sub> flake vs. Li insertion voltage. (f) transmittance vs. wavelength for lithiated MoS<sub>2</sub> at three different stages. (g) Thickness dependence of transmittance of MoS<sub>2</sub> flakes before and after lithiation.....145

**Figure 8.6** Performance of the composite electrodes in coin cells. (a) Cycling performance (at 50 mA/g for 30 cycles and 250 mA/g for 70 cycles) of MoS<sub>2</sub>/NFC/CNT Li ion batteries at different initial lithiation conditions. Inset is a coin cell. (b) Voltage profile of two types of coin cells at 15<sup>th</sup> cycle. (c). Initial rapid charged coin cells cycle at different charge/discharge current density.....148

**Figure 9.1** Outline of NIL process for Si nanowalls anode on an SS substrate (the SS substrate is not shown in this figure).....154

**Figure 9.2** (a) SEM images of a large area and uniformly distributed Si nanowalls structures, (b) SEM image which shows the dimensions of the Si nanowalls (c). SEM EDS mapping images of Si nanowalls, (d) Energy dispersed X-ray spectroscopy of Si nanowalls/substrate, with peaks of Si, Cr and Fe.....156

**Figure 9.3** (a). Electrochemical cycling performance of Si nanowalls anodes (b) Voltage profile of 1st, 10th, 20th and 40th cycle of the Si nanowalls (c) EIS plot of the battery

before cycling (blue) and after 40 cycles (red) (d) The rate performance of the Si nanowalls half cell.....158

**Figure 9.4** (a) and (b) SEM images at different magnifications of the Si nanowalls anode after cycling. A residual Cr layer from the mask is observed on top of the nanowalls. (c) High magnification SEM of Si nanowalls after cycling shows porous structure with an average pore size of ~30 nm.....160

**Figure 9.5** Lithiation/delithiation-induced mean stresses in the nanowalls. (a) Schematic of the simulation model. The origin of the coordinate system is defined with origin at the centroid of the bottom surface. (b) and (c) show the mean stress distribution within the mid-plane of the nanowalls ( $z = 0$ ) and outer surface of nanowalls ( $z = h/2$ ) during the lithiation half cycle, respectively, with extent of lithiation described by  $x_{\text{average}} = 1$ . (d) and (e) are the counterparts of (b) and (c) during delithiation half cycle, respectively.....164

## Chapter 1: Introduction

### 1.1 Introduction to 2D materials

#### 1.1.1 What are 2D materials?

2D materials are a class of materials that are of one or few atomic layer thick that exhibit distinct different properties of its bulk form.<sup>1-7</sup> Graphene, an air-stable atomic layer thick carbon with honeycomb structure was first exfoliated in 2004 and exhibit unique “Dirac-cone” bandstructure (Figure 1.1 (a-b)) and ultrahigh electron mobility thus lead to excellent electrical and optical properties.<sup>3, 8-10</sup> Since the discovery of graphene, numerous 2D materials (Figure 1.1 (c-e) and table 1.1) have been studied with interesting physical and chemical properties. For example, hexagonal  $\text{MX}_2$  (2H- $\text{MX}_2$ , i.e.  $\text{MoS}_2$ ,  $\text{WS}_2$ ) in its bulk form is a semiconductor with an indirect bandgap.<sup>11</sup> When the its layer number decreases, the indirect bandgap increase at  $\Gamma$  point due to the decoupling between each X-M-X interlayers, where its state originate from a combination of d-orbitals on M atoms and antibonding  $p_z$  orbitals on X atoms. While the states at the K point are primarily composed of strong localized M d-orbital, and this bandgap is independent with layer numbers since the M atoms are in the middle of the X-M-X layer, isolated from neighbor M atoms between layers. The indirect bandgap of quantitative change from bulk  $\text{MX}_2$  to its monolayer brings a qualitative change in bandgap, where a direct bandgap generate at K point.<sup>11, 12</sup> (Figure 1.2) Also, phase change can be induced in  $\text{MX}_2$  materials from 2H to 1T phase via chemical treatment, where its semiconducting nature of  $\text{MX}_2$  will change to metallic, with conductivity increase with orders of magnitude.<sup>13</sup> The variety and novel properties of 2D materials spur fundamental studies and technological

advancements for a wide range of applications including (opto)electronics,<sup>14, 15</sup> superconductors,<sup>16</sup> photonics,<sup>17</sup> catalysis,<sup>6</sup> piezoelectric devices<sup>18</sup> as well as energy storage<sup>19-21</sup> and conversion devices.<sup>22</sup>

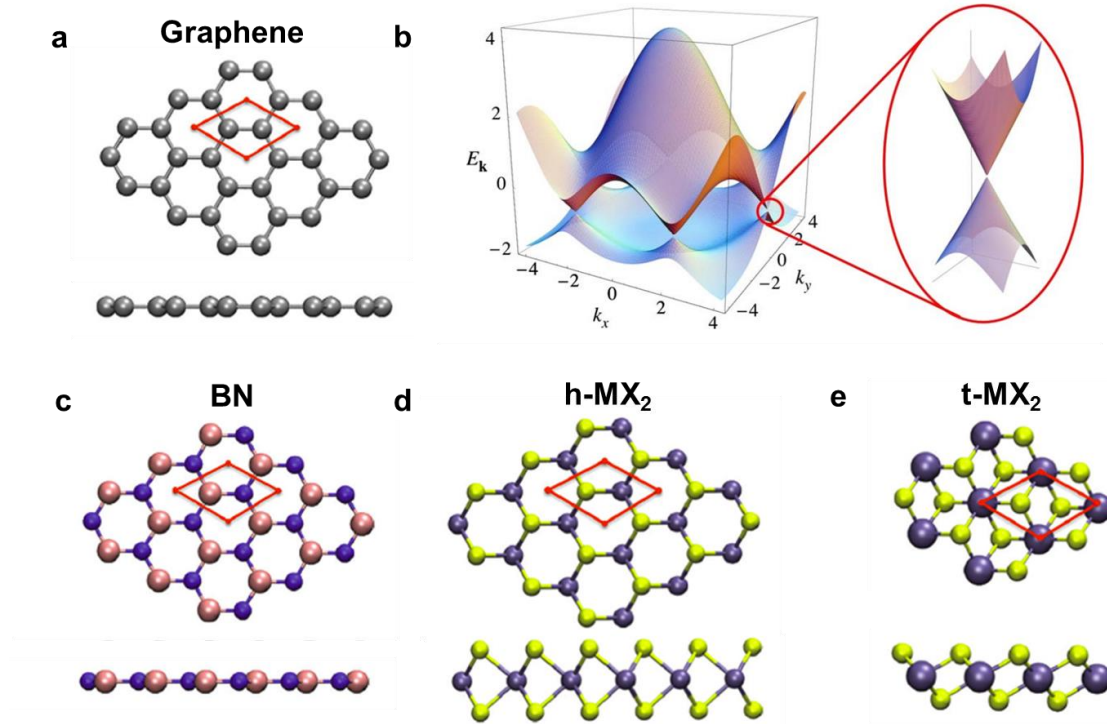


Figure 1.1. (a) schematic of atomic structure of graphene (top view and side view),<sup>7</sup> (b) calculated bandstructure of monolayer graphene, zoomed-in Dirac cone structure,<sup>8</sup> (c-e) schematic atomic structure (top view and side view) of Boron Nitride, hexagonal and tetragonal metal dichalcogenide<sup>7</sup>.

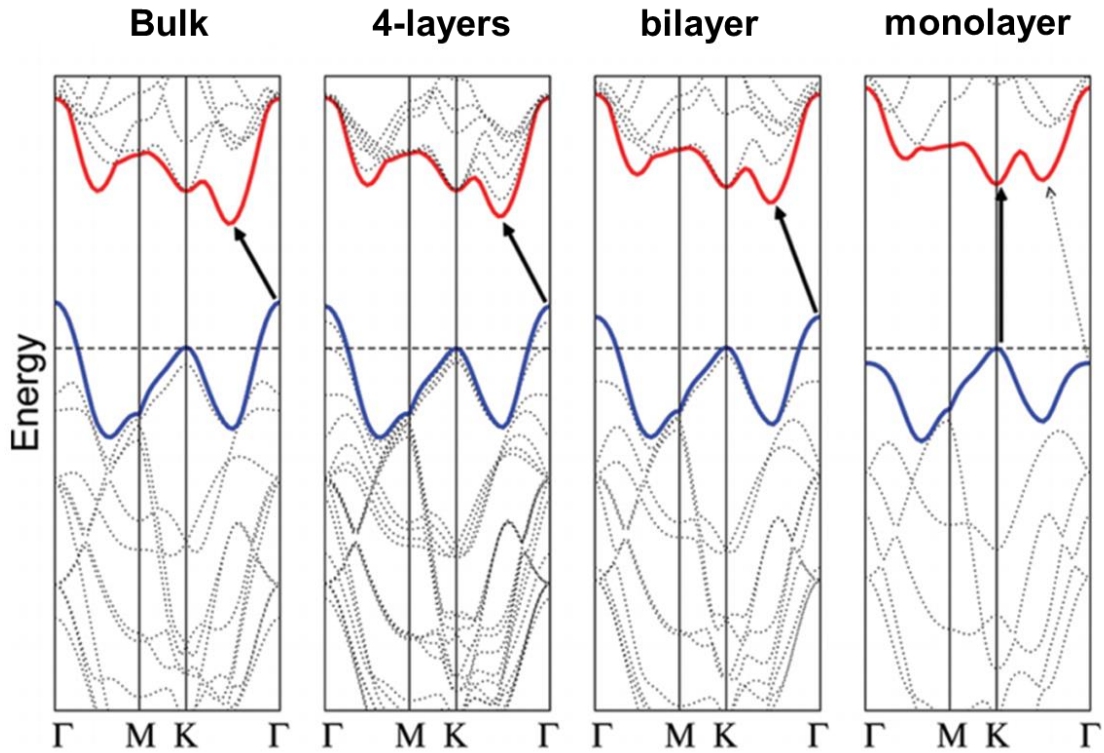


Figure 1.2 Calculated bandstructure of bulk, 4-layers, bilayer and monolayer MoS<sub>2</sub>.<sup>12</sup>

Table 1.1 A summary of 2D materials, including graphene family, 2D chalcogenides and 2D oxides.<sup>2</sup>

Graphene family	Graphene	hBN 'white graphene'	BCN	Fluorographene	Graphene oxide
2D chalcogenides	MoS <sub>2</sub> , WS <sub>2</sub> , MoSe <sub>2</sub> , WSe <sub>2</sub>		Semiconducting dichalcogenides: MoTe <sub>2</sub> , WTe <sub>2</sub> , ZrS <sub>2</sub> , ZrSe <sub>2</sub> and so on	Metallic dichalcogenides: NbSe <sub>2</sub> , NbS <sub>2</sub> , TaS <sub>2</sub> , TiS <sub>2</sub> , NiSe <sub>2</sub> and so on	
				Layered semiconductors: GaSe, GaTe, InSe, Bi <sub>2</sub> Se <sub>3</sub> and so on	
2D oxides	Micas, BSCCO	MoO <sub>3</sub> , WO <sub>3</sub>	Perovskite-type: LaNb <sub>2</sub> O <sub>7</sub> , (Ca,Sr) <sub>2</sub> Nb <sub>3</sub> O <sub>10</sub> , Bi <sub>4</sub> Ti <sub>3</sub> O <sub>12</sub> , Ca <sub>2</sub> Ta <sub>2</sub> TiO <sub>10</sub> and so on		Hydroxides: Ni(OH) <sub>2</sub> , Eu(OH) <sub>2</sub> and so on
	Layered Cu oxides	TiO <sub>2</sub> , MnO <sub>2</sub> , V <sub>2</sub> O <sub>5</sub> , TaO <sub>3</sub> , RuO <sub>2</sub> and so on			Others

### 1.1.2 Preparation and growth of 2D materials

To date, single- and multi-layered 2D materials have been prepared using numerous mechanical, chemical and electrochemical methods.<sup>23</sup> In general, the parent compounds of 2D materials are layered structures held together by strong in-plane covalent bonds and weak out-of-plane van der Waals forces. Exfoliation of these layered materials is enabled by taking advantage of their weak interlayer forces. Since Novoselov et al. successfully exfoliated bulk layered crystals into atomically thin layers (2D materials), the mechanical exfoliation (or scotch tape method) has gained widespread use to fabricate 2D materials as well as unique planar devices.<sup>3, 24, 25</sup> This method was originally developed for exfoliating 2D graphene layers from bulk graphite but has been universally applied to additional 2D materials including graphene analogs such as hexagonal boron nitride (hBN) as well as numerous 2D transition metal dichalcogenides, among others.<sup>4</sup> Unfortunately, the material yield from mechanical exfoliation is not sustainable for large-scale production.<sup>26</sup>

Chemical vapor deposition (CVD) is a well-known bottom-up growth technique for 2D materials (graphene, MoS<sub>2</sub>, boron nitride, among others) providing large-scale synthesis of mainly single-layered sheets.<sup>9, 27-34</sup> In this growth process, the deposition of solid materials occurs via chemical reactions of the precursor species which are controlled through processing parameters such as growth temperature, atmospheric conditions, the type of precursor, substrate and catalyst.<sup>9, 27, 28, 35</sup> CVD of monolayer graphene is conventionally done on inexpensive copper foil substrates.<sup>27-29, 35, 36</sup> However, transfer methods (such as the poly(methyl methacrylate) method) must be employed to relocate the 2D materials to the substrate of choice.<sup>27, 37-39</sup> This adds extra processing steps and creates polymeric residue on the sheets which must be removed to regain the

2D materials' desired properties for fundamental studies and/or functional devices. Additionally, structural defects are often introduced during the growth and transfer processes which alter the material's properties.

An alternative approach to obtain large scale production of 2D materials is through chemical methods via liquid-based exfoliation.<sup>9, 40-50</sup> Liquid-phase exfoliation relies on intercalation chemistry where foreign species are inserted into the van der Waals gap of each layer. The insertion of guest species such as solvent molecules increases the interlayer spacing, weakens the adhesion between layers and facilitates separation into 2D nanosheets. To initiate the intercalation and exfoliation of the 2D materials, sonication and centrifugation techniques are conventionally employed. However, sonication breaks the layers into sheets with small lateral dimensions (typically <1-2  $\mu\text{m}$ ) and creates mainly few-layered 2D materials.<sup>40, 45, 51</sup> Due to the presence of solvent and shear forces through sonication, the exfoliated flakes usually have chemical residues and a surplus of structural defects. This limits the potential of liquid exfoliated 2D materials since high-performance practical devices typically rely on high aspect ratio materials (i.e. the lateral width of 2D flakes is much larger than the flake thickness or number of layers) with low defect densities to improve properties. Additionally, the choice of solvent is crucial since efficient exfoliation relies on a stable dispersion as well as matching surface energies and solubility parameters (Hansen solubility parameters, Hildebrand parameter, etc.).<sup>40</sup> The types of solute-solvent interactions describe the dispersion process and are typically broken down into dispersion, polar and hydrogen bonding interactions, as denoted by the Hansen solubility parameters.<sup>40</sup>

Electrochemical intercalation method has also been applied to obtain 2D materials. Similar to liquid-phase exfoliation via solvent intercalants, ions or ionic compounds can be intercalated into layered materials, which reduce the interlayer adhesion between layers and create thin 2D nanosheets.<sup>52, 53</sup> Among these intercalation methods is ion exchange where the intercalants (i.e. ionic compounds) can weaken the interlayer forces by transferring charge to the 2D layers and enable exfoliation through shear forces. Numerous ion-based intercalants have successfully exfoliated graphite as well as transition metal dichalcogenides.<sup>9, 43, 52-56</sup>

### 1.1.3 Modification of 2D materials

Despite the unique intrinsic properties of 2D materials, various modification methods have been applied to these materials that yield even more exciting outcomes. We summarize the common modification methods of 2D materials in the following categories: (1) dimension sizing,<sup>57</sup> (2) vertical/lateral heterojunctions,<sup>2, 58</sup> (3) alloying and hybridization,<sup>59, 60</sup> (4) intercalation,<sup>61, 62</sup> (5) external field tuning,<sup>63, 64</sup> (6) stacking order,<sup>65</sup> (7) strain engineering,<sup>66</sup> among others. Each of these categories provide unique perspectives in studying both the fundamentals and applications of 2D materials. For example, dimensional sizing of MoS<sub>2</sub> from few layers to a monolayer alters the material's band structure from an indirect to a direct band gap,<sup>11</sup> which drastically improves its performance for optoelectronic devices. The narrowing of width also leads to a band gap in graphene.<sup>57</sup> In heterostructures, since many 2D materials are self-stable in air without dangling bonds, there is no need to consider lattice mismatches when stacking different

2D materials together. Thus, rationally designed 2D vertical structures provide a new degree of freedom for novel band engineering methods and applications.

Although intercalation of layered materials in their bulk form has been extensively investigated,<sup>67, 68</sup> the advent of 2D materials has significantly renewed interest in the field. As long as more than one atomically thin layer is present, intercalation is a possibility. Recent studies demonstrate that the intercalation of nanoscale-thickness layered materials has distinct differences compared to intercalation of the bulk materials, and in many cases the differences can result in drastically improved performance with potential in numerous applications.<sup>13, 61, 62, 69, 70</sup> In this thesis, we will refer to these nanoscale-thickness layered materials as “2D materials” for simplicity, with the assumption that the thickness of the material is much less than its lateral extent. Typically the nanometer scale (1-100 nm) is the range in which confinement of the electrons and phonons begins to alter the electrical, optical, mechanical, and other materials properties, hence the material begins to be two-dimensional.

#### 1.1.4 Intercalation of 2D materials

Among all modification methods, the intercalation of 2D materials stands out as a unique method to tune the properties of 2D materials for the following six reasons: (1) intercalation provides the highest possible doping and/or phase change to the pristine 2D materials, especially for few-layered 2D materials, (2) the intercalation process is typically reversible and intrinsically changes the properties of 2D materials, and (3) intercalation is controllable, for example by electrochemical voltage, where the

concentration of the intercalation species is tunable over a wide range; (4) changes in intercalated 2D materials during materials preparation can be *in situ* or monitored in real time; (5) intercalation can induce structural changes, such as lattice expansion or even phase changes, for improved or novel physical and chemical properties; (6) the intercalation method is not exclusive to other modification methods that adds a new degree of freedom for tuning 2D materials. Thus, we will review the state-of-the-art status of intercalated 2D materials, their preparation methods, physical and chemical properties as well as their applications (Figure 1.3).

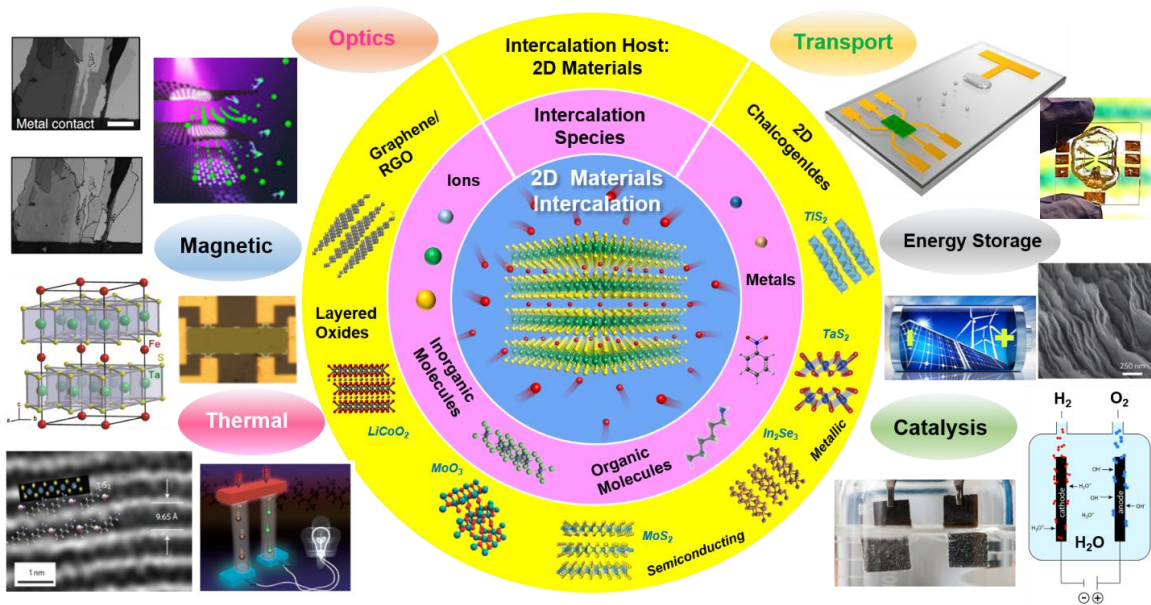


Figure 1.3 Schematic illustration of tunable intercalation in 2D materials. Summary of the intercalation species, intercalation host (i.e. 2D materials), properties, and applications of intercalation tuned 2D materials.

### 1.1.5 preparation of intercalated 2D materials

Intercalated functional 2D materials are typically prepared via chemical or electrochemical methods. Intercalation methods irrespective of both oxidation state changes and maintaining charge neutrality are also possible. Zerovalent intercalation relies on solution-based reactions to insert zerovalent metal species within the van der Waals gap of 2D materials.<sup>71-73</sup> In this way, numerous zerovalent metals including Cu, Ag, Au, Co, Fe, In, Ni, Pd and Sn and organic compounds can be intercalated into 2D materials such as Bi<sub>2</sub>Se<sub>3</sub> and modify its physical and chemical properties.<sup>72</sup>

Inorganic molecules can also be intercalated into 2D materials through chemical vapor-phase reactions. The most common preparation procedure is the two-zone vapor transport method where both the intercalant (such as metal chlorides and other diatomic molecules) and host materials (such as FLG, MoS<sub>2</sub>, among others) are heated at different temperatures and the gradient between them enables well-controlled intercalation stages.<sup>67, 74, 75</sup> Several groups have demonstrated enhanced electrical and optical properties by intercalating few-layer graphene with ferric chloride (FeCl<sub>3</sub>) for use in novel optoelectronic devices.<sup>76-78</sup>

Electrochemical methods enable the intercalation of cations (such as Li<sup>+</sup>) or anions (such as PF<sub>6</sub><sup>-</sup>) in the interlayer spacing of 2D materials (such as few layer graphene) through electrochemical reactions.<sup>79, 80</sup> These electrochemical approaches typically rely on a test cell configuration where the ions are supplied by the reference metal (i.e. Li) anode and intercalate into the 2D material cathode through the ionically conducting liquid electrolyte through an external bias. Additionally, electrochemical exfoliation of layered materials has been successfully demonstrated.<sup>81-86</sup> For instance, graphite can be electrochemically exfoliated into thin nanosheets with lateral dimensions

on the order of tens of microns in minutes by applying a low static bias followed by a high ramp bias between graphite and platinum electrodes in various electrolytes such as sulfuric acid.<sup>81</sup>

## 1.1.6 Current status of intercalation tuned 2D materials

### 1.1.6.1 Intercalation tuned electronic properties

Earlier electrical transport studies focused on the intercalation of layered materials have been recently revisited using their atomically-thin counterparts: 2D materials.<sup>61, 78, 87</sup> Since intercalated species induce charge transfer in the host 2D materials, the Fermi energy is shifted and the density of energy states at the Fermi level increases which in turn, increases the charge carrier density of the 2D materials. Such an extreme doping capability is far beyond conventional electric-field-induced doping levels in film devices<sup>63, 64</sup>, or electron-double-layer (EDL) surface gating<sup>88-90</sup> using an ionic liquid (Table 2). Intercalation generally provides more robust chemical compounds than a simple physical/chemical adsorption of molecules on the surface. This is due to the chemically inert and impermeable atomic thick crystals (such as graphene) that protect and encapsulate the unstable intercalants.

Table 1.2 Maximum (max) carrier density of 2D materials with different doping methods.

Doping method	Max carrier density ( $n_{2D}$ )	References
<i>Electric field gating</i>	$0.005 \times 10^{15} \text{ cm}^{-2}$	21, 22
<i>Ionic liquid</i>	$0.2 \times 10^{15} \text{ cm}^{-2}$	92, 93
<i>Chemical intercalation</i>	$(0.3-0.9) \times 10^{15} \text{ cm}^{-2}$	73
<i>Ion intercalation</i>	$(0.6-1) \times 10^{15} \text{ cm}^{-2}$	19,92

An early experimental study of electrical transport in intercalated 2D materials was reported by Kim et al.<sup>91</sup> where ferric chloride ( $\text{FeCl}_3$ )<sub>n</sub> was intercalated into bilayer graphene (BLG) using a two-zone method to achieve a vapor-phase reaction of  $\text{FeCl}_3$  and BLG. By patterning the BLG sheet to a Hall-bar geometry (Figure 1.4a inset), the local intercalation structure can be extracted by analyzing Shubnikov-de Haas oscillations (SdHO) (Figure 1.4a), represented as the longitudinal resistance ( $R_{xx}$ ) vs. perpendicular magnetic field B at different temperatures. At low temperatures,  $R_{xx}$  (B) oscillates with two distinct frequencies, which arise from two different carrier densities associated with the intercalated bilayer (decoupled to two separate monolayers) and the unintercalated bilayer (coupled). Figure 1.4b represents such spatially inhomogeneous intercalation of  $\text{FeCl}_3$ , with the intercalated domain size much smaller than 500 nm across the whole sample. Additionally, the band diagrams of two domains exhibit different electronic properties as shown in Figure 1.4c. A similar work<sup>78</sup> was later reported by Khrapach et al., using an exfoliated five layer (5L) graphene device. At low temperatures, SdHO also exhibits two distinct types of periodic magneto-oscillations (Figure 1.4d), with further analysis indicating the presence of four parallel hole gases, of which one possesses unintercalated bilayer character and three have monolayer character (Figure 1.4e).

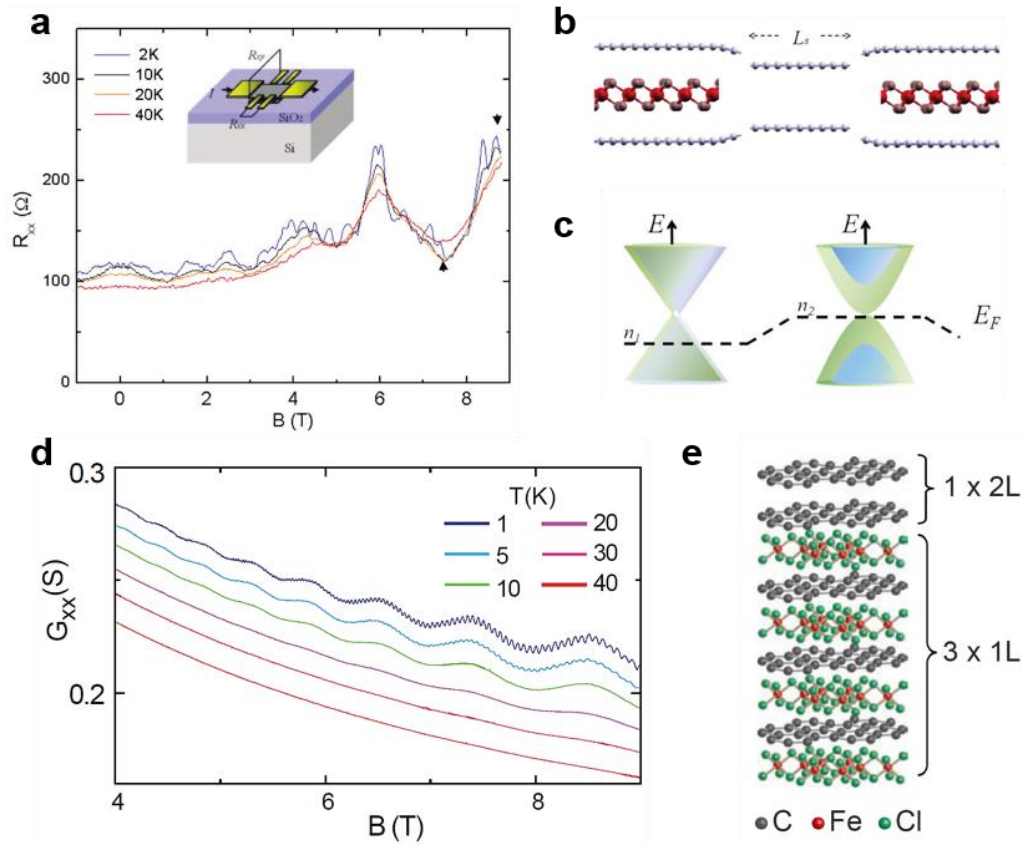


Figure 1.4 <sup>78, 91</sup> Electrical properties of FeCl<sub>3</sub>-intercalated FLG (a) SdH oscillations in  $R_{xx}(B)$  are recorded at temperatures of 2, 10, 20, and 40 K. Inset shows a schematic of an intercalated bilayer graphene device. (b) Atomic structural model of intercalated and unintercalated bilayer graphene domains. (c) Band diagrams of two domains exhibiting different electronic properties, especially chemical potential, carrier density, and band structures. (d) Longitudinal conductance as a function of magnetic field at different temperatures (curves shifted for clarity). (e) Schematic crystal structure of a 5L FeCl<sub>3</sub>-FLG in which the detailed structure was determined by electrical transport measurements.

Due to the phase transition of MoS<sub>2</sub> induced by reversible Li intercalation, Kappera et al. developed a methodology to locally convert regions of the semiconductive 2H-

MoS<sub>2</sub> nanosheets into metallic 1T-Li<sub>x</sub>MoS<sub>2</sub> phases and use them as electrodes to achieve MoS<sub>2</sub> FETs with low contact resistance.<sup>13</sup> In Figure 1.5, Au metal pads were contacted to the 1T phase areas, and the contact resistance was extracted using the transfer length method (TLM). In comparison to the typical MoS<sub>2</sub> devices, the resistance of the 1T contacts decreased by a factor of ~5 from 1.1 kΩ·μm to 0.2 kΩ·μm at zero gate bias. By further tuning the back gate voltage, the contact resistance decreased by another factor of three at a gate bias of +30V, as shown in the inset of Figure 1.5b.

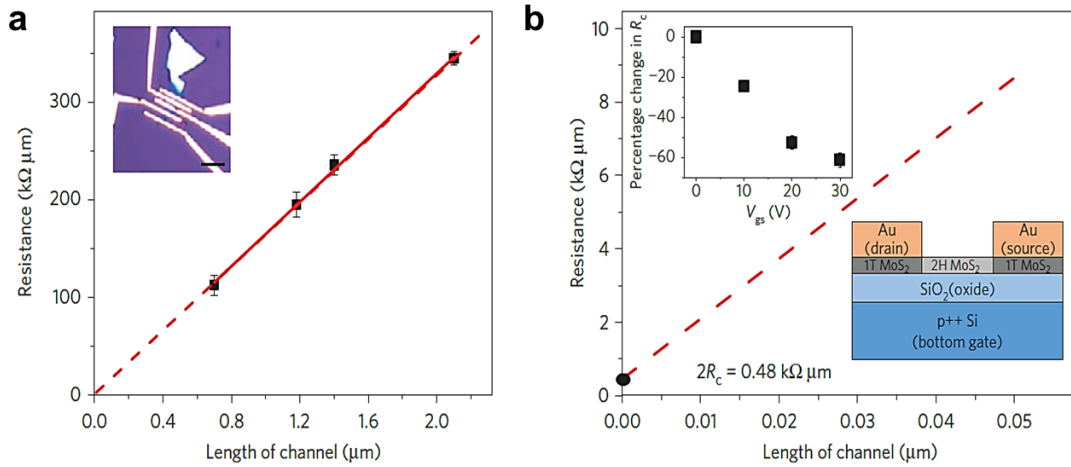


Figure 1.5 Electrical properties of tunable Li intercalation in MoS<sub>2</sub> (a) Extrapolation of the red lines yields contact resistances ( $R_c$ ) of 0.2 kΩ·μm for 1T phase contacts at zero gate bias. Inset in (b) shows the percentage decrease in contact resistance with different gate voltages. An optical microscope image and device schematic are also shown as insets.<sup>13</sup>

In addition to MoS<sub>2</sub> crystals, phase transitions also occur in TaS<sub>2</sub> during Li intercalation. Yu et al.<sup>62</sup> studied various charge-ordered states in 1T-TaS<sub>2</sub> ionic field-effect transistors (iFETs) with different crystal thickness, in which gate-controlled Li ion

intercalation modulates the phase transition (Figure 1.6a). The intercalation controlled phase transitions can be further probed by measuring the temperature-dependent resistance in samples at various fixed gate voltages (i.e. fixed Li concentrations), as shown in Figure 1.6b-d. A clear thickness dependence is present for each sample: the 14-nm-thick sample retains all the charge-density wave (CDW) phases; the 8-nm-thick sample is in the quasi-two-dimensional limit, where all but the commensurate CDW (CCDW) phases remain; the 3.5-nm-thick sample is an insulator without any phase transitions. At 10K under Li intercalation, the 14-nm device spans three different phases and shows resistance changes of five orders of magnitude (Figure 1.6e, upper panel). The volumetric charge carrier density  $n_{3D}$  in the three phases can also be determined from Hall measurements (Figure 1.6e, lower panel). More information about the competition, coexistence and cooperation of various collectively ordered states of intercalated TaS<sub>2</sub> are summarized in the phase diagrams shown in Figure 1.6f-h.

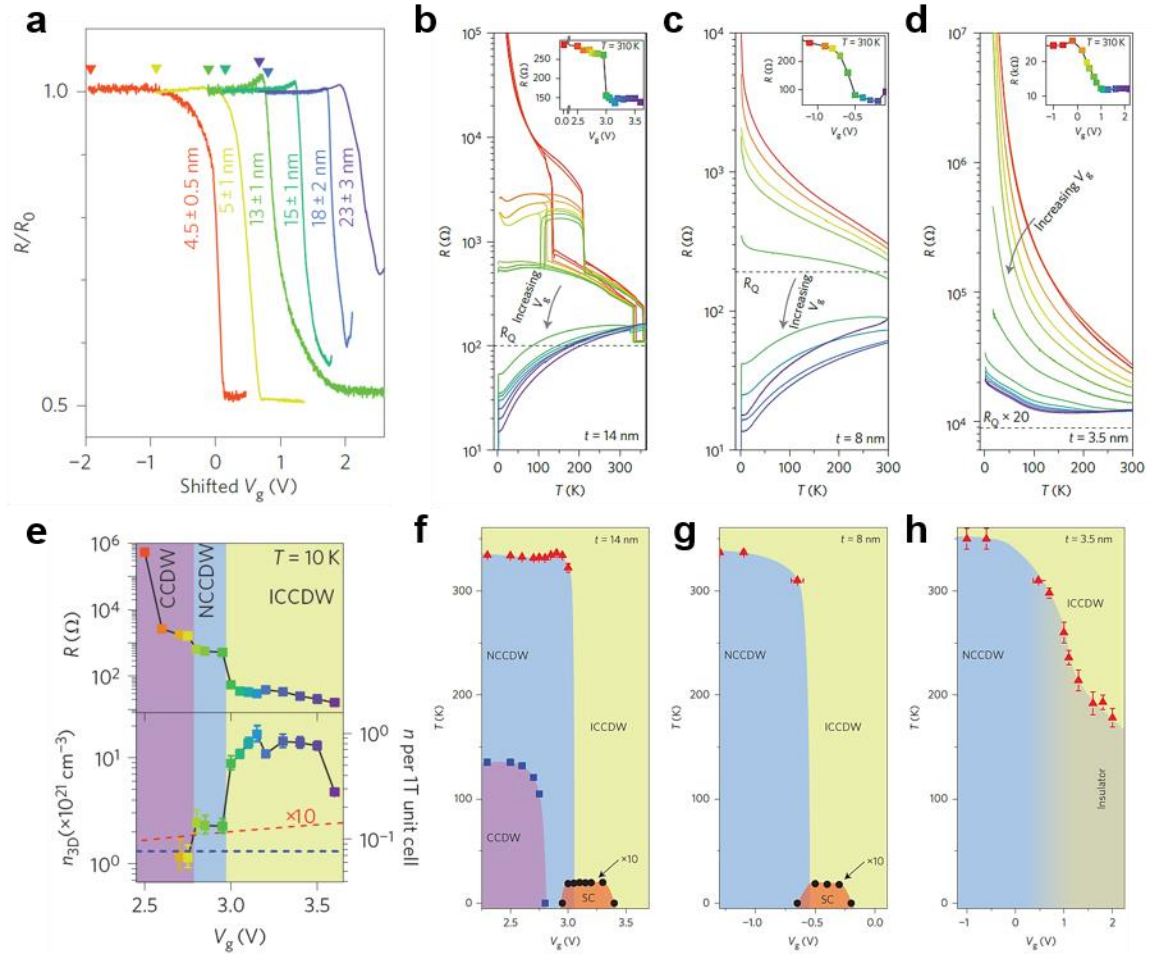


Figure 1.6 Electrical properties of Li-intercalated TaS<sub>2</sub> (a) Resistance  $R$  (normalized to its initial value  $R_0$ ) shown as a function of  $V_g$  for samples with varying thicknesses. The phase transition is manifested as the sudden drop in resistance by one-half. (b-d) Temperature-dependent resistances at fixed  $V_g$  for three sample thicknesses: 14 nm, 8 nm and 3.5 nm. The inset in each panel displays the gate-induced phase transition at 310 K. (e) Resistance and volumetric carrier density measured as a function of  $V_g$  at 10 K in the same 14-nm-thick sample shown in (b). (f-h) Doping–temperature phase diagrams of 1T-TaS<sub>2</sub> sheets in bulk, quasi-two-dimensional and two-dimensional regimes, respectively.<sup>62</sup>

### 1.1.6.2 Intercalation tuned optical properties

Besides the electrochemical intercalation of metal ions, other intercalation methods and guest species have been employed. Among them, zerovalent metal intercalation in  $\text{Bi}_2\text{E}_3$  ( $\text{E} = \text{S}, \text{Se}$ ) materials and metal oxides have attracted tremendous attention recently (Figure 1.7a-c).<sup>92-94</sup> Zerovalent metal intercalation in  $\text{Bi}_2\text{E}_3$  changes its electronic band structure (Figure 1.7d), induces optical properties changes of the host materials in both the visible (Figure 1.7e) and the near-infrared range (Figure 1.7f). Co-intercalation of various zerovalent metals in these materials has also been demonstrated.<sup>95</sup> A recent study on the chemical intercalation of zerovalent metals in metal oxides reveals the capability of reversible intercalation for chemochromic applications (Figure 1.7g-i).<sup>96</sup> Chemical intercalation can be further applied with organic intercalation species, which induces shifts in the plasma peak of the host material (Figure 1.7j-l).<sup>93</sup> Overall, intercalation has been demonstrated as a very effective way to change the optical properties of 2D materials. We believe rational designs for the intercalation of 2D materials will lead to further advances with potential applications in photonics and optoelectronic devices.

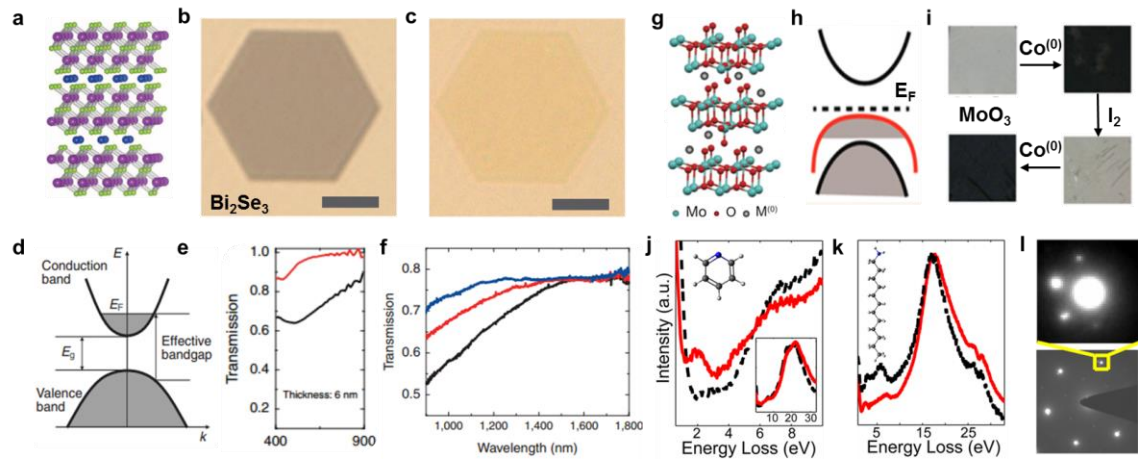


Figure 1.7 Optical and photonic properties of zerovalent metal and organic intercalated 2D materials. (a) Schematic of Cu-intercalated  $\text{Bi}_2\text{Se}_3$ . Microscope image of  $\text{Bi}_2\text{Se}_3$  (b) before and (c) after Cu intercalation. (d) Band structure of Cu-intercalated  $\text{Bi}_2\text{Se}_3$ . Optical transmittance of  $\text{Bi}_2\text{Se}_3$  over the (e) visible and (f) near-infrared spectral range before and after Cu intercalation. Schematics of zerovalent metal intercalated  $\text{MoO}_3$ : (g) crystal structure and (h) band structure. (i) Digital images of the reversible intercalation of Co metal in  $\text{MoO}_3$ . (j-l) EELS and diffraction patterns of intercalated  $\text{Bi}_2\text{Se}_3$  with organic molecules.<sup>92-94, 96</sup>

### 1.1.6.2 Intercalation tuned thermal properties

Intercalation also affects the thermal properties of 2D materials, since phonon propagation can be effectively tuned by the structural changes induced by intercalant insertion into the van der Waals gaps. For a given thermoelectric material, the ability of generating thermoelectric power is determined by its dimensionless figure of merit defined as  $ZT = \sigma S^2 T / \rho$  where  $S$ ,  $\sigma$ ,  $\rho$ , and  $T$  are the Seebeck coefficient, electrical conductivity, thermal conductivity and absolute temperature, respectively. One

approach to increase  $ZT$  is to suppress thermal conductivity while maintaining or even increasing the electrical conductivity. In this manner, the intercalation method can provide new strategies to tune 2D materials for thermoelectric applications.

Wan et al. reported that intercalating a SnS layer into layered  $\text{TiS}_2$  (Figure 1.8a) can improve the thermoelectric performance in the parallel and perpendicular directions with respect to the layers,<sup>97</sup> which is due to softening of the transverse sound velocities as well as vertical phonon localization (Figure 1.8b), which lead to a decrease in thermal conductivity. Therefore, the  $ZT$  value of  $(\text{SnS})_{1.2}(\text{TiS}_2)_2$  is significantly enhanced in the in-plane direction (Figure 1.8c), while in the cross-plane direction through hetero-interfaces, the  $ZT$  value remains nearly constant due to simultaneous scattering of both electrons and phonons. The same group also used organic cations ((hexylammonium)<sub>x</sub>(H<sub>2</sub>O)<sub>y</sub>(DMSO)<sub>z</sub>) as an intercalant to create a flexible hybrid superlattice (Figure 1.8d).<sup>87</sup> Due to intercalation, the thermoelectric properties and the figure of merit,  $ZT$ , is improved: 0.28 vs. <0.08 at 373 K (Figure 1.8e-f).

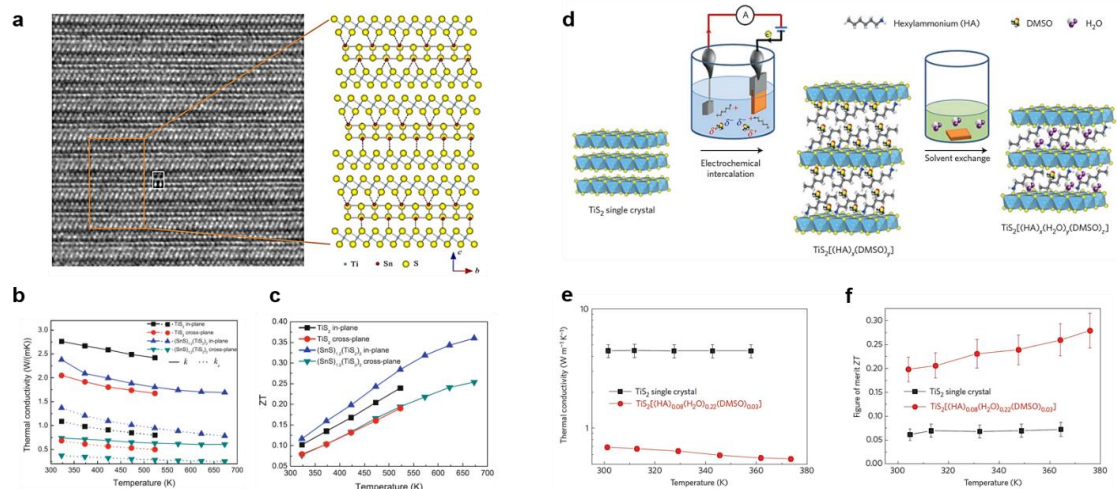


Figure 1.8 Thermoelectric properties of tunably intercalated  $\text{TiS}_2$  (a) High resolution TEM image of  $(\text{SnS})_{1.2}(\text{TiS}_2)_2$  along the  $[100]$  zone axis. The zoom-in image depicts the

actual crystal structure of  $(\text{SnS})_{1.2}(\text{TiS}_2)_2$ , reconstructed from the area indicated in the HRTEM image. (b) Total thermal conductivities  $k$  and the electron component  $k_e$  of  $\text{TiS}_2$  and  $(\text{SnS})_{1.2}(\text{TiS}_2)_2$  in both the in-plane and cross-plane directions. (c)  $ZT$  values of  $\text{TiS}_2$  and  $(\text{SnS})_{1.2}(\text{TiS}_2)_2$  in both the in-plane and cross-plane directions. (d) The process to electrochemically intercalate a  $\text{TiS}_2$  single crystal to create a  $\text{TiS}_2[(\text{HA})_x(\text{H}_2\text{O})_y(\text{DMSO})_z]$  superlattice. (e) In-plane thermal conductivity vs. temperature. (f) In-plane thermoelectric figure of merit vs. temperature.<sup>87</sup>

The electrochemical intercalation of  $\text{Li}^+$  ions effectively modulates the thermal conductivity of lithium cobalt oxide ( $\text{LiCoO}_2$ ), a layered crystal commonly used as a lithium-ion battery cathode. Cho et al.<sup>98</sup> designed an *in situ* measurement cell (Figure 1.9a) to probe the thermal conductivity during lithiation. The representative time-domain thermoreflectance (TDTR) data shown in Figure 1.9b was used to extract the thermal conductivity of lithiated and delithiated  $\text{Li}_x\text{CoO}_2$  films. The work demonstrated that both the thermal conductivity and the elastic modulus changes significantly from  $\text{Li}_{1.0}\text{CoO}_2$  to  $\text{Li}_{0.6}\text{CoO}_2$  (Figure 1.9c-d). The composition dependence suggests that the change in thermal conductivity with decreasing lithium concentration is related to not only the softening of the lattice but also to the  $\text{Li}_x\text{CoO}_2$  phase behavior.

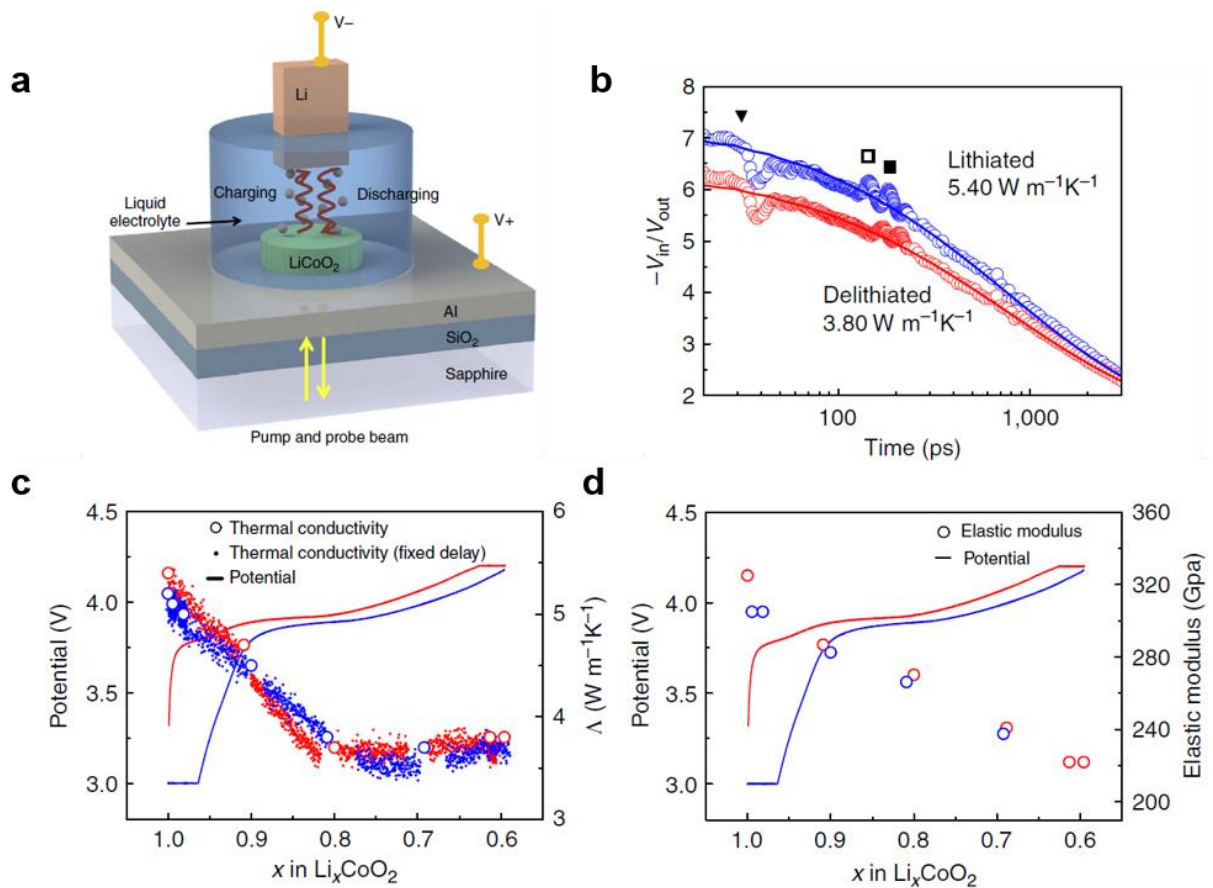


Figure 1.9 Thermal properties of tunable Li intercalation in  $\text{LiCoO}_2$ . (a) Schematic of the *in situ* measurement cell consisting of  $\sim 500$  nm  $\text{LiCoO}_2$ , 70 nm Al transducer and 100 nm  $\text{SiO}_2$  thermal isolation layer on a sapphire substrate. (b) TDTR data (open circles) and thermal conductivity fit (lines) for representative lithiated ( $x=1.0$ ) and delithiated ( $x=0.6$ )  $\text{Li}_x\text{CoO}_2$ . (c) Thermal conductivity and potential as a function of lithium insertion. (d) The lithiation-dependent longitudinal elastic modulus of  $\text{Li}_x\text{CoO}_2$  calculated from the longitudinal speed of sound. In both (c) and (d), the data in red and blue corresponds to the delithiation process and the lithiation process, respectively.<sup>98</sup>

The manipulation of thermal properties by intercalation could be applied to numerous layered materials and a range of intercalants including atoms, ions and molecules with

various sizes and charges can be used to further diversify the compositions of 2D hybrid structures. In this manner, intercalation provides a new avenue to optimize thermoelectric performance.

### 1.1.6.3 Intercalation tuned magnetic properties

Proper intercalation of magnetic species also permits wide tunability of the magnetic properties of the host 2D materials. Bointon et al. demonstrated the successful intercalation of large area multilayer epitaxial graphene with  $\text{FeCl}_3$  (Figure 1.10a).<sup>70</sup> Figure 1.10b shows the measured weak localization signal at different temperatures, where the phase coherence length  $L_\phi$  can be extracted (Figure 1.10c). Between 280mK and 80K, the estimated  $L_\phi$  of  $\text{FeCl}_3$ -FLG is much larger than previously reported pristine graphene:  $L_\phi \approx 1.2 \mu\text{m}$  at 280mK. The observed temperature dependence of  $L_\phi$  is also compatible with the occurrence of magnetic ordering in stage one  $\text{FeCl}_3$ -FLG. Morosan et al. reported that Fe can be intercalated into layered  $\text{TaS}_2$  to modify its magnetic properties (Figure 1.10d).<sup>99, 100</sup> Figure 1.10e-f displays the magnetoresistance (MR) measurements of bulk and exfoliated thin sheets of  $\text{Fe}_{0.28}\text{TaS}_2$  at different temperatures. In both cases, the largest  $\Delta\rho/\rho_0$  (close to 60%) was observed at  $T = 4 \text{ K}$ . However, the transitions at  $H_S$  are much sharper in the bulk material than in the 2D form at lower temperatures. This may imply that long range interlayer coupling between the Fe ions in different layers is weakened in the 2D crystals. The temperature dependence on switching field  $H_S$  and MR peak height for both bulk and 2D crystals is also similar (Figure 1.10e). However, the MR peak height increased monotonically with decreasing temperature for

the 2D crystals, while the bulk crystal increased until a maximum at 4 K and then decreased at lower temperatures (Figure 1.10f).

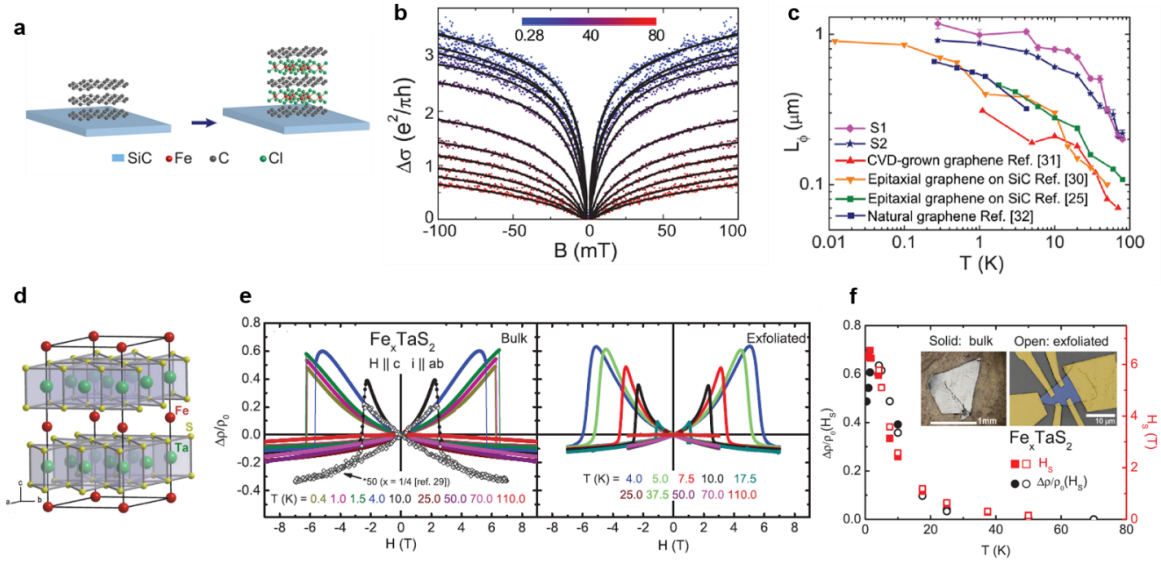


Figure 1.10 Magnetic properties of metal/molecule intercalated 2D materials. (a) Schematic crystal structure of trilayer FeCl<sub>3</sub>-FLG. (b) The measured weak localization contribution to the magneto-conductance (scatter points) and theoretical fits (solid line). (c) The temperature dependence of  $L_\phi$  for pristine graphene prepared by different methods. The values are compared to the estimated values of FeCl<sub>3</sub>-FLG. (d) The crystal structure of Fe<sub>0.25</sub>TaS<sub>2</sub>. (e) Measurement of magnetoresistance  $\Delta\rho/\rho_0$  for bulk and thin Fe<sub>0.28</sub>TaS<sub>2</sub> devices at selected temperatures for  $H \parallel c$  axis, and  $i \parallel ab$ -plane. (f) Comparison of  $H_S$  and  $\Delta\rho/\rho_0$  peak height values as a function of temperature for bulk (solid symbols) and thin 2D devices. The inset displays a typical bulk sample (left) and an exfoliated sample with metal contacts (right).<sup>70, 99</sup>

### 1.1.6.5 Intercalation tuned energy storage properties

Electrochemical capacitors and ion batteries have attracted tremendous interest for the past few decades due to an increasing need for clean and sustainable energy storage systems.<sup>19, 101-103</sup> In these devices, researchers search for materials that provide both high energy density and high power density for practical applications. Typically, electrochemical capacitors, also known as supercapacitors, store energy in an electrical double layer where charged ions build up on the electrode surface. This enables a rapid charge/discharge process but stores a limited amount of energy. On the contrary, ion batteries store ions via electrochemical reactions where ions diffuse between the electrodes upon charging/discharging. Diffusion is typically a slow process but the energy stored exceeds supercapacitors. Therefore, improving the energy density of capacitors and power density of ion batteries is of great interest. Through intercalation methods and tunable electrode materials, the performance of energy storage systems can be improved.

MoS<sub>2</sub> is not considered a supercapacitor electrode material since it has a stable 2H phase with semiconducting nature. However, by intercalation, Acerce et al. demonstrated that metallic 1T-MoS<sub>2</sub> can act as a high-performance supercapacitor electrode material.<sup>104</sup> These flakes can be re-stacked together to form flexible electrodes (Figure 1.11a-b). The 1T-MoS<sub>2</sub> electrode can be rapidly intercalated with H<sup>+</sup>, Li<sup>+</sup>, Na<sup>+</sup>, or K<sup>+</sup> ions with capacitances ranging from 400 to 700 F/cm<sup>3</sup> in aqueous electrolytes (Figure 1.11c). Chhowalla and coworkers identified increases in the interlayer distance depending on the type of solvated ions intercalated into MoS<sub>2</sub> (Figure 1.11d). The electrode can also operate under high voltages in nonaqueous solutions.

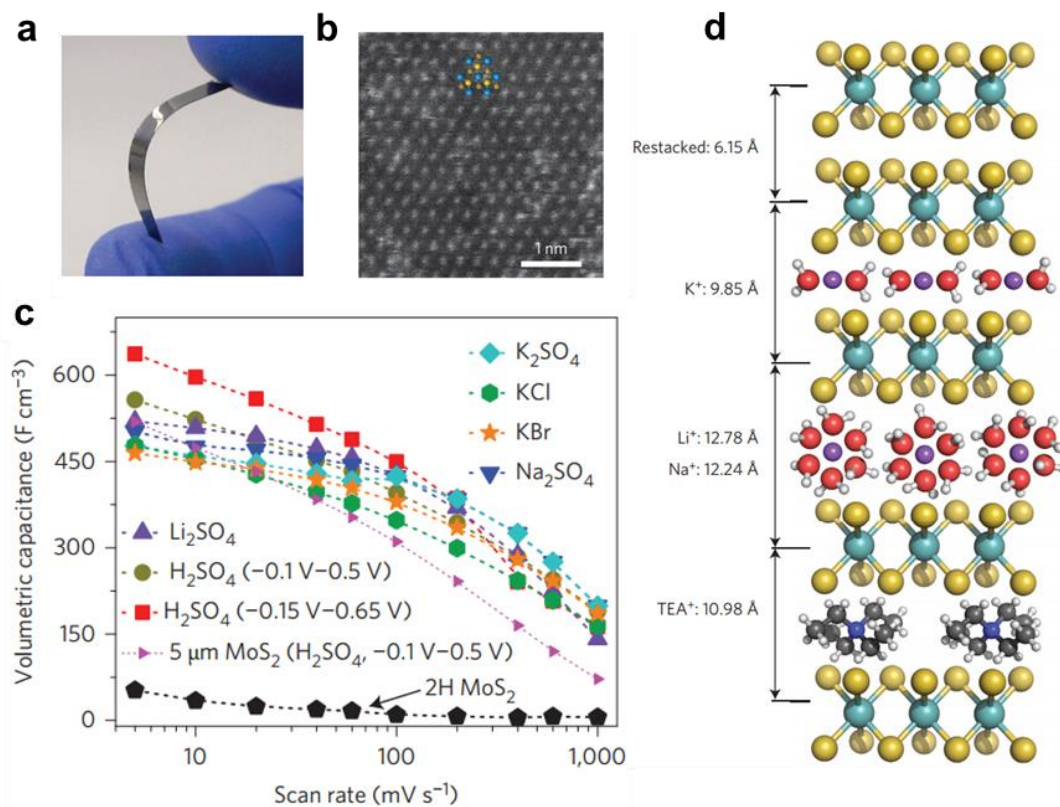


Figure 1.11 Enhanced energy storage properties for tunable Li-intercalated MoS<sub>2</sub> (a) Digital image of a flexible 1T-MoS<sub>2</sub> electrode. (b) HRTEM image of 1T-MoS<sub>2</sub>. (c) Capacitance of 1T-MoS<sub>2</sub> electrodes in various solutions. (d) Schematic of MoS<sub>2</sub> intercalated with different solvated ions.<sup>104</sup>

#### 1.1.6.6 Intercalation tuned catalytic properties

The effective generation of hydrogen through electrocatalysis at low cost and high energy efficiency has attracted tremendous research attention. The typical hydrogen evolution process via electrocatalysis undergoes a three step mechanism. First, protons are adsorbed on the electroactive sites, while electrons transferred to the adsorbed protons form the adsorbed H atoms. H<sub>2</sub> gas is then formed from the adsorbed H atoms before the

H<sub>2</sub> gas is desorbed due to the electrocatalyst's presence. It is well known that Pt group metals possess the best electrocatalytic performance, however, the cost of these noble metals is exorbitant. Therefore, finding a cost-efficient replacement for an electroactive, electrochemically stable catalyst has challenged researchers for decades. Recently, 2D TMDs such as MX<sub>2</sub> (M= Mo, W; X= S, Se) have emerged as promising HER electrocatalysts.<sup>6, 105, 106</sup> The general design principles for high-performance 2D TMD electrocatalysts include: (1) increasing the number and activity of catalysis sites as well as (2) increasing the charge transport during the catalytic process. Various nanostructures have been reported to increase the active edge sites of 2D TMDs as well as the conductivity between the catalytic material and the conductive substrate, which leads to high-performance composite electrocatalysis materials. However, for 2D TMD nanosheets, the low density of metallic catalytic active sites and overall semiconducting nature of the 2D TMDs hinders the catalytic behavior, charge transport, and thus the overall catalytic performance of these materials. Therefore, intrinsically improved catalytic activity and electronic conductivity in 2D TMD materials will lead to an overall enhancement in catalytic performance.

Intercalation provides a unique approach to optimize the catalytic activities of MX<sub>2</sub> materials. We previously mentioned that Li intercalation in MX<sub>2</sub> materials not only facilitates the exfoliation of bulk materials, but also induces phase changes such as conversion of a semiconducting 2H phase to a metallic 1T phase.<sup>105, 107</sup> This intercalation induced phase change is ideal for electrocatalysis, since it provides not only enhanced catalytic activity, but also higher electronic conductivity. Voiry et al. demonstrated significant improvements in the HER activity of 1T WS<sub>2</sub> by chemically intercalated and

exfoliated 2H WS<sub>2</sub>.<sup>108</sup> From DFT calculations, Chhowalla and coworkers demonstrated that a distorted 1T structure will provide greater catalytic performance, due to the lower reaction free energy. Lukowski et al. obtained similar results for both chemically intercalated 1T MoS<sub>2</sub> and 1T WS<sub>2</sub> nanoflowers (Figure 1.12 a-f).<sup>105, 109</sup> An outstanding overpotential of -142 mV vs. RHE at 10 mA/cm<sup>2</sup> was achieved by 1T WS<sub>2</sub> nanoflowers, which corroborates the potential of intercalation tuned MX<sub>2</sub> electrocatalysts.

Vertically aligned MoS<sub>2</sub> nanoflakes can also act as high-performance HER catalysts after electrochemical Li intercalation (Figure 1.12g).<sup>69, 110</sup> Unlike chemical intercalation, electrochemical intercalation is more controllable, which allows the catalytic activity of MoS<sub>2</sub> at various Li concentrations to be studied. Surprisingly, Wang et al. demonstrated that the catalytic performance improves as the Li concentration increases even before the 2H to 1T phase transition occurs. This behavior is explained by a synergistic effect between the electronic structure changes due to interlayer space expansion as well as the electron doping of the Mo d-band with intercalated Li. The highest catalytic performance of MoS<sub>2</sub> corresponds to 1T MoS<sub>2</sub> electrochemically intercalated at 1.1V (Figure 1.12h-i). As more Li is intercalated, the catalytic performance decreases due to the formation of inactive Mo and Li<sub>2</sub>S. A variety of nanostructures using intercalation tuned MX<sub>2</sub> electrocatalytic materials has been similarly demonstrated. Note that the electrochemical intercalation method not only applies to MX<sub>2</sub> HER electrocatalysts. Additional electrochemically intercalated layered materials have a wide range tunability, such as LiCoO<sub>2</sub>,<sup>111</sup> and can act as electrocatalysts which is not possible via chemical intercalation methods.

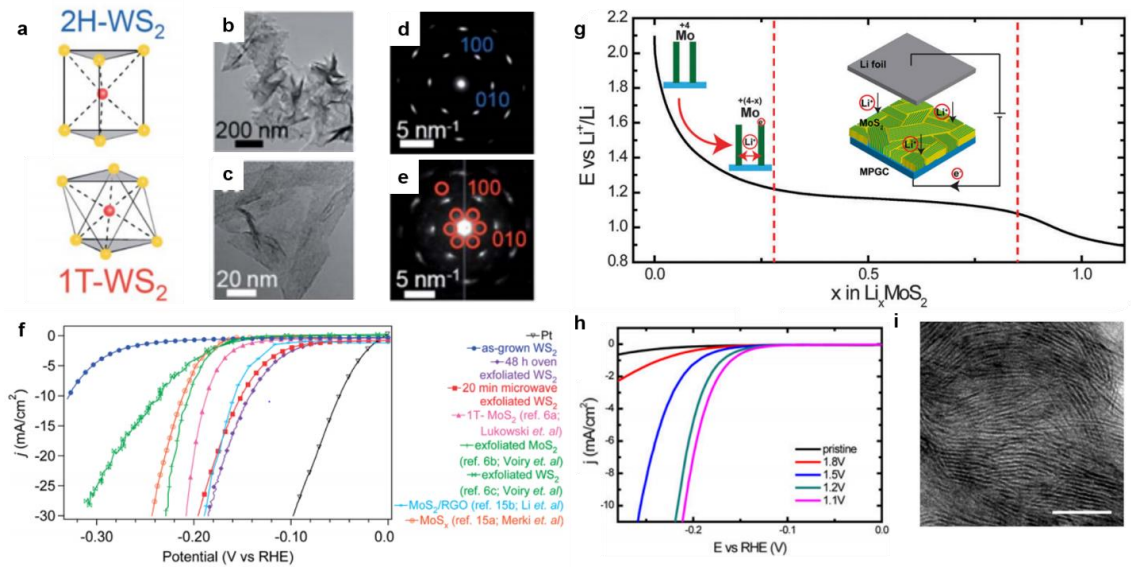


Figure 1.12 Catalytic properties of tunable Li-intercalated MX<sub>2</sub> 2D materials (a) Schematic of WS<sub>2</sub> with 2H and 1T phases. TEM images of (b), (c) and diffraction pattern of (d), (e) of WS<sub>2</sub> before and after Li intercalation. (f) Tafel plot of MoS<sub>2</sub> and WS<sub>2</sub> catalyst with different forms. (g) Electrochemical preparation of 1T-MoS<sub>2</sub> for water splitting. (h) Tafel plot of 1T-MoS<sub>2</sub> as a water splitting catalyst. (i) SEM image of the 1T-MoS<sub>2</sub> catalyst.<sup>69, 105</sup>

## 1.2 Li-ion batteries and Na-ion batteries

### 1.2.1 Introduction to Li-ion batteries and Na-ion batteries

Li-ion batteries are one type of rechargeable energy storage devices which only lithium ions moves from positive electrode to negative electrode in charging process and vice versa in discharging process. Since its high energy density with both high specific capacity and high voltage, Li-ion batteries dominate the market of consumer electronics and marching into electrical vehicles.<sup>112-114</sup> One typical Li-ion cell contains current

collectors, negative electrodes, separators, positive electrodes and electrolyte. The electrode materials usually composed with large amount of active materials, then binder and conductive additive.<sup>115-118</sup> A schematic of Li-ion battery is shown in Figure 1.13. Na-ion batteries are very similar to Li-ion batteries, except its moving ions in electrolyte are Na-ions. Na-ion batteries have attracted a great amount of research interest recently, for its potential lower-cost than Li-ion batteries. Despite their similarities, sodiation/desodiation chemistry is different than lithiation/delithiation chemistry. For instance, Si can alloy with Li and store up to 4.4 Li-ions per Si.<sup>101</sup> However, Si can hardly form alloy with Na at the same condition. In order to make high energy density, high power density Na-ion batteries, novel active materials needs to be developed and their storage mechanism needs to be studied.

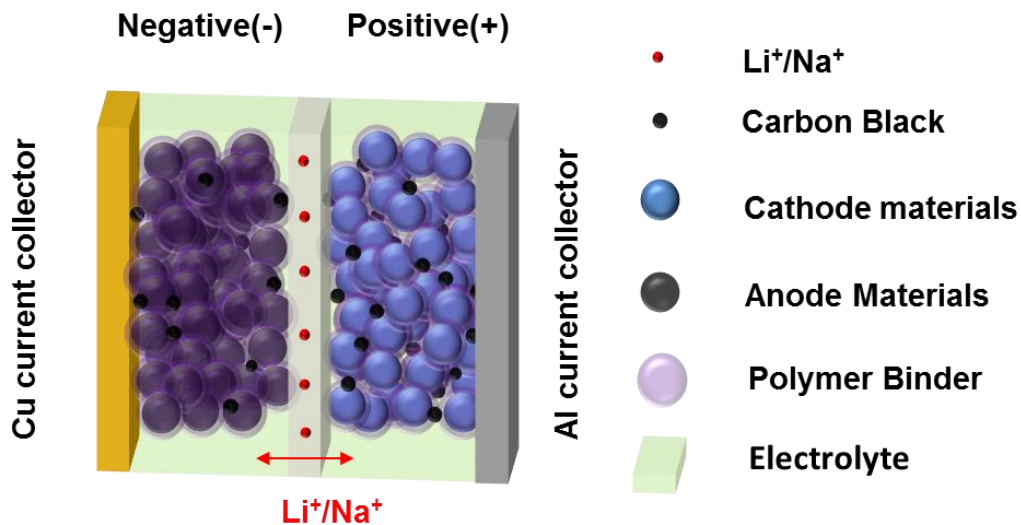


Figure 1.13 Schematic of a standard Li-ion or Na-ion battery with liquid electrolyte.

## 1.2.2 Layered materials for batteries

In fact, layered  $\text{TiS}_2$ ,  $\text{MoS}_2$  and graphite are the most popular electrode materials in history and have been widely studied and applied in commercial renewable Li ion batteries even today<sup>119-122</sup>. The components and products of intercalation compound at different potentials are well understood, the different intercalation stages can be controlled by setting cut-off voltages. For example, figure 1.14 shows the voltage profile of graphite as negative electrode in Li-ion batteries. Li intercalation process initials at around 0.22V (vs.  $\text{Li/Li}^+$ ), and the intercalation process continues as constant current charging. At the end of each voltage plateau, the intercalated Li-graphite compounds are defined as stage IV  $\text{LiC}_{36}$ , stage III  $\text{LiC}_{18}$ , stage II  $\text{LiC}_{12}$  and Stage I  $\text{LiC}_6$ , respectively, as shown in the following chemical reactions [IV], [III], [II], [I]. The stage numbers are defined as the number of graphene layers between each two intercalated Li layers. The occurrence of plateaus in voltage profiles is a common phenomenon during lithiation and delithiation process, which results from two-phase reaction according to Gibbs phase rule. Similar voltage profiles can be found in  $\text{TiS}_2$  and  $\text{MoS}_2$  lithiation voltage profiles, although intercalation will lead to conversion reaction at the final stage. Thus, electrochemical monitoring of lithiation in layered materials, or 2D materials is possible with voltage profile.<sup>79</sup>

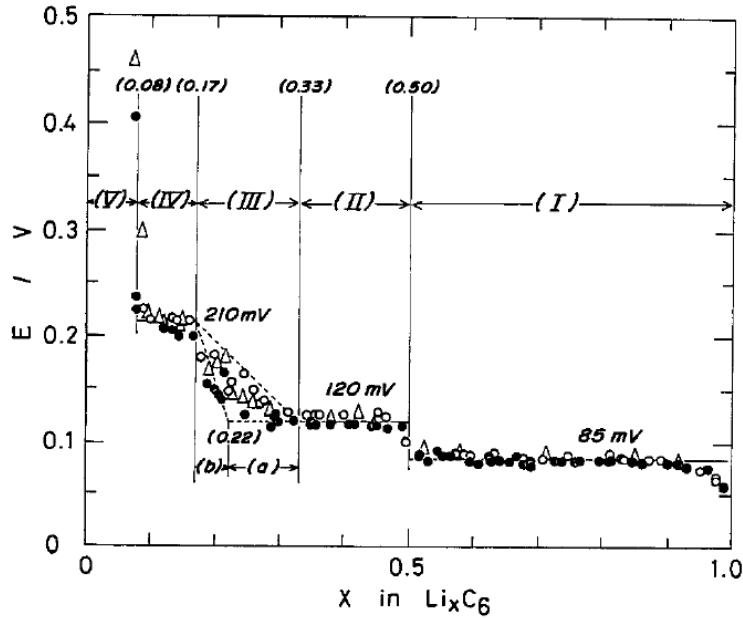


Figure 1.14 Voltage profile of Li intercalation in graphite, with different intercalations stages.



### 1.2.3 Current technology for *in situ* characterization of 2D battery materials upon intercalation

*In situ* characterization of 2D materials upon lithiation is crucial both in understand the lithiation chemistry and physical properties such as structure changes, mechanical stability, optical properties, electrical transport properties, etc. In the meantime, the understanding of intrinsic properties of battery materials on a single crystalline is lacking. *In situ* TEM techniques are advantageous for structural

identification and can yield much insight into the electrochemical insertion process. Liu et al. glued graphene nanoribbons to an aluminum rod and used the grown  $\text{Li}_2\text{O}$  layer on the Li/tungsten rod as the solid electrolyte for *in situ* TEM.<sup>123</sup> The structural evolution of graphene nanoribbons can be investigated during the lithiation and delithiation processes.<sup>123</sup> Fig. 3f shows the graphene nanoribbon (GNR) before lithiation, during Li insertion and after delithiation, respectively.<sup>123</sup> The lithiation/delithiation processes were reversible and the graphene nanoribbons accommodated the strains associated with Li insertion easily. In this case, the graphene materials, which were synthesized by splitting carbon nanotubes, have potential as mechanically robust and durable LIB electrodes. Even though the *in situ* TEM is a powerful tool in understanding the structural changes and mechanics of 2D electrode materials, it lacks the ability to monitor other property changes such as optical and electrical transport properties. Thus, other *in situ* characterization techniques need to be developed, both in discovery of novel intercalated 2D materials, as well as their use for battery electrodes.

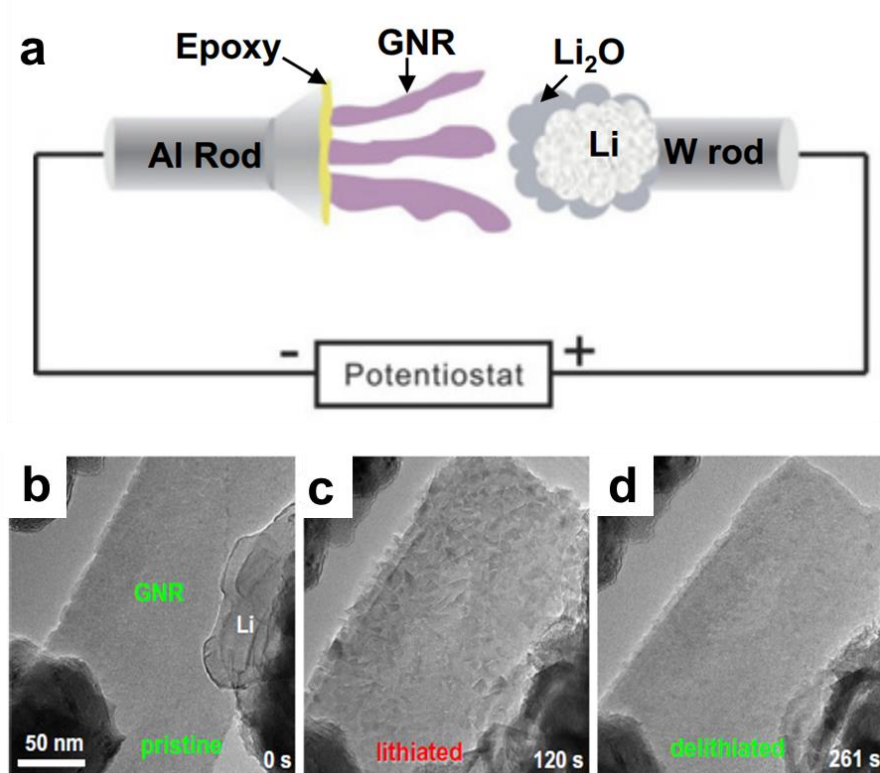


Figure 1.15 (a) schematic of in situ TEM set up for lithium intercalation in GNR (b-d) Morphological evolution of a (de)lithiated GNR using *in situ* TEM.<sup>123</sup>

### 1.3 Objective of this research

#### 1.3.1 Problem statement

Despite all the advantages of electrochemical intercalation of 2D materials, and the necessity in developing a device that is able to *in situ* and real time characterize their ion intercalation process. Tremendous challenges exist to achieve such devices. First, batteries, especially Li ion batteries, are fabricated and work in a sealed environment without contaminations such as water and oxygen. The designed devices need to be water/oxygen proof and bubble free for at least 48 hours, in order to finish a whole

lithiation/delithiation cycle. Second, a transparent device with Hall bar electrodes in microns need to be fabricated in order to simultaneously measure the optical/transport properties of intercalated 2D materials. Third, large, uniform, single flake 2D materials is needed for study the properties of individual flakes, and the volume expansion of 2D materials during intercalation process will break the Hall bar electrode fabricated by traditional evaporation method. Additionally, the fabrication of proof-of-concept device in large scale is even more challenging, for large area uniformly coating of 2D materials is difficult and the leaking problem of liquid electrolyte is more severe than devices in smaller scales. Thus, the problems arise with above ideas and obstacles which list in below:

1. Can we develop a novel methodology to synthesis/characterize intercalated 2D materials with extraordinary properties? How to monitor the properties of the 2D materials while intercalation?
2. How do we apply and make a contribution of this technology to R&D in real applications?

### 1.3.2 Objective

Thus, the objective of this thesis study lies in:

- a. Fundamentals: develop a simple methodology to intercalate typical 2D materials (ultrathin graphite/MoS<sub>2</sub> and other 2DNMs), investigate optical, electrical, optoelectronic, and structural properties.

b. Applications: using the methodology and novel intercalated 2DNM to demonstrate proof-of-concept devices for transparent conductors, electrochromic applications and batteries.

Figure 1.1.6 provide the overview of the thesis research. The five sets of figures above the green arrow are optoelectronic studies on metal ion intercalation in 2D graphitic materials; the four sets of figures under the green arrow are the studies of metal ion intercalation in 2D materials for their electrochemical energy storage applications.

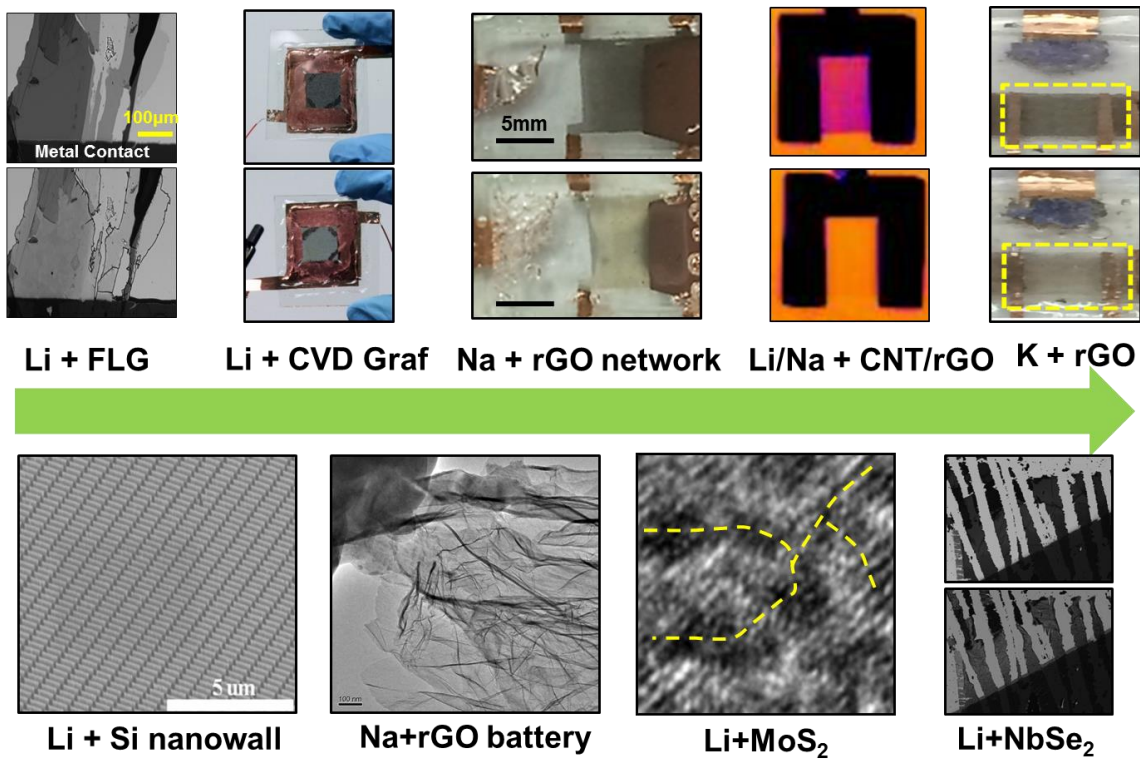


Figure 1.16 Master chart of the thesis research: ion intercalation in 2D materials for their optoelectronic (above the green arrow) and electrochemical energy storage performances (under the green arrow).

## Chapter 2: Design and build *in situ* planar battery for 2D materials intercalation

Wenzhong Bao,  Jiayu Wan , Xiaogang Han, Xinghan Cai, Hongli Zhu, Dohun Kim, Dakang Ma, Yunlu Xu, Jeremy N. Munday, H. Dennis Drew, Michael S. Fuhrer, Liangbing Hu Nature Communications 2014, 5, 4224

### 2.1 Introduction

In this chapter, we will discuss the design principle and fabrication process of planar batteries. Within my PhD research scope, different types of planar batteries are developed with different usages. Generally, the fabrication of planar batteries for optical measurements is simpler than that of simultaneous electrical transport studies. The planar battery for optical transmittance measurements and Raman spectroscopy only needs two electrodes, while the ones for electric transport measurements needs hall bar structure with at least five electrodes in total. Detailed description of the structure and fabrication of the devices will be discussed in the sections below.

### 2.2 Experimental

#### 2.2.1 Planar battery for *in situ* optical studies

To study optical properties (transmittance) of ion intercalated 2D materials, we design a sandwich-structured cell with electrolyte (1 M LiPF<sub>6</sub> in w/w = 1/1 ethylene carbonate/diethyl carbonate) that is sealed by bottom and top layers of thin transparent

glass. 2D materials and the metal source (lithium metal) are deposited on the bottom glass layer and connected to separate electrical contacts. The fabrication process of the planar battery for optical measurements is as following: pristine 2D material sheets are first obtained by mechanical exfoliation of the layered materials onto 0.2 mm thick glass substrate (Fisher Scientific), followed by deposition of electrical contacts (50 nm copper) on top of 2D materials sheets using a shadow mask technique in electron beam evaporator. The device is then transferred into a glove box filled with argon gas, and a small metal pellet (i.e. Lithium metal) is deposited onto an isolated electrical contact, followed by the addition of a small amount of electrolyte ( $\text{LiPF}_6$  in EC:DEC w:w = 1:1) to cover the region with both 2D materials and metal source. At last the center region with electrolyte/lithium/ ultrathin graphite is covered by another piece of 0.2 mm thick glass and sealed by PDMS, as shown in Figure 2.1.

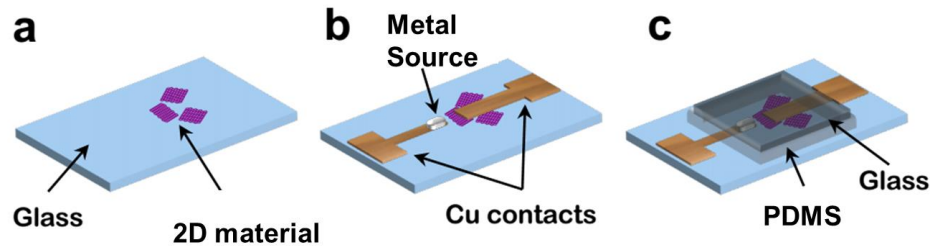


Figure 2.1 Fabrication process of planar device for optical measurements of 2D materials with ion intercalation.

In this planar nanoscale half-cell battery (planar nano-battery), metal source is used as the counter electrode and ultrathin graphite as the working electrode. The

intercalation process is controlled by a Bio-Logic SP-150 electrochemical workstation and the voltage of planar nano-battery can be measured simultaneously during the electrochemical Li-intercalation. The thickness of the ultrathin graphite is determined by an atomic force microscope (AFM) before cell capsulation. (Figure 2.2) The transmittance at a particular wavelength of pristine and intercalated 2D materials can be characterized by analyzing the grey-scale images acquired by transmission optical microscopy (Nikon Eclipse Ti-U) using a broadband light source (Thermo Oriel), a monochromator (Spex 500M), and a charge-coupled device (CCD) camera. A schematic of *in situ* transmittance measurement system is shown in Figure 2.2. Our transparent planar nano-battery setup also allows further characterization using Raman microscopy. (Horiba Jobin Yvon with a 633 nm laser source).

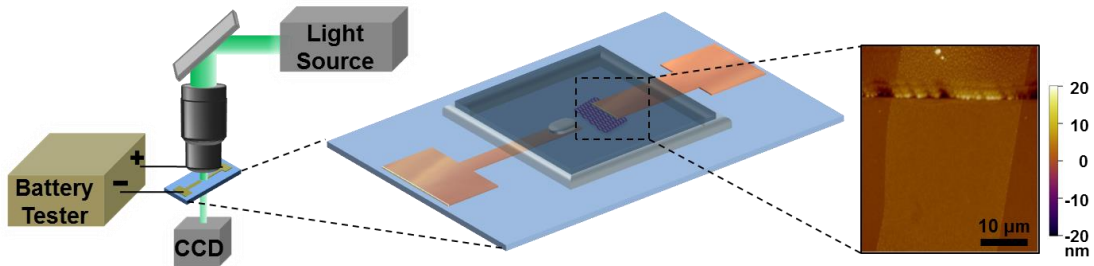
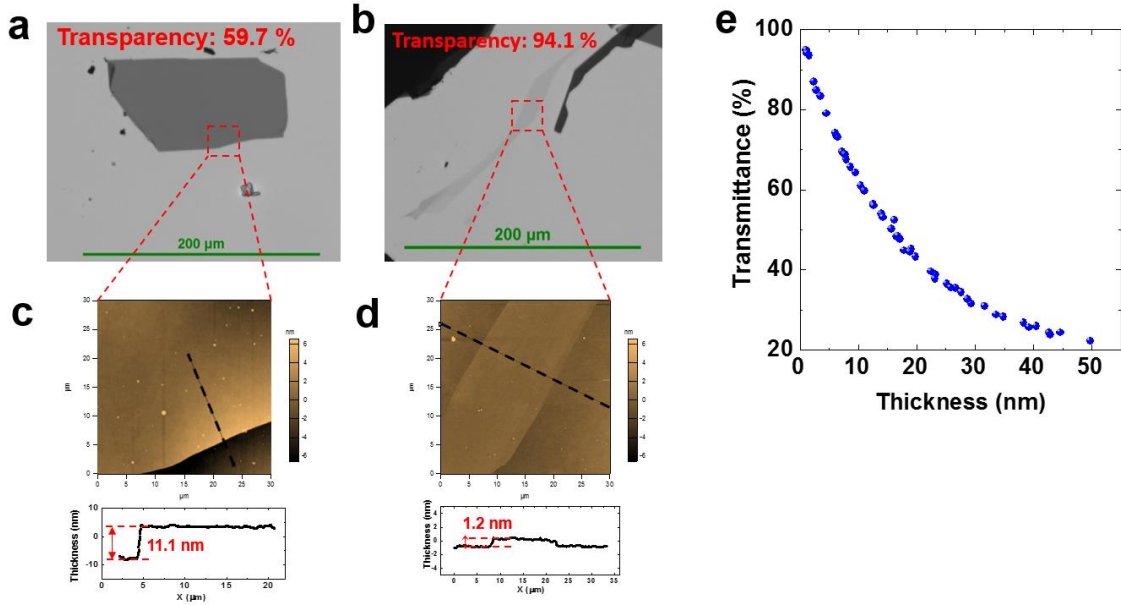


Figure 2.2 Schematic of optical transmittance measurement of 2D materials by intercalation, controlled with battery tester. Inset demonstrate the AFM image of FLG with metal electrode on glass substrate.

Figure 2.2 demonstrates the large, uniform thickness of FLG flakes by mechanical exfoliation method. Other 2D materials in this study such as MoS<sub>2</sub> are prepared with the

same technique. The large area uniformity ensured the reliability of the optical as well as the electrical transport measurement of our experiments. Grey scale optical images as well as AFM images of two typical mechanical exfoliated FLG on glass substrate are shown in Figure 2.2 a-d. Figure 2.2e is the plot of the thickness vs transmittance of FLG.



**Figure 2.2** a-b Optical transmission (550nm light source) images of uniform isolated ultrathin graphite samples deposited on glass substrate by mechanical exfoliation. c-d corresponding AFM images. e. Transmittance (550nm light source) vs AFM thickness for all measured flakes.

### 2.2.2 Planar nano battery for *in situ* electrical transport studies

During the ion intercalation process the volume of 2D materials gradually expands because of the insertion of lithium atoms. For example, the layer spacing of  $\text{LiC}_6$  is ~10% larger than that of pristine graphite.<sup>124</sup> Therefore, the narrow metal electrodes fabricated by the normal method of thermal evaporation on top of ultrathin graphite usually crack

after intercalation. Here we use a lithography-free fabrication method shown in Figure 2.3a-c. The 50 nm thick copper Hall-bar/metal source-contact electrodes are pre-patterned on a blank glass wafer. A uniform exfoliated ultrathin graphite sheet is then transferred onto the top of the electrodes aligned by a micro-manipulator. The rest of the device fabrication is the same as described above. Using this method, 2D materials are attached to the top of the electrodes and can expand freely during Li-intercalation.

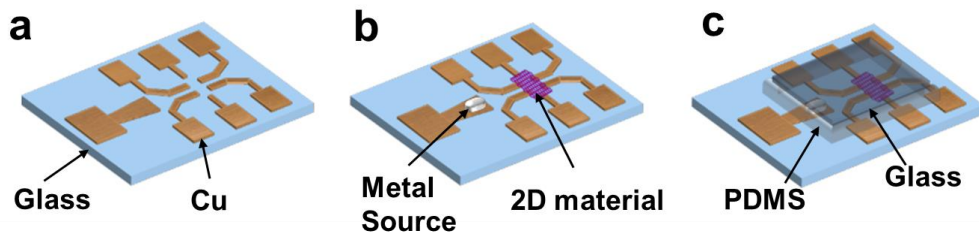


Figure 2.3 Fabrication process of planar nanobattery for electrical transport measurements of 2D materials with ion intercalation.

Photo images of the fabrication process are shown to illustrate the details of our multi-functional planar nanobattery device. The transfer method we used is similar to the one developed by Zomer et al.<sup>125</sup>

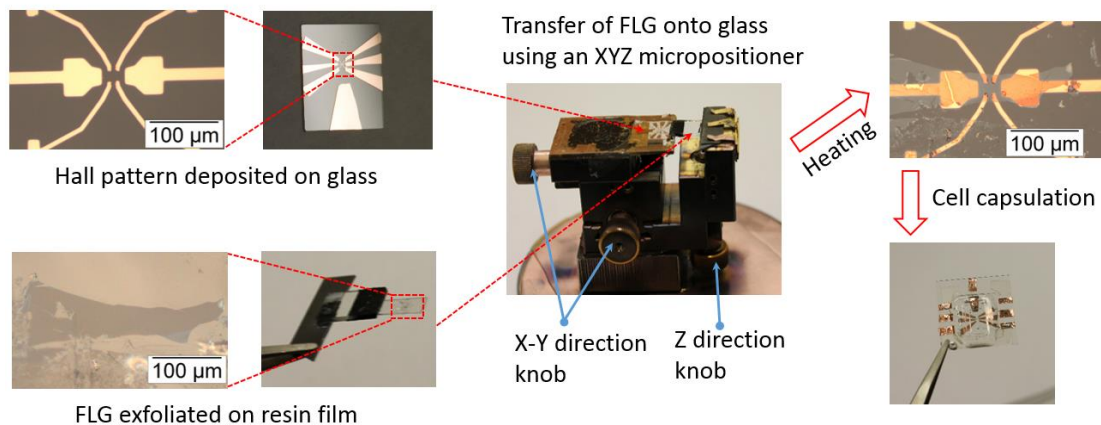


Figure 2.4 Process flow of ultrathin graphite transfer and cell encapsulation.

Typical images of 2D materials on top of pre-evaporated Cu Hall bar are shown in the Figure 2.5, which further shows large uniform ultrathin graphite transferred on Hall bar.

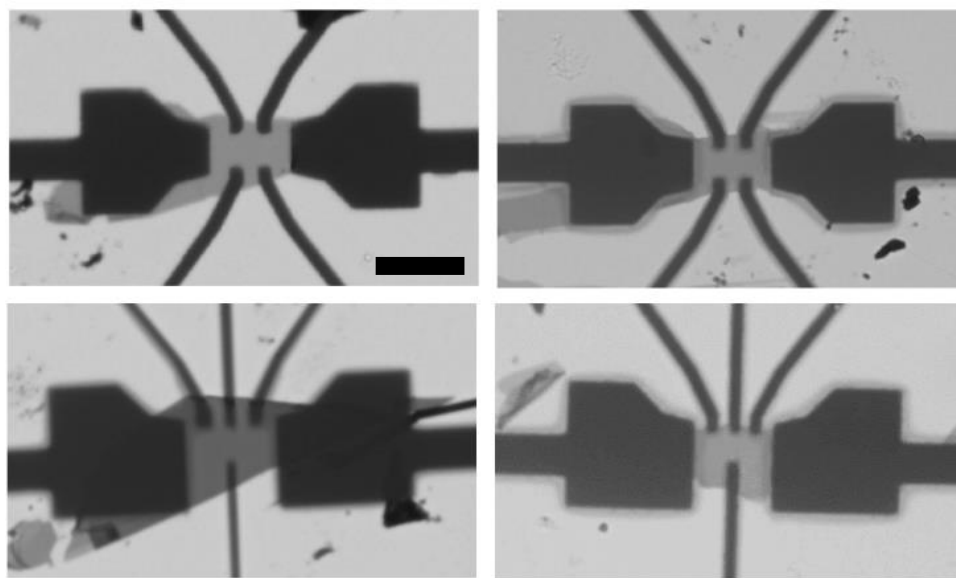


Figure 2.5. Optical transmission images of devices with ultrathin graphite sheets transferred onto pre-fabricated Hall bar electrodes. The scale bar is 20  $\mu\text{m}$ .

## Chapter 3: Li-ion intercalation in few layer graphene—approaching the limits of transparency and conductivity in graphitic materials

Wenzhong Bao,  Jiayu Wan, Xiaogang Han, Xinghan Cai, Hongli Zhu, Dohun Kim, Dakang Ma, Yunlu Xu, Jeremy N. Munday, H. Dennis Drew, Michael S. Fuhrer, Liangbing Hu Nature Communications 2014, 5, 4224

### 3.1 Introduction

Two-dimensional (2D) graphene has attracted much interest in fundamental research and technological development due to its extraordinary electrical, mechanical, thermal and optical properties<sup>8, 126-130</sup>. Recently, graphitic films (from monolayer graphene to ultrathin graphite) have been explored as candidates for flexible transparent electrodes for electronics and optoelectronics<sup>131, 132</sup>. An excellent performance of 30  $\Omega$  per sq at 90% transmittance has been achieved using doped four-layer chemical-vapor-deposition (CVD) graphene<sup>22</sup>. Bulk materials with 2D layered structures such as graphite have also been studied and used extensively for electrochemical energy storage based on intercalation.<sup>120, 133, 134</sup> Fundamental studies on intercalation in graphite have been extensively carried out,<sup>135</sup> and nanostructured 2D materials have gained recent interest.<sup>136</sup> Reports on the intercalation of various species such as  $\text{FeCl}_3$ <sup>78, 91</sup>,  $\text{Br}$ <sup>137</sup> and  $\text{Ca}$ <sup>138</sup> in few-layer graphene (FLG) have offered a new route to designing and synthesizing graphene-based materials with novel conductive, magnetic, or superconductive properties.

It has long been known that the optical transmission of graphite increases upon metallization by intercalation with e.g. caesium.<sup>139</sup> This unusual property results from the

unique band structure of the graphene layer; intercalation heavily dopes ultrathin graphite, shifting the Fermi level upward more than any other band engineering method<sup>63, 78, 140-143</sup>, suppressing interband optical transitions due to Pauli blocking thus increasing transmittance of light in the visible range. The increase in optical transmittance is expected to be accompanied by an increase in conductivity since the carrier concentration increases upon intercalation, an ideal situation for conductive transparent films. All studies to date of doped graphene films as transparent electrodes, however, do not report increased transmission in the visible range. It also has been assumed by some researchers that the transmission of ultrathin graphite can never exceed that of undoped graphene of similar layer number.<sup>144</sup> Moreover, no studies of electrical conductivity and optical transmission have been carried out for lithium-intercalated ultrathin graphite.

Here we use *in situ* electronic and optical measurements to understand the electrochemical intercalation process and simultaneously measure the electrical conductivity and optical transmission of exfoliated ultrathin graphite crystallites ranging from 3-60 graphene layers in thickness. Upon intercalation we observe a large improvement in the optical transmittance, and at the same time a dramatic increase of sheet conductivity. The Dirac electronic bandstructure allows for very low electron-phonon resistivity even at relatively low carrier concentration<sup>145</sup>, hence high DC conductivity is achieved with low optical conductivity below the visible range. In addition to elucidating the limits of conductivity and transparency in ultrathin graphite, we expect that the experimental techniques developed here will be broadly useful for studying the intercalation dynamics and correlated optoelectronic properties of other 2D nanomaterials that can be intercalated electrochemically.

### 3.2 *In situ* optical measurements and results

A series of optical images (550 nm illumination) corresponding to different stages are shown in Figure 3.1a-d, along with a schematic of the lattice structure of  $\text{LiC}_6$  (Figure 3.1e). A clear increase in the transmittance upon intercalation can be seen from Figure 3.1a to 3.1d, as discussed below in detail. Furthermore, the optical transmittance change is highly reversible, as shown in Figure 3.1f.

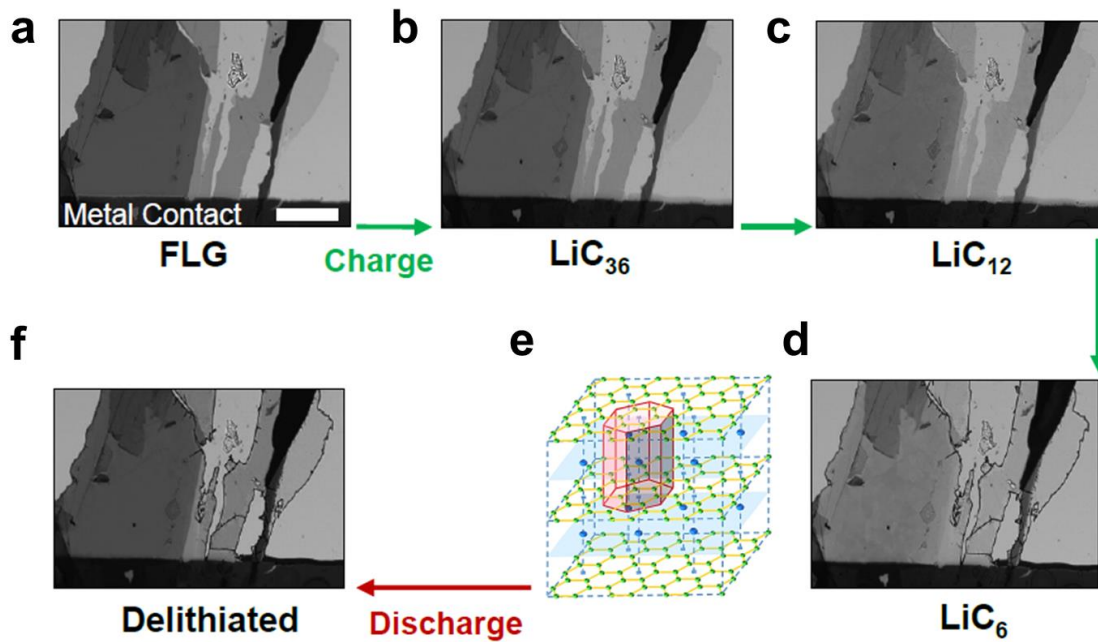


Figure 3.1 Photo images of FLG upon lithium intercalation at different stages taken by optical microscope. (a). pristine, (b).  $\text{LiC}_{36}$ , (c).  $\text{LiC}_{12}$ , (d).  $\text{LiC}_6$ , (e). atomic structure of  $\text{LiC}_6$  and (f). delithiated FLG.

Raman spectrum of the intercalated graphite can be used to confirm the stages of Li intercalation, and it can be generally applied to other 2D materials.<sup>146</sup> A commercial micro

Raman spectrometer (Labram Aramis model manufactured by Horiba Jobin Yvon) is used for *in situ* measurements. The grating is 600 gr/mm, the laser source is a 633 nm He-Ne laser with 9mW power, and a D1 filter is used so the actual power is 0.9 mW. *In situ* and real time Raman spectrum of FLG upon intercalation is shown in figure 3.2a. The black line depicts the initial Raman spectra of an ultrathin graphite sample at a voltage of 1.00 V (vs. Li/Li<sup>+</sup>), for which the Raman shift shows a typical G peak of graphene at 1580 cm<sup>-1</sup>. The G peak shifts upward to 1600 cm<sup>-1</sup> at dilute Li intercalation stage (LiC<sub>72</sub>), where the upshift due to Li doping.<sup>141</sup> When stage IV (LiC<sub>36</sub>) starts to form, the G peak splits into two (1576.2 cm<sup>-1</sup> and 1601.8 cm<sup>-1</sup>), which represents the interior and bounding layer modes of Li intercalated ultrathin graphite.<sup>147</sup> Upon further intercalation, the upper shifted peak grows while the lower peak vanishes, indicating a dominating bounding layer mode and the formation of the stage II intercalation compound (LiC<sub>12</sub>). Finally, the two G peaks completely disappear, indicating the formation of Stage I (LiC<sub>6</sub>), which can be simply understood as the Pauli blocking of the interband optical transition, hence there is no resonant Raman process<sup>148</sup>. The Raman spectra for Li-intercalated ultrathin graphite sheets agree well with previous studies of bulk samples,<sup>147</sup> therefore, Raman microscopy can be used as one of the tools for differentiating lithiation stages of ultrathin graphite.

We also obtained Raman spectra over a wider range of Raman shift of 1200 - 3000 cm<sup>-1</sup> from a different sample, as shown in Figure 3.2b. The absence of D peak (1345 cm<sup>-1</sup>) indicates that no degradation of the crystalline quality of ultrathin graphite occurred during electrochemical cycling. We also observed a vanishing of the 2D peak, and before the vanishing, the 2D frequency shifted from 2687.75 cm<sup>-1</sup> (pristine graphite) to 2677.73 cm<sup>-1</sup> (dilute stage) and then 2604 cm<sup>-1</sup> (LiC<sub>36</sub>).

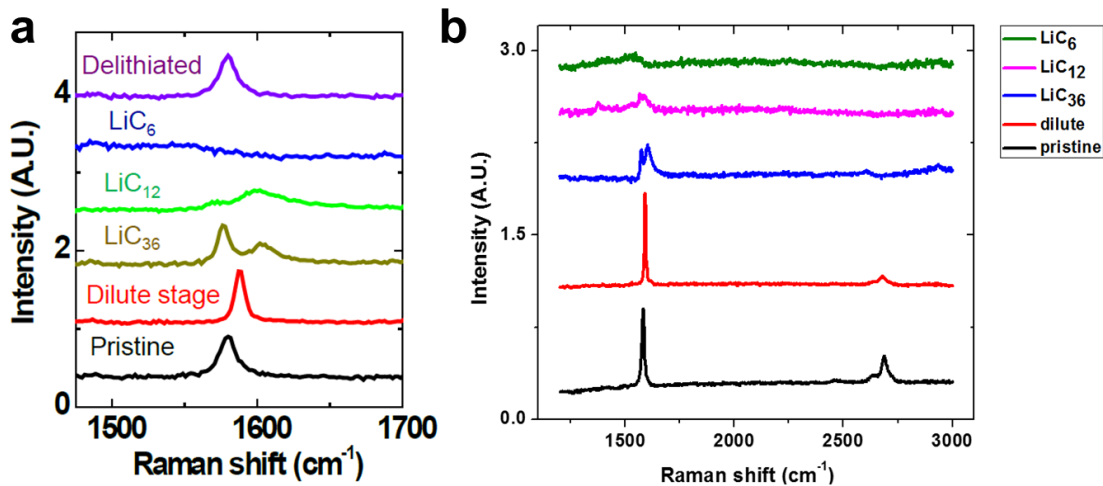


Figure 3.2 Raman spectrum of FLG intercalation at different stages (a) range from 1400-1700 cm<sup>-1</sup>, (b) range from 1200 to 3000 cm<sup>-1</sup>.

We also observed an *in situ* and real time transmittance change of Li intercalated ultrathin graphite at different Li<sub>x</sub>C<sub>6</sub> stages by charging the Li-graphite nano-batteries (Figure 3.3a), with a constant charge current. The black line represents a typical voltage profile of the Li-graphite nano-battery and the red, green, blue open circles depict the transmittance evolution of ultrathin graphite sheets (dotted regions in the inset of Figure 3.3a) with different thicknesses during Li-graphite intercalation. The voltage initially drops rapidly with time until it reaches 0.8 V, where an obvious slope change in the voltage profile is observed. This is due to the decomposition of the electrolyte and a solid electrolyte interphase (SEI) formation<sup>133, 149</sup>. No obvious change in the transmittance of the ultrathin graphite samples is observed for voltages greater than 0.2 V. A sudden increase in the transmittance (18-layer graphite from 74.4% to 77.2%, 38-layer graphite from 55.9% to 59.2%) occurs after 0.2 V, which we identify with the

formation of  $\text{LiC}_{36}$  (stage IV)<sup>79</sup> from ultrathin graphite sheets. From 0.2 V to 0.1 V, a gradual change in the transmittance is observed, presumably due to the formation of  $\text{LiC}_{27}$  and  $\text{LiC}_{18}$ <sup>79</sup>. As time increases a second plateau appears in the voltage at  $\sim 0.1$  V, which we identify with the formation of  $\text{LiC}_{12}$  (stage II). At the end of the 0.1 V plateau we expect the entire sample has been converted to  $\text{LiC}_{12}$ , and the transmittance dramatically increased to 85.8% (18-layer) and 71.9% (38-layer). A third voltage plateau appears at a value of  $\sim 0.05$  V, indicating the formation of  $\text{LiC}_6$  (stage I). At this stage the transmittance of the 18-layer sample has increased to 90.9%, and the 38-layer sample has increased to 79.2%. Only two distinct stages are observed for the 3 layer sample (from 94.5% to 95.2%, and finally 97.7%), consistent with the fact that there are only two interstitial galleries and hence only Stage I and Stage II are meaningfully defined. Figure 3.3b shows the low potential region of the potential vs. time trace in which the distinct potential plateaus can be seen more clearly.

The changes in optical transmission in our planar nano-battery allow a direct observation of the lithiation process on an individual ultrathin graphite sheet with excellent spatial and temporal resolution. As shown in Figure 3.3c-g, a clear lithiated ( $\text{LiC}_{36}$ ) and dilute stage ( $\text{LiC}_{72}$ ) interface (i.e. a lithiation front) is observed within 100 seconds, and the lithiated area becomes more transparent and the  $\text{LiC}_{36}$  area increases linearly with time (Figure 3.3h). This agrees well with our electrochemical testing scheme with a constant current charge/discharge process. Thus our integrated system provides a powerful tool to investigate the intrinsic lithiation kinetics in the two-phase reaction at the nanoscale.<sup>150</sup>

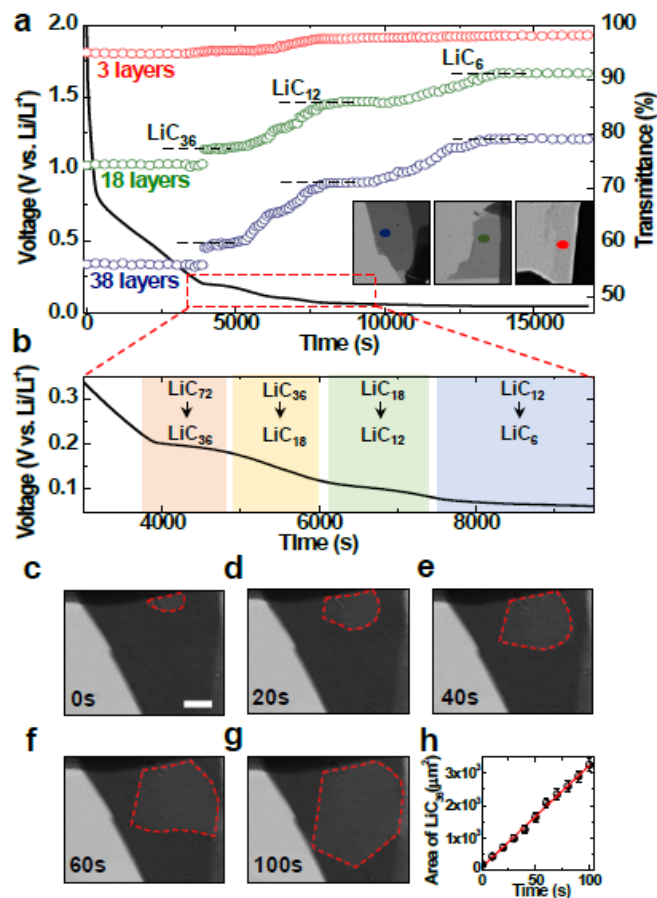


Figure 3.3 (a) Optical transmittance (right) and electrochemical potential (left) vs. lithiation time are plotted. (b) Detail of voltage profile vs. time near the intercalation plateau. (c-g) Optical images of an ultrathin graphite sheet at different time points during intercalation as indicated in each panel, showing a clear lithiation front (red dashed line) between LiC<sub>36</sub> (lighter contrast) and LiC<sub>72</sub> (darker contrast). The ultrathin graphite sample is about 120 layers thick and the scale bar in (c) is 20 μm. (h) Lithiated LiC<sub>36</sub> area vs. time extracted from images such as (c-g).

We next consider the layer-number and wavelength dependence of the *in situ* optical transmission of individual ultrathin graphite sheets. In Figure 2.7a-c, the

wavelength dependence of the transmittance is shown in the visible range from 400 nm to 800 nm for samples of various thicknesses. For pristine ultrathin graphite (Figure 3.4a), the transmittance is weakly dependent on the wavelength, consistent with previous reports<sup>130</sup>; the absorption by ultrathin graphite is approximately  $n\pi\alpha$  ( $\pi\alpha = 2.3\%$ ), where  $\alpha$  is the fine structure constant and  $N$  the number of graphene layers. This absorption results from interband transitions in the Dirac spectrum of graphene, which give a nearly constant optical conductivity  $\sigma \approx \pi e^2/2h$  where  $e$  is the elemental charge and  $h$  Planck's constant. For LiC<sub>12</sub> stage (Figure 3.4b), the transmittance depends more strongly on wavelength, increasing the most for longest wavelengths. For the LiC<sub>6</sub> stage (Figure 3.4c), the wavelength dependent transmittance shows a maximum around 500 nm, and the transmittance of LiC<sub>6</sub> is still higher compared to pristine ultrathin graphite. Interestingly, the transmittance of LiC<sub>6</sub> still increases compared to LiC<sub>12</sub> for wavelengths well below the maximum, while above the transmittance maximum the LiC<sub>6</sub> transmittance decreases compared to LiC<sub>12</sub>.

Figure 3.4d and 3.4e show the optical transmittance for pristine and intercalated ultrathin graphite sheets as a function of layer number. For both 550 nm and 800 nm, a clear increase of the optical transmittance is seen after intercalation, both for LiC<sub>12</sub> and LiC<sub>6</sub>. For 550 nm wavelength (Fig. 3.4d), the transmittance increases monotonically with Li concentration; for LiC<sub>6</sub> vs. pristine ultrathin graphite, the transmittance increase can be as high as 55% (for a sample of 60-80 layers). For 800 nm wavelength (Figure 3.4e), the transmittance for all measured thicknesses first increases (LiC<sub>12</sub>) and then decreases (LiC<sub>6</sub>); for LiC<sub>12</sub> vs. pristine ultrathin graphite, the transmittance has an increase up to twofold (for a sample more than 100 layers). We also observed that in thicker sheets

(insets of Figure 3.4d and e), the transmittance of  $\text{LiC}_6$  increases less and starts to approach the value of its pristine state at both wavelengths of 550 nm and 800 nm, i.e. at 550 nm for 90-layer thickness the transmittance at  $\text{LiC}_6$  state starts to approach the value of  $\text{LiC}_{12}$  state and approaches the value of pristine state at about 150 layers, and for 800 nm wavelength the transmittance of  $\text{LiC}_6$  becomes lower than the value of pristine state with layer number greater than 60.

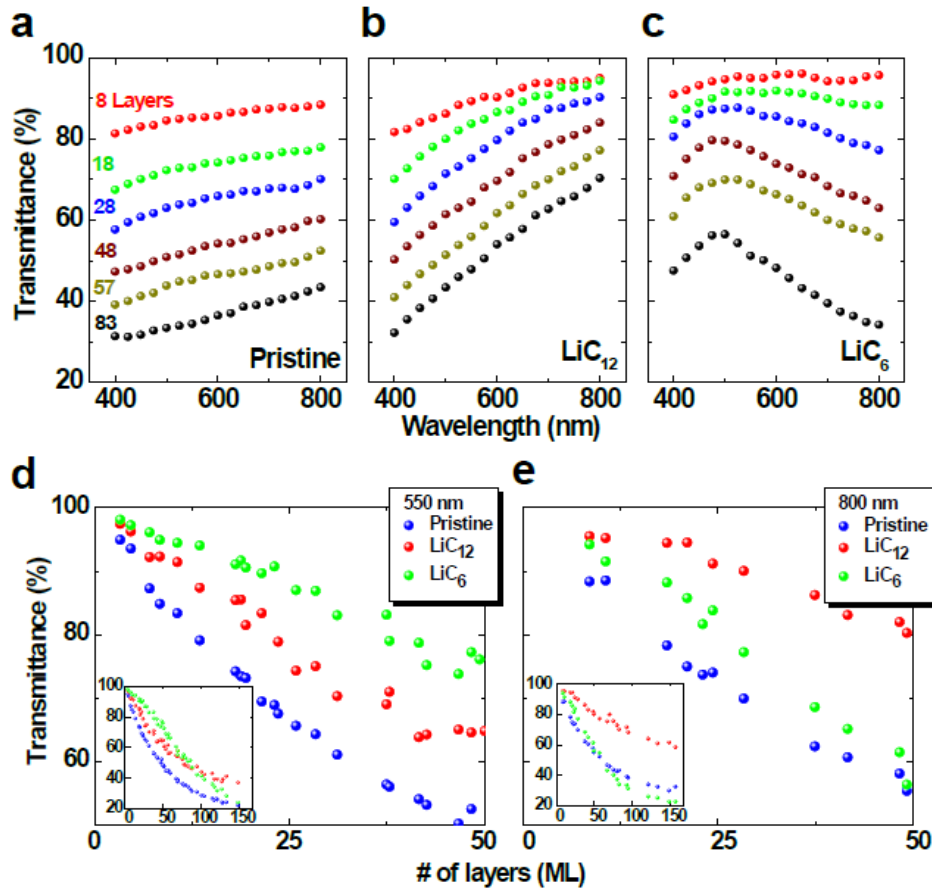


Figure 3.4 Wavelength-dependent optical transmittance of intercalated ultrathin graphite. (a-c). Transmittance as a function of wavelength for different thickness ultrathin graphite samples for pristine ultrathin graphite (a),  $\text{LiC}_{12}$  (b),  $\text{LiC}_6$  (c) stages. (d-e) Transmittance as a function of thickness plot for pristine ultrathin graphite,  $\text{LiC}_{12}$ , and  $\text{LiC}_6$  at

wavelengths 550 nm (d) and 800 nm (e). Insets show transmittance at same wavelength over a larger range of thicknesses.

### **3.3 Drude and interband contribution of increased transmittance in intercalated ultrathin graphite**

The changes in optical transmittance in the visible range described above can be qualitatively understood as follows. The result of the Li intercalation is electron doping due to the lowest electrochemical potential of Li metal. As shown in Figure 3.5a, intercalation of Li heavily dopes the ultrathin graphite, shifting the Fermi level up. The magnitude of Fermi level shift is associated with the carrier density, which increases monotonically with lithium concentration. The doping concentration is as high as  $\sim 6 \times 10^{14}$  cm<sup>-2</sup>/layer for LiC<sub>6</sub>, corresponding to  $E_F \approx 1.5$  eV<sup>151</sup>, higher than the highest doping that can be achieved in graphene with electrolytic gating.<sup>143</sup> The increase in Fermi energy leads to the suppression of interband optical transitions for photon energies  $\omega < 2E_F$ , thus decreasing the optical conductivity and increasing the transmission. As doping increases, however, intraband (Drude) absorption by free carriers becomes important, decreasing the transmission for  $\hbar\omega < \hbar/\tau$  (where  $\tau$  is the carrier relaxation time) due to the electron – longitudinal optical (LO) phonon interaction. Thus we expect that the transmission of ultrathin graphite is enhanced upon doping for a window of photon energies  $\hbar/\tau < \hbar\omega < 2E_F$ .

This phenomenon has been observed previously in gated monolayer and FLG samples, where doping levels were much lower than explored here and the window

occurred in the infrared<sup>64</sup>. A decrease in the absorption coefficient is also observed in the graphite intercalation compound (GIC) by Hennig et al.<sup>139</sup> In Li-intercalated graphite, the window manifests as a minimum in reflectivity occurring near 740 nm for bulk LiC<sub>12</sub> and 440 nm for bulk LiC<sub>6</sub><sup>152</sup>. The reflectivity minimum previously observed for bulk LiC<sub>6</sub> corresponds reasonably well to our observation of a transmission maximum near 500 nm. For LiC<sub>12</sub> the transmission maximum may occur at a longer wavelength than our experiment accesses, and we observe only an enhancement of long-wavelength transmission. Thus we conclude that the overall reduction in interband transitions by Pauli blocking is responsible for the transmission increase, and the higher Drude conductivity of more strongly doped LiC<sub>6</sub> is responsible for the observed reduction in transmission at long wavelength and the non-monotonic doping dependence of transmission at these wavelengths.

Further insight into these results is gained by examining the optical transmittance in terms of the optical conductivity. On a substrate with refractive index  $n$ , the transmittance of ultrathin graphite with optical (sheet) conductivity  $\sigma_{opt} = \sigma_1 + i\sigma_2$ , relative to that of the bare substrate, can be expressed as<sup>153</sup>:

$$T = \frac{1}{\left|1 + \frac{Z_0 \sigma_{opt}}{1+n}\right|^2} \quad (1)$$

where  $Z_0$  is the free space impedance. Li *et al.*<sup>64</sup> and Stauber *et al.*<sup>154</sup> reported the optical conductivities of doped monolayer graphene in the IR range. For  $\hbar\omega < 2E_F$ , i.e. below the Pauli blocking edge,  $\sigma_1 \gg \sigma_2$ ;  $\sigma_1$  is large due to LO phonon emission and  $\sigma_2$  passes through zero near the plasma edge ( $\epsilon_1 = 0$ ) (also see the Supplementary

Information) so that the transmission reaches a maximum. Therefore near the transmission maximum  $\sigma_{opt} \sim \sigma_1$ .

We then modeled the optical transmittance based on optical conductivity with a Drude contribution from the free carriers and an interband contribution that turns on, i.e.  $\sigma(\omega) = \sigma_d + \sigma_{ib}$ . The conductivity is modeled as  $N$  layers of graphene. The Drude

sheet conductivity can be written as<sup>8</sup>  $\sigma_D = \frac{n_{2D}e^2N}{m(\gamma - i\omega)} = \frac{e^2E_F N}{\pi\hbar(\gamma - i\omega)}$ , where  $n_{2D}$  is the

carrier density per layer,  $m$  the effective mass,  $\gamma = 1/\tau$  is the carrier relaxation rate, and  $N$  is the number of layers. For  $\hbar\omega > 2E_F$  the interband conductance turns on and

its real part is given by  $\text{Re } \sigma_{ib} = \frac{\pi e^2 N}{2h}$ ; however, this step in  $\sigma(\omega)$  produces a non-

zero imaginary part given by  $\text{Im } \sigma_{ib} = -\frac{e^2 N}{2h} \ln \left| \frac{2E_F + \hbar\omega}{2E_F - \hbar\omega} \right|$ . The thermal broadening of

the Pauli blocking leads to<sup>155</sup>  $\text{Re } \sigma_{ib} = \frac{\pi e^2 N}{2h} \left[ \tanh\left(\frac{2E_F + \hbar\omega}{4kT}\right) + \tanh\left(\frac{2E_F - \hbar\omega}{4kT}\right) \right]$ ,

and the imaginary part of  $\sigma_{ib}$  is obtained from Kramers-Kronig relation. The optical

properties of Li intercalated ultrathin graphite can be simply modeled as doped ultrathin graphite with a 1.5 eV Fermi energy. Figure 3.5c shows a schematic of

$\sigma_1 / N\sigma_0$  vs. the photon energy from the model for  $N$ -layer ultrathin graphite before

and after Li intercalation.  $\sigma_1$  in the visible range significantly decreases upon Li

intercalation, which leads to a large increase in the optical transmittance. The

modeled transmittance of both 8-layer and 83-layer ultrathin graphite (Figure 3.5b,

solid curves) closely resemble the corresponding experimental data, and the

sharpening of the transmission maximum for thicker films is a consequence of the plasma edge.

The complex dielectric function is also obtained from the optical conductivity by  $\varepsilon(\omega) = \varepsilon_1 + i\varepsilon_2 = \varepsilon_\infty + i\frac{4\pi}{\omega}\sigma(\omega)$ , where  $\varepsilon_\infty$  is the high frequency dielectric constant ( $\omega \approx W$ , where  $W$  is the bandwidth). The Pauli blocking edge produces a positive contribution to  $\varepsilon_1(\omega)$ , which, because of the negative free carrier contribution, leads to a plasma edge when  $\varepsilon_1 = 0$  near the Pauli blocking edge. The real part of the conductivity from this model was shown schematically in Figure 3.5c. The  $\varepsilon_1 = 0$  also implies  $\sigma_2 \approx 0$  near the maximum in the transmission, which allows the approximation of  $\sigma_{opt}$  real in the Figure of Merit analysis. In Figure 3.5d we show  $\varepsilon_1(\omega)$  from the optical model. The  $\varepsilon_1 \approx 0$  corresponds to the onset of transmission for bulk materials. Calculations of the transmission in our model conductivity and using the full slab transmission formulas accounts for the sharpening of the peak in the transmission curves for thicker films shown in Figure 3.5b.

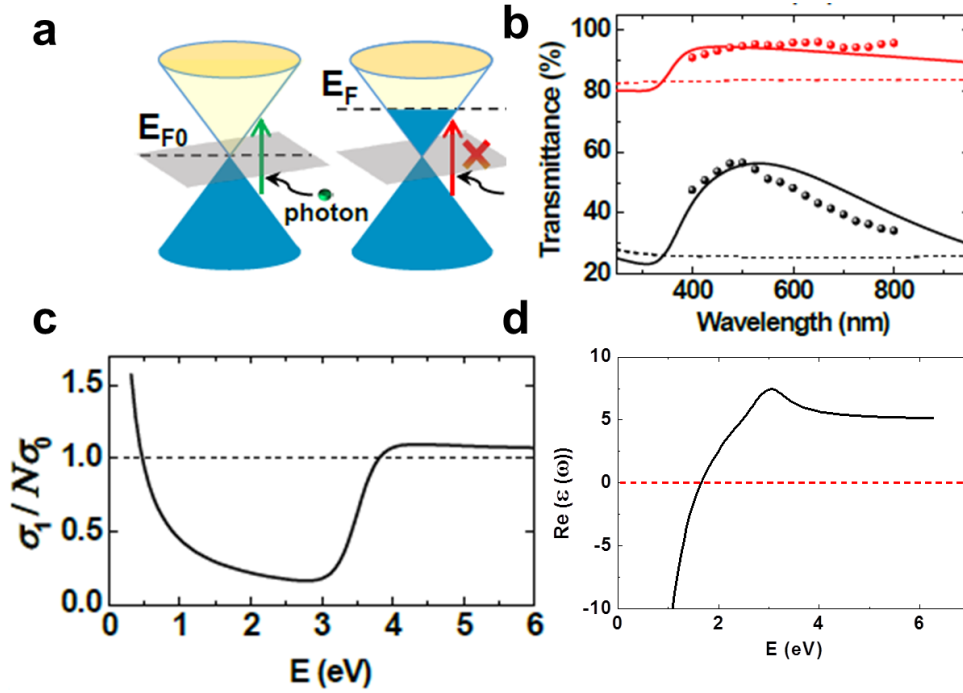


Figure 3.5 (a) Schematic of doped graphene bandstructure illustrating suppression of optical transitions due to Pauli exclusion principle. (b-c) Modeled results for transmittance (b), and the real part of optical conductivity,  $\sigma_1/N\sigma_0$  (c) of pristine ultrathin graphite (dashed line) and intercalated  $\text{LiC}_6$  (solid line). For the model we assume  $E_F = 1.5$  eV,  $n = 1.5$ ,  $T = 300\text{K}$ , and  $1/\tau = \gamma = 200$   $\text{cm}^{-1}$ . The red and black colors in (b) correspond to 8 and 83-layer ultrathin graphite sheets, respectively. Experimental data of 8 and 83-layer shown in (Figure 3.4c) are also plotted in (b) for comparison with the model, (d). Modeled result for the real part of dielectric constant  $\epsilon$  vs. photon energy.

### 3.4 in situ measurement of electrical transport properties

In order to understand the prospects for highly transparent Li-intercalated ultrathin graphite for conducting transparent electrode applications, we adapted our planar nano-battery setup for *in situ* conductivity measurements of ultrathin graphite

during electrochemical cycling. We transferred ultrathin graphite onto pre-deposited electrical contacts in a Hall-bar arrangement (Figure 3.6a inset). Figure 3.6a shows the room temperature sheet resistance  $R_S$  for ultrathin graphite samples with different thickness before intercalation as well as intercalated to  $\text{LiC}_{12}$  and  $\text{LiC}_6$ . As expected, all intercalated ultrathin graphite samples invariably exhibit a lower resistivity compared to their pristine state. Note that  $R_S$  measured on both stage I and II is inversely proportional to the sample thickness (before intercalation) as indicated by the dashed lines. Considering the expansion of the graphite-layer spacing during Li-intercalation<sup>124</sup> we can estimate that  $\rho(\text{LiC}_6) \sim 3.1 \times 10^{-6} \Omega \cdot \text{cm}$  and  $\rho(\text{LiC}_{12}) \sim 1.4 \times 10^{-5} \Omega \cdot \text{cm}$ . The intrinsic limit of the conductivity for doped graphene at room temperature is set by electron-acoustic phonon scattering and is approximately  $\sigma_{\text{dc,phonon}} = 33 \text{ mS per layer}$ <sup>145, 156</sup> for Fermi energies in the linear portion of the band structure, while we observe a DC sheet conductivity  $\sigma_{\text{dc}} \approx 11 \text{ mS per layer}$  in  $\text{LiC}_6$ . At the high doping levels present in  $\text{LiC}_6$ , we expect significant band curvature and reduction in the Fermi velocity, likely reducing the limiting conductivity. Additionally, disorder may play a role. Thus our approach within a factor of  $\sim 3$  to the limiting conductivity value for the graphene Dirac band is impressive.

In order to elucidate the type and density of charge carriers we investigated the Hall resistance at perpendicular magnetic fields. The linear  $R_{xy}(B)$  curves with negative slope (Figure 3.6b) indicate that charge carriers are electrons for a 4 nm-thick FLG device after Li-intercalation. The carrier density  $n_H$  is readily determined by a measurement of the Hall coefficient  $R_H = R_{xy}/B$ , where  $R_H$  is related to  $n_H$  by  $n_H = 1/eR_H$ . With the information of expanded thickness of lithium intercalated ultrathin graphite, our measurements reveal that bulk  $n_H$  ranges from  $3 \times 10^{21}$  to  $7 \times 10^{21} \text{ cm}^{-3}$  for  $\text{LiC}_{12}$  and

from  $1.5 \times 10^{22}$  to  $3.5 \times 10^{22} \text{ cm}^{-3}$  for  $\text{LiC}_6$ , with no observable dependence on sample thickness, as shown in Figure 3.6c. These values compare reasonably well with the full ionization values of  $1.7 \times 10^{22} \text{ cm}^{-3}$  for  $\text{LiC}_6$  and  $9.0 \times 10^{21} \text{ cm}^{-3}$  for  $\text{LiC}_{12}$ , which are indicated in Figure 3.6c as guidelines. Figure 3.6d shows the temperature dependence of the sheet resistance.  $R_s(T)$  is metallic, i.e.  $R_s$  decreases with decreasing  $T$ , for samples at  $\text{LiC}_6$  state, while  $\text{LiC}_{12}$  exhibits a moderate temperature dependence, and pristine samples always exhibited weakly non-metallic behavior consistent with previous studies<sup>127</sup>. The strong decrease in  $R_s$  with lowering  $T$  for  $\text{LiC}_6$  is consistent with phonon-limited conduction and further corroborates that we have approached the phonon-limited conductivity in Li-intercalated ultrathin graphite<sup>141</sup>.

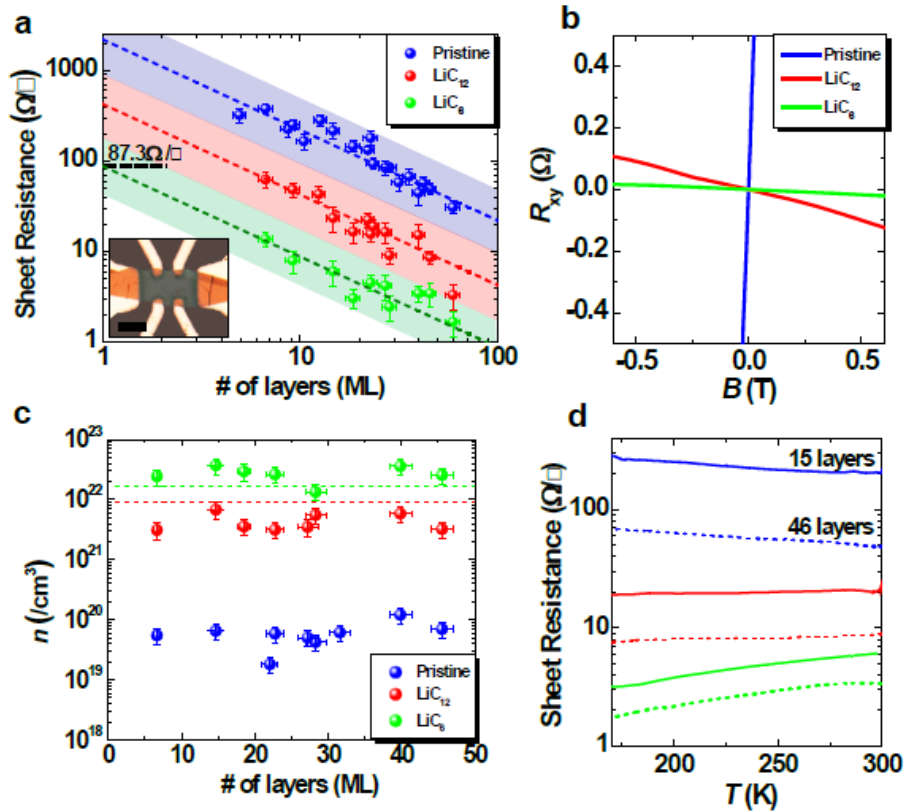


Figure 3.6 Transport measurement of Li intercalated ultrathin graphite sheets. (a) Resistivity vs. thickness for ultrathin graphite sheets with different thickness. Data for pristine (red) and two lithiated stages ( $\text{LiC}_{12}$  and  $\text{LiC}_6$  indicated as green and blue) are shown. Inset: An optical image of an ultrathin graphite device with Hall bar geometry before intercalation. The scale bar is 10  $\mu\text{m}$ . (b) Hall resistance of a 4-nm-thick pristine FLG sheet and its  $\text{LiC}_{12}$  and  $\text{LiC}_6$  states as a function of magnetic field. (c) Carrier density calculated from Hall measurement as a function of ultrathin graphite thickness. (d) Temperature dependent sheet resistance for two ultrathin graphite samples. Blue, red and green colors indicate pristine,  $\text{LiC}_{12}$  and  $\text{LiC}_6$  stages, respectively.

### **3.5 transparent conductor performance of Li intercalated ultrathin graphene**

By attaching an electrical probing setup to the transmission optical microscope, transmittance and four-probe resistance can be measured simultaneously on the same sample. Such data is plotted as solid circular points in Figure 3.7, which locate very close to the original data, supporting the validity of the previous correlation.

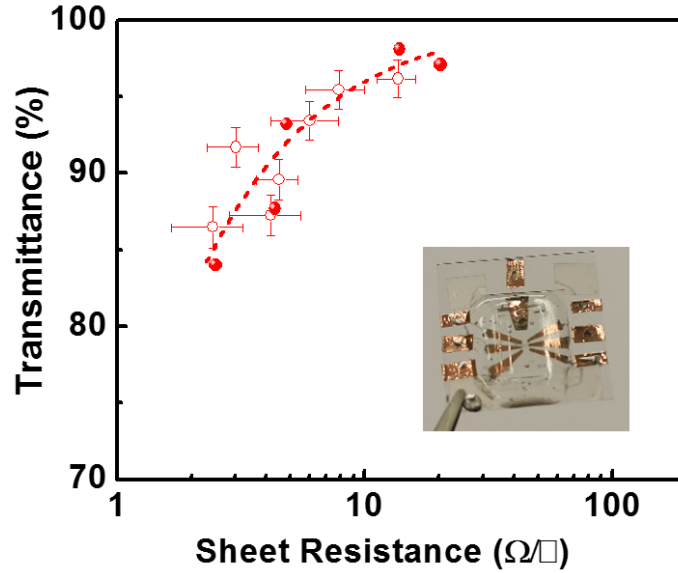


Figure 3.7 Optical transmittance *vs.* sheet resistance for two batches of devices. Solid data points are taken on the same device using a concurrent optical/electrical measurement setup.

In the race to find better transparent electrodes researchers have investigated numerous candidate materials.<sup>144, 157-159</sup> Figure 3.8 shows the transmittance *vs.* sheet resistance of Li-intercalated ultrathin graphite as well as other high-performance transparent conducting materials, including other carbon-based materials,<sup>78, 160</sup> and the best commercial indium-tin-oxide (ITO) electrodes.<sup>159, 161</sup> In previous doped-graphene studies an improvement in the electrical conductivity was observed; however, little or no change of transmittance in the visible range was obtained.<sup>22, 78</sup> When  $\sigma_1 \gg \sigma_2$  and  $n = 1$ , to compare the performance of a freestanding film in vacuum, Equation (1) becomes:

$$T = \frac{1}{\left(1 + \frac{[1000 \Omega] \sigma_{opt}}{R_S \sigma_{dc}}\right)^2} \quad (2)$$

where the sheet resistance is  $R_s = 1 / \sigma_{dc}$ . Thus at a given sheet resistance, the transmission is determined by the ratio  $\sigma_{dc}/\sigma_{opt}$  which can be used as the Figure of Merit (FOM) to characterize the performance of a transparent conductor.

As shown in Figure 3.7a we fit the data for our Li-intercalated FLG devices to Eqn. 1 using  $\sigma_{dc}/\sigma_{opt}$  as a fitting parameter, and fitting result gives  $\sigma_{dc}/\sigma_{opt} = 920$ . For the best sample at  $\text{LiC}_6$  state we measured transmittance of 91.7 % and 3.0  $\Omega$  per sq, obtaining  $\sigma_{dc}/\sigma_{opt} = 1400$ . Figure 3.8b shows the best measured  $\sigma_{dc}/\sigma_{opt}$  for the material systems shown in Figure 3.8a;  $\sigma_{dc}/\sigma_{opt}$  for our  $\text{LiC}_6$  exceeds that of  $\text{FeCl}_3$  intercalated FLG ( $\sigma_{dc}/\sigma_{opt} = 235$ )<sup>78</sup> and the best commercial transparent electrode ITO ( $\sigma_{dc}/\sigma_{opt} = 118$ )<sup>159</sup>. In fact,  $\sigma_{dc}/\sigma_{opt}$  of few-layer  $\text{LiC}_6$  exceeds that for all other carbon based materials, and as far as we can determine is the highest for any uniform thin film. Higher transparency at a given conductivity has only been achieved in inhomogenous conductors such as metal nanowire networks<sup>162</sup>, which may not be suitable for many applications. It also exceeds the intrinsic limit for doped graphene<sup>22, 157</sup> previously expected ignoring the increased transparency due to Pauli blocking. The sheet resistance and transparency easily meet the need for optoelectronic device applications where 90% and 10  $\Omega$  per sq is required. Thus we expect that electrochemically intercalated FLG is promising for applications where the highest DC conductivity at a given optical transparency is needed.

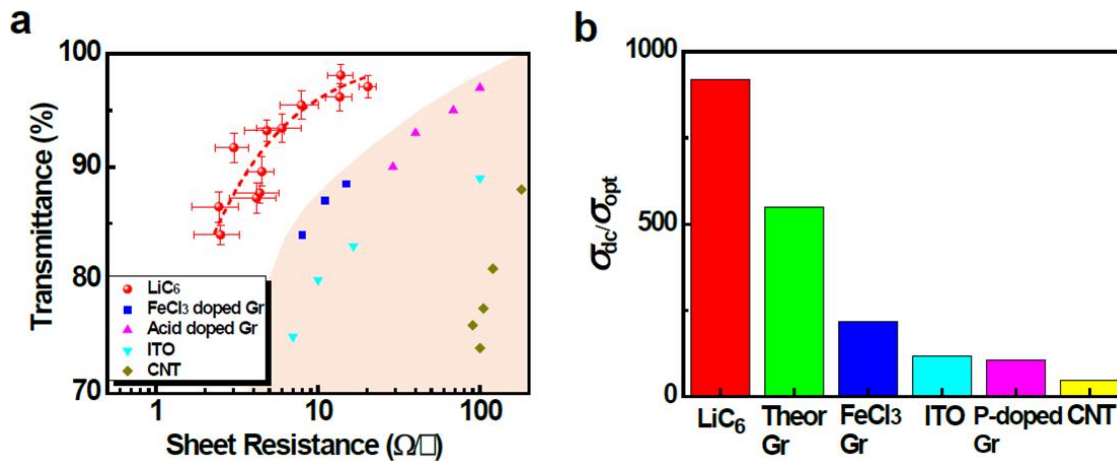


Figure 3.8. Optoelectronic properties of intercalated ultrathin graphite sheets and comparison with other materials. (a) Transmittance at 550 nm vs. sheet resistance for our LiC<sub>6</sub> FLG, and other high-performance carbon-based transparent conducting materials FeCl<sub>3</sub>-doped graphene<sup>78</sup>, acid-doped graphene<sup>22</sup>, and carbon nanotube (CNT) films<sup>160</sup>, as well as indium tin oxide (ITO)<sup>161</sup>. The red solid line is a fit with equation 3 with  $\sigma_{dc}/\sigma_{opt} = 920 \pm 100$ . (b) Figure of merit ( $\sigma_{dc}/\sigma_{opt}$ ) for various materials. A higher value for  $\sigma_{dc}/\sigma_{opt}$  leads to better performance in transparent conductor.

### 3.6 Scalable application of Li intercalation with large area CVD graphene

To demonstrate the feasibility of ultrathin graphite as transparent electrode for industrial applications, we successfully fabricated stable millimeter-scale devices using encapsulated commercially-obtained chemical vapor deposition-grown (CVD) thin graphite. CVD ultrathin graphite on Nickel foil (2" × 2") is obtained from Graphene Supermarket and cut into 1.5 cm × 1.5 cm pieces. A solution based (1M FeCl<sub>3</sub> in DI water as etchant, Sigma Aldrich) etching/transfer method is then carried out to transfer ultrathin graphite onto transparent substrates (e.g. glass and PET). A gel electrolyte film is

prepared by mixing P (VDF-HFP)/Acetone/DI water (w:w:w = 1:19:1, Sigma Aldrich) as a mixed solution. The electrolyte is then drop-cast on glass and ready for use after drying in a vacuum oven (MTI corp.). A sandwiched device structure of glass/ultrathin graphite/gel electrolyte/PET is assembled in an argon-filled glove box. The transmittance of the device is measured by a UV-vis spectrometer (PerkinElmer Lambda 35).

Comparison of two 40 nm and 80 nm thick devices before and after Li intercalation are shown in Figure 3.9a, b. Transmittance spectra are also characterized before and after Li intercalation, as shown in Figure 3.9c, which are very similar to the results of single exfoliated ultrathin graphite sheets. Changes in the sheet resistance were also measured for 40-nm-thick devices by the Van der Pauw method (Figure 3.9d). The sheet resistances of three different devices dropped drastically upon complete lithiation from 35.4, 47.7, 57.0  $\Omega$  per sq (graphite) to 3.0, 3.9, 1.7  $\Omega$  per sq ( $\text{LiC}_6$ ), respectively (Figure 3.9e). The 1.7  $\Omega$  per sq correspond to a single layer sheet resistance of 200  $\Omega$  per sq, only 2.3 times larger than the single flake value (87.3  $\Omega$  per sq) from our experiment, leads to a FOM of 400.

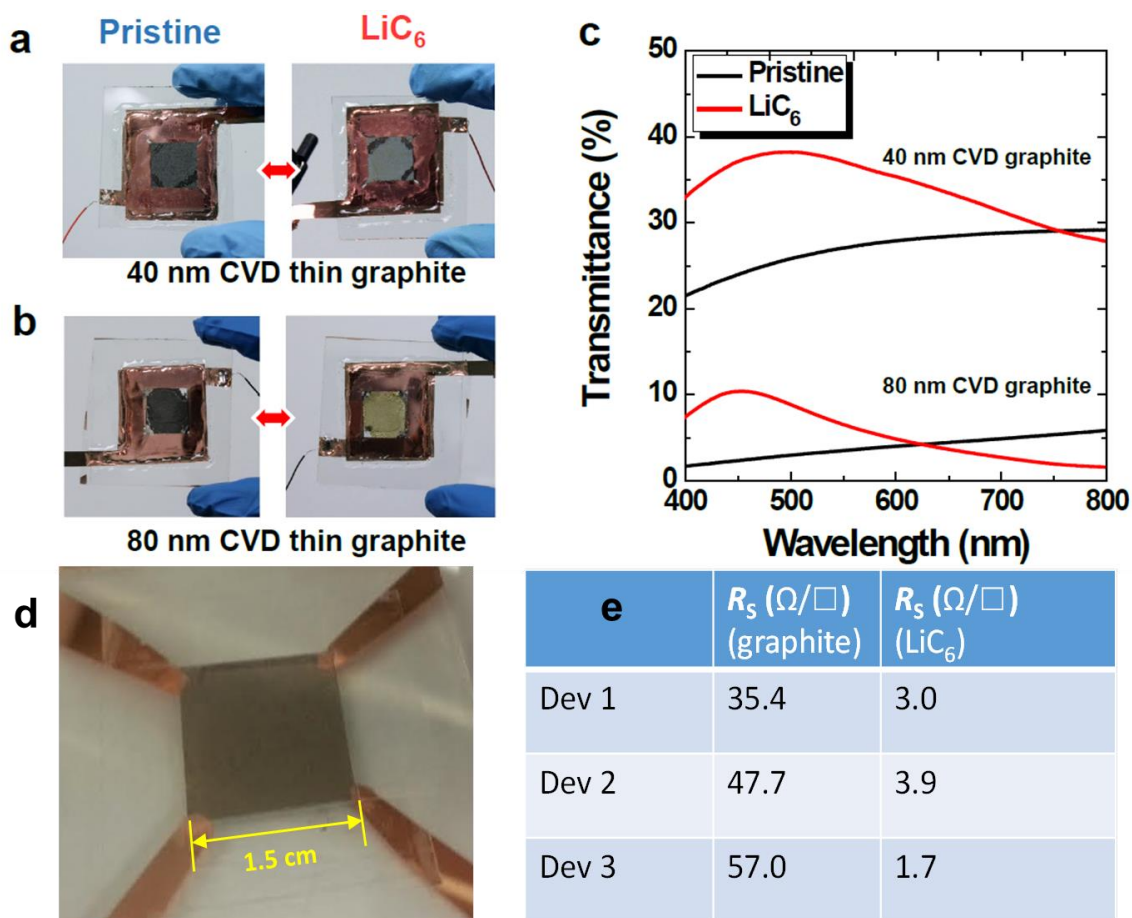


Figure 3.9 Demonstration of encapsulated large-area transparent electrode (a-b) Photographs of 40- and 80-nm thick CVD grown thin graphite before and after full Li intercalation. (c) Corresponding transmittance spectra of the two devices before and after full intercalation, (d) Van de Pauw measurement of CVD ultrathin graphite, and (e)  $R_s$  of pristine graphite and  $\text{LiC}_6$  for three 40-nm-thick CVD graphite devices.

In order to determine the stability of large scale  $\text{LiC}_6$  films for transparent electrode application, we also carried out an initial stability test using commercially-obtained ultrathin graphite films grown by chemical vapor deposition (CVD), as shown in Figure 3.10. After epoxy encapsulation, a CVD ultrathin graphite device was lithiated to  $\text{LiC}_6$  state and stayed stable in ambient condition for over 48 hours, as shown in Figure 3.10 a-c.

We also confirmed that  $\text{LiC}_6$  is unstable if exposed in air, as shown in Figure 3.10 d-g. Therefore we conclude that once the device is appropriately sealed it is stable for transparent electrode applications. Again, standard industrial sealing techniques as used for Li-ion batteries should suffice to produce stable  $\text{LiC}_6$  films. Figure 3.9 d-e shows the sheet resistance measurement using Van der Pauw method, and results of  $R_s$  for three 40-nm-thick CVD graphite devices.

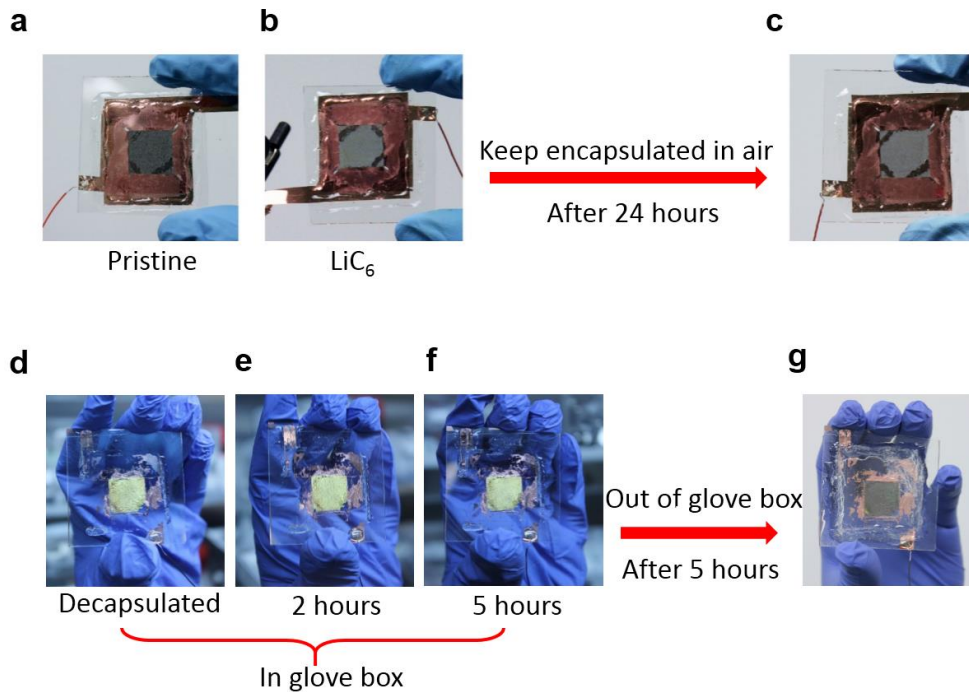


Figure 3.10 (a-c) Stability of encapsulated CVD thin graphite device in air. (d-g), Decapsulated thick  $\text{LiC}_6$  is stable in glove box but unstable in air.

### 3.7 Discussion and Summary

We discuss the ultimate limits to conductivity and transparency of doped graphene-based systems. Previous studies<sup>144</sup> of graphene as a transparent conductor have

ignored changes in the optical conductivity, assuming it remains limited by interband transitions and is fixed at  $\sigma_{\text{opt}} = \sigma_{\text{ib}} \approx N\pi e^2/2h = N\sigma_0$ , with  $N$  the number of layers, as discussed above. For phonon-limited conduction at room temperature  $\sigma_{\text{dc}} = N\sigma_{\text{dc,phonon}}$  where  $\sigma_{\text{dc,phonon}} = 33 \text{ mS}$ <sup>145, 156</sup>. This predicts a maximum value of  $\sigma_{\text{dc}}/\sigma_{\text{opt}} \approx 550$ , while our intercalated ultrathin graphite significantly exceeds this value. However, as noted previously, below the Pauli blocking edge  $\sigma_{\text{opt}}$  is the free carrier Drude conductivity that can be smaller than  $\sigma_{\text{ib}}$ . Optical measurements on doped monolayer graphene gives  $f \equiv \sigma_1/\sigma_0 \approx 0.3$  below the interband edge for  $E_F \approx 0.3 \text{ eV}$ <sup>64</sup>. Assuming this value of  $f$  implies  $\sigma_{\text{dc}}/\sigma_{\text{opt}} \approx 1800$  in reasonable agreement with our best observation; however, there are no experimental results on the magnitude of  $\sigma_1$  and hence  $f$  for the  $E_F \approx 1.5 \text{ eV}$  conditions of our intercalated graphene. Theory predicts that the Drude optical conductivity for frequencies above the LO phonon frequency is limited by the electron - LO phonon relaxation rate,  $\gamma = 1/\tau_{LO}$ <sup>163</sup>. At the higher  $E_F$  of our experiments the electron phonon scattering rate will be stronger because of the larger electronic density of states ( $\sim E_F$ ), but the high frequency Drude conductivity falls off as  $\sigma_1 \sim E_F \gamma/(\gamma^2 + \omega^2) \sim E_F \gamma/\omega^2$ . This suggests  $\sigma_1$  and hence  $f$  at  $\omega \leq 2E_F$  are approximately independent of  $E_F$  so that  $f \equiv \sigma_1/\sigma_0 \approx 0.3$  may also be valid at  $E_F \approx 1.5 \text{ eV}$ , and our estimate of the intrinsic limit of  $\sigma_{\text{dc}}/\sigma_{\text{opt}} \approx 1800$  is reasonable. Thus we believe that our real devices approach the ultimate limits of transparency at a given conductivity for the doped graphene system.

In summary, we have designed a methodology *via* a planar nano-battery for *in situ* study of the electrical and optical properties of individual ultrathin graphite sheets during electrochemical intercalation and de-intercalation. Metallic-like temperature dependent transport is observed in Li-intercalated ultrathin graphite with conductivities approaching

the acoustic-phonon limit at room temperature and is comparable to good metals. Due to the unusual band structure of graphene, Li-intercalation can simultaneously increase the DC electrical conductivity and increase optical transmission in the visible, allowing Li-intercalated FLG to achieve an unprecedented FOM  $\sigma_{dc}/\sigma_{opt} = 920$ , significantly higher than any other material and approaching the ultimate limit expected for doped graphene systems. Our technique will allow similar studies to be carried out in other 2D materials. Furthermore, the methodology reported in this study can be applied to *in situ* investigations of the intercalation process with good spatial and temporal resolution in materials for electrochemical energy storage applications.

## Chapter 4: Na-ion intercalation in large-scale, printed RGO network as high performance transparent conductors

Jiayu Wan, Feng Gu, Wenzhong Bao, Jiaqi Dai, Fei Shen, Wei Luo, Xiaogang Han, Daniel Urban, and Liangbing Hu, *Nano Lett.*, 2015, 15 (6), pp 3763–3769

### 4.1 Introduction

Ultrathin two-dimensional (2D) materials such as graphene are highly attractive for transparent electrode applications due to their high transparency and carrier mobility, which lead to an excellent combination of sheet conductance and optical transmittance in the visible range.<sup>8, 14, 126, 132, 164</sup> Large-area graphene prepared by chemical vapor deposition (CVD) has shown 30 Ohm/sq and 90% transmittance, comparable with traditional indium tin oxide (ITO) electrodes;<sup>22</sup> however, the high cost of CVD-based transparent electrodes is one of the main obstacles to replace ITO.<sup>165</sup> Solution-based, large-scale, printed transparent conductors using liquid exfoliated graphene<sup>166-171</sup> or reduced graphene oxides (RGO)<sup>172-179</sup> show potentially much lower cost, and have been successfully applied to a range of electronic devices such as solar cells<sup>180-182</sup> and organic light-emitting diodes (OLED).<sup>183, 184</sup> However, the high sheet-sheet junction resistance largely limits the sheet conductance of printed film<sup>144</sup>, similar to previous works on carbon nanotube network transparent electrodes.<sup>161</sup> Chemical doping<sup>22</sup> and intercalation<sup>78, 92</sup> have been explored as effective methods to increase carrier density, and thus lower the sheet resistance with little decrease or even an increase in the optical transmittance. Recently, we reported a method by electrochemical lithium-ion intercalation in mechanically-exfoliated graphene sheets, which leads to a drastic

simultaneous improvement of sheet conductivity and optical transmittance in the visible range.<sup>61</sup> The Li-intercalated graphene sheets are unstable in air, however, and the methodology is limited by the size of exfoliated sheets, which narrows its range for practical applications.

In this work, we report sodium-ion (Na-ion) intercalation in a printed graphene oxide network after a thermal reduction. Compared with liquid exfoliated multilayer graphene that hinders the insertion of Na-ions due to its small interlayer distance, RGO has larger sheet size (therefore better junction contact),<sup>178</sup> and an expanded interlayer distance that allows Na-ion insertion.<sup>185, 186</sup> As a result, a relative increase in the transmittance as large as 120% (from 36% to 79%), with a 270 times decrease of sheet resistance (from 8.3 kohms/sq to 311 ohms/sq) are achieved in sodiated RGO (S-RGO) network. Such an intercalated network shows the best performance in RGO-based transparent electrodes. Surprisingly, we found that S-RGO is much more stable than a Li-intercalated graphene, which may be attributed to the self-termination of oxidation products at the edges of RGO sheets by the reaction between Na-ion and water/CO<sub>2</sub>/O<sub>2</sub>. Thus, Na-ion intercalation of a printed RGO network is a promising approach leading to scalable applications as transparent conductors.

Figure 4.1a-b show a schematic illustration of Na-ion intercalation into RGO network. To carry out the electrochemical intercalation in electrolyte, a constant current source is applied between the intercalant (Na metal) and the host material (printed RGO film). Na-ions can electrochemically intercalate into RGO interlayers and RGO-RGO junctions. Due to the low electrochemical potential, the accumulation of intercalated Na-ions will introduce the electron doping (n-doping) and thus shifts the Fermi level up. Due

to the large storage capacity of RGO for Na ions, the electron doping level is high as well. The large electron doping is expected to cause the “Pauli blocking”<sup>63, 64, 130</sup> of incident light in the visible range. This results in a large enhancement of the optical transparency of the RGO network. On the other hand, electron doping will also improve the conductivity of individual RGO flakes. Junctions in printed RGO networks usually act as barriers for charge transport, and reduce the entire conductivity of the network.<sup>161</sup> Na-ion intercalation can provide electron pathways in junctions and greatly reducing the junction resistance. We focus on printed RGO network toward scalable nanomanufacturing. Figure 4.1c shows an AFM image of RGO network, which exhibits a nanoscale surface smoothness, and curved lines are ripples or overlapped edges of RGO sheets. Figure 4.1d shows that printed RGO after sodiation is highly stable even when exposed in air for a month, which demonstrates the potential for its utilization in practical applications.

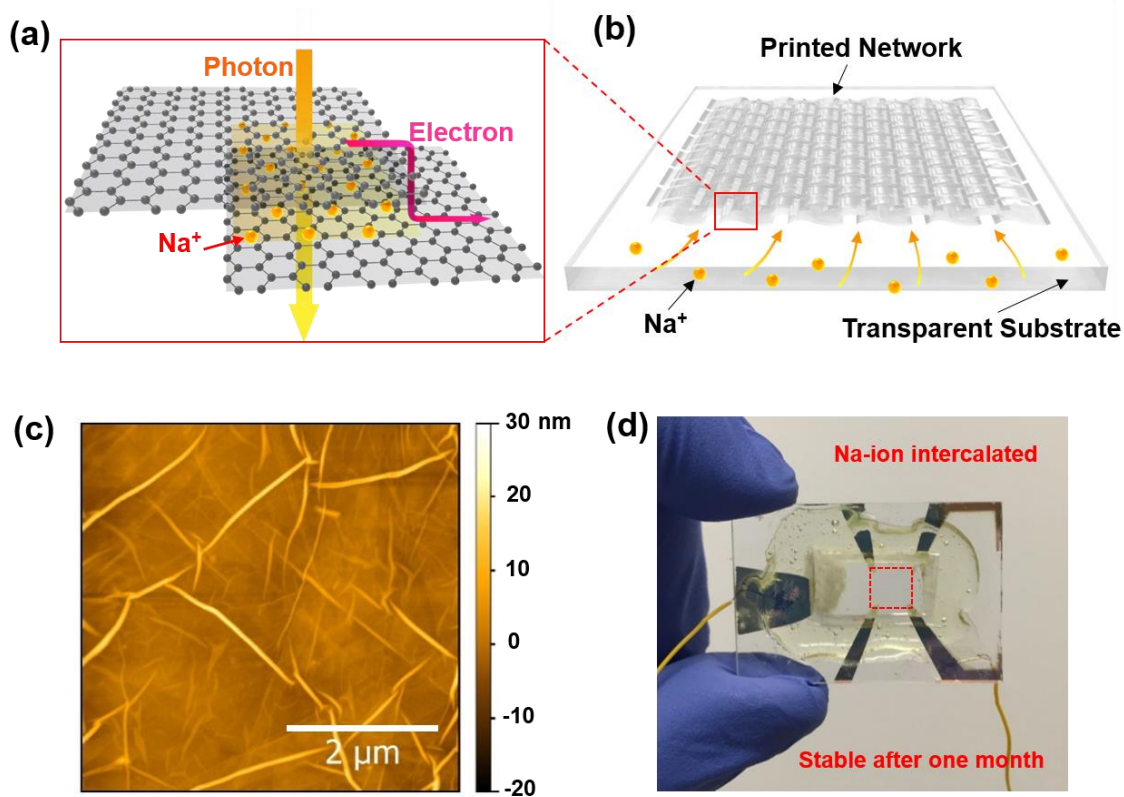


**Figure 4.1** (a) Schematic of Na-ion intercalation between two RGO sheets, enhancing simultaneously their optical transmittance and electrical conductivity. (b) Schematic of Na-ion intercalation in printed RGO network on transparent substrate. (c) AFM image of a printed RGO network. (d) Highly transparent and stable S-RGO film (confined in red dotted square) in air after one month.

## 4.2 Electrochemical characterization of Na-ion intercalation in RGO thin film

We have two motivations to use Na-ion as intercalants for such novel transparent electrodes. Firstly, Na-ions are much more cost-efficient and more abundant than Li. Secondly, Na-ion is expected to form a more stable barrier layer to prevent further oxidation toward better stability than Li ion. However, Na-ion cannot intercalate into

graphene as demonstrated by others before. Recently, Na ion intercalation in RGOs has been demonstrated. To prove that Na-ions can intercalate into RGO materials prepared in our lab, several characterization tests were carried out. First, a coin cell was made using free-standing RGO film and Na metal as positive and negative electrodes, respectively. Figure 4.2a shows the voltage profile (2<sup>nd</sup> cycle) of sodiation/desodiation in RGO thin film at a low current density of 25 mA/g, indicating a reversible Na-ion intercalation/de-intercalation process in RGO network. From the voltage profile, the specific capacity for sodiation is 170 mAh/g, and 127 mAh/g for desodiation. The irreversible capacity is mainly due to the electrolyte decomposition and side reactions during Na-ion intercalation process, which is commonly observed for carbon anodes in Na-ion batteries.<sup>185-187</sup> The amount of intercalated Na-ions in the RGO network is 0.028 per carbon atom, calculated from the reversible specific capacity.

We also applied X-ray diffraction (XRD) on the same RGO thin film before and after sodiation to confirm the actual intercalation process. During the XRD characterization, samples were protected by a thin layer of plastic wrap to avoid chemical reactions under ambient condition. In Figure 4.2b, a sharp peak is shown in the RGO film before Na-ion intercalation. The peak position is at  $25.35^\circ$ , which corresponds to an interlayer distance of  $3.49 \text{ \AA}$ . This interlayer distance is larger than that of graphite ( $3.35 \text{ \AA}$ ). The light green shadowed area represents a peak with full width at half maximum (FWHM) in length of  $1.02 \text{ \AA}$ . After Na-ion intercalation, the XRD peak shifted to left, indicating a larger interlayer distance of  $3.76 \text{ \AA}$  in average. The peak shape is also much broader than what was observed before Na-ion intercalation, with a FWHM changes to  $1.67 \text{ \AA}$ . The enlarged interlayer distance is indicative of a successful

intercalation of Na-ions between RGO layers. The peak around  $18^\circ$  is due to the sealing plastic wrap. The broadening of the peak at  $25.35^\circ$  may be due to the non-uniform intercalations of Na-ions in the printed RGO flakes.

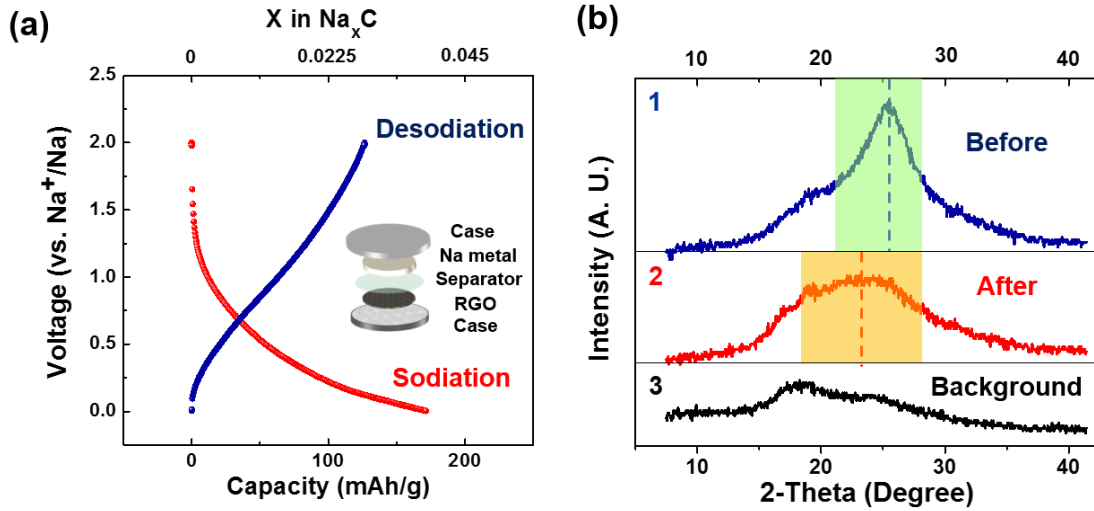


**Figure 4.2** Electrochemical and XRD characterizations of Na-ion intercalation in RGO thin films. (a) Voltage profile of RGO film as positive electrode in coin cell. Inset is the schematic of RGO-Na coin cell (b) XRD of RGO film before, after Na intercalation, and plastic wrap as background.

### 4.3 Optical transmittance characterization of printed RGO film upon Na-ion intercalation

To demonstrate a scalable application of Na-ion intercalated RGO as high performance transparent electrodes, printable GO ink is prepared (figure 4.3a). Commercial surfactant Zynol as added to decrease the surface energy of GO ink in water to be printable. Meyer rod coating method was applied to deposit GO film, which shows excellent uniformity (figure 4.3b). GO coated on glass slides were then thermally

reduced to RGO, and trimmed by blading to a desired shape. Copper current collectors were deposited by thermal evaporation, then Na metal and 1M NaPF<sub>6</sub> in EC:DEC (1:1=v:v) were added as the negative electrode and electrolyte, respectively. The entire device was finally sealed with an epoxy in an argon-filled glove box. The schematic and photo images of the electrochemical intercalation device<sup>188</sup> are shown in figure 4.3c. After electrically connecting the two electrodes of RGO and Na metal, RGO film can be fully intercalated by Na-ions within 10 minutes, as shown in Figure 4.3d, leading to a uniform transmittance enhancement to the S-RGO network.

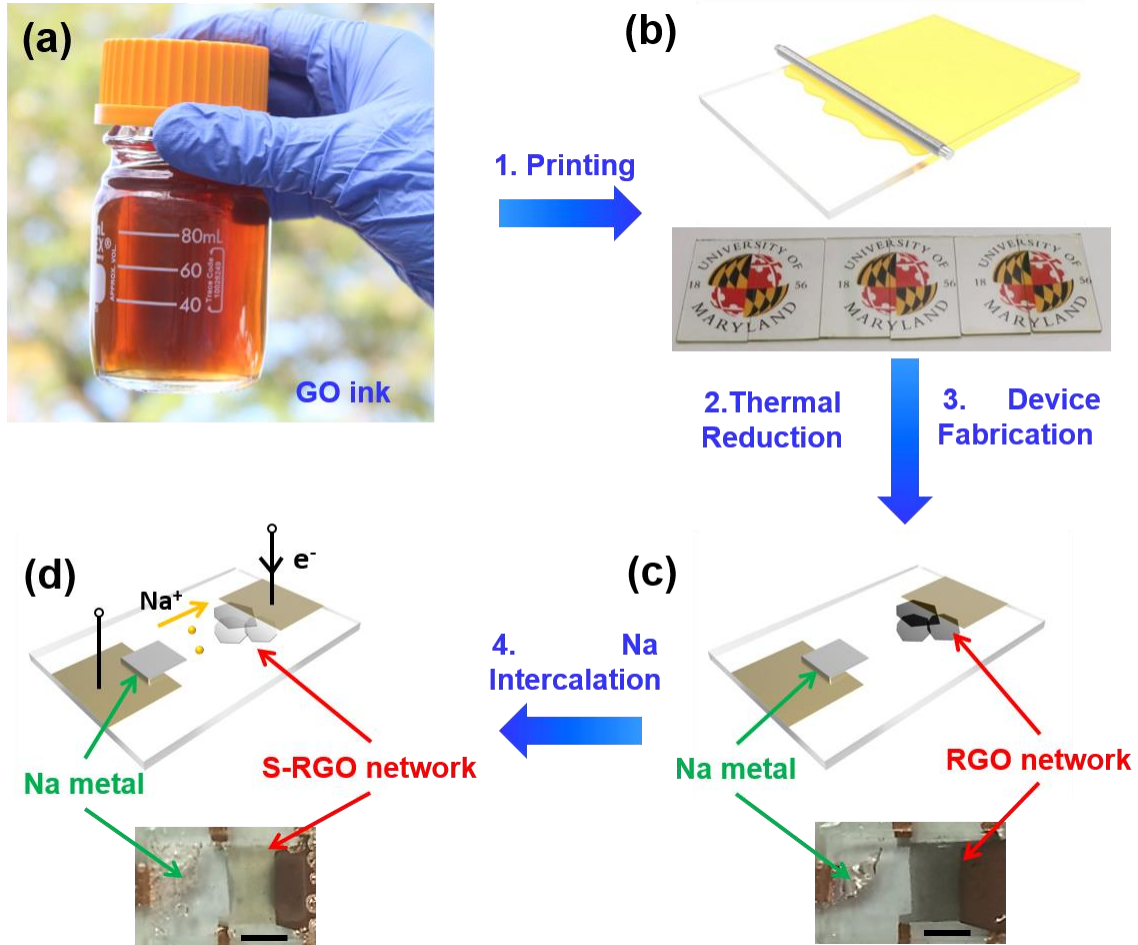


**Figure 4.3** (a) A bottle of as prepared GO ink to be added with Zynol to tailor the surface energy for printing purpose. (b) Meyer rod coating of GO ink with excellent uniformity on glass substrate. (c) A two terminal, lateral device with RGO network as working electrode, Na metal as the counter electrode and 1M NaPF<sub>6</sub> in EC:DEC (1:1=v:v) as the electrolyte. (d) After Na ion intercalation, the RGO network becomes more transparent.

The transmittance of RGO network before and after Na-ion intercalation is quantitatively illustrated by grey scale images captured by an optical microscope (operated in transmission mode), as shown in figure 4.4a and b, respectively. Note that the increase of optical transmittance is very uniform across the entire printed RGO network.

Figure 4.4c plots the transmittance change of RGO network before and after complete sodiation at wavelength of 550 nm for samples with different thickness. It is clear that all samples exhibited a drastic transmittance increase. Note that the substrate is excluded in the transmittance measurement. The percentage of relative increase in transmittance is also plotted in Figure 4.4c inset. For instance, RGO network with transmittance of 46.1% increased to 91.5% after sodiation, which is nearly a 100% increase compared to its original value. Wavelength dependent spectrum from 450 nm to 900 nm was shown in Figure 4.4d. The increase of optical transmittance is flat in the visible range, which indicates a neutral color and is beneficial for a range of applications.

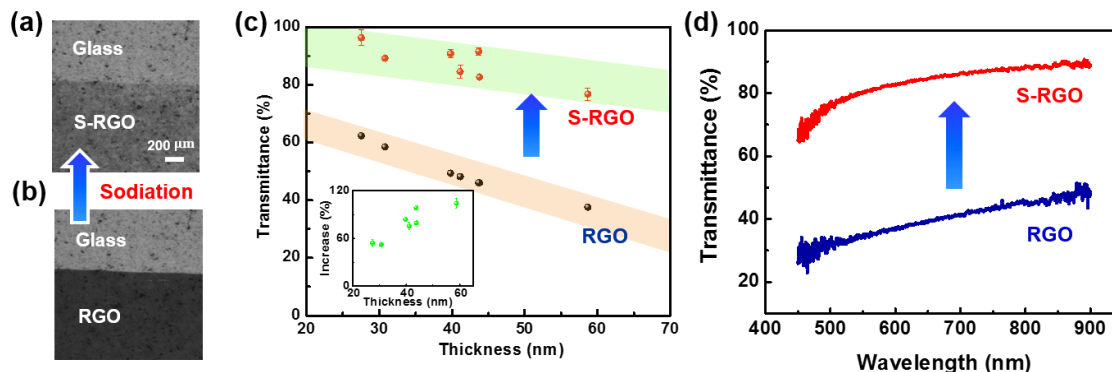


**Figure 4.4** Optical transmittance of a RGO network device before and after Na-ion intercalation. (a-b) show optical microscope (transmission mode) images of the same RGO network before and after sodiation. (c) Transmittance vs. thickness of RGO network before and after sodiation at 550 nm. The inset is the percentage of relative increase in transmittance at 550 nm. (d) Transmittance vs. wavelength of the same RGO network before and after sodiation with a visible spectrum from 450 nm to 900 nm.

#### 4.4 Performance of Na-ion intercalated RGO as transparent conductor

To further demonstrate the feasibility of S-RGO as transparent conductors, sheet resistance of RGO films before and after Na-ion intercalation was investigated. The resistance measurement was carried out by a four-point probe method (schematic device image shown in the inset of Fig 4.5a to eliminate the contact resistance between Cu electrodes and sample film. I-V curves taken from a RGO device before and after sodiation are shown in figure 4.5a, starting with a large sheet resistance at 100 kohm/sq since the GO film was only partially reduced at a relatively low temperature of 300 °C.

<sup>189</sup> Surprisingly, with an increased transmittance after sodiation, the sheet resistance also

decreased by 300 folds, from 523 kohms/sq to 1467 ohms/sq. The other typical decrease in sheet resistance is from 83 kohms/sq to 311 ohms/sq (Fig. 4.5b). It is expected that Na ion doping largely enhances the carrier density in RGO, which leads to the conductivity increase of individual RGOs.<sup>29, 31</sup> Meanwhile, Na ion intercalation will potential improve the RGO-RGO contacts which overcomes the obstacle of conventional network conductors.<sup>161</sup>

This synergistic effect in increase of optical transmittance and decrease of sheet resistance can be qualitatively explained by large electron doping upon sodiation. Due to the large Na ion storage capacity of RGO and low electrochemical potential of Na metal, intercalated Na ions are compensated with the same amount of electron doping to RGO. The large electron doping leads to a large Fermi energy, which blocks optical transition in the visible range and increases the optical transmittance. Electron doping also leads to the large increase of the conductivity. This synergistic effect in increase of optical transmittance and decrease of sheet resistance leads to an excellent performance of S-RGO as a transparent conductor. For fair comparison, we compare our data with other 2D network based materials including RGO and exfoliated graphene (figure 4.5a). S-RGO shows clear better performance than other materials. To quantify this comparison, the figure of merit (FOM, defined as ratio of electrical to optical conductivity,  $\sigma_{dc}/\sigma_{opt}$ ) is calculated based on sheet resistance and optical transmittance at 550 nm (figure 4.5d). Sheet resistance and optical transmittance of approximately 80-85% were used for FOM calculations. S-RGO network has the highest FOM value. Better performance is expected with large RGO flakes, which will have a low percolation threshold and better initial performance as transparent conductor before Na ion intercalation.

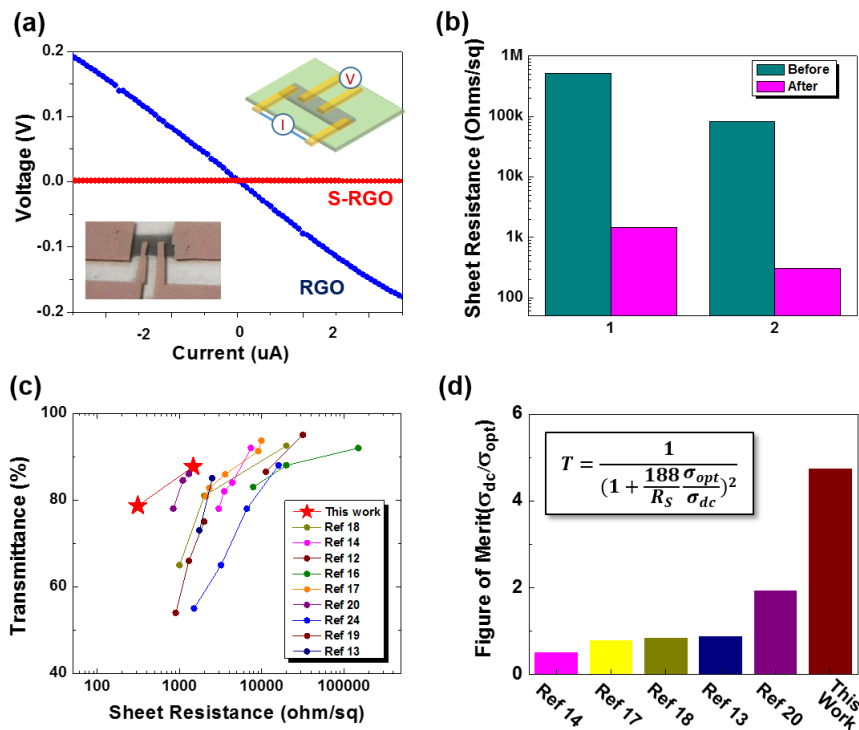


**Figure 4.5** (a) Four-point probe I-V measurement of a RGO network before and after sodiation. Insets are the schematic and photo images of four-probe measurement on RGO network. (b) Sheet resistance change of two different samples. (c) Transmittance vs. sheet resistance plots of S-RGO vs. reported RGO network transparent conductors. (d) FOM of network transparent electrodes, including exfoliated graphene, S-RGO and RGO.

#### 4.5 Air stability of Na-ion intercalated RGO transparent conductors

Air-stability of sodium ion intercalated RGO is a potential concern due to the high reactivity of Na. To evaluate the stability, S-RGO network was first fully sodiated in encapsulated devices. One device was then disassembled and S-RGO on glass was

exposed in ambient environment. Optical images captured by a microscope on S-RGO film over different spots on the same device were recorded after 0, 0.5, 2, 3 and 13 hours. Optical transmittance of S-RGO on glass was obtained based on microscope images. After complete Na intercalation, transmittance at 550 nm of the RGO sample (red bar) increased from 57% to 90%. The sample shows small degradation after immediate exposure in air. Then the transmittance is stabilized over time even after 13 hours. Our continuing observations show that S-RGO does not change the optical transmittance after one month. Photo images of S-RGO network in air for the first a few hours are shown Figure 4.6b.

As we demonstrated before, Li-intercalated ultrathin-graphite has the highest FOM among all continuous thin film so far.<sup>61</sup> However, the large diffusivity/reactivity of Li-ions in the intercalant causes poor stability and requires further device encapsulation. Graphene flakes become highly transparent after Li ion intercalation. But intercalation compound completely changes back to the original, much lower transmittance after a few hours in air.<sup>61</sup> The better stability of Na ion intercalated RGO than Li ion intercalated graphene flakes is explained as the following. Intercalated alkaline ions such as Li and Na are extremely reactive and thus will react with air, oxygen and water in ambient environment immediately. The reactants on the edges of the 2D materials will prevent further reaction of alkaline ions, which explains the initial decrease of the optical transmittance in the first half hour. The difference between Li ion and Na ion is likely explained by their different diffusivity through the self-formed barrier layer. The large Na ion size could lead to a much slower diffusion through the barrier layer than Li ion. Therefore, the reactants on the edges of 2D materials prevent

further reaction of Na atoms with O<sub>2</sub>, H<sub>2</sub>O and CO<sub>2</sub> in air, and seals intercalated Na atoms inside the sheets.

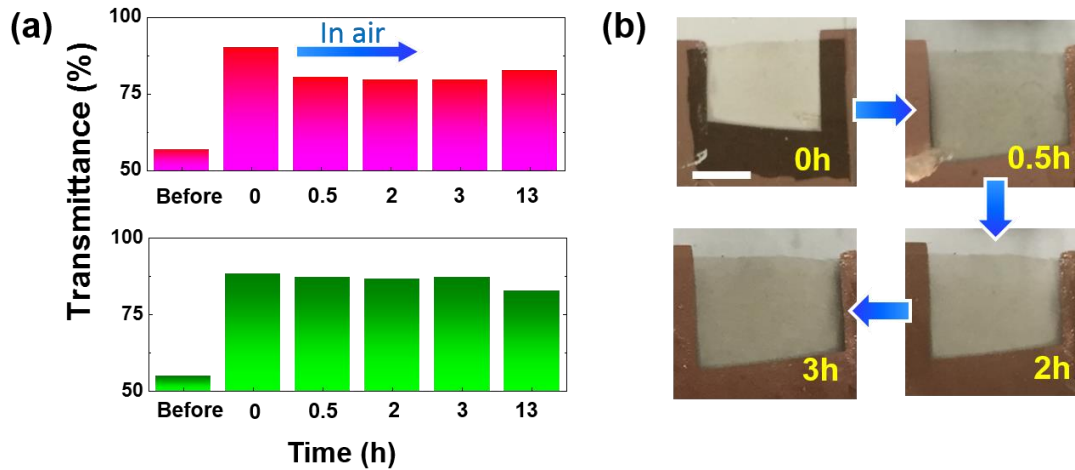


**Figure 4.6** Stability in air of transparent conductor based on S-RGO network. Photo images of S-RGO in air after 0, 0.5, 2 and 3 hours. The scale bar (white) is 2 mm.

## 4.6 Summary

For the first time, we demonstrated that Na-ion can be intercalated into RGO network that simultaneously increase the optical transmittance (~ 100%) and conductivity (~ 300 times) dramatically. The intercalated RGO network shows superior performance as transparent conductor, better than any other RGO network based transparent electrodes. Surprisingly, such transparent electrodes shows excellent stability in ambient environment, much more stable than Li ion intercalated graphene. The processes including GO network printing, thermal reduction and electrochemical intercalation can all be potential scaled toward practical applications. Further improvement of transmittance and sheet resistance can be achieved with GO networks with large size of

individual flakes. Fundamental studies including air stability mechanism based on Na ion transport through the reactant layer, charge transport through RGO-RGO layers after ion intercalation, etc. will be further investigated in the future. This work demonstrated the great feasibility of using metal ion intercalations in 2D materials for promising transparent conductor applications.

## Chapter 5: In situ TEM study of Na-ion interaction with high performance RGO anodes

### 5.1 Introduction

Sodium-ion batteries (SIBs) have attracted great attention due to their potential applications in grid scale energy storage system.<sup>190-195</sup> Advantages of SIBs over lithium-ion batteries (LIBs) are obvious. Sodium resources are abundant and available worldwide, while lithium resources are limited and concentrated only in certain areas around the world.<sup>193</sup> Despite the similarities of SIB chemistry to LIB chemistry, great challenges remain for high performance SIBs. One of the major obstacles is that Na-ion is almost 3 times larger than Li-ion in volume, making the pulverization problem more severe. Meanwhile, Na-ion kinetics are much more sluggish.<sup>196</sup> In spite of the disadvantages, recent development of cathode materials for SIBs showed excellent promise with high voltage and stable cyclability.<sup>197-201</sup> Unfortunately, the anode side remains a challenge, since Si and graphite, the most investigated anode materials in LIBs, cannot be applied in SIBs.<sup>185, 202</sup> To date, a number of anode materials for SIBs have been investigated, such as metal/metal alloys,<sup>196, 202</sup> metal oxides,<sup>203-205</sup> red phosphorus,<sup>206-208</sup> and organic compounds.<sup>209</sup> Despite their advantages, cost-efficiency, stable cyclability, performance and operation safety issues, still hinder their further applications as SIB anode materials.

Carbon materials have been intensively studied as promising materials for energy devices due to their high capacity, abundance, and low cost.<sup>210</sup> As for SIBs, hard carbon, a non-graphitized carbon, has attracted great attention due to its high specific capacity of

~250 mAh/g.<sup>187, 211</sup> However, the rate capability of hard carbon is poor because of its low conductivity and its kinetics limited nanopore-filling Na-ion storage process. Most recently, a number of researchers reported reduced graphite oxide and reduced graphene oxide (rGO) as promising Na-ion storage materials, including Na-ion intercalated transparent conductors.<sup>185, 212, 213 214</sup> In contrast to graphite, above-mentioned materials obtain larger interlayer distance (larger than 0.335 nm), allowing Na-ions to intercalate/de-intercalate between each graphitic layer. However, the thermal reduction process of graphite oxide/graphene oxide (GO) requires hours of operation, a high temperature reduction process, and a special atmosphere. More importantly, a trade-off between interlayer distance and conductivity of rGO exists with different reduction temperatures/times. This dilemma results in a poor performance of rGO as SIB anode, with reversible specific capacity lower than 300 mAh/g. Thus, a green and simple method for obtaining high power, high specific capacity rGO as SIB anode is highly in demand. Despite solely performed as active electrode materials, rGO is also widely applied as functional additive materials in SIBs anodes, mostly utilizing its large specific area and high electrical conductivity.<sup>215, 216</sup> In both scenarios, rGO electrochemically interact with Na-ions actively in SIBs, regardless of their physical or chemical properties are considered in the design of experiment process. Consequently, the understanding of sodiation-desodiation process is crucial for rGO containing SIBs. Despite previous attempts to unveil this process, it remains controversial and lack of direct evidence.

Herein, we conducted *in situ* transmission electron microscopy (TEM) to study the sodiation-desodiation process of rGO. Our study provides the first direct observation of reversible Na metal cluster (diameter larger than 10 nm) formation on rapid-rGO

surface upon sodiation and desodiation, which reveals an important Na-ion storage mechanism in rGO anodes. The phenomenon is evidenced by both selected area electron diffraction (SAED) pattern and atomic-resolved HRTEM image of the electrode/Na metal, enabled with state-of-the-art K2 summit electron-counting camera with an extremely low electron beam dose rate. The observation supports our record high rGO reversible specific capacity of 450 mAh/g, obtained from the rapid reduced GO (in 2 seconds). Moreover, the rapid reduced GO sustained a highly stable cycling with 750 cycles of around 200 mAh/g at 250 mA/g. Direct observation of irreversible Na<sub>2</sub>O formation with *in situ* TEM results also evidenced the capacity loss during the 1<sup>st</sup> cycle with rGO containing SIB electrodes.

## 5.2 preparation and characterization of rapid RGO Na-ion battery anode

GO was prepared using an improved Hummer's method.<sup>217</sup> rGO samples are firstly prepared for *in situ* TEM and electrochemical characterizations. High temperature treatment of GO has long been known as an effective method to separate the graphitic layers, and produce few-layered reduced graphene flakes.<sup>218</sup> During this process, oxygen containing functional groups (such as hydroxyl groups, carboxyl groups and epoxy bridges) are unstable at high temperature (usually above 300 Celsius), thus decomposing into carbon dioxide (CO<sub>2</sub>) and water (H<sub>2</sub>O).<sup>218, 219</sup> Two types of high temperature reduced GO has been prepared in this work, as illustrated in Figure 5.1. When stacked GO sheets are reduced at a "regular" process (i.e. hours of reduction at high temperature),<sup>214</sup> most functional groups on GO are removed and the interlayer distance are decreased, as shown in Figure 1b. In this process, CO<sub>2</sub> and H<sub>2</sub>O are slowly released, thus rGO layers

get restacked after reduction. When it is reduced at a “rapid” process, in which the reduction occurs within minutes or even seconds, the decomposed molecules will be abundantly released, and leave much larger spacing than the “regular” process (Figure 5.1c). The rapidly released gases not only lead to a larger interlayer spacing and even some separated monolayer reduced graphene sheets, but also create a loosely packed structure for rGO.<sup>220</sup> A large interlayer spacing contributes to a high specific capacity, while a loosely packed structure is beneficial for high surface functional group Na-ion storage as well as an excellent ionic accessibility, which supports electrochemical reaction at high rate. Thus, the rapid reduced GO (rapid-rGO) is chosen for *in situ* TEM study and SIB anode. The regular reduced GO is used as a control sample for SIB anode.

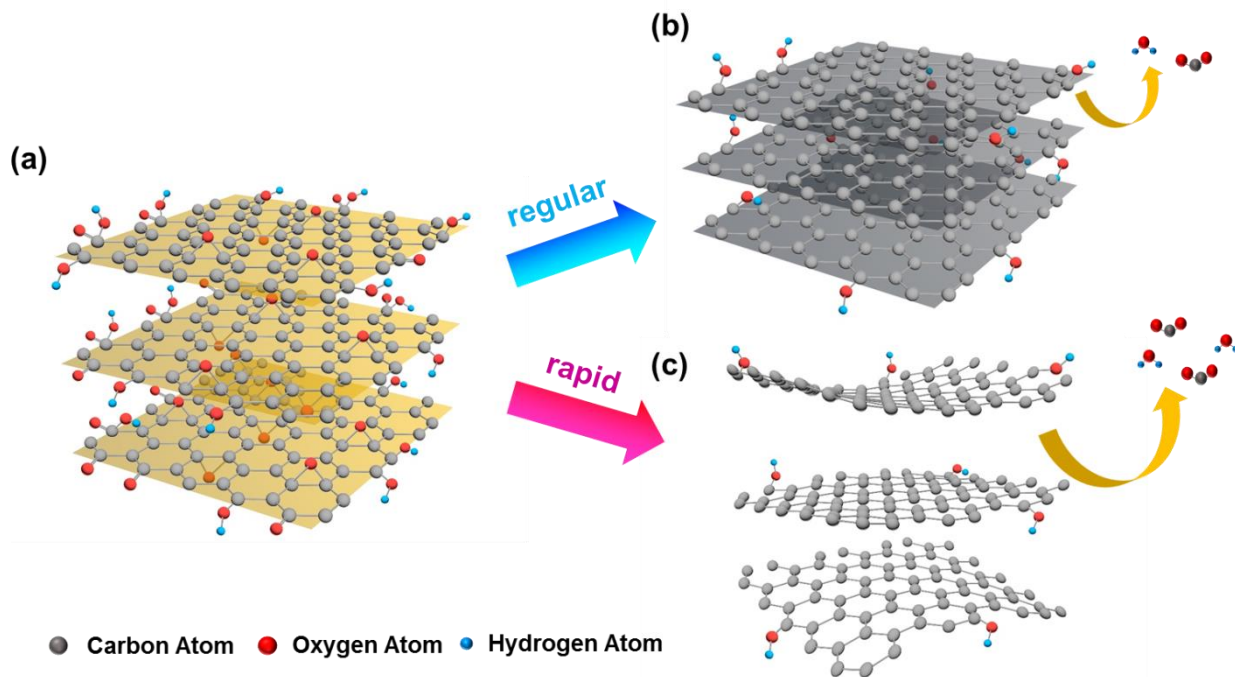


Figure 5.1 Schematics of two types of GO reduction process (a) stacked GO sheet is (b) slowly thermal reduced and (c) rapidly reduced.

Photothermal reduction of GO is chosen here as a simple, controllable, green method, as well as a rapid reduction process. Photons in the infrared/visible range absorbed by GO can locally heat up the material, and reduce GO to rGO in an exceedingly short time.<sup>220</sup> In this study, a Xexon lamp is adopted as light source for the reduction process. When a free-standing GO film is exposed under the Xexon light, the reduction process happens in 2 seconds on average. Figure 5.2a shows a schematic of Xexon lamp for reduction of GO. To understand the photothermal reduction of GO, X-ray diffraction (XRD), X-ray photoelectron spectroscopy (XPS) and scanning electron microscope (SEM) are applied to study the as-synthesised GO and rapid-rGO film. As shown in Figure 5.2b, the orange line and black line describe the XRD patterns of GO and rapid-rGO, respectively. XRD pattern of GO shows a sharp peak, with  $2\theta$  at  $10.2^\circ$ , corresponding to a  $d$ -spacing of  $8.70 \text{ \AA}$ . After rapid reduction,  $2\theta$  of rapid-rGO XRD pattern shows a broad distribution from  $14.0^\circ$  to  $36.9^\circ$ , with a peak position at  $24.5^\circ$ .  $d$ -spacing of the peak is calculated to be  $3.65 \text{ \AA}$ , which indicates a successful reduction from GO to rGO.

XPS analysis shows the surface chemical composition of GO and rapid-rGO films, respectively.<sup>221</sup> As shown in Figure 5.2c, orange and black curves represent the XPS results of GO and rapid-rGO, where C 1s peak presents at  $\sim 285 \text{ eV}$  and O 1s presents at  $\sim 533 \text{ eV}$ .<sup>185</sup> The height of these two peaks provide a qualitative information of C/O ratio of the two materials, so it is obvious that rapid-rGO has a higher C/O ratio than GO. A quantitative analysis of C/O from XPS is shown in Table I, where the ratio percentage increases from 2.54 to 5.94 after rapid reduction. The C1s spectrum of rapid-rGO reveals that the C–C bond at  $284.8 \text{ eV}$  dominates the carbon bond in rapid-rGO. The

small portion of oxygen containing bonds are found to be C–O (286.3 eV), –C=O (287.5 eV), and –O–C=O (291.5 eV) (Figure 5.2d).<sup>216, 222</sup> The remaining oxygen containing groups in rapid-rGO are essential to maintaining a relatively large interlayer distance, which enables Na-ion intercalation. Both XRD and XPS results confirm a successful reduction of rapid-rGO by our photothermal method in 2 seconds. Figure 2e shows a typical SEM of tightly packed free standing GO film. After photothermal reduction, the SEM images shows a very loose packing of rapid-rGO layers (Figure 5.2f), unlike the rGO obtained in a slow thermal reduction process (show in Figure 5.5c). In quite a few places, the rapid-rGO flakes show a very thin characteristic thickness (few layer or even monolayer rGO), as shown in Figure 5.2f inset.

Table 5.1 Atomic percentage of carbon and oxygen from XPS analysis. (450 stands for rGO regular reduced at 450 °C, details in supplementary materials)

XPS analysis	GO	Rapid-rGO	450 °C
C/O	2.45	5.94	11.00

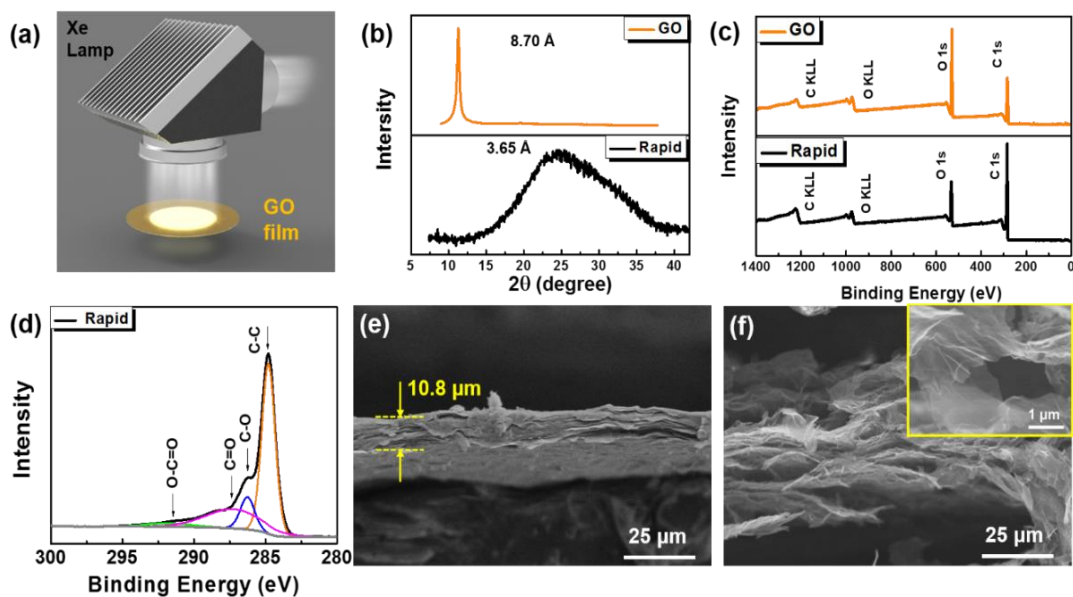


Figure 5.2. Methods and characterization of GO and rapid-rGO. (a) A schematic image of rapid reduction process by Xexon lamp, (b) XRD patterns of GO film and rapid-rGO, (c) XPS spectra of GO film and rapid-rGO, (d) C 1s spectrum of rapid-rGO, SEM images of (e) dense GO film and (f) rapid-rGO, inset a higher magnification SEM image of rapid-rGO.

### 5.3 In situ TEM characterization of Sodiation process with rapid RGO

*In situ* TEM is a powerful tool to understand the electrochemical process of a battery material upon ion insertion and desertion.<sup>123, 223-225</sup> Usually, only a solid state electrolyte is in contact with the active materials, which provide an extremely clean and pure environment to study their electrochemical process. Thus, we chose *in situ* TEM to perform the sodiation-desodiation study with rapid-RGO. As shown in a schematic in Figure 5.3a, the Na/Na<sub>2</sub>O is working as counter electrode and solid state electrolyte, while the rapid-rGO is using as working electrode. After applying a negative bias (-0.5

V) to the working electrode, the Na migrated into the rGO, as shown in Movie S1. Figure 5.3b and c show TEM images of the rGO before and after the first sodiation. The morphology of the pristine rGO nanosheet is well presented with a clean surface in Figure 4a. The corresponding SAED, in Figure 5.3d, clearly shows the (100) and (110) rings of a typical graphite structure (space group:  $P6_{3mc}$ ) with a  $d$ -spacing of 2.14 Å and 1.23 Å, respectively. This indicates that the nanosheet is pure rGO without any contamination. Interestingly, it was observed that the rGO nanosheet was curled up and coated with a layer of extraneous material on the surface after the first sodiation, as shown in Figure 5.3c. The coating layer was determined to be with  $\text{Na}_2\text{O}$  ( $d_{200}=2.80$  Å,  $d_{220}=1.95$  Å, and  $d_{311}=1.67$  Å), and Na ( $d_{200}=2.10$  Å,  $d_{211}=1.75$  Å, and  $d_{310}=1.35$  Å), as proved by the corresponding SAED in Figure 5.3f.

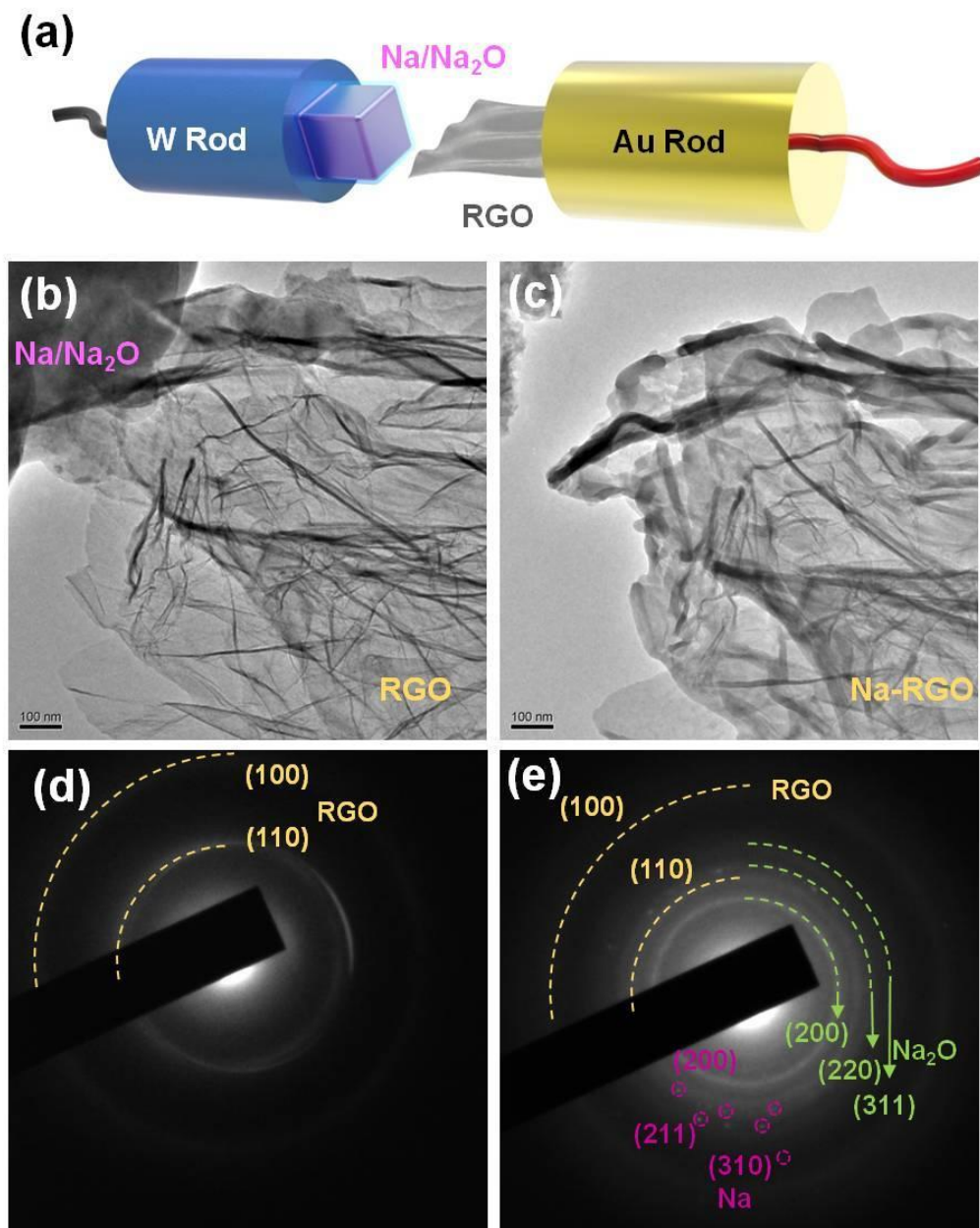


Figure 5.3. *In situ* TEM study of the first sodiation of rGO. (a) Schematic of in situ TEM set-up (b) TEM image of Na/Na<sub>2</sub>O as counter electrode/solid electrolyte and rGO as working electrode before sodiation (b) after sodiation (d) Diffraction pattern of rGO before sodiation (e) after sodiation.

Figure 5.4a shows a typical HAADF image of sodiated RGO nanosheet. Coverage of extraneous material made the sodiated RGO nanosheet with a rough surface. The elemental mapping of the sodiated RGO clearly shows that Na and O elements were distributed on the surface of the RGO.

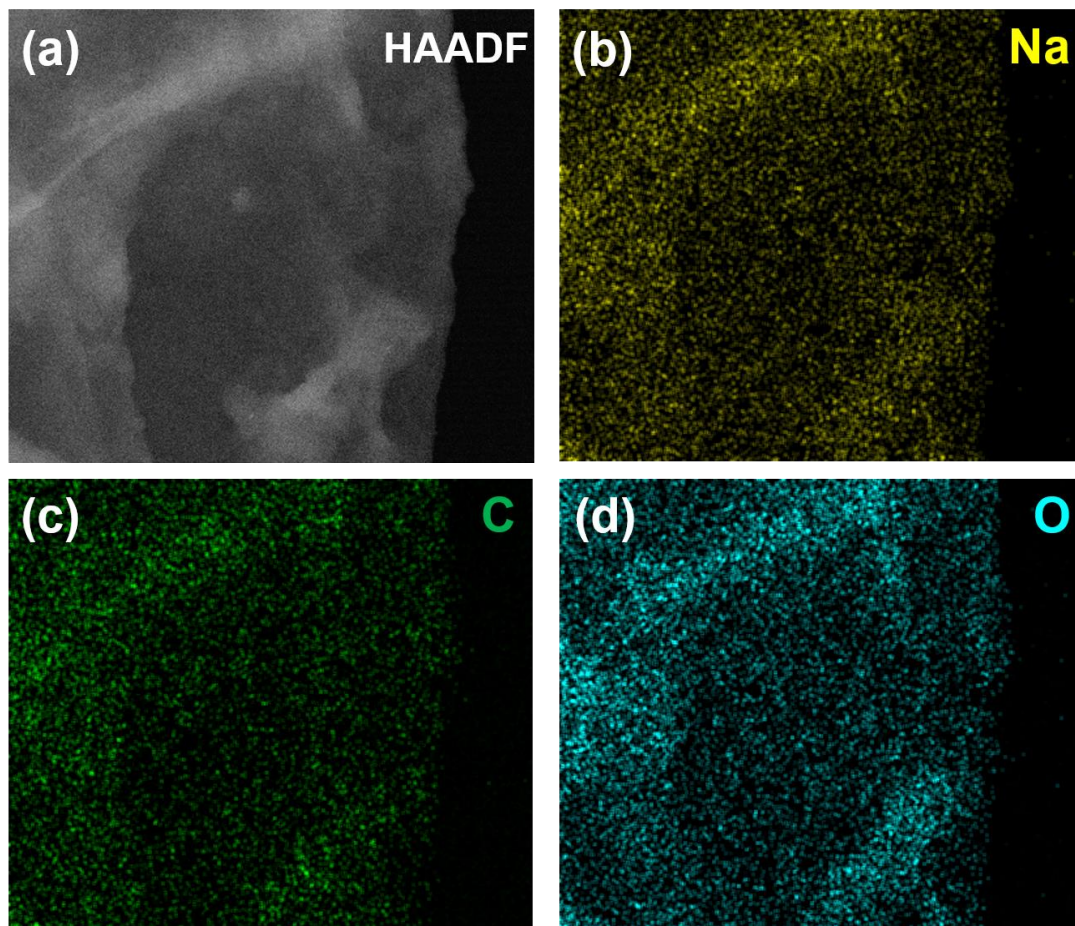


Figure 5.4. (a) High angle annular dark field (HAADF) image of sodiated RGO (b-d) Elemental distribution of sodiated RGO mapped by Energy-dispersive X-ray (EDX).

To further understand this phenomenon, HRTEM images of the rGO after the first sodiation was taken, as shown in Figure 5.5. Particularly, to avoid the effect of the

electron beam, the HRTEM was recorded with an extremely low electron dose rate (2.0 electrons pixel<sup>-1</sup>s<sup>-1</sup>) by using a state-of-the-art K2 summit electron-counting camera. As shown in Figure 5.5a, several nanocrystals with lattice fringes formed on the surface of the rGO. Two of them with good orientations were chosen for a deeper investigation. Figure 4b shows an atomic-scale HRTEM image of one nanocrystal in Figure 5.5a. The  $d$  spacing of two vertical lattice planes was measured to be 3.0 Å, which matches well with that of the {110} lattice planes of body centered cubic (BCC) Na metal, as shown in Figure 5.5c. This suggests that the Na metal forms on the surface of rGO. To the best of the authors' knowledge, Figure 5.5a displays the first published atom-resolved HRTEM image of Na metal. An atomic-scale HRTEM image of another nanocrystal from the green box is shown in Figure 5.5d. This HRTEM image also shows two vertical lattice planes with an equal  $d$  spacing values of 2.8 Å, which are determined to belong to the {200} planes of face centered cubic (FCC) Na<sub>2</sub>O crystal structure, as shown in Figure 5.5e. Above analysis indicates that Na metal and Na<sub>2</sub>O formed after the first sodiation of rGO.

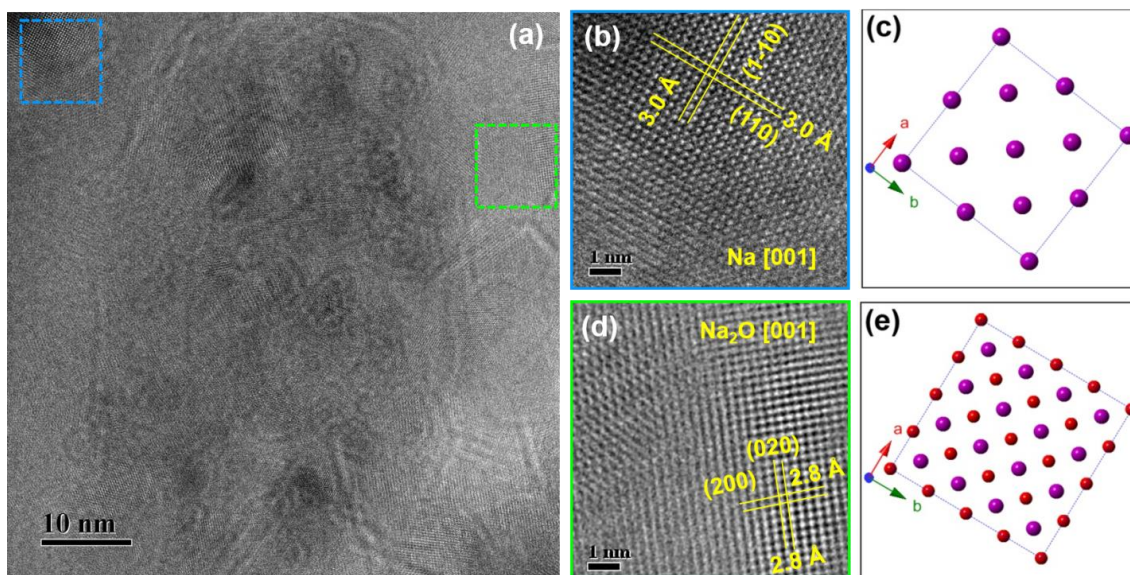


Figure 5.5. HRTEM images of sodiated rGO. (a) Low-mag HRTEM image recording the surface of the sodiated rGO. (b) High-mag HRTEM image taken from the blue box in the panel a. (c)  $2 \times 2 \times 2$  supercell for BCC Na metal. (d) High-mag HRTEM image taken from the green box in the panel a. (e)  $2 \times 2 \times 2$  supercell for FCC  $\text{Na}_2\text{O}$ .

The desodiation process of the rGO was also captured by our *in situ* TEM, as shown in Figure 5.6. Figure 5.6a shows a HRTEM image of a domain in the sodiated rGO. The *d-spacing* of 3 equivalent lattice planes of inset in Figure 5.6a was measured to be  $3.0 \text{ \AA}$ , belonging to the  $\{110\}$  planes of BCC Na metal. The corresponding Fast Fourier Transform (FFT) pattern further confirms that the lattice belongs to the BCC Na metal structure taken with the  $[1-11]$  zone axis. Interesting, this Na metal particle was slipping away after applying a positive bias (+2 V) to the rGO nanosheet. After a total desodiation, we found that the  $\text{Na}_2\text{O}$  retained on the surface of the rGO, as indicated by the HRTEM image and corresponding SAED pattern in Figure 5.6b. However, we did not find the existence of Na metal. The observation of reversible Na metal formation on rGO

surface evidences the hypothesis of a Na-ion storage mechanism in rGO and related carbon materials. This result also indicates that the formation of irreversible  $\text{Na}_2\text{O}$  on the surface of rGO is a main reason for the first cycle capacity loss.

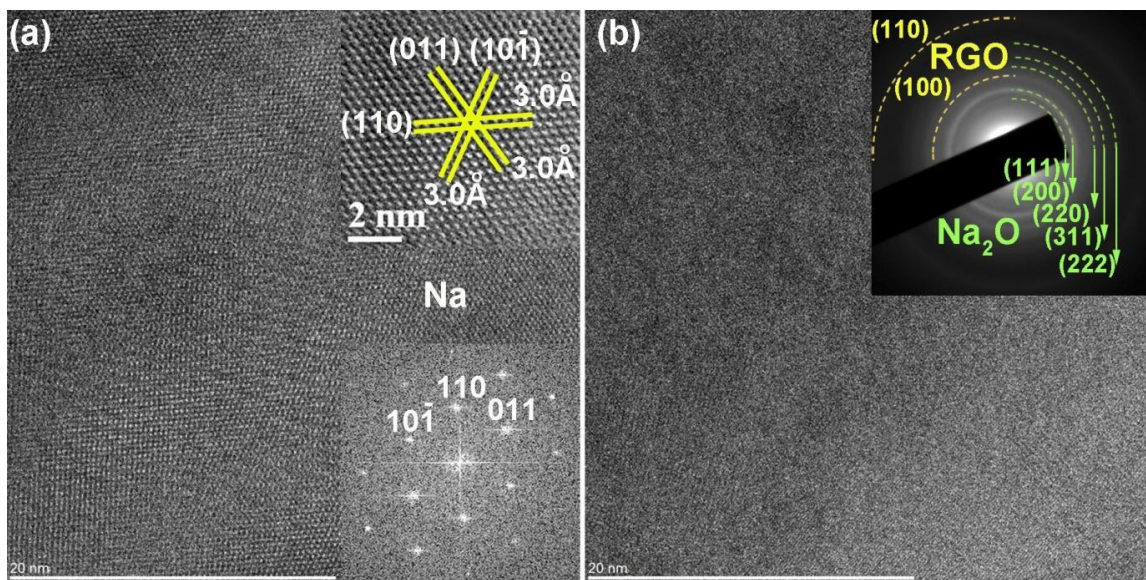


Figure 5.6 HRTEM images recording the first desodiation process of rGO. (a) HRTEM image of material on rGO before desodiation. Inset shows atomic scale HRTEM image of a Na metal and the corresponding FFT pattern. (b) HRTEM image of material on rGO after desodiation. Inset of the panel (b) shows an SAED pattern of the totally desodiated rGO.

#### 5.4 Electrochemical performance of rapid RGO as Na-ion battery anode

The electrochemical properties of the rapid-rGO film in SIB were characterized using coin cells with Na metal as the counter/reference electrode and a 1.0 M  $\text{NaPF}_6$  solution in ethylene carbonate/diethyl carbonate (EC:DEC = 1:1 by volume) as the electrolyte. Figure 5.7 shows the potential profiles of rapid-rGO electrode at current densities of 25

mA/g, 50 mA/g, 125 mA/g, 250 mA/g and 500 mA/g in a potential window from 0.01 to 2.0 V vs Na/Na<sup>+</sup>. Figure 6b shows the average desodiation specific capacity is 428 mAh/g, 316 mAh/g, 237 mAh/g, 194 mAh/g and 162 mAh/g for 25 mA/g, 50 mA/g, 125 mA/g, 250 mA/g and 500 mA/g, respectively. Surprisingly, rapid-rGO exhibits an excellent rate performance, which is much better than hard carbon and other rGO anodes.<sup>185, 214</sup> The enhanced rate capability in this study is attributed to the greater ionic accessibility in the loose-packed of rGO sheets than tight packed ones. After that, the rapid-rGO electrode is further cycled to 750 cycles at 125 mAh/g, showing a very stable performance of around 200 mAh/g. The capacity loss is only 0.025% per cycle, indicating a very stable cycling performance. The electrochemical characterizations of rapid-rGO demonstrates its great potential as simultaneously high energy density and high power density anode materials for SIBs.

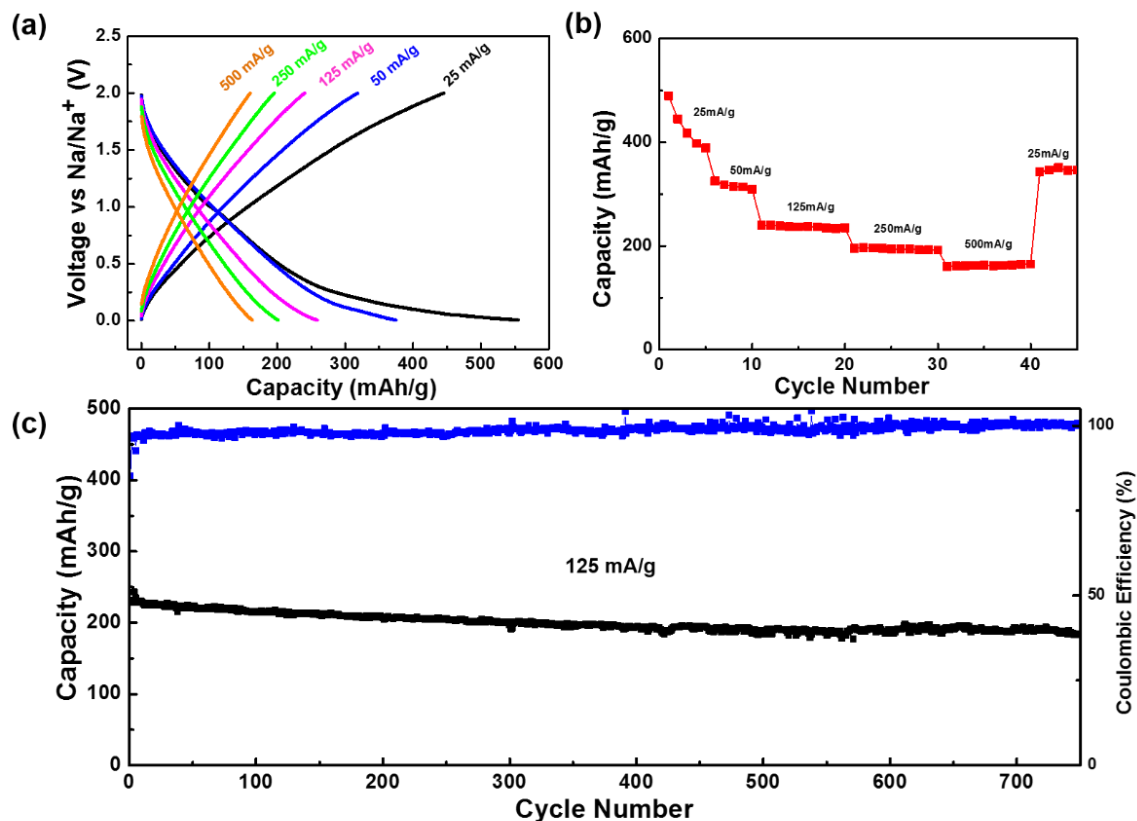


Figure 5.7 Electrochemical performance of rapid-rGO as anode for SIBs: (a) potential profiles of rapid-rGO anode at 500 mA/g, 250 mA/g, 125 mA/g, 50 mA/g and 25 mA/g, (b) rate performance of rapid-rGO at above-mentioned current rates, (c) cycling performance of rapid-rGO.

Here we discuss the Na-ion storage mechanism in rapid-rGO electrodes in detail. Clearly, from the sodiation potential profile at 25 mA/g (Figure 3a), the sodiation process for our rapid-rGO consists of two parts: (1) a sloping region between 2.0-0.3 V and (2) an inclined potential plateau below 0.3 V. According to recent studies on rGO anodes and hard carbon anodes, we propose the Na-ion storage mechanism for our rapid-rGO negative electrode as following: the sloping region between 2.0-0.3 V corresponds to the

Na ion storage by functional groups/defective sites,<sup>213, 226-228</sup> the inclined potential plateau below 0.3 V consists of the intercalation of Na-ions between rGO interlayers (relatively higher voltage)<sup>185, 211, 226-228</sup> and Na-atom cluster adsorption on rGO surface. Part of the proposed mechanism has been previously verified in recent reports: the functional group/defective sites for reversible Na ion storage from 2.0V to 0.3V has been confirmed with ex situ XPS, Raman combined with electrochemical analysis,<sup>211, 226-228</sup> and the Na-ion intercalation in between rGO layers below 0.3V has been proven with ex situ XRD measurements.<sup>211, 226, 227</sup> Na metal cluster formation, even though as a widely accepted mechanism in hard carbon anodes, is indirectly proven by in situ small angle X-ray scattering analysis,<sup>229, 230</sup> and unclear in rGO anodes. Our in situ TEM result, provide the first direct evidence for Na metal cluster formation at low voltages with rGO based SIB anodes. In addition, we noticed that the first cycle Coulombic efficiency (CE) for our rapid-rGO anode is at a low value of 18.5%, just like other rGO or rGO containing anodes and porous carbon anodes.<sup>231</sup> Such low CE is also revealed to be mainly attributed to the irreversible chemical reaction upon first sodiation with in situ TEM.

## 5.5 Summary

In summary, we applied the first *in situ* TEM characterization to study the sodiation-desodiation mechanism of rGO. These *in situ* TEM results provide the first direct evidence of Na metal cluster reversibly formation on rGO anodes, as a Na storage mechanism for rGO electrode materials. It supports our rational designed “2 second” rapid-rGO SIB anode, which we obtained a record high reversible capacity of 450 mAh/g among all carbon based SIBs anodes. In addition, we unveiled the origin of the capacity

loss of rGO SIB anodes in the first cycle, evidenced by the side reaction of irreversible formation of  $\text{Na}_2\text{O}$  on rGO surface. These discoveries are not only significant in rGO as SIB anode material, but also helpful in understanding the electrochemistry and a rational design of all SIB electrode materials containing rGO, or carbon of other forms.

## Chapter 6: Electrochemical K-ion intercalation with graphite and RGO materials

Wei Luo, Jiayu Wan, Burak Ozdemir, Wenzhong Bao, Yanan Chen, Jiaqi Dai, Hao Lin, Yue Xu, Feng Gu, Veronica Barone, and Liangbing Hu, *Nano Lett.*, 2015, 15 (11), pp 7671–7677

### 6.1 Introduction

Graphite intercalation compounds (GICs) which are formed by the intercalation of guest species in between the graphite layers, exhibit tunable physical and chemical properties that can be controlled by varying the guest species and concentrations.<sup>67</sup> Due to this unique feature, GICs have been intensively investigated as conductive materials, battery electrodes, hydrogen-storage materials, and catalysts etc.<sup>232,233</sup> Additionally, GICs have been recently used as starting materials for synthesizing graphene, which have attracted great interest.<sup>4, 65, 129</sup> To date, more than hundreds of chemical species that can be intercalated into graphite have been reported.<sup>234</sup> Among them, alkali metal (Li, K, Rb, and Cs) based GICs are the most widely studied ones. Particularly, the most extensively known examples of GICs are the well-developed Li based GICs, as graphite is the standard anode for lithium-ion batteries (LIBs).<sup>79, 235</sup>

Recently, concerns about the shortage and uneven geographical distribution of Li resources have led to an increased research attention to other battery technologies for replacing LIBs, such as sodium-ion batteries (SIBs). This shift is attributed to the abundant world-wide Na resources and its much lower cost. However, developing anodes

for SIBs is still a great challenge as only very limited amounts of Na can be intercalated into graphite.<sup>115, 229, 230, 236, 237</sup> The limited capacity is mainly attributed to the large size of Na ions compared to the interlayer spacing in graphite, as well as a weak interaction of intercalated Na species to carbon layers (Figure 1). One may expect potassium (K) ions are more difficult to intercalate into graphite due to their even larger ionic size. Contrarily, K-ion based GICs have been well-known for a long time and they have driven a broader interest since K-GICs have shown the ability to adsorb molecular hydrogen and present superconducting properties.<sup>238</sup> In the field of battery applications, K-ion based electrochemical energy storage technologies also exhibit a great promise due to the high natural abundance and low cost of K. Moreover, the redox potential of K/K<sup>+</sup> (−2.92 V vs standard hydrogen electrode) is even lower than that of Na/Na<sup>+</sup> (−2.71 V vs standard hydrogen electrode), indicating a higher working voltage of K-ion based batteries. However, to date, only O<sub>2</sub>/K,<sup>239</sup> S/K,<sup>240</sup> and Prussian blue<sup>16, 241</sup> battery systems have been reported, and a K-containing cathode/graphite battery analogous to conventional LIBs has not yet been investigated. Furthermore, although K-GICs have long been studied, a two-zone vapor-phase synthesis technique is still the most common method to prepare K-GICs. To our knowledge, the electrochemical synthesis of K-GICs has never been reported.

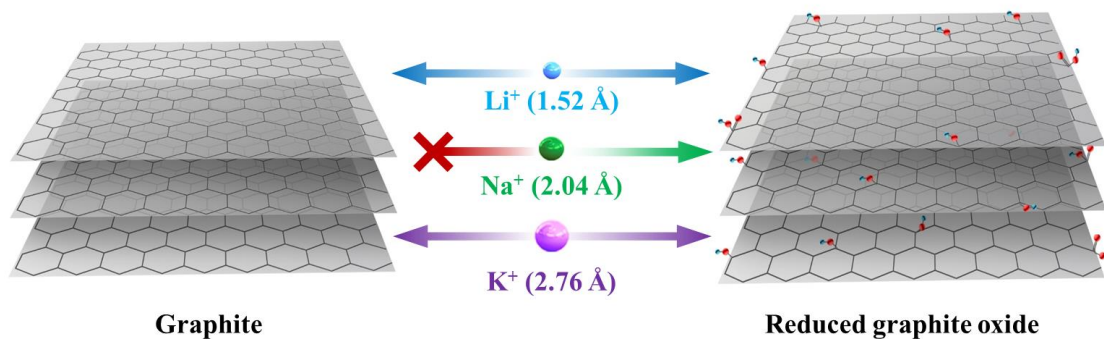
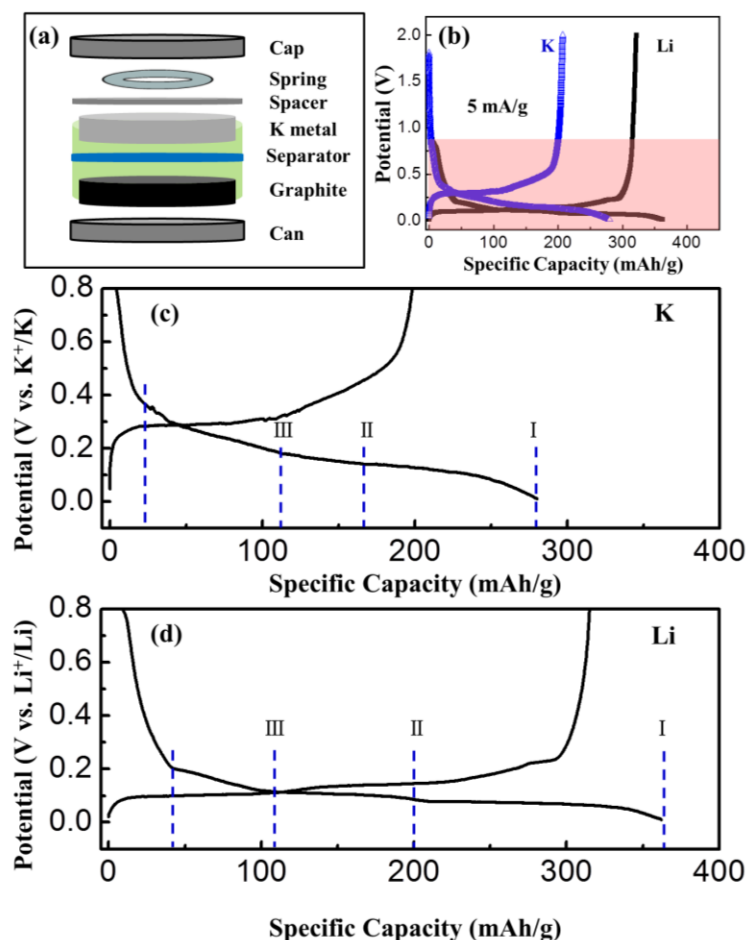


Figure 6.1 Schematic illustration of electrochemical intercalation of Li, Na, and K ions into graphite and reduced graphene oxide (RGO). Li and K ions can electrochemically intercalate into both graphite and RGO, while Na ions can only be electrochemically intercalated into RGO.

Motivated by this, here we use a simple graphite/K metal half-cell with a non-aqueous electrolyte to investigate the electrochemical intercalation process of K ions into graphite. By applying a small current density of 5 mA/g, we observe, for the first time, that graphite can deliver discharge/charge capacities of 280/207 mAh/g, respectively. At the end of the discharging process (full intercalation), the color of graphite electrodes have changed from grey to brass-yellow, confirming the successful formation of Stage-I  $\text{KC}_8$ . This is also proven by *ex situ* X-ray diffraction (XRD) and Raman measurements. In addition, we have also demonstrated the formation of K intercalated reduced graphene oxide (RGO) compounds. Our RGO film electrode exhibits a high reversible K ion storage capacity of 222 mAh/g, indicating a promising anode for K-ion based batteries.

## 6.2 Electrochemical intercalation of K-ions in graphite electrodes

As seen in Figure 6.2a, coin-cells consisting of graphite working electrodes (80wt% graphite and 20wt% polyvinylidene fluoride binder), K metal counter/reference electrodes, and 0.5 M KPF<sub>6</sub> in ethylene carbonate/diethyl carbonate (EC:DEC = 1:1 by volume) electrolyte are assembled for electrochemical measurements. Figure 6.2b shows the first discharge/charge curve of the graphite electrode tested at a current density of 5 mA/g in the potential range between 0.01 and 2.0 V vs. K/K<sup>+</sup>, (blue curve). It can be observed that the potential drops fast from the open circuit voltage (OCV) to 0.8 V. The curve then develops into four parts in the first discharge process (K ions intercalation). As displayed in the zoomed-in discharge profile (Figure 6.2c), the first part is a short slope from 0.8 V to 0.35 V, which gives a capacity of 26 mAh/g. This short slope is probably due to the decomposition of electrolyte and formation of solid-electrolyte-interface (SEI).<sup>242-244</sup> We therefore focus on the later three parts in the first discharge profile. As discussed in previously reported vapor pressure experiments, K-intercalated graphite forms specific stages: KC<sub>36</sub> (Stage-III), KC<sub>24</sub> (Stage-II), and finally, KC<sub>8</sub> (Stage I). Our electrochemical experiments, however, seem to present a different staging mechanism than the ones presented in the previous literature.



**Figure 6.2.** Electrochemical intercalation of K and Li ions into graphite at ambient temperature and pressure. (a) A schematic of graphite electrode/K metal within coin-cell. (b) Discharge/charge profiles vs. K (blue) and Li (black) at 5 mA/g for graphite electrode; the highlighted part in (b) is enlarged and shown in (c) for a graphite/K system and (d) for a graphite/Li system.

In order to understand the behavior observed in Figure 6.2c, we have performed density functional theory (DFT) calculations of potential profiles for K ions intercalation into graphite. In Figure 6.3a we present *first-principles* calculations for different K staging scenarios (blue and green lines) in combination with averaged experimental

values (red) to facilitate a direct comparison (see details in Supporting Information). Calculated potential profiles are obtained using the dispersion corrected vdW-DF2 functional as implemented in Quantum Espresso.<sup>245, 246</sup> The calculated voltage profiles are derived from the following relation

$$V = - \frac{E(K_x C_8) - E(K_{x_0} C_8) - (x - x_0) E(K_{metal})}{q (x - x_0)} \quad (1)$$

where  $E(K_x C_8)$  is the energy of  $K_x C_8$ ,  $E(K_{metal})$  is the energy of K in its pure bulk form, and  $x$  is the fraction of K in  $K_x C_8$  which is then converted to capacity (mAh/g) by assuming a full electron transfer from the K atom to the graphite host, and  $q$  is the net charge of the K ions ( $q = +1 e$ ).

As shown in Figure 6.3a, the maximum stable stoichiometry corresponds to  $KC_8$ . For larger K content, K metal is expected to form as the potential becomes negative, suggesting that  $KC_6$  cannot be formed electrochemically in this potential window (2–0.01 V vs K/K<sup>+</sup>). When analyzing the results of our calculations for the staging sequence  $KC_{24}$  (Stage II)  $\rightarrow$   $KC_8$  (Stage I) (green line), we observe that not only is  $KC_{24}$  (Stage-II, theory b) about 0.1 eV less stable than  $KC_{24}$  (Stage-III, theory a), but also the potential profile shows an increase in voltage from Stage II  $\rightarrow$  Stage I. However, this voltage increase is not observed in the experiment. Contrarily, a staging in which the Coulomb repulsion between ions separated by empty galleries is minimized, corresponding to the staging mechanism:  $KC_{24}$ -Stage-III  $\rightarrow$   $KC_{16}$ -Stage-II and  $KC_8$ -Stage-I (blue line), is energetically more stable. This agrees very well with the potential profile obtained in our experiments (black solid line and averaged red dotted line). These results seem to indicate that the staging of K intercalation into graphite in electrochemical experiments behaves

similarly to the one in Li intercalation. Therefore, the experimental results shown in Figure 2c can be interpreted as follows. After the initial formation of SEI, a relatively flat slope is observed from 0.35 V to 0.18 V, which delivers a capacity of about 93 mAh/g. This capacity is related to the formation of  $\text{KC}_{24}$  in Stage III. Closer inspection reveals that there is another transition at about 0.14 V corresponding to  $\text{KC}_{16}$  in Stage II (47 mAh/g). The total first intercalation capacity reaches about 270 mAh/g, suggesting the synthesis of Stage I K-GICs ( $\text{KC}_8$ ). It is worthwhile to point out that this is the first time in which  $\text{KC}_8$  is achieved by an electrochemical method at room temperature and pressure.

In the following charging process (de-intercalation of K ions from  $\text{KC}_8$ ), the overall charge capacity is 208 mAh/g, giving a 1st cycle Coulombic efficiency (CE) of 74.3%. In order to corroborate the electrochemical behavior of the graphite/K system, a well-known graphite/Li system is also studied as control. The graphite/Li system uses the same graphite electrode with Li metal counter/reference electrode and 1.0 M  $\text{LiPF}_6$  in EC/DEC electrolyte. As shown in Figure 6.2d, the first discharge curve of graphite/Li cell at 5 mA/g displays a typical Li ions intercalation process where the intercalation starts at 0.2 V vs.  $\text{Li}^+/\text{Li}$  and exhibits three plateaus later on. This is related to the typical phase change from  $\text{LiC}_{36}$  (Stage III) to  $\text{LiC}_{12}$  (Stage II) and then to  $\text{LiC}_6$  (Stage I), as intensively studied previously.<sup>247, 248</sup> The following charge curve shows the corresponding de-intercalation process. The first discharge/charge capacities are 362/322 mAh/g, demonstrating a 1st cycle CE of 89.0%. Compared to the electrochemical behavior in the graphite/Li system, graphite shows a very similar result in the graphite/K system as stage I GICs ( $\text{KC}_8$ ) is formed after full intercalation.

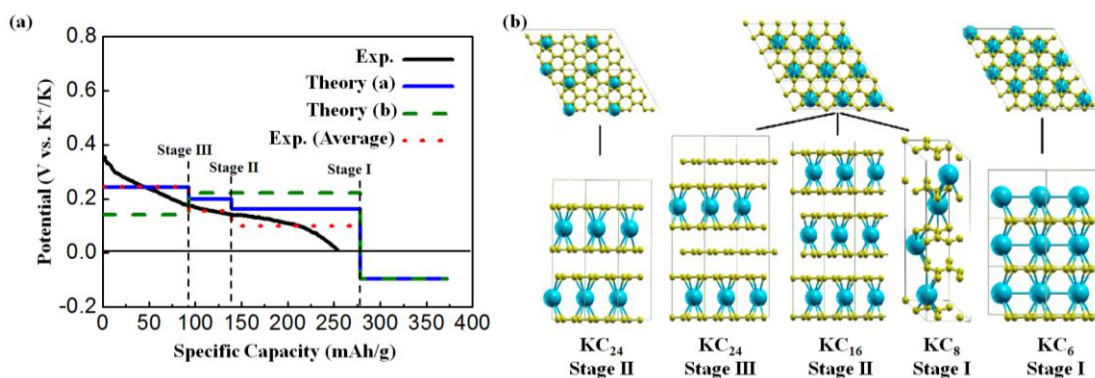


Figure 6.3. DFT calculations. (a) Calculated potential profile for K ions intercalation into graphite for different staging scenarios. Blue line (Theory (a)) corresponds to an intercalation staging:  $\text{KC}_{24}$ (Stage III)  $\rightarrow$   $\text{KC}_{16}$  (Stage II)  $\rightarrow$   $\text{KC}_8$  (Stage I). Green dotted line (Theory (b)) corresponds to calculated values for the previously reported staging:  $\text{KC}_{24}$  (Stage II)  $\rightarrow$   $\text{KC}_8$  (Stage I). Red dotted line corresponds to the averaged experimental data shifted by 26 mAh/g to correct the capacity contribution from SEI formation. (b) Scheme of the different stages of K-intercalated graphite, K shown in blue and C in yellow.

*Ex situ* optical images, XRD patterns and Raman spectra of graphite electrodes are also collected after the electrochemical intercalation of K ions. As shown in Figure 4a, the color of a graphite electrode changes from dark gray to brass-yellow after it is discharged to 0.01 V, supporting the formation of Stage-I K-GICs.<sup>249</sup> In the XRD measurements, graphite electrodes show a sharp diffraction peak at  $26.6^\circ$ , corresponding to (002) plane of graphite (Figure 6.4b). After K ions intercalation, the (002) peak shifts to  $16.6^\circ$ , indicating a sharp increase of the interlayer spacing. According to the Scherrer

equation, the interlayer spacing of the as-formed  $\text{KC}_8$  is 5.35 Å. Additionally, there are two small peaks at  $20.5^\circ$  and  $30.1^\circ$ , which can be ascribed to  $\text{KC}_{24}$ . This probably due to the partial existence of stage-III K-GICs. Furthermore, the Raman G-peak of graphite at  $1580\text{ cm}^{-1}$  shifted to  $1549\text{ cm}^{-1}$  for electrochemical intercalated  $\text{KC}_8$  (Figure 6.4c). The G-peak also became broader after intercalation, which is due to the mode coupling of in-plane and c-axis folding effects in a continuous states.<sup>250</sup> The Raman result is consistent with previous works and additionally confirms the formation of  $\text{KC}_8$ .<sup>135, 250-252</sup>

To further investigate the electrochemical reaction of graphite/K cell, cyclic voltammetry (CV) measurements are carried out. As shown in Figure 6.5, redox couples can be clearly observed in the CV curves. In the first cathodic process, a broad peak near 0.75 V appears. This broad peak can be attributed to the decomposition of the electrolyte and formation of the SEI, which is consistent with the first discharge profile in Figure 6.2. Then, the sharp cathodic peak between 0.4 to 0.01 V is related to the intercalation of K ions into graphite. In the following anodic sweep, the broad peak between 0.3 V to 0.8 V corresponds to the de-intercalation of K ions from graphite. In the subsequent cycles, the cathodic peak near 0.75 V disappears, which suggests that the SEI mainly forms in the first cathodic process. Furthermore, the other cathodic/anodic peaks are highly reversible and overlap, indicating the high reversibility of the intercalation/de-intercalation of K ion into/from graphite. Rate capability of graphite electrodes are also tested at various current densities. As shown in Figure 6.4d, when the current density is increased to 10 and 50 mA/g, graphite can still deliver intercalation capacities of 266 and 234mAh/g, respectively, which indicates a good response to the current density variation in this range. However, when the current density is further increased to 200 mA/g, the

intercalation capacity declines to 141 mAh/g, suggesting a slow kinetics of the K ion intercalation process compared to Li ion. Our results demonstrate the potential of graphite anodes for K-ion batteries with significant reversible capacity and an acceptable 1st cycle CE. Considering the natural abundance and wide availability of K resources, K-ion based non-aqueous batteries using graphite anodes may become an attractive alternative for large scale energy storage systems.

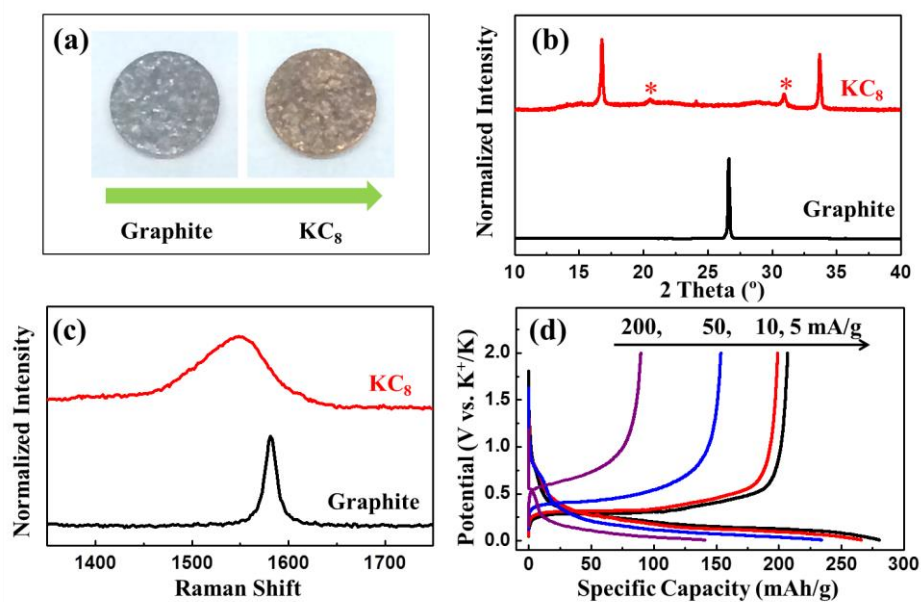


Figure 6.4 *Ex situ* measurements of  $KC_8$  and the rate performance of graphite electrode. (a) Photo images, (b) XRD patterns, and (c) Raman spectra of graphite electrodes before and after electrochemical intercalation of K ions. (d) Discharge/charge profiles for graphite electrodes at various current densities.

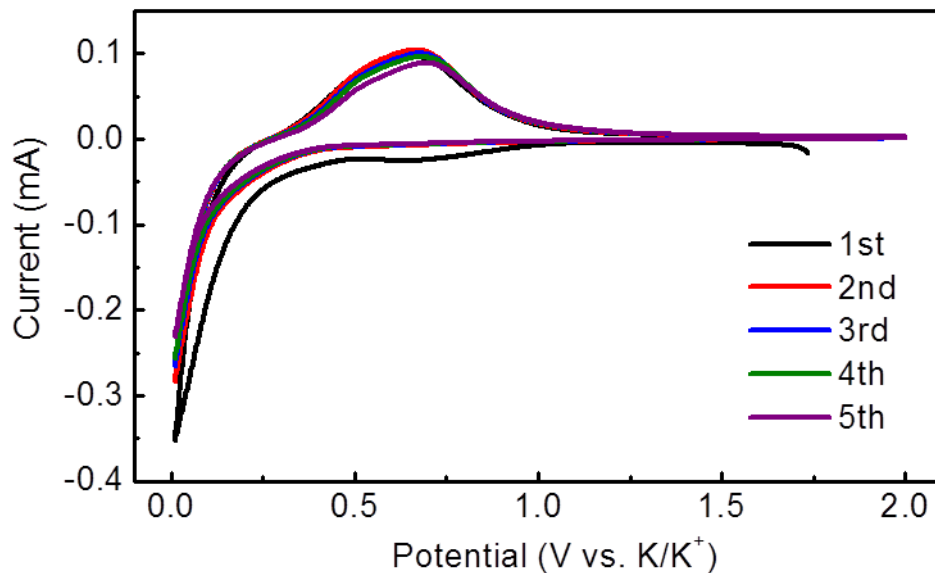


Figure 6.5. CV curves of graphite electrode in graphite/K cell.

### 6.3 Electrochemical intercalation of K-ions in rGO electrodes

To further explore the K-ion storage in graphitic materials, we investigated the K-ion storage properties of RGO. Derived from graphite, RGO is an extensively studied and cost-efficient material utilized in LIBs. Specifically, RGO is known for its larger interlayer distance compared with graphite, which even enables a relatively large storage capacity of Na ions.<sup>185, 213, 252, 253</sup> These properties also suggest the potential of RGO as a K-ion storage material. Additionally, RGO thin films have been widely studied as transparent electrodes as RGO flakes are electrically conductive and optically transparent.<sup>16, 254</sup> Our recent results show that upon metal ions (Li ion/Na ion) intercalation into graphitic materials, the system will simultaneously achieve better dc conductivity and optical transmittance in the visible range.<sup>61, 212</sup> Thus, it is also of great interest to investigate K ion storage performance of RGO, as well as the optical properties of K ion intercalated RGO film.

We obtained the RGO film from graphene oxide (GO), which is prepared using the modified Hummer's method.<sup>217</sup> The XRD pattern of the RGO film shows a peak at  $24.3^\circ$ , which corresponds to an interlayer distance of  $3.66 \text{ \AA}$  (Figure 6.6a). The Raman spectrum exhibits peaks at  $\sim 1340 \text{ cm}^{-1}$  and  $1590 \text{ cm}^{-1}$ , suggesting a typical RGO structure (Figure 6.6b). Scanning electron microscope (SEM) image also depicts a typical RGO morphology, where a large number of RGO flakes with sizes of tens of microns are stacked together (Figure 6.6c). To evaluate its K ion storage properties, the as-prepared RGO free-standing film is directly used as electrode without using any binder, carbon additives, and current collector. Figure 6.6d shows the first two cycles of a RGO film tested at  $5 \text{ mA/g}$  in the potential window of  $0.01 \text{ V} - 2.0 \text{ V}$  vs.  $\text{K/K}^+$ . Firstly, a plateau is observed near  $0.7 \text{ V}$  in the first discharge curve. But the plateau disappears in the second cycle, suggestive of an irreversible formation of SEI. Later on, a long slope is exhibited, which delivers an overall first discharge capacity of  $442 \text{ mAh/g}$ . Then, a corresponding slope is found in the following charge curve, which shows a first charge capacity of  $222 \text{ mAh/g}$  with a 1st cycle CE of  $\sim 50\%$ . Clearly, RGO film exhibits higher intercalation/deintercalation potential, higher capacity and lower 1st cycle CE than graphite, which agrees well with the results observed in RGO/Li systems.<sup>255</sup> Similar to RGO/Li, the unique electrochemical behavior could be attributed to the rich surface functional groups of RGO. We then study the current rate and cycling performance of RGO film. The RGO film delivers a stable capacity of  $\sim 200 \text{ mAh/g}$  at  $5 \text{ mA/g}$ . When the current density is increased to  $10$ ,  $20$ , and  $50 \text{ mA/g}$ , the RGO film can still exhibit capacities of  $150$ ,  $130$  and  $90 \text{ mAh/g}$ , respectively. However, the RGO film can only give a capacity of  $\sim 50 \text{ mAh/g}$  at  $100 \text{ mA/g}$ . Compared to a graphite electrode, the RGO film shows a poorer rate

capability, which could be due to the poorer electronic conductivity of RGO. To further investigate the cycling performance, the RGO film is tested at 10 mA/g for a long-term cycling. We found that the RGO film can still deliver a stable capacity of 150 mAh/g after 175 cycles, which indicates a great cycling stability of RGO as anode for non-aqueous K-ion batteries.

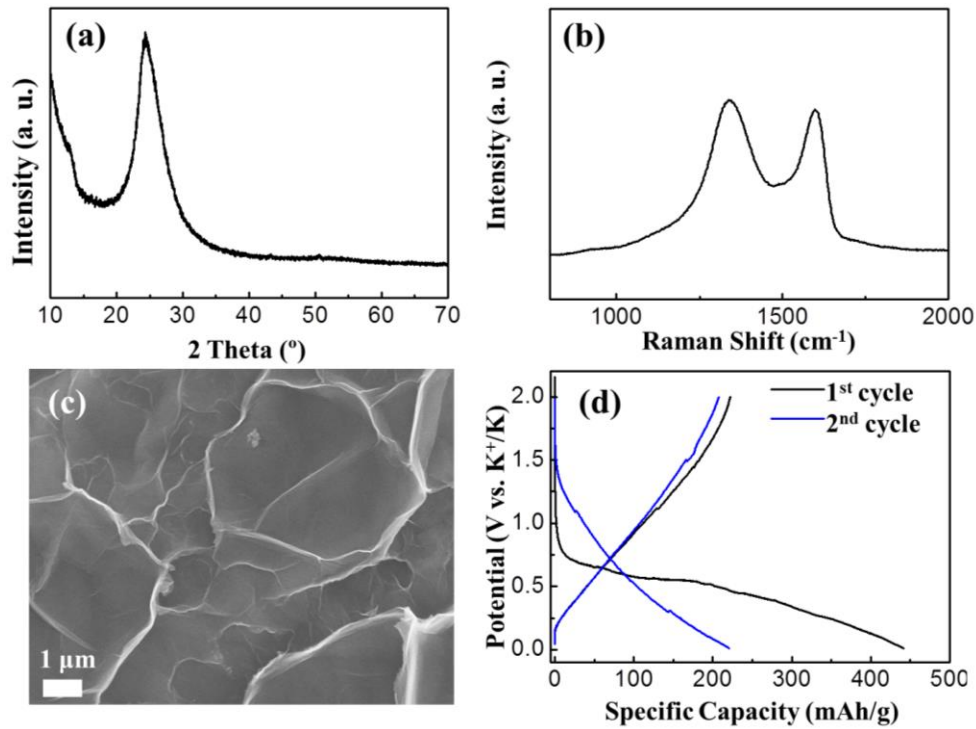
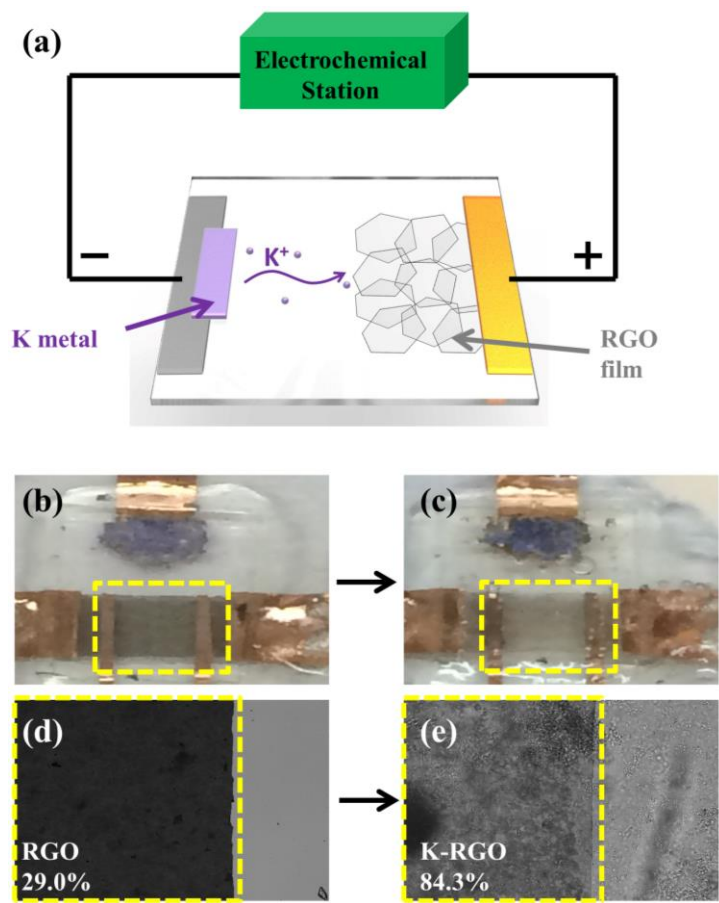


Figure 6.6. Characterizations of RGO film and electrochemical intercalation of K ions into RGO film. (a) XRD pattern, (b) Raman spectrum, (c) SEM image and (d) discharge/charge profiles for the first two cycles at 5 mA/g of RGO film.

Electrochemical intercalation of K ions allows a controllable and reversible modification of the band structure of graphitic carbons, which results in a range of new properties. Here, to study the effect of K ions intercalation on the optical transmittance of

the RGO film, we have built a planar RGO/K cell for *in situ* optical transmittance measurements. As schematically shown in Figure 6.7a, the printed RGO film and K metal pellets are deposited onto copper current collectors at each side, respectively. After injecting the electrolyte (0.5 M KPF<sub>6</sub> in EC/DEC), the potential between the RGO film and K is kept at 0.0 V by the external circuit. Three hours later, the printed RGO film becomes much more transparent (Figure 6.7b and 6.7c). To quantitatively illustrate the transmittance change, we capture the gray scale images using an optical microscope (operated in transmission mode). As shown in Figure 6.7d, the RGO film exhibits an optical transmittance of 29.0%. After K ions intercalation, it increases drastically to 84.3%, which is about 3 times larger than in the pristine RGO film (Figure 6.7e).



**Figure 6.7.** *In situ* optical measurements of RGO film. (a) Schematic of K ions intercalation into a printed RGO film. (b, c) Photo and (d, e) optical microscope images of the RGO film before and after K ions intercalation.

In order to understand the fundamental mechanism of the obvious increase in optical transmittance, we performed electronic structure calculations in pristine graphite and  $\text{KC}_8$  as model systems. The band structure of  $\text{KC}_8$  changes dramatically with respect to the one in pristine graphite. The calculation suggests an upshift of the Fermi level due to the heavy electron doping which can be most clearly observed in the  $\text{K} \rightarrow \text{H}$  path in the corresponding Brillouin zone (Figure 6.8a and 6.8b). As discussed in a previous work, this shift may cause a change in the optical spectrum of the material due to the

suppression of inter-band transitions caused by Pauli blocking. Our band structure calculations show that  $\text{KC}_8$  becomes a conductor with bands crossing the Fermi level not only along the layer planes but with additional conducting channels along the  $c$ -direction. We also calculated the dielectric function,  $\epsilon_1$  and  $\epsilon_2$ , within the Random Phase Approximation (RPA) for pristine graphite as well as K intercalated graphite by using the Yambo code.<sup>256</sup> Although more robust approaches need to be considered for obtaining accurate optical spectra, our RPA calculations can shed light on the trends that take place in the optical properties upon intercalation. The imaginary part of the dielectric function is directly related to the absorption coefficient, and as shown in Figure 6.8d, it significantly decreases upon K ions intercalation. This calculated trend for a suppressed absorption upon K ions intercalation is in line with the increased transmittance observed in our experiments.

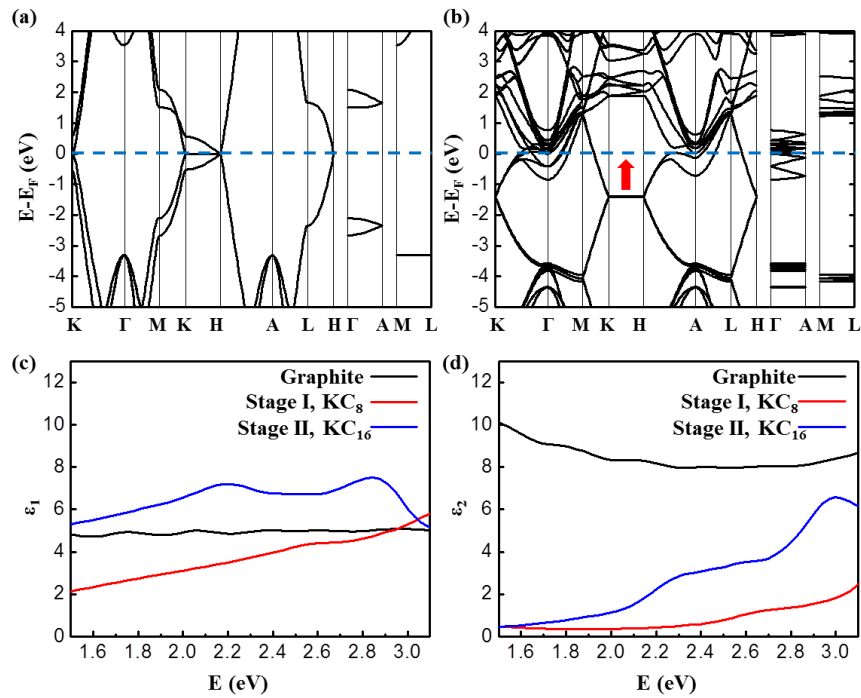


Figure 6.8 Calculated band structure of (a) graphite and (b)  $\text{KC}_8$  (Stage-I), where the arrow between K-H indicates the shift in the Fermi level with respect to graphite; (c)  $\epsilon_1$  and (d)  $\epsilon_2$  calculated within the RPA in the visible range for pristine graphite as well as K intercalated graphite.

## 6.4 Conclusion

In conclusion, we have demonstrated, for the first time, the electrochemical intercalation of K ions into graphitic materials under ambient temperature and pressure. The electrochemical intercalation process clearly displays the formation of stages in K-GICs. Our electrochemical intercalation stages are different from the ones reported in gas phase experiments and are supported by our *first-principles* calculations. We find that graphite delivers a reversible capacity of 208 mAh/g. Furthermore, we find that reduced graphene oxide also exhibits a high reversible capacity of 222 mAh/g. Moreover, K ions intercalation can effectively increase the optical transparency of RGO film from 29.0% to 84.3%. Our first-principles calculations suggest that this trend is attributed to a decreased absorbance produced by K ions intercalation. Our results not only open opportunities for novel non-aqueous K-ion based electrochemical energy-storage technologies, but also demonstrate the great potential of K ions intercalation to improve the performance of printed RGO films for optical applications.

## Chapter 7: Tunable broadband printed carbon transparent conductor by Li-ion and Na-ion intercalation

### 7.1 Introduction

Simultaneously optical transparent and electrical conducting materials are ubiquitously used in optoelectronic devices, such as solar cells, organic light-emitting devices (OLEDs), touch screen displays, and smart glass.<sup>162, 257</sup> High performance doped metal oxides such as indium tin oxide (ITO) has dominated the transparent conductor electrodes (TCEs) market.<sup>258</sup> However, an increasing research effort exists to replace ITO in the past decades due to the scarcity of indium sources, the high growth cost of ITO, and the brittle nature of the ceramics. Metal nanowires, metal grids,<sup>259, 260</sup> conductive polymers,<sup>261</sup> carbon nanotubes (CNTs),<sup>262</sup> graphene<sup>172</sup> and their hybrids<sup>157</sup> have been intensively investigated as high performance TCEs. Despite the success of these materials, most studies on TCs are focused on the visible range. Simultaneous transparency and conductivity is also of great importance in other regions of the electromagnetic spectrum, such as the infrared region.<sup>92</sup> IR transparent conductors are needed in multi-junction solar cells,<sup>263</sup> IR image and sensing,<sup>264</sup> IR emission devices<sup>265</sup> for military, astronomy, and telecommunication applications.<sup>266</sup> Thus, further investigation on how to achieve broadband TCEs is crucial for functional IR transparent conductor and devices.

Carbon materials such as CNT and graphene have attracted tremendous attention recently as transparent conducting materials for optoelectronic devices due to their unique simultaneously high conductivity and transmittance.<sup>267</sup> Like many other new generation TCE materials, carbon based transparent conductors are potentially low cost, resourceful, appropriate for large scale processing and patterning, stable, and flexible.

Still, there are several unique advantages of carbon materials over all other transparent conductor materials. First, CNTs and graphene are not only transparent in the visible range, but also transparent in a broad range (i.e. visible to IR range).<sup>130</sup> Second, the transmittance and/or conductivity of carbon based transparent conductors can be modulated with electric fields,<sup>163</sup> electrical double layers,<sup>268</sup> and intercalation species.<sup>269</sup> These modification methods not only improve the overall transmittance and conductivity of the thin carbon films, but also provide possible tunability in a broad range. It is exciting to envision a transparent conductor thin film with reversibly tunable transmittance in the broadband used for smart windows in energy saving buildings.<sup>270</sup> Additionally, a tunable transmittance in the broadband can also be potentially applied for thermal camouflage.<sup>271</sup> Thus, our goal here is to achieve a carbon based transparent conductor with reversible modulation of transmittance in a broad range.

To this end, we designed a CNT/rGO/CNT sandwich structure and achieved reversible broadband transmittance modulation through alkali ion intercalation. We have been able to demonstrate that upon ion intercalation in these structures, a wide transmittance modulation from the visible range (450 nm) to the mid-infrared range (5  $\mu\text{m}$ ) can be achieved. We also show the reversibility of the process by optical and *in situ* Raman spectroscopy. Our calculations in Li intercalated few-layer graphene indicate that interband transitions are significantly reduced along with absorption and reflection upon intercalation. However, a plasmon resonance also appears within the visible region due to increased conduction electron density which causes high reflectance at lower energies. This result is in contrast to rGO experimental results where an increase in transmittance

occurs in a broad energy region including infrared. This effect is attributed, at least partly, to a reduction in plasmon energy due to a decrease in conductivity in rGO.

## **7.2 Fabrication of large scale, printed CNT/rGO/CNT sandwich thin film**

In the chapter 4, we reported Na-ion intercalation in large area, printed rGO network and achieved highest performance of pristine rGO based transparent conductor. However, in the previous studies, reversible intercalation/deintercalation of ions in rGO network film has not been demonstrated, although the reversible process is well known for rGO or graphite as battery electrodes. The key difference between rGO as battery electrode and transparent conductive thin film is that in battery electrodes, rGO is surrounded by functional additives such as carbon black and polymer binder (i.e. PVDF) while in thin film, rGO network is tightly attached to a transparent substrate (i.e. glass). Just like any battery electrode materials, when ion intercalation/deintercalation occurs, rGO experiences volume expansion/shrinking. In real batteries, the polymer binder holds the position of adjacent rGO flakes during intercalation/deintercalation process; while in planar batteries, the rGO network hold up each other with only Van der Waals force without binder. Therefore, during the volume expansion/shrinking process, rGO network is easy to break, leads to an irreversible ion intercalation process. As shown in Figure 7.1a to 7.1b, during the ion deintercalation process, rGO network starts to break and peels off. Figure 7.1c shows two breaking lines of pure rGO film at the 2<sup>nd</sup> intercalation process.

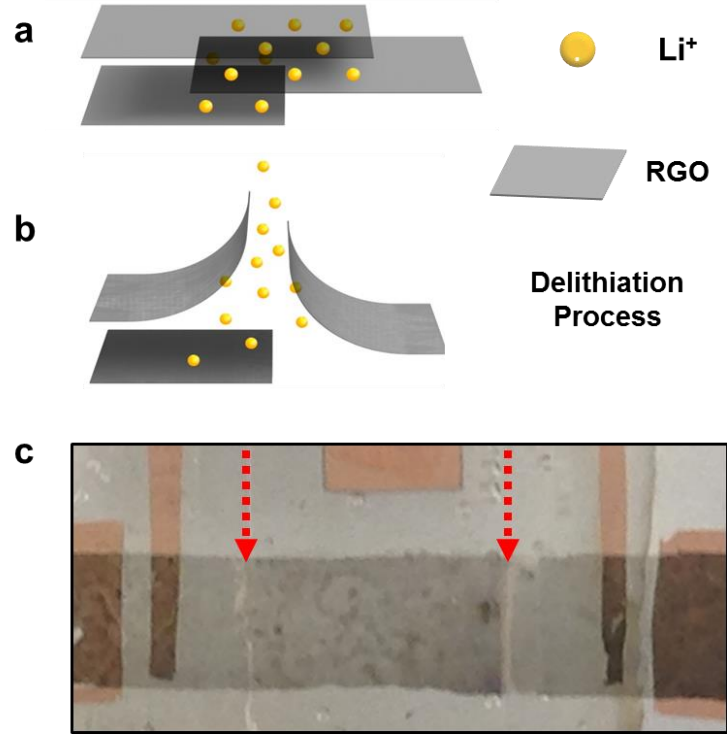


Figure 7.1 Failure mechanism of pure rGO thin film during lithiation/delithiation process (a) schematic of ion intercalated rGO film, (b) schematic of ion deintercalation in rGO film. (c) photo image of cracked pure rGO film after ion deintercalation.

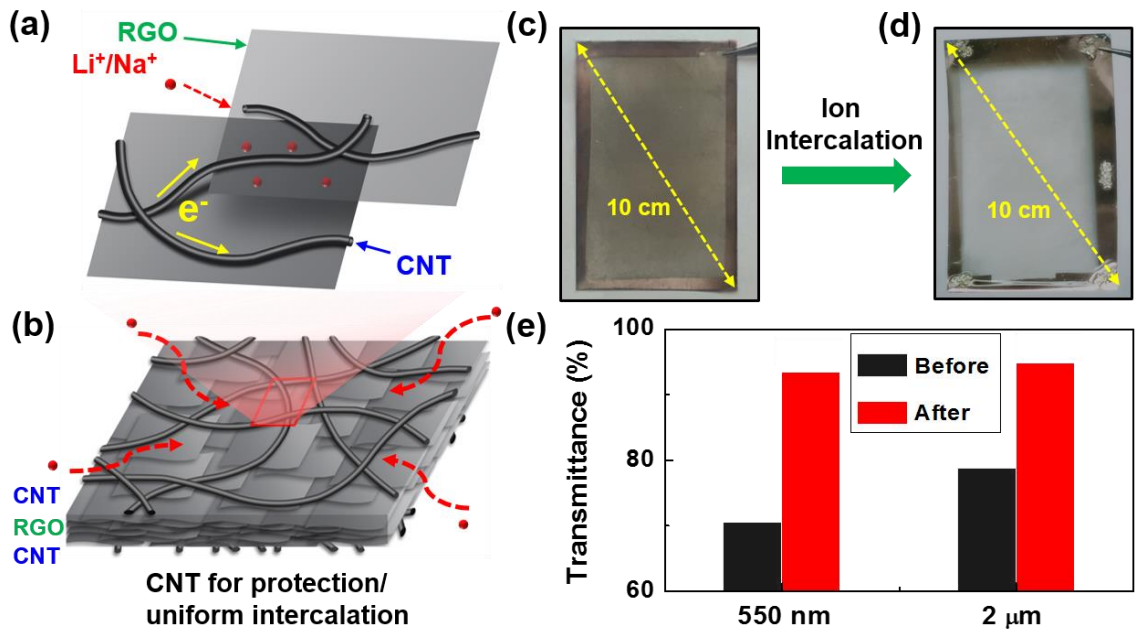


Figure 7.2 (a) Schematic of alkali ion intercalation in a CNT/rGO thin film. (b) Schematic of the CNT/rGO/CNT sandwich structure. Large scale printed CNT/rGO/CNT film on PET substrate before Li-ion intercalation (c) and after Li-ion intercalation (d). (e) Typical transmittance change of carbon film before and after Li-ion intercalation for selected wavelengths of 550 nm (visible range) and 2 $\mu$ m (infrared range).

In order to achieve reversible optical modulation of the large-scale rGO network thin film, we designed a CNT/rGO/CNT sandwich structure that reinforces the bonding of the rGO network (Figure 7.2 a-b). The advantages of the CNT/rGO/CNT structure is as following: (1) the two CNT layers provide a mechanical protection to the rGO network in between and prevent the crack of rGO during ion intercalation/deintercalation, (2) the CNT network mechanical protection layer is significantly porous and thus allows the ions to access the rGO interlayers, (3) the CNT network is also electrically conductive thus contributing to the fast and uniform ion intercalation throughout the entire rGO network thin film, (Figure 7.2 c-d) (4) Li-ions and Na-ions cannot electrochemically intercalate in CNT, and (5) the CNT thin film is transparent to photons in the IR regime. Thus, the addition of CNT network would not affect the optical modulation of rGO with ion intercalation process in the visible and IR regime we are interested in. A typical transmittance change at both visible range (550 nm) and IR range (2  $\mu$ m) before and after Li ion intercalation in the CNT/rGO/CNT film is shown in figure 2e.

### **7.3 Reversible change of transmittance with intercalation/deintercalation**

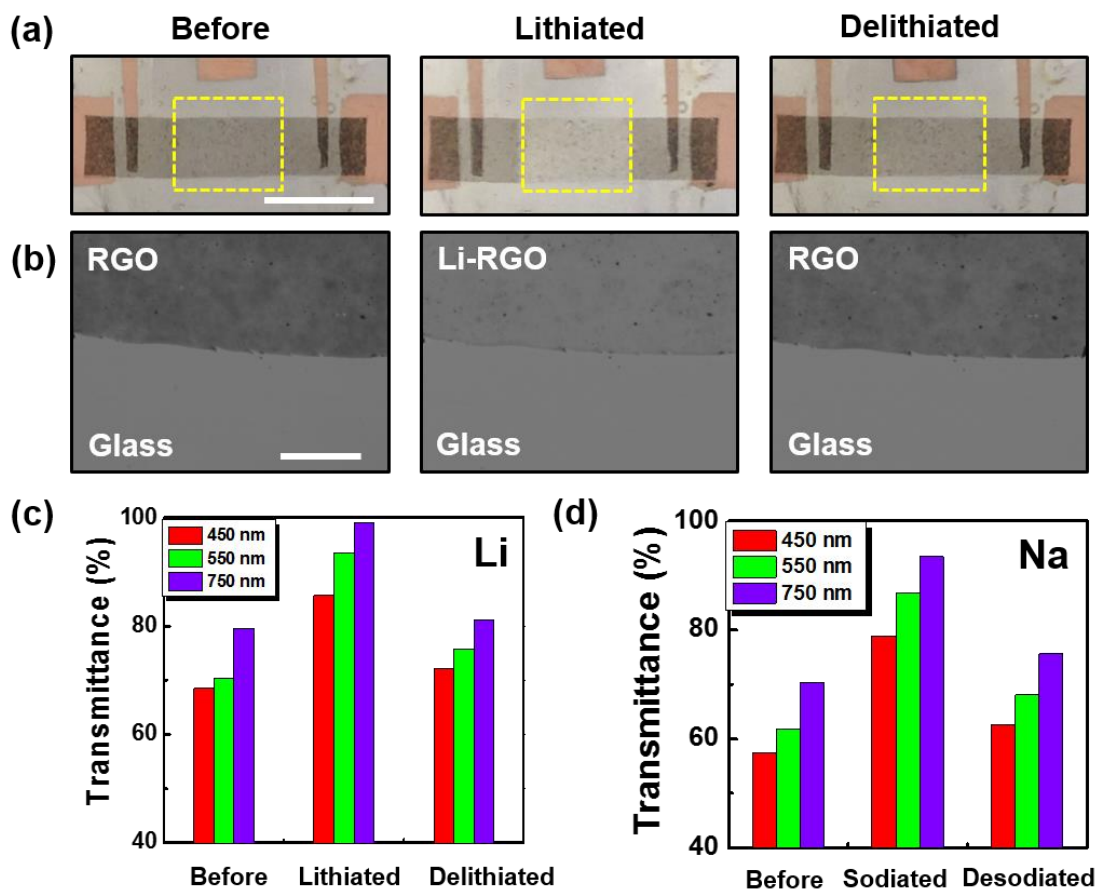


Figure 7.3 (a) photo images and (b) microscope images of pristine, lithiated and delithiated CNT/rGO/CNT film. Reversible transmittance change at visible range (wavelengths of 450 nm, 550 nm, 750 nm). The length of scale bars in figure (a) and (b) are 1 cm and 50  $\mu\text{m}$ , respectively. Transmittance obtained in (c) pristine, lithiated, and delithiated CNT/rGO/CNT network and (d) pristine, sodiated, and desodiated CNT/RGO/CNT network.

We first demonstrate the optical modulation of CNT/rGO/CNT in the visible range with Li-ion intercalation. As shown in Figure 7.3a, photo images of CNT/rGO/CNT thin film (grey strip) on planar battery before intercalation, after intercalation, and after deintercalation are taken. The region inside the yellow dash line box is the

CNT/rGO/CNT thin film confined inside the PDMS reservoir, in which the electrolyte is accessible, thus enables ion intercalation/deintercalation process. Clearly, our results successfully demonstrate a reversible modulation of CNT/rGO/CNT film in the visible range *via* Li-ion intercalation. Figure 7.3b shows the microscope images of the sandwich film in the pristine, lithiated, and delithiated states. We also measured the optical transmittance change of the CNT/rGO/CNT film by analyzing the grey scale image of the films at three different wavelengths in the visible range (450 nm, 550 nm, 750 nm). The transmittance change before intercalation, after intercalation, and after deintercalation is 68.5%, 85.6%, 72.1% for 450 nm, 70.4%, 93.4%, 75.8% for 550 nm, and 79.5%, 99.1%, 81.2% for 750 nm, respectively. The drastic reversible modulation in the three typical wavelengths demonstrates ion intercalation as an effective tuning method in the visible range. Note that in all cases, the transmittance after deintercalation did not fully recover its original value, which should be mainly caused by irreversible reactions after Li-ion intercalation with residual functional groups on rGO.<sup>272</sup> The doping effect simultaneously increased the conductivity of the sandwich film, which was manifested in a decrease of sheet resistance after intercalation. A typical change of sheet resistance from 3.0 k $\Omega$ /sq to 2.1 k $\Omega$ /sq after Li-ion intercalation was observed. Na-ion intercalation and deintercalation in the CNT/rGO/CNT network exhibits a similar transmittance modulation in the visible range, as shown in Figure 7.3d.

Although the reversibility of the ion intercalation process is well known for rGO or graphite in battery electrodes,<sup>273</sup> until now, a reversible intercalation/deintercalation of ions in pure rGO network thin films on substrate has not been demonstrated. The key difference between rGO in battery electrodes and in transparent conductive thin films is

that in battery electrodes, rGO is surrounded by functional additives such as carbon black and polymer binder (i.e. PVDF) while in the thin film, the rGO network is tightly attached to a transparent substrate (i.e. glass). Just like in any battery electrode materials, when ion intercalation/deintercalation occurs, rGO experiences a significant volume expansion/shrinking. In normal batteries, the polymer binder holds the position of adjacent rGO flakes during the intercalation/deintercalation process; while in planar batteries, the rGO network holds itself only through van der Waals forces without a binder. Therefore, during the volume expansion/shrinking process, the rGO network is prone to breakage, which leads to an irreversible ion intercalation process. During the ion deintercalation process, the rGO network breaks and peels off. This result demonstrate the need of CNTs in our design in order to preserve the structural integrity of the rGO network.

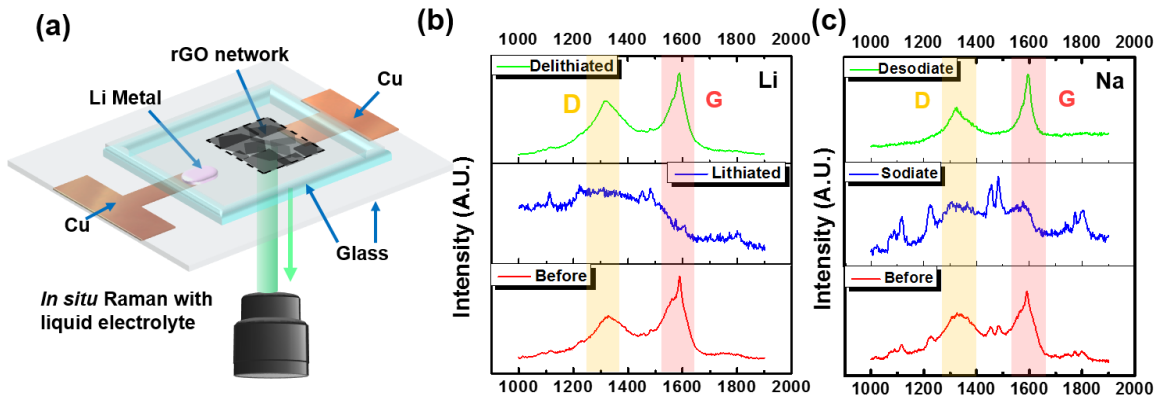


Figure 7.4 (a) Schematic of in situ Raman with planar battery of CNT/rGO/CNT thin film with ion intercalation and deintercalation process. Raman spectrum of (b) pristine, lithiated, delithiated and (c) pristine, sodiated and desodiated CNT/rGO/CNT thin film.

To further confirm the reversible modulation of CNT/rGO/CNT film *via* ion intercalation, we conducted *in situ* Raman spectroscopy on the planar battery film. Figure 7.4a illustrates the schematic of *in situ* Raman set up with the planar battery. The CNT/rGO/CNT film is connected to a Cu electrode on one side and to Li/Na metal and a Cu electrode on the other side. After the planar batteries are sealed, they are transferred and integrated with the electrochemical station and Raman spectrometer. The He-Ne laser (633 nm) shoots directly on the back side of the planar battery and focuses on the surface of the CNT/rGO/CNT thin film through the glass. Figure 7.4b shows the Raman spectrum of the hybrid film before and after intercalation, and after deintercalation of Li, respectively. As shown in figure 7.4b, the Raman spectrum of the sandwich film shows two typical peaks, which correspond to the D and G peaks of graphitic materials. After Li-ion intercalation, both peaks diminish and disappear after intercalation. This result is very similar to the Raman spectrum of Li intercalated graphite at the  $\text{LiC}_6$  stage.<sup>147</sup> After full delithiation, both D and G peaks are recovered, demonstrating the reversible Li intercalation and deintercalation in the sandwich film. The small peaks in both intercalated states in figure 4b are probably result from the electrolyte. The sandwich film interacting with Na ions shows similar characteristic than in the Li ion case, demonstrating its successful reversible intercalation.

#### **7.4 Optical modulation of CNT/rGO/CNT in Infrared region via ion intercalation**

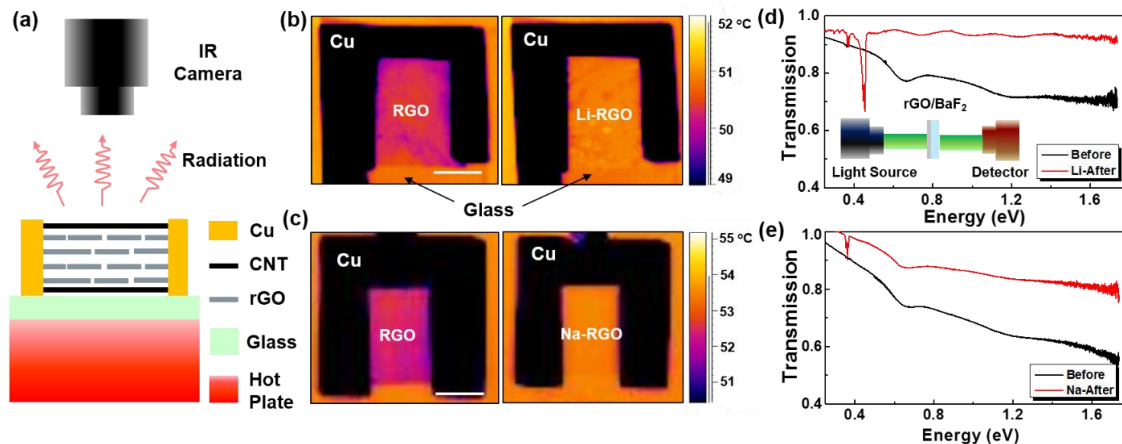


Figure 7.5 (a) Schematic of IR transmission characterization with CNT/rGO/CNT film by IR camera. False color image of the CNT/rGO/CNT film before and after (b) Li ion intercalation and (c) Na ion intercalation. Transmission change of the CNT/rGO/CNT before and after (d) Li ion intercalation, inset a simplified schematic (e) Na ion intercalation, as a function of energy in the infrared range.

We then used an IR camera to qualitatively demonstrate the modulation of the sandwich thin film *via* intercalation. The temperature distribution of the samples was characterized by a temperature controlled isothermal hot plate beneath the sample and then measuring the resulting temperature distribution with an FLIR Merlin MID IR camera, as shown in figure 7.5a. At a fixed hot plate temperature (55-60 °C), the surface temperature distribution of the thermalized samples was detected by the IR camera. The glass substrate is quite transparent in the IR range (the emitted radiation region), but the CNT/rGO/CNT film coatings on glass surface is not as transparent. As a result, the non IR transparent coating will block the radiation to the IR camera causing a temperature difference on the thermal map (figure 7.5b-c). The black region is the Cu electrodes overlaid on the rGO network, which indicate that the metal totally blocks the IR radiation.

The pink region marks the lower temperature display caused by the relatively low transparency of the rGO coating while the orange region is the glass substrate. Before ion intercalation, the color difference corresponds to the temperature difference caused by different IR transparencies on the surface. The average temperature difference between the film-coated area and the glass substrate is 0.5-0.6 °C. However, after Li-ion or Na-ion intercalation, the temperature difference between the film-coated area and the glass is only 0-0.1 °C, indicating that intercalation greatly improves the IR transparency of the sandwich nanocarbon film-coated area.

We additionally measured the transmission spectra of the CNT/rGO/CNT film and the Li-ion intercalated film with a FTIR spectrometer Bomem DA3. In this case, the film was coated on a BaF<sub>2</sub> substrate instead of glass since BaF<sub>2</sub> has a much wider transparent window (0.2 um to 12 um in wavelength). Cu thin film electrode is evaporated on top of the sandwich thin film to assist Li-ion intercalation. Two spectrometer configurations were used. In the mid infrared, we used global source, KBr beam splitter, and MCT detector. In the near infrared, we used a quartz lamp, quartz with TiO<sub>2</sub> film beam splitter, and InSb detector. (Simple schematic in Figure 7.5d inset) Special care was taken to minimize degradation of the intercalated graphene. The two spectra merge very well without scaling which is evidence of good reproducibility. As shown in Figure 7.5d and 7.5e, the black and red line depicts the transmission spectrum of sandwich film before and after Li ion and Na ion intercalation, respectively. In both cases, it is obvious that after intercalation, a drastic increase in transmission has occurred in both near infrared region and mid infrared region.

## 7.5 DFT Calculation for broadband transmittance with intercalation

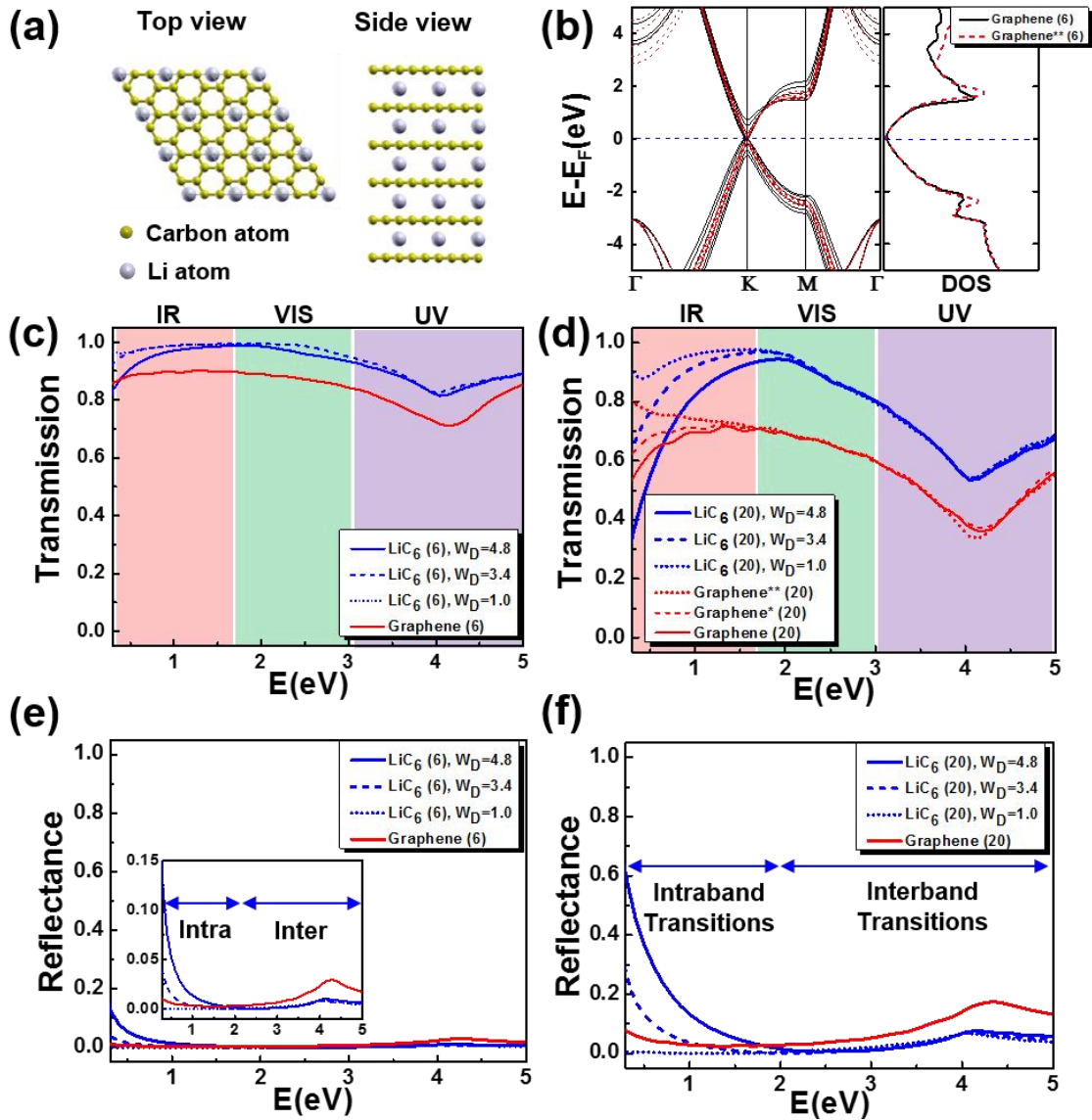


Figure 7.6 (a) Top and side views of  $\text{LiC}_6$  structure; yellow and gray balls represent C and Li atoms, respectively. (b) Electronic structure of 6 layers of graphene using the optimized interlayer separation of 3.311 Å labelled as “Graphene (6)” and using an increased interlayer separation of 4.00 Å labelled as “Graphene\*\* (6)”. Transmission of (b) 6 and (c) 20 layers of graphene and  $\text{LiC}_6$ , and reflectance of (d) 6 layers and (e) 20

layers of graphene and  $\text{LiC}_6$ . All the results are obtained from the electronic structure of 6 layers, except “Graphene\* (20)” which is obtained by using the electronic structure of bulk graphite. “Graphene\*\* (20)” is obtained from the electronic structure of 6 layers of graphene with 4 Å of increased interlayer spacing instead of the LDA optimized value of 3.311 Å. Blue arrow in (e) and (f) denote the intraband transitions and interband transitions of the intercalated graphene.

The chemical nature of rGO is highly dependent on the synthetic routes although it is generally characterized by the presence of different and randomly spaced defects and chemical groups, which broaden Raman peaks and increase the resistance in the material. These effects make reliable electronic structure calculations challenging as the atomic structure of the material is not known. Therefore, in order to understand the excellent transmittance modulation of the sandwich film with ion intercalation, we started by calculating the reflection and transmission of a few-layers of pristine graphene (6 and 20 layers) and  $\text{LiC}_6$  in between glass. Figure 7.6a shows the schematic top view and side view of  $\text{LiC}_6$  and Figure 7.6b shows the electronic structure of 6 layers of graphene. After Li ion intercalation, the 6 layered graphene shows an increased broadband transmission (Fig. 7.5c).

We first discuss the broadband transmittance of the original graphitic film. In order to understand the effect of thickness in few-layers of graphene, we considered 20 layers of graphene in addition to 6 layers. For 20 layers of graphene, transmission is calculated by using the electronic structure of 6 layers of graphene and bulk graphite (solid and dashed red lines labeled as “Graphene (20)” and “Graphene\* (20)” in Fig.

7.6d). For energies larger than 1 eV both results are identical, however below 1 eV, results begin to differ and at 0.3 eV the transmission obtained from the electronic structure of 6 layers of graphene is about 10% lower than the transmission obtained by using the electronic structure of bulk graphite. This is due to a slightly larger absorption ( $\epsilon_2$ ) of 6 layers of graphene with respect to bulk graphite below 1 eV, caused by a broken degeneracy of the energy bands around the Fermi level. However, in contrast to the results of our calculations, the experimentally observed transmission of rGO increases towards 0.3 eV.

Importantly, the interlayer distance in rGO is larger than in graphite which affects transmission in the IR region through a weaker interlayer coupling. This can be observed through the marked difference in transmission below 1 eV of 20 layers of graphene obtained from the electronic structure of: i) 6 layers of graphene, ii) AB-stacked bulk graphite, and iii) 6 layers of graphene with an artificially increased interlayer spacing of 0.4 nm (Figure 7.5b and 7.5d). As seen in Figure 6d, in the latter case, transmission increases towards 0.3 eV in agreement with the experimental observation in rGO. The difference in transmission between the results for 20 layers of graphene with different interlayer spacing is large (about 30%). Therefore, an increase in the interlayer separation and decoupling of the layers can result in significant gain in the IR region transparency in few-layers of graphene due to a reduction in interband transitions with increased degeneracy of the bands around the Fermi level as shown in Figure 6b. Since, rGO is known to have a larger interlayer spacing than graphite and the experimental material consist of network of rGO layers, the layers are expected to be decoupled and the experimental result of increased transmission towards 0.3 eV is comparable to expanded

few-layers of graphene. Furthermore, sensitivity of the optical transitions to interlayer spacing and also possibly to stacking of the layers in the IR region of the spectrum is an interesting aspect, considering the recent efforts to find a reliable experimental method for the determination of the complex refractive index of few-layers of graphene where wavelengths in the visible region have been used.

We then discuss the transmittance modulation of rGO film with ion intercalation. Upon intercalation, transmission increases by about 20–30% for 20 layers from the infrared to the ultraviolet regions of the spectrum. In the infrared region of 0.3–1.6 eV, the description of plasmons becomes important in order to study reflection and transmission. The system with 20 layers of  $\text{LiC}_6$  shows decreasing transmission (solid blue line in Fig. 7.6d) for energies below 2 eV due to a screened plasmon resonance in good agreement with recent experimental results within the visible range. This behavior shifts to lower energies (below 1 eV) for 6 layers. Calculations show that the increased transparency for few-layers is assisted by interference due to internal reflection. This effect, which is highly dependent on plasmon energy, quickly disappears as the number of layers increases.

However, in Figure 7.5, in Li intercalated rGO we do not observe this decrease in transmission within the visible or infrared regions, although the thickness of the experimental rGO film is larger than few-layer graphene. Therefore, there is clearly a significant difference between rGO and graphite in terms of plasmon energy which affects reflectance and transmittance enormously. For example, a decrease in the plasmon energy of about 1.4 eV results in an increased transmission for both 6 and 20 layers, and similar to experimental result, a flat transmission in the IR region is obtained at 1 eV of

plasmon energy for 20 layers (dashed blue lines Fig. 7.6d and 7.6e). These results seem to indicate that plasmon energies are lowered in intercalated rGO flakes with respect to few-layers of graphene thus reducing the reflectance significantly (7.6d and 7.6e) and therefore exhibiting improved transparency in the infrared region. A larger effective mass and/or smaller conduction electron density in intercalated rGO compared to graphite can result in lower plasmon energy. Intercalated large scale rGO network presents a significantly higher sheet resistance (2.1 k $\Omega$ /sq) than intercalated few layer graphene (about 3  $\Omega$ /sq). This difference can be caused by increased resistivity due to the intrinsic lower conductivity of rGO to graphene or the connections between rGO flakes in the large network of flakes. The observed almost constant transmission of Li intercalated rGO in the IR region can be understood with a relatively small amount of reduction in plasmon energy as well as a decoupling of the graphene layers due to increased interlayer separation. For example, the transmission of Na intercalated rGO increases towards 0.3 eV instead of being constant, this can be understood with a further reduction in plasmon energy due lower Na concentration compared to Li in rGO. We note that the effect of CNT layers on reflectance and transmittance is ignored in our discussion. However, the CNT layers are transparent both in the infrared and visible region.<sup>274</sup>

DFT calculation methods are illustrated as follows. Density-functional theory calculations within the local density approximation (LDA) are carried out using the Quantum-Espresso software employing a plane-wave basis set with periodic boundary conditions.<sup>51</sup> Norm-conserving pseudopotentials are used to replace core electrons of C and Li atoms. Kinetic energy cut-off of the wavefunctions is 140 Ry. The Monkhorst-Pack grid of k-points is used. Structure optimization is carried out with a k-point grid of

14×14×1 for 6 layers of graphene and 8×8×1 for LiC<sub>6</sub>. Marzari-Vanderbilt smearing with smearing width of 0.02 Ry is used for Li intercalated metallic systems. Convergence threshold of stress and interatomic forces for structure optimizations are 0.5 kbar and 10<sup>-3</sup> Ry/Bohr. Separation along the vacuum direction for 6 layers of graphene and LiC<sub>6</sub> are 12.4 Å and 13.1 Å, respectively. For the density-of-states calculations, 64×64×1 and 40×40×1 k-point grids are used for 6 layers of graphene and Li intercalated structures, respectively. LiC<sub>6</sub> gallery structure in 6 layers of graphene has the stoichiometry Li<sub>0.83</sub>C<sub>6</sub>, due to the absence of Li atoms on the surfaces with an AA stacking of layers both C and Li atoms (Figure 7.6a). The Yambo code<sup>256</sup> is used to obtain optical interband transitions within the random-phase approximation (RPA) and intraband transitions in the metallic system (intercalated) are taken into account through the Drude model with damping energy of 0.3 eV.<sup>152</sup> Exchange-correlation contributions to the full polarizability are neglected in the RPA and the problem is reduced to finding independent-particle polarizabilities. The dielectric function obtained with the Drude model for intraband transitions in a metal can be expressed as

$$\epsilon(\omega) = 1 - \frac{\omega_D^2}{\omega(\omega - i\Gamma)}, \quad \omega_D = \left( \frac{4\pi e^2 N}{mV} \right)^{1/2}$$

where  $\omega$  is the frequency,  $\Gamma$  is the scattering rate (damping),  $N$  is the number of conduction electrons,  $m$  is the free electron mass, and  $V$  is the volume. The independent-particle polarization is used to obtain the RPA dielectric function for the interband transitions,

$$\chi_{\vec{G}\vec{G}'}^0(\vec{q}, w) = 2 \sum_{n \neq n'} \int_{BZ} \frac{d\vec{k}}{(2\pi)^3} \rho_{nn'\vec{k}}^*(\vec{q}, \vec{G}) \rho_{nn'\vec{k}}(\vec{q}, \vec{G}') f_{n\vec{k}-\vec{q}} (1 - f_{n'\vec{k}}) \\ \times \left[ \frac{1}{w + \varepsilon_{n\vec{k}-\vec{q}} - \varepsilon_{n'\vec{k}} + i\eta} - \frac{1}{w + \varepsilon_{n'\vec{k}} - \varepsilon_{n\vec{k}-\vec{q}} - i\eta} \right]$$

where  $\rho_{nn'}(\vec{k}, \vec{q}, \vec{G}) = \langle n\vec{k} | e^{i(\vec{q}+\vec{G})\cdot\vec{r}} | n'\vec{k} - \vec{q} \rangle$ ,  $f_{n\vec{k}}$  is the occupation number, and  $\varepsilon_{n\vec{k}}$  is the Kohn-Sham eigenvalue. In the vanishing momentum limit the macroscopic dielectric function is defined as  $\epsilon_M(w) = \lim_{\vec{q} \rightarrow 0} \frac{1}{[\epsilon(\vec{q}, w)^{-1}]_{\vec{G}=0, \vec{G}'=0}}$ . The macroscopic dielectric function of in-plane polarization obtained for the supercell containing 6 layers of graphene (bare and intercalated) including a large vacuum space is scaled to a volume with a perpendicular distance corresponding to the distance between the 6 layers plus 3.311/2 Å for each external surface. This distance is half the LDA interlayer distance between sheets and it is expected that the charge density as well as the dielectric response should be low beyond this distance towards vacuum. The calculated unscreened plasmon energy is 4.8 eV for 6 layers of LiC<sub>6</sub> suspended in vacuum which is lower than the bulk value since there is a contribution to conduction electron density due to out-of-plane periodicity in the bulk system. For example, the reflectance of 16 layers of KC<sub>8</sub> is found to be in better agreement with experimental results when a plasmon energy reduced by about 15% from the bulk value is used for the Drude model calculation.<sup>275</sup> Reflectance and transmission are calculated by including internal reflections and phase changes, similar to the recent works on optical reflection of bare and potassium intercalated few-layers of graphene.<sup>154</sup> The equations for reflection coefficient ( $r$ ) and transmission coefficient ( $t$ ) are defined as

$$r = \frac{r_{01} + r_{10} e^{-2i\beta}}{1 - r_{01} r_{12} e^{-2i\beta}}, \quad t = \frac{t_{01} t_{12} e^{-i\beta}}{1 - r_{10} r_{12} e^{-2i\beta}}$$

where  $r_{01} = \frac{n_0 - n_1}{n_1 + n_0}$ ,  $t_{01} = 1 + r_{01}$ , and  $\beta$  is the phase difference due to the optical path length also involves attenuation coefficient. Reflectance results for graphite and 35 layers of bare graphene in vacuum (using the dielectric function of bulk graphite) can be compared in the infrared as well as the visible region of the spectrum to the experimental results reported in the literatures. Here, we considered the systems are contained in between glass with refractive index of 1.5 instead of vacuum. With these approximations we find that the reflectance is reduced and therefore, the transmission is increased with respect to the system being in vacuum and in better agreement with a recent experimental study on transparency of Li intercalated few-layers of graphene.

## **7.6 conclusion**

In conclusion, we designed and fabricated CNT/rGO/CNT sandwich thin film, not only demonstrated its broadband response in optical transmission, but also achieved reversible optical modulation via ion intercalation/deintercalation. The experimental results in intercalated reduced graphene oxide show an increase in transmission in the infrared as well as in the visible region in contrast to calculated results for intercalated few-layers of graphene. This disagreement can be understood by considering a reduced plasmon energy and also an increased interlayer spacing in rGO in addition to possible empty spaces in the large network of rGO flakes. Assisted by interference of light, the plasmon energy down shift quenches the reflectance in the infrared region in rGO in contrast to what would occur in few-layers of graphene. We additionally show that the sandwich thin film is also highly scalable with flexible PET substrate via an all solution based process. The demonstration of the scalable, printable, broadband responsive, carbon based sandwich

film is significant in optoelectronic and electrochromic<sup>47</sup> devices for consumer electronics, communication and military uses.

## Chapter 8: Li intercalation in MoS<sub>2</sub> with planar batteries—resistance change matters in battery electrodes

Jiayu Wan, Wenzhong Bao, Yang Liu, Jiaqi Dai, Fei Shen, Lihui Zhou, Xinghan Cai, Daniel Urban, Yuanyuan Li, Katherine Jungjohann, Michael S. Fuhrer, Liangbing Hu, *Adv. Energy Mater.* 2015, 5, 1401742

### 8.1 Introduction

MoS<sub>2</sub> is an earth-abundant mineral material that has been widely studied for its many applications such as lubrication, hydrodesulfurization catalysis, and as an electrical energy storage electrode.<sup>122, 276, 277</sup> Recently, two dimensional (2D) MoS<sub>2</sub> crystals have attracted tremendous research interest for their unique properties in photonics, optoelectronics, electronics and energy applications.<sup>4, 5, 11, 12, 15, 69, 278-280</sup> Liquid phase exfoliation of layered materials can provide an excellent approach for mass production of 2D materials,<sup>23, 43, 281</sup> enabling applications which require a large quantity of materials, particularly electrical energy storage. Indeed the large van der Waals gap of MoS<sub>2</sub> enables excellent electrochemical performance, and MoS<sub>2</sub>-based Li-ion, Na-ion, and Mg-ion batteries are being explored for electric vehicles and grid-scale storage.<sup>121, 134, 200, 282-288</sup>

Battery electrode materials are complex composites with structure at several length scales, being composed of active materials (e.g. MoS<sub>2</sub>), conductive additives (e.g. carbon black), and binders (e.g. polyvinylidene difluoride). Conventional electrochemical characterization techniques, such as cyclic voltammetry (CV), galvanostatic intermittent titration technique (GITT), electrochemical impedance spectroscopy (EIS), etc. reveal the

performance of the bulk composite electrode, but cannot probe the intrinsic properties of the active material itself during ion insertion. Recent *in situ* TEM studies of nanostructured electrodes have partially overcome this, successfully observing the structural changes during the charge/discharge process,<sup>223, 289, 290</sup> leading to a better understanding of mechanical properties and kinetics, and thus a better electrode design. Still, information about the electronic structure of the active material, and its intrinsic electronic transport properties, which are at least equally important in making better batteries, is still lacking.

We have designed a planar microbattery that allows *in situ* electrical transport measurement during electrochemical charge and discharge in micron-sized individual crystallites of 2D layered nanosheets, as well as optical studies (transmittance, Raman spectroscopy), which can give information about the electronic structure of the active material. To demonstrate the utility of our microbattery platform, we study the lithiation of MoS<sub>2</sub> crystallites. We observe that the electrical conductivity of the 2D MoS<sub>2</sub> crystallites is highly dependent on thickness and the rate of lithiation in the first cycle. We use *in situ* TEM to confirm that upon rapid first-cycle lithiation the formation of a Mo conductive network imbedded in the Li<sub>2</sub>S matrix leads to an enhanced electrical conductivity compared to the pristine MoS<sub>2</sub>. We applied the results in Li-MoS<sub>2</sub> coin cells with composite electrodes, demonstrating that batteries with fast lithiation on the first cycle showed significantly higher specific capacity than batteries lithiated slowly. The microbattery platform can be generally applied to other energy storage materials and a wide range of characterization techniques, and is thus a powerful tool to uncover the properties of nanoscale materials undergoing electrochemical modification. As in the

example demonstrated here, we expect this platform will lead to new insights into the operation of battery materials at the nanoscale, leading to new strategies in improving the cell performance.

## 8.2 Electrical measurement of MoS<sub>2</sub> upon lithiation by planar nano battery

A schematic crystal structure of 2H-MoS<sub>2</sub> is illustrated in Figure 8.1a, with the lattice parameters  $a = 3.16 \text{ \AA}$  and  $c = 12.29 \text{ \AA}$ . Our microbattery platform developed for the *in situ* measurement of the optical transmittance and electronic transport of 2D nanomaterials is illustrated in Figure 8.1b. A MoS<sub>2</sub> crystal and lithium metal are deposited on top of the Cu transport electrodes and current collector respectively. The MoS<sub>2</sub> flake can be charged/discharged by connecting transport electrodes and current collector to an electrochemical workstation. Coupling the microbattery with a transmission optical microscope/probe station, we can then carry out *in situ* optical transmittance and electronic transport measurements on the same MoS<sub>2</sub> crystal. Optical images of uniform-thickness mechanically exfoliated MoS<sub>2</sub> crystals are shown in Figure 8.1c and d, with dimensions as large as  $100 \text{ \mu m} \times 100 \text{ \mu m}$ . We used atomic force microscopy (AFM) to determine the morphology and thickness of exfoliated MoS<sub>2</sub>, in Figure 8.1e and f. A photograph of the complete microbattery device is shown in Figure 8.1g. The region of the transport electrodes is expanded in Figure 8.1h, showing a large uniform area of MoS<sub>2</sub> crystal spanning the electrodes.

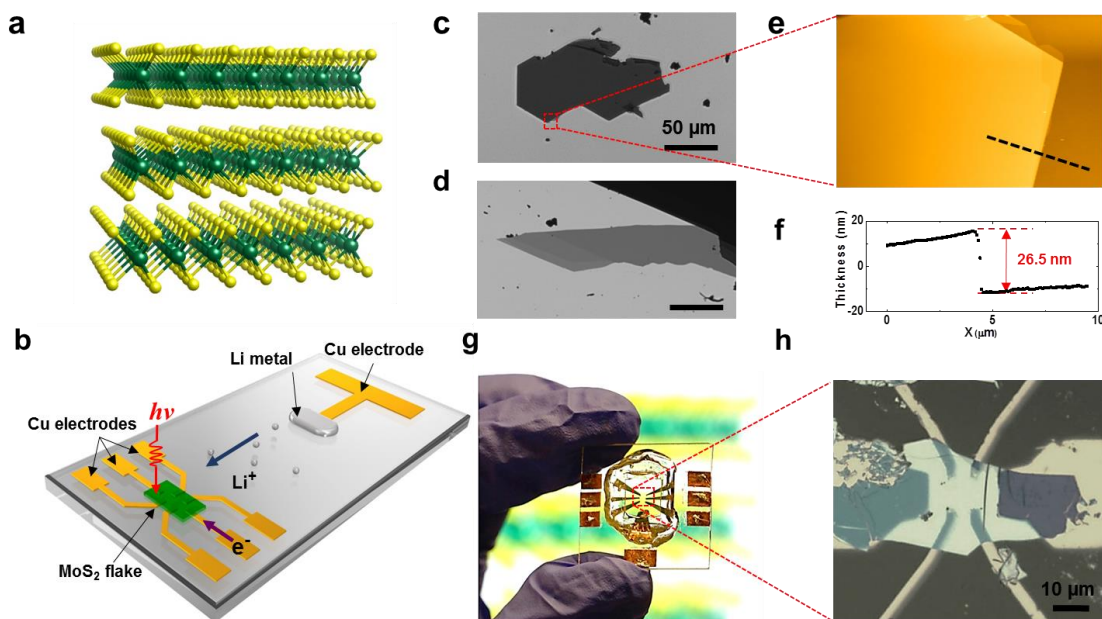
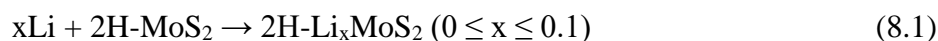
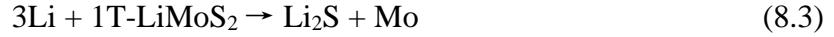
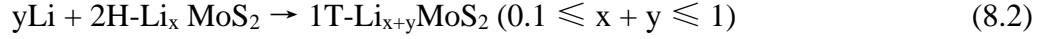


Figure 8.1 Li-MoS<sub>2</sub> microbattery. (a) Lattice structure of 2H-MoS<sub>2</sub>. (b) Schematic of MoS<sub>2</sub>-Li microbattery. (c), (d) Optical images of large area uniform MoS<sub>2</sub> crystals on glass substrates at 550 nm wavelength under transmission mode; both scale bars are 50 μm. (e) AFM image of MoS<sub>2</sub> crystal in (c). (f) Line trace of AFM image along dashed line in (e). (g) Photograph of microbattery. (h) Micrograph of electrode area with MoS<sub>2</sub>.

To understand the intrinsic resistance change during lithiation, an *in situ* electrical transport measurement was carried out using our microbattery setup. Figure 7.2a shows the simultaneously measured resistance and electrochemical potential at a small constant lithiation current at 0.5 μA for a single MoS<sub>2</sub> crystal of thickness 35 nm. Figure 7.2a inset illustrates the experimental setup; the MoS<sub>2</sub> crystal in the microbattery was lithiated at a constant current, while the electrochemical potential and 4-probe electrical resistance of the crystal were monitored. During the first cycle of lithiation, three reactions occur:





We identify these three reactions with the regions marked I, II, and III respectively in Figure 8.2a. In region I, we observe a rapid decrease of the electrochemical potential, and a rapid decrease and rise of the resistance. We interpret this as the region where reversible Li intercalation of the Van de Waals gaps of 2H-MoS<sub>2</sub> occurs with little lattice distortion [Eqn. (1);  $0 < x < 0.1$ ] <sup>276</sup>. With increasing concentration of Li, a reversible phase change occurs from 2H-Li<sub>x</sub>MoS<sub>2</sub> to 1T-Li<sub>x</sub>MoS<sub>2</sub> corresponding to Eqn. (8.2), and is marked by a clear plateau of ~1.1 V. The resistance in region II is always lower than the initial resistance, consistent with the formation of the metallic 1T-Li<sub>x+y</sub>MoS<sub>2</sub> phase. The completion of Eqn. 8.2 at 1T-LiMoS<sub>2</sub> marks the end of region 2. Region III shows another clear plateau in at ~ 0.6 V, corresponding to Eqn. (8.3), the conversion reaction from 1T-LiMoS<sub>2</sub> to Li<sub>2</sub>S and Mo metal. The resistance jumps abruptly at the onset of region III, consistent with the formation of the insulating matrix, and stays always higher than the initial resistance of the pristine MoS<sub>2</sub>.

Importantly, qualitatively different behavior of the resistance is observed in the same setup upon rapid discharging, accomplished by shorting the Li electrode to the MoS<sub>2</sub> electrode to promote rapid insertion of Li into MoS<sub>2</sub>. A large overpotential between the two electrodes enables a rapid formation of Mo and Li<sub>2</sub>S. Figure 8.2b shows the time profile of the resistance for a shorted MoS<sub>2</sub> crystal (thickness 46 nm); a schematic of the measurement setup is shown in Figure 8.2b inset. In contrast to slow discharging (Figure 8.2a), here a drastic decrease in the resistance within a few minutes was observed of over 3 orders of magnitude, from  $5 \times 10^5$  to 190 ohms. After shorting for 24 hours the

resistance stayed the same, which suggested the low resistance is associated with the MoS<sub>2</sub> reaction products and not due to Li plating (also no Li plating was observed optically). After the microbattery was disconnected for 36 hours, the resistance increased only a little to 210 ohms, which indicated the high stability of the final product. The process was repeated for many MoS<sub>2</sub> crystals of different thicknesses with results shown in Figure 8.2c. Strikingly, we observe a thickness dependent relationship on the final resistance of the Li-inserted MoS<sub>2</sub>. For pristine MoS<sub>2</sub> crystals of thickness greater than 30 nm, a drastic resistance drop occurred after lithiation. However, with thinner crystals, an increase in the resistance was observed, of magnitude similar to that observed for slow lithiation (Figure 8.2a).

Since we expect that in all cases the final product of lithiated MoS<sub>2</sub> is Mo nanoparticles and Li<sub>2</sub>S,<sup>291</sup> the complexity of resistance change suggests that the morphology and connectivity of the nanostructured Mo may change with different lithiation rates. We hypothesize that slowly lithiated MoS<sub>2</sub> forms isolated Mo nanoparticles which do not enhance the conductivity, thus the resistance is dominated by the insulating Li<sub>2</sub>S (Figure 8.2d) while upon rapid lithiation of thick MoS<sub>2</sub>, Mo nanoparticles form a percolating metallic network, enhancing the conductivity (Figure 8.2e). Thinner MoS<sub>2</sub> always shows more resistive behavior, and we suppose this is due to the difficulty of forming a percolating network in a thin sample (Figure 8.2f).

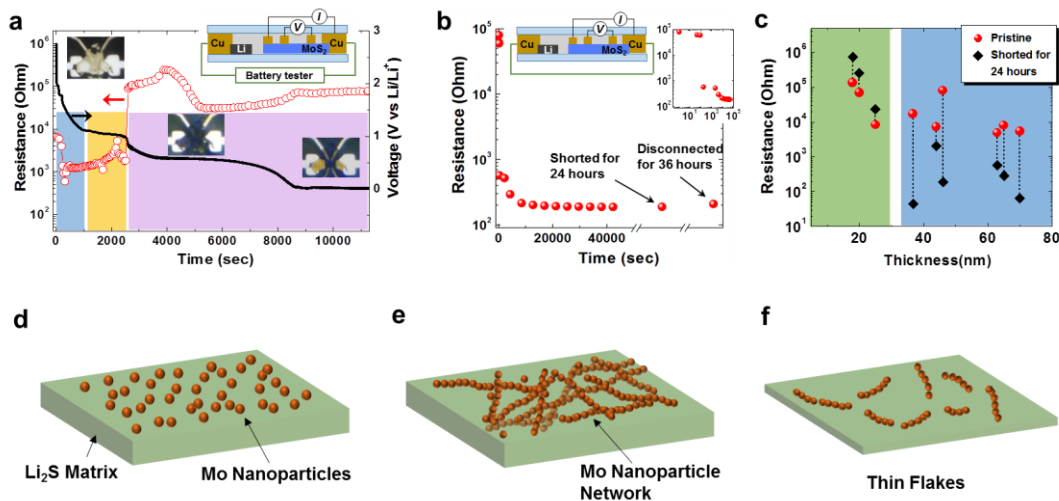


Figure 8.2 Electronic transport measurement. (a) Resistance vs. time of MoS<sub>2</sub> flake undergoing electrochemical lithiation at constant current. Insets show a schematic of the microbattery setup for *in situ* resistance measurement (upper right), and optical images of lithiated MoS<sub>2</sub> at stages I, II, and III, from left to right. (b) Resistance vs. time for a MoS<sub>2</sub> crystal after electrically shorting the microbattery. Insets show a schematic of the microbattery for *in situ* resistance measurement during shorting, and a log-log plot of the resistance vs. time. (c) Resistance vs. thickness phase diagram of shorted MoS<sub>2</sub> crystals; red circles show resistance of pristine MoS<sub>2</sub>, black diamonds show resistance after shorting of microbattery. (d) Schematic showing discontinuous Mo particles imbedded in Li<sub>2</sub>S matrix resulting from slow lithiation in thick MoS<sub>2</sub>. (e) Schematic showing percolative Mo nanoparticle network imbedded in Li<sub>2</sub>S matrix resulting from fast lithiation in thick MoS<sub>2</sub>. (f) Schematic of discontinuous Mo particle network imbedded in Li<sub>2</sub>S matrix resulting from fast lithiation in thin MoS<sub>2</sub> crystallite.

### 8.3 In situ TEM characterization of MoS<sub>2</sub> upon Lithiation

In order to confirm our hypothesis that charging rate-dependent Mo nanostructure determines the conductivity of MoS<sub>2</sub> after lithiation, we used transmission electron microscopy (TEM) with *in situ* electrochemistry to determine the structure of the final product. Figure 8.3a illustrates the principle of the *in situ* electrochemical TEM setup. MoS<sub>2</sub> flakes obtained from liquid exfoliation<sup>[14]</sup> were attached to an Au rod, serving as the working electrode. Li metal was attached to a W rod, serving as the counter and reference electrodes. A thin layer of native oxide Li<sub>2</sub>O was formed during the transfer process and acted as the solid-state electrolyte for Li ion transport. The Li/Li<sub>2</sub>O electrode was controlled by nano-manipulator inside the TEM, and made contact with the selected MoS<sub>2</sub> nanoflake (also see Supplemental Figure 1). Fig 8.3b shows a bright-field TEM image of a pristine MoS<sub>2</sub> crystallite attached to the Au electrode. Fig 8.3c shows the diffraction pattern of the MoS<sub>2</sub>. The diffraction spots marked in red circles show a 6-fold symmetry and correspond to the 2H crystal structure of MoS<sub>2</sub>. Additional diffraction spots correspond to additional MoS<sub>2</sub> crystals with different rotational orientations. Figure 8.3d shows a high-resolution TEM (HRTEM) image of pristine MoS<sub>2</sub>, clearly showing in which the periodic triangular lattice of Mo atoms is resolved. The Mo-Mo distance is 0.27 nm as expected for 2H-MoS<sub>2</sub>.

In the *in situ* electrochemical TEM experiment, the lithiation process is controlled by the voltage difference between the two electrodes. When a large voltage difference of -2 V was applied on the MoS<sub>2</sub> electrode against the Li counter electrode, the lithiation process started. After full lithiation, a large volume expansion resulted in a curving flake compared to the pristine MoS<sub>2</sub>, shown in Figure 8.3e. The corresponding diffraction pattern (Figure 8.3f) indicates the formation of polycrystalline Li<sub>2</sub>S and a very fine Mo

metal nanostructure in the final product. From the HRTEM image of the final product as shown in Figure 8.3g, the dark contrast corresponds to Mo nanoparticles with diameter about 1 nm, which can be seen to form a continuous network that we believe provides the electron transport pathway within the insulating  $\text{Li}_2\text{S}$  matrix. This observation confirms our explanation of the reduction in the resistance of the fully lithiated  $\text{MoS}_2$  flakes after shorting. The formation of Mo nanoparticles can be explained by the non-equilibrium process with a large over-potential, where the nucleation of Mo nanoparticles occurs rapidly, with limited time for growth and ion diffusion. This may also partially be the result of the low diffusivity of Mo atoms, similar to Fe in the case of  $\text{FeF}_2$  lithiation recently reported <sup>292</sup>. The formation of conductive paths by metal nanoparticles after lithiation has also been reported in  $\text{RuO}_2$ ,<sup>293</sup>  $\text{FeF}_2$  <sup>292</sup>and  $\text{NiO}$ <sup>294</sup>.

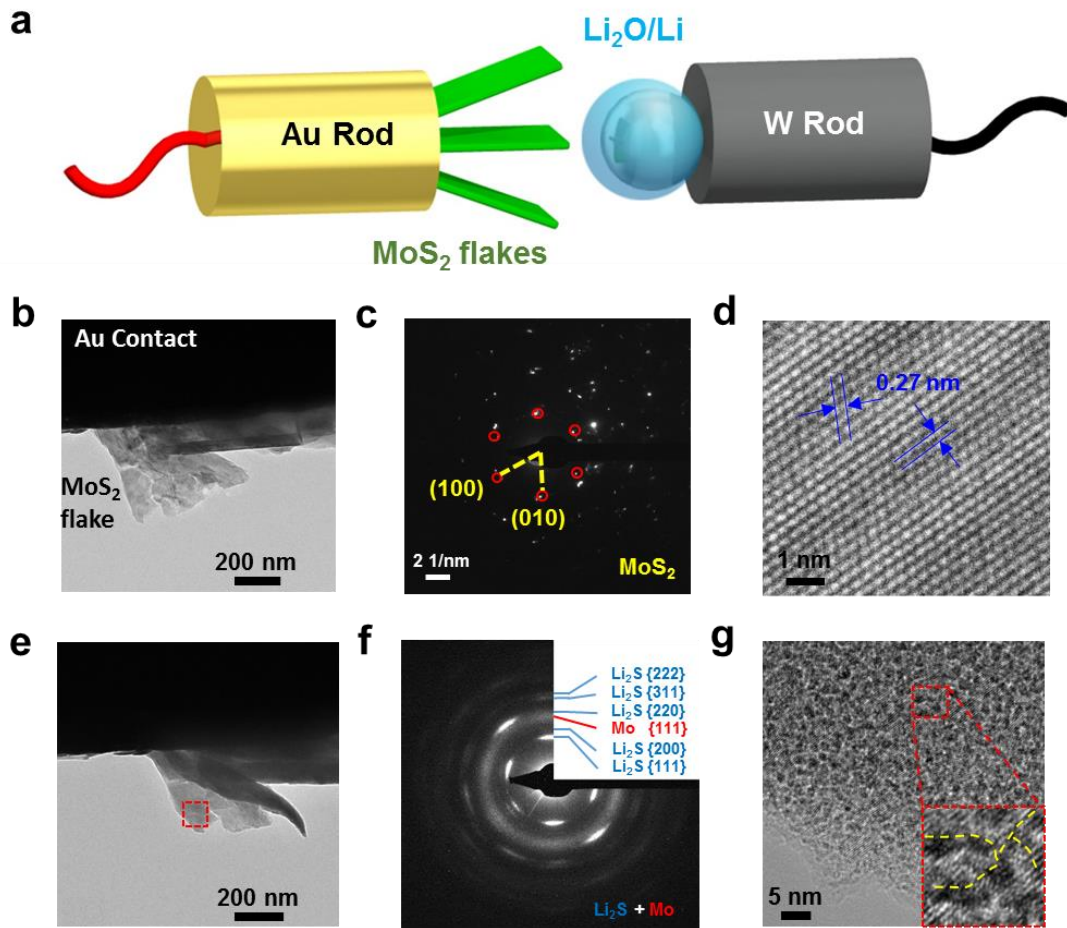


**Figure 8.3** *In situ* TEM of MoS<sub>2</sub> lithiation. (a) Schematic illustration of *in situ* TEM microbattery setup. (b) Pristine MoS<sub>2</sub> nanoflake attached on Au substrate. (c) Electron diffraction pattern of pristine MoS<sub>2</sub>, the spots circled by red correspond to the 2H crystal structure of MoS<sub>2</sub>. (d) HRTEM of the MoS<sub>2</sub> flake showing lattice constant of 0.27 nm. (e) TEM of final product after full lithiation. (f) Electron diffraction pattern of final product. Rings in the diffraction pattern correspond to randomly oriented crystallites; the corresponding crystal indices for Mo and Li<sub>2</sub>S are indicated in the legend. (g) HRTEM image of the final product.

Figure 8.4a shows an image of a MoS<sub>2</sub>/Li<sub>2</sub>O/Li (positive electrode/electrolyte/negative electrode) nano battery in TEM. After applying a potential difference between the two electrodes, a lithiated product of Li<sub>2</sub>S and Mo flake is shown in Supplementary Figure 8.4b.

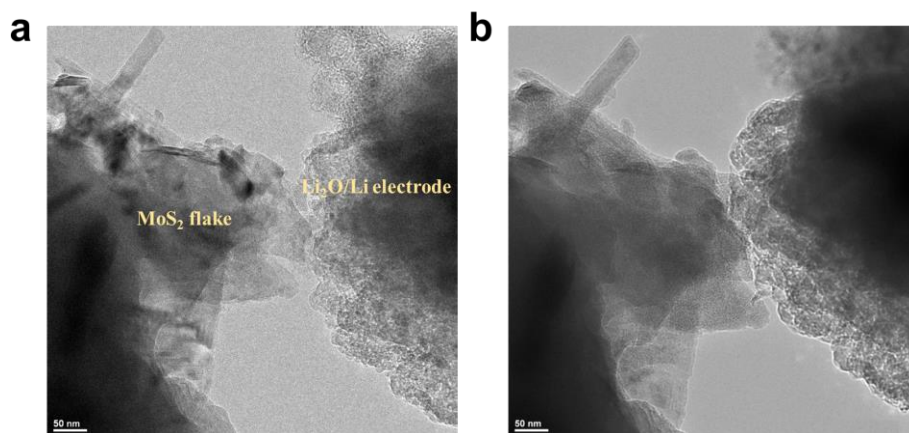


Figure 8.4 Transmission electron micrographs of MoS<sub>2</sub> and Li<sub>x</sub>O/Li electrode (a) before and (b) after lithiation of MoS<sub>2</sub>.

#### 8.4 In situ optical characterization of MoS<sub>2</sub> upon lithiation

An *in situ* optical transmittance measurement was also made during lithiation of MoS<sub>2</sub> using with the microbattery setup, as illustrated in Figure 8.5a. Figure 8.5b-d show the optical images of a MoS<sub>2</sub> crystal under 450 nm wavelength at potentials of 2.8 V, 0.9 V, and 0.05 V (vs. Li<sup>+</sup>/Li). With increasing lithiation, these three typical images clearly show an increase in the transmittance of the crystal. This is further depicted in Figure 8.5e where the optical transmittances of a crystal (blue dots, 7.9 nm) were monitored as a function of time simultaneous to the electrochemical potential (black line) as lithiation proceeded with a constant current. Again we denote the three different regions in

electrochemical potential as I, II, III. Here we see that each region corresponds well to a plateau in optical transmission, as can be seen in Figure 8.5e. In region I, a slightly increase of transmittance is observed as Li intercalated into  $\text{MoS}_2$  (before 2500 s). From region I to region II, a sudden increase of transmittance occurred, corresponding to a phase transition from 2H to 1T upon Li insertion. At the end of the second plateau (~12500 s), we observe a graduate increase of transmittance from 65% to 80%, indicate a conversion reaction from 1T-LiMoS<sub>2</sub> to Li<sub>2</sub>S plus Mo. The delay of the transmittance change relative to the voltage profile from region II to region III is due to kinetic limitation, resulting from the high resistance of this thin (7.9 nm) 1T-LiMoS<sub>2</sub>/Li<sub>2</sub>S+Mo flake.

Figure 8.5f shows the wavelength dependent transmittance of each stage. Stage I shows a typical wavelength dependence for pristine  $\text{MoS}_2$  crystals.<sup>295, 296</sup> Stage II shows increased transmittance at shorter wavelengths (less than 700 nm), and decreased transmittance at longer wavelengths, compared to the pristine  $\text{MoS}_2$ . The final product, after region III, corresponding to Li<sub>2</sub>S and Mo metal, shows higher transmittance than  $\text{MoS}_2$  at all measured wavelength (400 nm – 800 nm). We investigated a wide thickness range of  $\text{MoS}_2$  crystals, all showed an increase of transmittance after lithiation. While more work is needed to understand the details of the transmittance spectra, the changes in optical properties during electrochemical lithiation are qualitatively as expected for the structure changes as discussed above. While  $\text{MoS}_2$  has a bandgap in the visible range with limited transmittance, reaction product Li<sub>2</sub>S is insulating and expected to be fairly transparent. The percolative Mo network is also fairly transparent due to the small thickness.

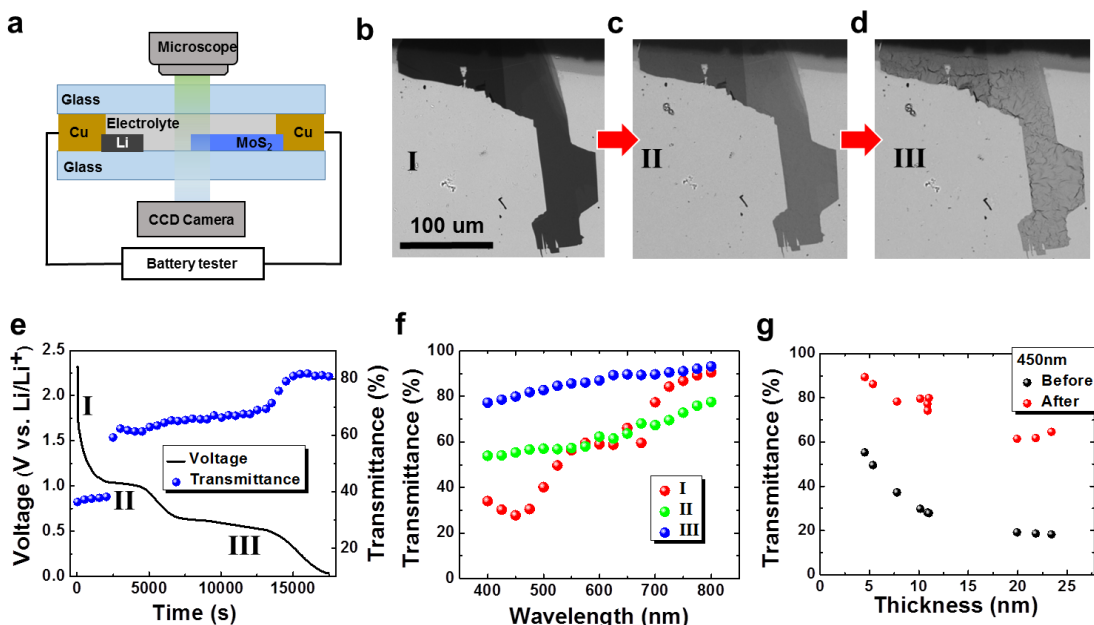


Figure 8.5 *In situ* optical transmittance measurement. (a) Schematic of *in situ* optical transmittance measurement of MoS<sub>2</sub> lithiation. (b-d) Optical images of a MoS<sub>2</sub> flake at 2.8 V, 0.9 V and 0.05 V. (e) Transmittance of MoS<sub>2</sub> flake vs. Li insertion voltage. (f) Transmittance vs. wavelength for lithiated MoS<sub>2</sub> at three different stages. (g) Thickness dependence of transmittance of MoS<sub>2</sub> flakes before and after lithiation.

## 8.5 Scalable application of MoS<sub>2</sub> electrode materials in Li ion batteries

Our microbattery measurement scheme can provide crucial information for the development of macroscopic batteries. In the case discussed here, the formation of a conducting Mo nanoparticle network has significant implications for sulfur-based batteries. After the first lithiation cycle, our system corresponds to a Li-S battery with Mo nanoparticles,<sup>122</sup> and we expect that the formation of the percolated conductive network can improve the storage and cycling performance by increasing the electrical connectivity

of the insulating  $\text{Li}_2\text{S}$ . In order to verify the contribution of the Mo nanoparticle percolative network on the electrochemical performance of Li- $\text{MoS}_2$  batteries, we constructed coin cells using  $\text{MoS}_2$ /nanocellulose fiber (NFC)/Carbon Nanotube (CNT) (w:w:w = 8:2:2) composite free standing film and lithium metal as electrode materials. Here, NFC serves as a binder, and CNT as a mechanical scaffold and conductive additive in the thin film electrode. After cell assembly, two groups of cells were cycled by electrochemical workstation at constant and identical current rate. In the experimental group, before constant current cycling, we performed a first rapid lithiation by shorting the cells, which we expect to form a conductive Mo network. The control group was cycled as regular batteries at constant current, with no rapid lithiation in the first cycle. The cycling performance of two typical coin cells from each group is shown in Figure 8.6a. Both coin cells show a steady cycling performance for 100 cycles. However the experimental group shows a higher specific capacity than the control group at same current densities. The first 30 cycles of the two cells were cycled at 50 mA/g, where the next 70 cycles at 250 mA/g. The experimental group (charged rapidly in the first cycle) shows a higher capacity (900 mAh/g) than control battery (800 mAh/g) at low rate, with the difference becoming much larger at high charging rate (500 mAh/g compared to 150 mAh/g). Figure 8.6b shows typical voltage profiles of two cells at 250 mA/g. The plateaus at  $\sim 2.2\text{V}$  (delithiation) and  $\sim 2.0\text{V}$  (lithiation), characterize the  $\text{MoS}_2$  coin cells after 1<sup>st</sup> cycle. Again, the experimental group not only shows a much larger capacity, but also a smaller voltage drop after 30 s of rest. Figure 8.6c shows the specific capacity of an experimental group coin cell charged/discharged at different current densities. A high specific capacity of 1100 mAh/g is demonstrated at a low current density (50 mA/g) with

the composite electrode. At high current density (500 mA/g), a high specific capacity of about 400 mAh/g is still maintained, demonstrate a great promise of MoS<sub>2</sub> as a cathode material for Li ion batteries. All these results are consistent with a lower internal electrical resistance which provides higher capacity at high power, supporting our hypothesis that the Mo conductive network formed by the first rapid charge provides an electron pathway inside each nanoscale Li<sub>2</sub>S/Mo flake. The results demonstrate the power of *in situ* techniques for understanding the structural and electronic changes in electrode materials undergoing electrochemical reactions, and the use of that understanding to improve battery performance. We expect that the *in situ* techniques here will be applied to study a range of phenomena in other conversion electrode materials, with the outcomes used to improve the corresponding battery technologies.

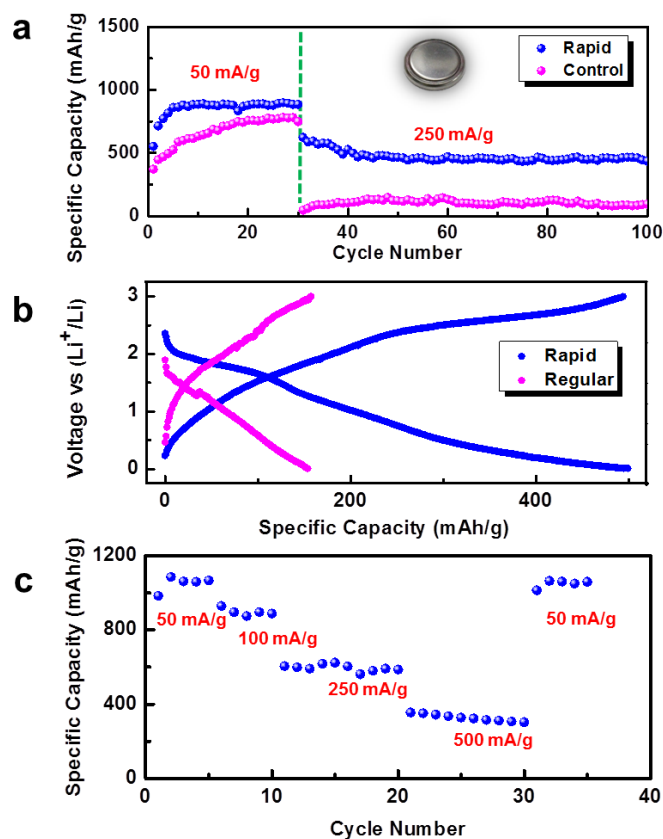


Figure 8.6 Performance of the composite electrodes in coin cells. (a) Cycling performance (at 50 mA/g for 30 cycles and 250 mA/g for 70 cycles) of MoS<sub>2</sub>/NFC/CNT Li ion batteries at different initial lithiation conditions. Inset is a coin cell. (b) Voltage profile of two types of coin cells at 15<sup>th</sup> cycle. (c). Initial rapid charged coin cells cycle at different charge/discharge current density.

## 8.5 Summary

In summary, we have applied *in situ* microbattery techniques to observe the changes in electrical resistance, optical transmission, and nanoscale structure of MoS<sub>2</sub> upon electrochemical lithium insertion. We observe the formation of an interconnected Mo nanoparticle network after rapid lithiation of thick MoS<sub>2</sub> crystals, which achieves a

simultaneous increase of optical transmittance and electrical conductivity compared to pristine MoS<sub>2</sub>. Our *in situ* investigation of lithiation at the scale of single MoS<sub>2</sub> crystals guided the design of higher performing Li-MoS<sub>2</sub> coin cell batteries, where we demonstrated a threefold increase in capacity after rapid lithiation on the first cycle compared to cells which underwent a conventional constant-current discharge. We are the first to propose and confirm the battery performance improvement by such a new charging strategy in the first cycle, which is possible based on the fundamental studies at the nanoscale.

## Chapter 9: Li intercalation in 2D Si Nanowall array fabricated with nanoimprint lithiography

Jiayu Wan, Alex F. Kaplan, Jia Zheng, Xiaogang Han, Yuchen Chen, Nicholas J.

Weadock, Nicholas Faenza, Steven Lacey, Teng Li, Jay Guo, and Liangbing Hu, *J. Mater.*

*Chem. A*, 2014,2, 6051-6057

### 9.1 Introduction

Lithium (Li) ion batteries are one of the most important electrochemical energy storage devices and are widely used in portable electronics. For future Li ion battery powered electronic vehicles, however, electrode materials with higher energy/power density and longer cycle life are needed.<sup>297-302</sup> Silicon (Si), as a Li ion battery anode material, has a theoretical specific capacity of 4200 mAh/g, 10 times higher than the conventional graphite anodes used in commercial batteries. Additionally, Si is an earth abundant and environmentally friendly material with a mature manufacturing process in solar cells and semiconductors industrial that could enable mass production for batteries. Enthusiasm aside, there are significant challenges to use Si as an anode for Li ion batteries.<sup>101</sup> A large volume expansion (up to 400%) and contraction during lithiation and delithiation could result in pulverization of the Si anode. The cracked Si loses contact with the current collector, reducing the accessible capacity over time. The significant volume change also affects the stability of the solid electrolyte interface (SEI). Recently successful demonstration of using Si nanowires as anodes in Li ion batteries to mitigate pulverization and enhance the cycle life<sup>101</sup> has led to a surge of interests in developing

high performance Si nanostructures and Si nanocomposite anodes for Li ion batteries, including Si-C nanocomposites,<sup>303-307</sup> Si nanotubes,<sup>308, 309</sup> interconnected nanonets<sup>310</sup> and three dimensional (3-D) Si nanoparticles<sup>17</sup> et al. have been reported. In order to understand the mechanism of Si as an anode material, fundamental studies on its electrochemical,<sup>311</sup> nanomechanics,<sup>312-314</sup> and transport properties<sup>313</sup> have been reported. A problem of a low first Coulombic Efficiency (CE), however, still exists in the reported nanostructures.

The highly irreversible capacity of the first cycle in any nanostructured electrodes is largely attributed to side reactions and SEI formation, which are directly correlated with the high surface area of nanostructures.<sup>315</sup> This is a fundamental challenge of using nanostructures for electrochemical storage applications. On one side, nanostructured materials such as nanowires and nanoparticles can readily release the mechanical strain during charging, which reduce the potential for pulverization during the first cycle. On the other side, the large surface area of these nanostructures results in a greater amount of side reactions, which occur at the anode-electrolyte interface. The formation of the SEI layer consumes Li ions, contributing to an irreversible consumption of Li. The reduction of surface oxide layers on Si, which forms when exposing Si anode in air during sample preparation, also leads to irreversible consumption of Li. Thus, the large surface area of existing nanostructures plays a major role in the low first CE of those nanostructured Si anodes.

We propose a two-dimensional (2-D) nanowalls structure that can effectively address the issues associated with lower dimensional Si nanostructures. Such 2-D nanostructures are fundamentally better for Li-ion batteries, which has not been explored before. A

schematic image of the nanowalls is shown in Figure 8.1h. Each nanowall possesses sub-micron scale length and height, and can be as thin as 50 nanometers. The nanowalls structure maintains the advantages of other one dimensional (1-D) nanostructures: accommodates large volume expansion without pulverization, obtains direct electrical contact with current collector for fast electron transport, and maintains short Li insertion distance. Most importantly, the nanowalls structure has approximately 50% less specific surface area than nanowires of similar height and width. Thus, the first CE is expected to be higher for 2-D nanowalls structure than for 1-D nanostructured anodes in Li-ion batteries. Recently, there are a few reports <sup>316-318</sup> discussed 2-D electrodes including “nanowall” for Li ion batteries, which also provide alternative methods <sup>319</sup> for nanowall fabrication. However, the reported nanowalls show an inter-connected structure that is easy to pulverize during volume cycling, thus perform a low first CE.

Here, for the first time we designed a periodic, amorphous Si (a-Si) nanowalls structure *via* nanoimprint lithography (NIL) <sup>320</sup> and investigated its electrochemical and mechanical properties as anodes in Li ion batteries. We demonstrate a high CE for the first cycle due to the low specific surface area of the nanowalls electrode. Cycling results show that our Si nanowalls anodes created by NIL achieve a high first CE (83.4%), high stability (40 cycles) and a good rate performance (1000 mAh/g at 2C rate). The electrochemical properties, including first CE, can be further improved by optimizing the Si nanowalls anode including its dimensions, surface impurity and large area uniformity. Si nanowalls are expected to have excellent mechanical flexibility and suitable for flexible energy storages for portable electronics, flexible displays, etc.<sup>321-323</sup> Similar concepts can be applied to other devices <sup>318, 324, 325</sup> such solar cells, where nanostructures

are needed for light-trapping and low-surface area is required to avoid surface recombination.

## **9.2 Fabrication and Characterization of Si nanowalls for LIBs**

NIL can be used to generate high-resolution feature sizes on a scale of tens of nanometers over large areas. Recently, structures have been fabricated for applications in fields such as photonics,<sup>326, 327</sup> transparent metal electrodes,<sup>328</sup> solar cells,<sup>329</sup> and sensors,<sup>330</sup> to name a few. To fabricate the nanowalls structure, a typical thermal imprint process begins by placing a pre-patterned mold directly in contact with a resist-coated substrate. High temperature and pressure are then applied to reflow the resist into the mold, creating a mirror image of the pre-patterned features in the resist. Using these features to create a mask, we can then transfer nano-scale patterns into Si and create high aspect-ratio Si nanostructures with depths in the micron range. This is done with deep reactive ion etching (DRIE), specifically utilizing a cycled "Bosch" process, which has been used in the past to create nanostructures with aspect ratios greater than 50:1.<sup>331</sup> The NIL process is illustrated in Figure 9.1.

As shown in Figure 9.1 each Si nanowall is 900 nm high, 600 nm long and 50 nm thick. Perpendicular to the wall surface, the structure has a 220nm period, with a space of 170 nm between each wall. Lengthwise, the periodicity is 700 nm with 100 nm spacing between walls. A discontinuous nanowalls pattern rather than a continuous grating is proposed here to allow each nanowall to "breathe", relaxing the stress resulting from lithiation/delithiation induced volume expansion/contraction.

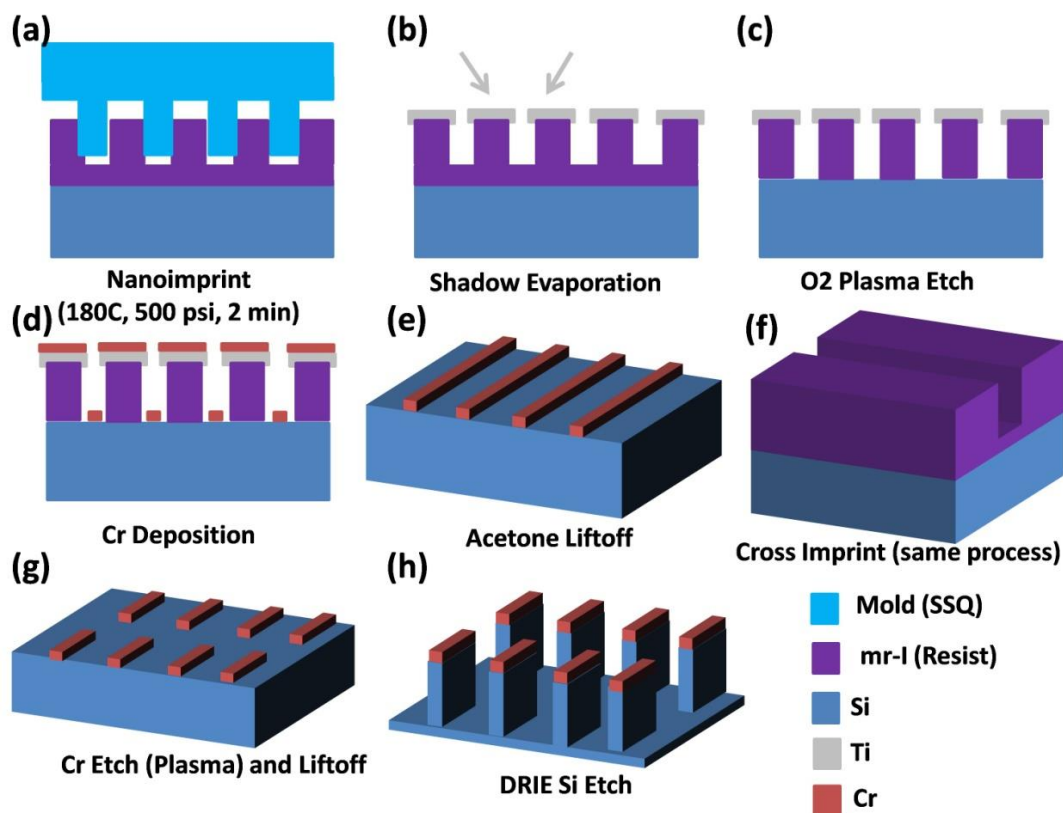


Figure 9.1 Outline of NIL process for Si nanowalls anode on an SS substrate (the SS substrate is not shown in this figure)

We characterized the morphology and composition of the prepared Si nanowalls structure with a scanning electron microscope (SEM) equipped with a Bruker EDS detector. The highly uniform size and lateral distribution of the Si nanowalls array is shown in Figure 9.2a. In Figure 9.2b (top view), the length and thickness of the nanowalls are measured to be about 600 nm and 50 nm, respectively. The space in between the nanowalls is designed to accommodate volume expansion during charge/discharge. Figure 9.2c show the EDS mapping image of the Si nanowalls. From Figure 9.2b and 9.2c we observed some edge roughness associate with nanowalls. This edge roughness is generated during fabrication due to the roughness of the shadow

evaporation, which masks the Cr deposition. There is also so-called "scalloping" which occurs during the DRIE Bosch process on the sidewalls of the nanostructure. Figure 9.2d shows the EDS analysis of one prepared Si nanowalls sample. We confirmed our composition of the whole electrode by Figure 9.2d, showing three elements of Si, Fe and Cr which correspond to nanowalls, the substrate and binding layer (also residual Cr mask), respectively.

The top down nanoimprint technique ensures that Si nanowalls are in direct electronic contact with the current collector, have a suitable specific surface area that allows for fast charge/discharge, while reduce the amount of SEI formation thus contributes to a low first CE. The small thickness of the nanowalls (50 nm in our experiment) allows for a short diffusion path of Li ions, increasing the potential for high power applications. The spacing between the nanowalls on four sides helps avoid the nanowalls touching each other during volume expansion, allowing a stable cycling performance of the nanowalls electrodes.

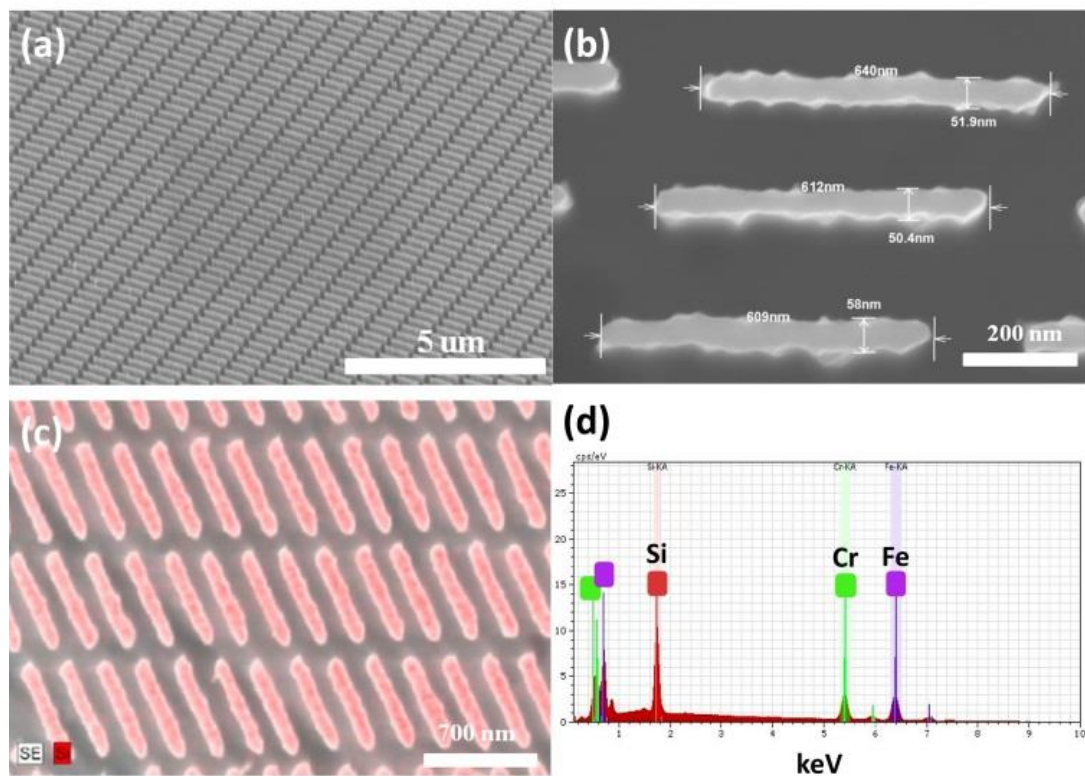


Figure 9.2. (a) SEM images of a large area and uniformly distributed Si nanowalls structures, (b) SEM image which shows the dimensions of the Si nanowalls (c). SEM EDS mapping images of Si nanowalls, (d) Energy dispersed X-ray spectroscopy of Si nanowalls/substrate, with peaks of Si, Cr and Fe.

### 9.3 Electrochemical properties of Si nanowalls in Li half cell

After fabrication, the samples were dried in a 100 °C vacuum oven overnight and then directly assembled into coin cells in an Ar filled glovebox. Electrochemical measurements were performed using a Biologic VMP3 electrochemical workstation, the cycling performance and electrochemical impedance spectroscopy (EIS) results are presented in Figure 9.3. Figure 9.3a shows the cycling performance and Coulombic

efficiency of the Si nanowalls at the rate of 840 mA/g for 40 cycles. The first charge and discharge capacity of the Si nanowalls is 2350 mAh/g and 1961 mAh/g, respectively, corresponding to a first CE of 83.4%. This initial CE of the Si nanowalls anodes still have room for improvement by optimize the design and fabrications of nanowalls or surface modification.<sup>332-334</sup> The Si nanowalls anode demonstrates stable cycling performance, retaining a discharge capacity of 1801mAh/g after 40 cycles, 90% of the initial value. The capacity retention is highlighted in Figure 9.3b, which plots the charge and discharge voltage profiles of the 1st, 10th, 20th and 40th cycles. The capacity suffers almost no losses during the first twenty cycles. The typical voltage profile of amorphous Si (a-Si) is seen, when lithiation of a-Si at approximately 0.49V vs. Li/Li<sup>+</sup>.<sup>10</sup> Figure 9.3c shows the EIS data of the Si nanowalls half cells. Both EIS data before and after cycling were taken at the fully delithiated state. The EIS results before cycling and after 40 cycles are shown by the blue and red curves, respectively. Bulk resistance of the cell is equal to the first intersection of the EIS curve with the real impedance axis. From the inset, we observed that the initial high-frequency resistance of 8 ohms (before cycling test) increases to 10 ohms after 40 cycles, indicating the formation of an SEI layer. The diameter of the semicircle represents the charge transfer resistance ( $R_{ct}$ ) of the cell. We observed that the charge transfer resistance of the Si nanowalls half cell decreases after cycling. Examination of the nanowalls structures after cycling in SEM helps to explain this phenomenon (Figure 9.4). After 40 cycles, the individual nanowalls have become more porous (Figure 9.4b). As the cycling progresses, the increasing porosity of the Si exposes more surface area to the electrolyte, increasing the charge transfer process and reducing  $R_{ct}$ . This is confirmed by the rate performance data in Figure 9.3d.

To determine the rate performance, the half cells were cycled at charge/discharge rates ranging from C/5 to 2C. Charging at higher rates reduces the capacity of batteries as the Li insertion reaction is limited by diffusion and reaction at interface. The formation of a porous structure during cycling increased the surface area of the electrode, resulting in an increasing capacity of the high rate cycles. Comparing the capacity of 1C battery at cycles 15-25 and 35-45 shows an increase of 200mAh/g for later cycles. The capacity of the battery at 2C is about 1000 mAh/g, 3 times higher than the capacity of conventional graphite electrodes.

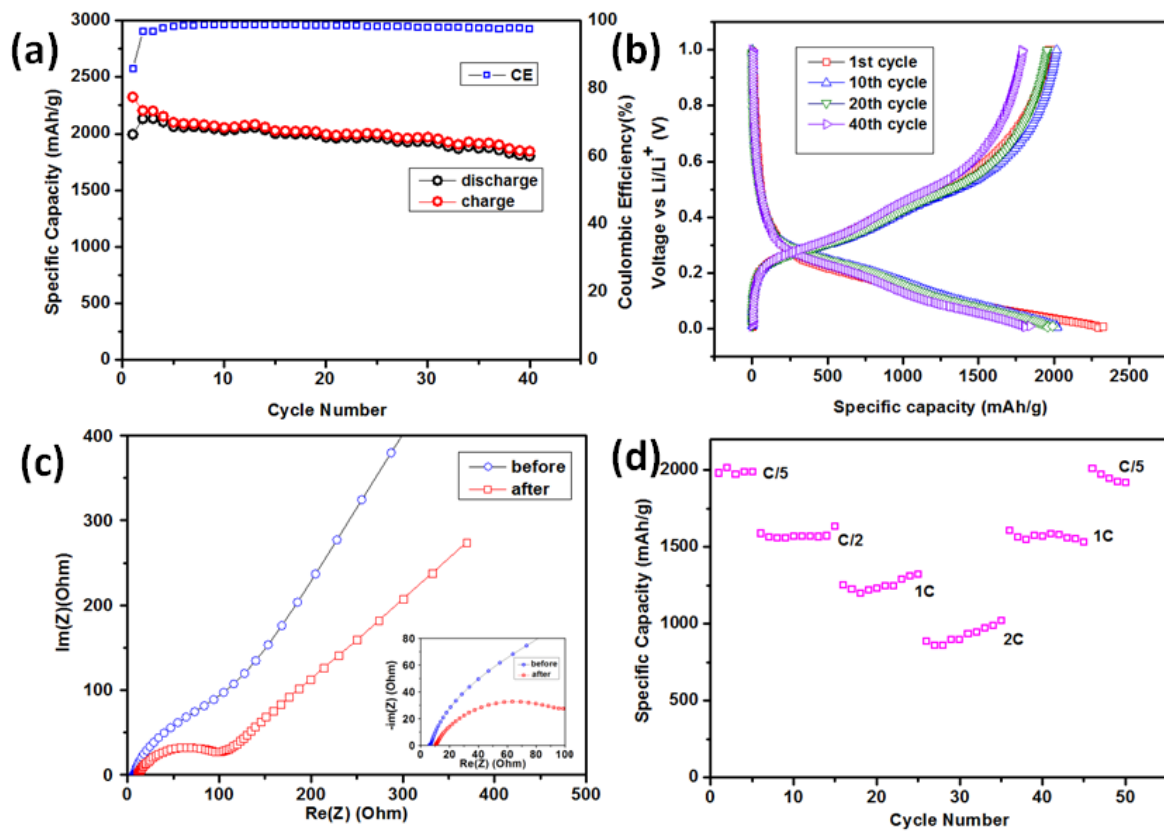


Figure 9.3 (a). Electrochemical cycling performance of Si nanowalls anodes (b) Voltage profile of 1st, 10th, 20th and 40th cycle of the Si nanowalls (c) EIS plot of the battery

before cycling (blue) and after 40 cycles (red) (d) The rate performance of the Si nanowalls half cell.

The half cells were disassembled in a glovebox in the delithiated state, and the residual electrolyte and SEI were washed away to expose the Si nanowalls. The morphology of the electrode was examined by SEM as shown in Figure 9.4. From Figure 9.4a we see that the Si nanowalls retain their wall structure and remain attached to the substrate, indicating good structural stability and binding. The cracked surface on top of nanowalls is a residual layer of Cr left over from the nanowalls fabrication. The cracking and distortion of this layer suggests large volume changes and stresses during cycling. The space between each nanowall is largely reduced, indicating a significant volume change of the Si nanowalls structure by lithiation. Figure 9.4b shows the porous structure of the Si nanowalls after cycling. Both of the sides and the top of the nanowall have become porous. We also observed a slight twisting of the nanowalls after 40 cycles in both Figure 9.4a and 9.4b. Overall, Si nanowalls can withstand significant volume changes associated with lithiation and delithiation. A higher magnification image of the porous structure on Si sidewall is shown in Figure 9.4c. It seems from this image that the porous structure formed many nano-channels in the Si sidewalls, allowing  $\text{Li}^+$  ions diffuse faster inside. However, during the formation of the porous structure, active material will detach from the walls, resulting in a slight capacity reduction.

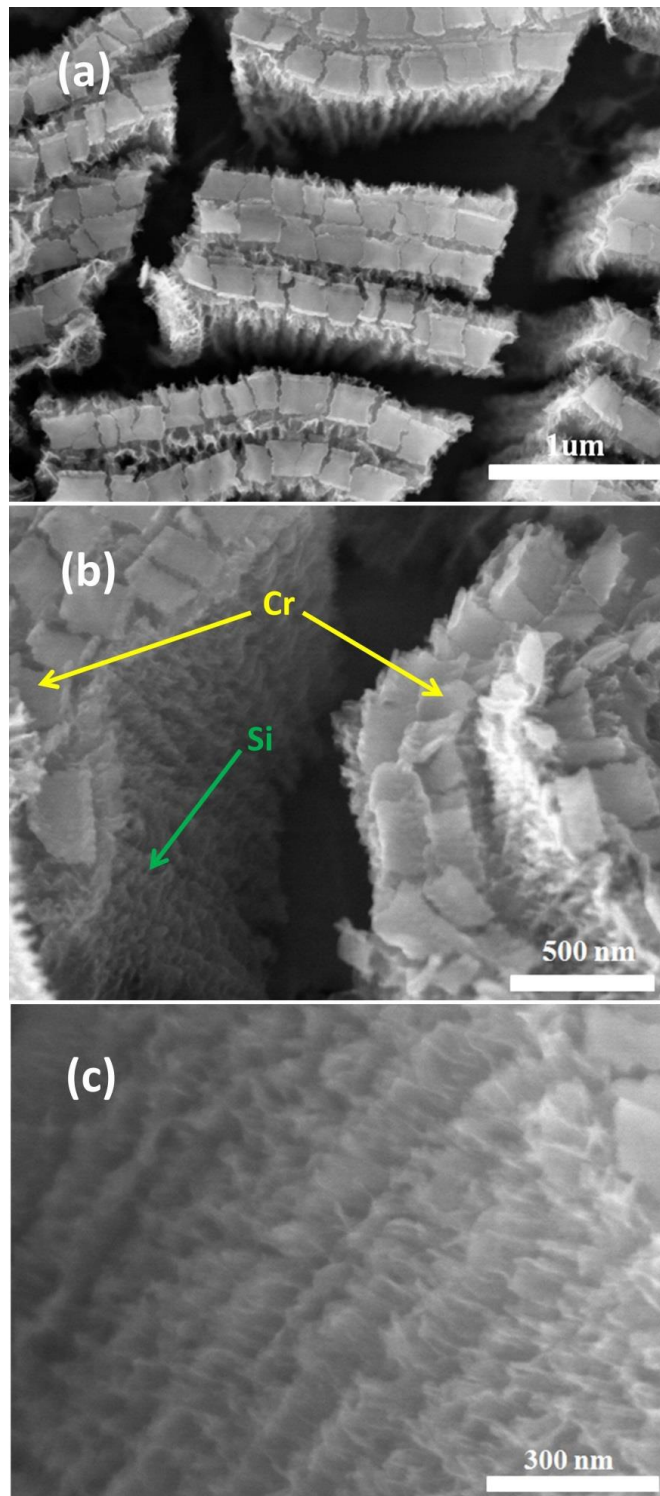


Figure 9.4 (a) and (b) SEM images at different magnifications of the Si nanowalls anode after cycling. A residual Cr layer from the mask is observed on top of the nanowalls. (c)

High magnification SEM of Si nanowalls after cycling shows porous structure with an average pore size of ~30 nm.

#### 9.4 Nanopore formation mechanism by modeling

As shown in Figure 9.4a and 9.4b the nanowalls structure thickens and develops a very rough surface morphology after 40 cycles, indicating pore formation at both the surface and the interior of the nanowalls. The formation of such a porous structure is attributed to the hydrostatic tensile stress in the nanowalls induced by lithiation and delithiation, as revealed by the following mechanics modelling. The size of the nanowalls in the modelling are 600 nm×50 nm×900nm (L×W×D) for each. During lithiation and delithiation, Li ions insert into and extract from the nanowalls, inducing large cyclic deformation of the Si. As to be shown later, the stress associate with the large deformation in the nanowalls is highly non-uniform (e.g., stress level varies with positions in the nanowalls) and tri-axial. If the Li concentration is sufficiently large, the associated stress can be high enough to cause the plastic flow of the lithiated Si. A cavity in a solid can unstably grow in size by atom diffusion away from the cavity surface driven by sufficiently high hydrostatic stress (defined as the mean stress  $\sigma_m = \frac{\sigma_{11} + \sigma_{22} + \sigma_{33}}{3}$ ). Therefore, if the lithiation/delithiation-induced mean stress in the Si is high enough, defects in the nanowalls (e.g., voids) could grow unstably, leading to a porous structure. The underlying energetics can be explained by a simple model. The free energy of a lithiated Si with an incipient spherical void of radius R under a mean stress  $\sigma_m$  applied to the void is given by  $G(R) = 4\pi R^2\gamma - \frac{4}{3}\pi R^3\sigma_m$ , where  $\gamma$  is the surface

energy of lithiated silicon. Under the lithiation/delithiation-induced stresses, the incipient void tends to grow or shrink to minimize the free energy  $G$ , from which one determines a critical void size  $R_c = 2\gamma/\sigma_m$ . That is, a void with  $R < R_c$  shrinks and thus may heal spontaneously while a void with  $R > R_c$  unstably grows into a pore of large size. Next, we calculated the lithiation/delithiation-induced stresses in the Si nanowalls, so that the critical void size in different regions of the nanowalls can be estimated, which in turn help decipher the formation of the porous structure after lithiation/delithiation cycles as observed in the experiments.

We simulated the concurrent Li diffusion and mechanical deformation during the initial lithiation and following delithiation of the amorphous Si nanowalls using finite element package ABAQUS 6.10. The extent of lithiation is described by the average Li/Si atomic ratio  $x_{\text{average}}$ , defined as the ratio of Li atoms in the nanowalls. For example,  $x_{\text{average}} = 1$  means that on average one Si atom takes one Li atom in the nanowalls. We assume the extent of volume expansion has a linear relationship with lithium content in  $\text{Li}_x\text{Si}$ .<sup>335, 336</sup> From our experiment,  $x_{\text{average}}$  reaches 2 at the end of the lithiation cycle, resulting in a 200% volume expansion of the nanowalls. Simulation results reveal that the mean stress level in the nanowalls increases with the extent of lithiation and nearly saturates as  $x_{\text{average}}$  approaches 1. The distribution of the mean stress at two representative planes of the nanowalls, i.e., the mid-plane ( $z = 0$ ) and the outer surface ( $z = h/2$ , where  $h$  is the nanowalls thickness), are shown in **Figure 9.5b** and **9.5c**, respectively. Here  $x_{\text{average}} = 1$ . The regions labelled by A through G undergo a significant tensile mean stress ranging from 150 to 600 MPa. As mentioned above, the tensile mean stress state acts as the driving force for the nucleation and growth of nano-

pores. For example, during lithiation nano-pore formation is likely to occur in the middle part of nanowalls (regions A, B and E) and near the bottom corners (regions C, D, F and G).

Moreover, simulation results show that during lithiation the area under significant tensile mean stress at the mid-plane of the nanowalls (regions A to D shown in Figure 9.5b) is much larger than that at the outer surface (regions E to G shown in Figure 9.5c). The mean stress level at the mid-plane is also even higher than that at the outer surface, indicating that the interior of nanowalls is more susceptible to pore formation during lithiation.

In the following delithiation half cycle shown in Figures 9.5d and 9.5e, the regions experiencing a significant tensile mean stress of 150MPa to 1GPa are labelled by a through k. Comparison between the mean stress distributions at the mid-plane and outer surface reveals that, during delithiation, pores are more likely to nucleate and grow near the nanowalls outer surface, opposite to the trend during the lithiation half cycle. It is interesting to note that the associated mean stress distribution is reversed with the transition from lithiation to delithiation: those regions initially under tensile mean stress are now mainly under compression and vice versa. This trend is clearly shown in Figure 9.5d and 9.5e. The regions labelled by a through k are geometrically complementary to those hydrostatically tensile regions denoted by A through G in Figures 9.5b and 9.5d. Therefore, nearly all of the nanowalls experience a significant tensile mean stress at a certain stage during a lithiation/delithiation cycle. As a result, pores are likely to form throughout the entire nanowalls after many cycles. This prediction is confirmed by the

experimentally-observed homogeneous pore distribution in the nanowalls structures observed in experiments (Figure 9.4).

The simulation results of significant tensile mean stress in the nanowalls can be used to derive the critical void size  $R_c$  for pore formation. For simplicity, we assume the surface energy  $\gamma$  of lithiated silicon is independent of lithium concentration with a value of  $1 \text{ J/m}^2$ .<sup>21</sup> The critical radii in all regions range from 2nm~13.3nm. Such an estimate agrees with experimental observation: the radii of the pores in the nanowalls after 40 lithiation/delithiation cycles are much greater than 13.3nm (Figure 9.4c), indicating that voids greater than the critical size grow into larger pores under significant tensile mean stress.

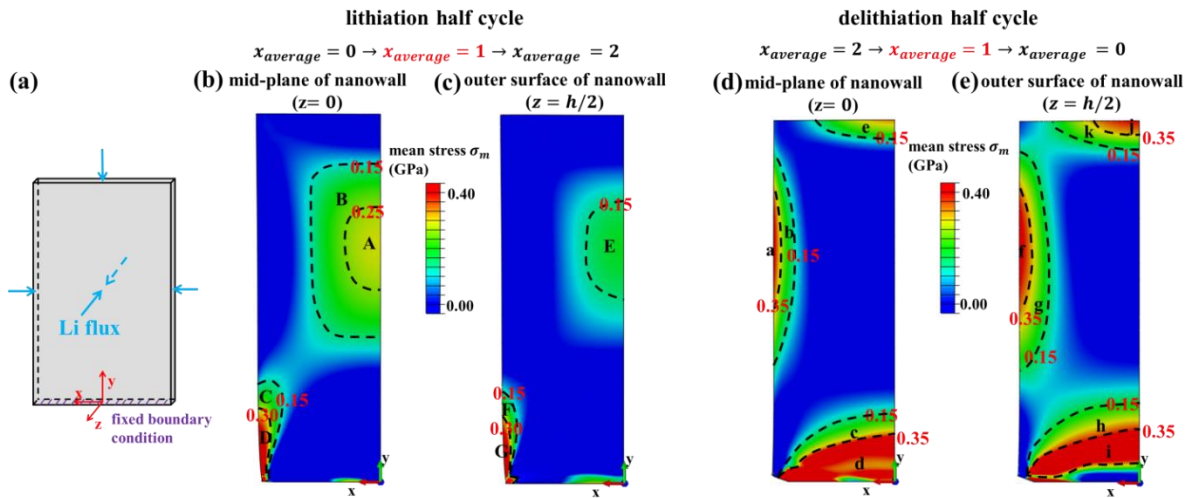


Figure 9.5 Lithiation/delithiation-induced mean stresses in the nanowalls. (a) Schematic of the simulation model. The origin of the coordinate system is defined with origin at the centroid of the bottom surface. (b) and (c) show the mean stress distribution within the mid-plane of the nanowalls ( $z = 0$ ) and outer surface of nanowalls ( $z = h/2$ ) during the

lithiation half cycle, respectively, with extent of lithiation described by  $x_{\text{average}} = 1$ . (d) and (e) are the counterparts of (b) and (c) during delithiation half cycle, respectively.

## 9.5 Summary

In conclusion, we designed a novel 2-D a-Si nanowalls structure as an anode for Li ion batteries that exhibits excellent electrochemical properties. The lower specific surface area of the nanowalls structure compared to 1-D/0-D nanostructures leads to a relatively high first CE. A high specific capacity of ~2100 mAh/g is obtained at C/5 and remains stable for over 40 cycles. Porous structures form throughout the nanowalls after cycles, which is attributed to the complementary distributions of the tensile mean stress in the nanowalls induced by lithiation and delithiation. The cycling performance of proof-of-concept devices can be further improved with improving the uniformity and bonding between Si nanowalls and the substrate. It is anticipated based on the mechanical modelling that the nanowall anodes can be excellent candidate for flexibility energy devices. Such nanostructures can potentially lead to many other applications including solar, water splitting and others, where both a nanoscale structure to manipulate electrons and photons and a low surface area to avoid side reaction and recombination are needed.

## Chapter 10: Conclusion

### 10.1 Conclusion

In summary, this work presents a novel approach that drastically modulates the properties of 2D materials. By using planar nanobatteries as platform, we successfully intercalate Li-ions into few layered graphene single crystalline, achieved the highest doping to modulate graphene. Through intercalation, we simultaneously increased the transmittance and dc conductivity of FLG, achieved the highest reported performance of continuous thin film transparent conductors with transmittance of 91.7% and sheet resistance of 3  $\Omega$ /sq. The ion intercalation method is then applied to large scale graphitic thin films such as CVD graphene and printed rGO network. We successfully achieved uniform, large area, ion intercalated CVD graphene and rGO network, with simultaneous increased optical transmittance and dc conductivity.

Other than Li-ions, potentially resourceful Na-ions has also been successfully intercalate in large scale rGO network. The Na-ion intercalated rGO network achieved the highest transparent electrode performance of 79%, 311  $\Omega$ /sq. Still, pure rGO network cannot achieve reversible ion intercalation/deintercalation because of the rGO flakes are easy to detach, lead to the crack of rGO film at the 1<sup>st</sup> cycle. We designed a CNT/rGO/CNT sandwich thin film, not only achieved its reversible modulation *via* ion intercalation, but also demonstrate its broadband responsivity from mid infrared to visible range. We also did the *in situ* TEM study of the electrochemical Na-ion interaction with rGO negative electrodes, proposed and verified Na storage mechanism with rGO

electrodes. Ultrahigh specific capacity of 450 mAh/g is achieved with our rGO negative electrodes.

Other 2D materials such as MoS<sub>2</sub> are also studied with planar nano-batteries. We demonstrate for the first time that the resistance of battery electrode materials can be measured *in situ* and real time. We demonstrated that the rapid lithiation in the first cycle of MoS<sub>2</sub> electrode would largely increase its conductivity, leads to a much better specific capacity and rate performance. We also demonstrate that 2D Si nanowall structure leads to a high first CE and stable cycling performance as negative electrode in Li-ion batteries.

## **10.2 Future Work**

### 10.2.1 Improve the air stability of the ion intercalated film for optoelectronic devices

Ion intercalated graphitic transparent conductors exhibit extraordinary optoelectronic properties, however, the air stability remains a problem for the intercalated films. The intercalated alkaline ions are likely to react with water and oxygen in the air, which limit the practical application of the intercalated films. Thus, the air stability of the ion intercalated film needs to be improved. Possible solutions to achieve air stable ion intercalated graphitic thin film is that: (1). use thin polymer coating (2). Use other CVD 2D materials (i.e. graphene, BN) coating on top of the intercalated film, to prevent the air from contact with intercalated film. Improving the surface roughness of the intercalated films is also needed in order to integrate them as high performance electronic devices such as OLED.

10.2.2 Investigate novel physical and chemical properties of a variety of 2D materials by intercalation

Table 10.1 summarizes the state-of-the-art research of intercalated 2D materials. In fact, a variety of 2D materials and species remain unexplored. Future investigations of tunable intercalated 2D materials rely on rational designs of the host materials and intercalation species, hybrid systems (i.e. hybrid 2D materials, co-intercalation), *in situ* experimental platforms or investigating unexplored properties (e.g. mechanical properties) in intercalated 2D systems. Further advances in engineering scalable, reproducible intercalated 2D materials for use in practical applications are also needed. With the advances in high-quality, scalable, cost-efficient 2D material preparation methods, intercalation modified 2D materials will receive even more research in the future.

Materials types	Graphene family	Metal Dichalcogenides (MX <sub>2</sub> )	Other Chalcogenides (MX, M <sub>2</sub> X <sub>3</sub> )	Layered Oxides
<b>2D materials (Properties)</b>	Graphene, rGO (Semimetal)	MoS <sub>2</sub> , WS <sub>2</sub> , TiS <sub>2</sub> (Semiconductors); TaS <sub>2</sub> , NbSe <sub>2</sub> (metals); TiSe <sub>2</sub> (Semimetal)	Bi <sub>2</sub> Se <sub>3</sub> , Sb <sub>2</sub> Te <sub>3</sub> ; (Topological insulators) In <sub>2</sub> Se <sub>3</sub> (Semimetal) GaSe (Semiconductor) FeSe (metal)	LiCoO <sub>2</sub> , MoO <sub>3</sub> ; (Insulators)
<b>Intercalation species/products</b>	Ions (Li <sup>+</sup> , Na <sup>+</sup> , K <sup>+</sup> , Ca <sup>2+</sup> , PF <sub>6</sub> <sup>-</sup> , ClO <sub>4</sub> <sup>-</sup> , etc.) Inorganic (Br <sub>2</sub> , FeCl <sub>3</sub> , etc.)	Ions (Li <sup>+</sup> , Na <sup>+</sup> , Mg <sup>2+</sup> ) Organic molecules; Zero-valent metal (Cu) Phase change	Zero-valent metals (Cu, Sn, Co, Ag etc.) Organic molecules; Co-intercalants	Zero-valent metals (Cu, Sn, Co etc.) Ions (Li <sup>+</sup> )
<b>Methods</b>	Electrochemical, Wet Chemical, Chemical Vapor Transport			
<b>Tuning Properties/Applications</b>	Electric, Optic, Optoelectronic, Magnetic	Electric (Superconductor, CDW), Optic, Catalytic, Thermoelectric, magnetic	Electric (Superconductor), Optic, Optoelectronic	Thermal, Catalytic Optic, chemochromic

10.2.3 Real time and *in situ* investigate the properties of battery materials during ion insertion/desertion.

To date, *in situ* TEM has been widely known and applied to study the properties of electrode materials during ion (Li-ion, Na-ion) insertion/deinsertion, and greatly improved the understanding of mechanisms in battery electrode reactions. The advantages of *in situ* TEM are that it provides structural information from materials point of view, and it can observe material changes in atomic scale. Still, to fully understand the electrochemical process in an electrode material while cycling, such as resistance change, compensate characterization methods are needed. As we learned from the previous sections, planar (nano) batteries not only enables *in situ* and real time resistance measurement of a single crystallite electrode material, but also enables *in situ* and real time Raman characterizations, and *in situ* AFM characterizations.<sup>337, 338</sup> Plus, planar batteries are designed for liquid electrolytes, which is the same environment with real batteries. Thus, a great promise lies in the future works to observe the changes of novel electrode materials with planar batteries.

## Bibliography / References

1. A. K. Geim, *Science*, 2009, **324**, 1530-1534.
2. A. K. Geim and I. V. Grigorieva, *Nature*, 2013, **499**, 419-425.
3. K. S. Novoselov, A. K. Geim, S. V. Morozov, D. Jiang, Y. Zhang, S. V. Dubonos, I. V. Grigorieva and A. A. Firsov, *Science*, 2004, **306**, 666-669.
4. K. S. Novoselov, D. Jiang, F. Schedin, T. J. Booth, V. V. Khotkevich, S. V. Morozov and A. K. Geim, *Proceedings of the National Academy of Sciences of the United States of America*, 2005, **102**, 10451-10453.
5. S. Z. Butler, S. M. Hollen, L. Y. Cao, Y. Cui, J. A. Gupta, H. R. Gutierrez, T. F. Heinz, S. S. Hong, J. X. Huang, A. F. Ismach, E. Johnston-Halperin, M. Kuno, V. V. Plashnitsa, R. D. Robinson, R. S. Ruoff, S. Salahuddin, J. Shan, L. Shi, M. G. Spencer, M. Terrones, W. Windl and J. E. Goldberger, *Acs Nano*, 2013, **7**, 2898-2926.
6. D. Deng, K. S. Novoselov, Q. Fu, N. Zheng, Z. Tian and X. Bao, *Nat Nano*, 2016, **11**, 218-230.
7. P. Miro, M. Audiffred and T. Heine, *Chemical Society Reviews*, 2014, **43**, 6537-6554.
8. A. H. Castro Neto, F. Guinea, N. M. R. Peres, K. S. Novoselov and A. K. Geim, *Reviews of Modern Physics*, 2009, **81**, 109-162.
9. M. Chhowalla, H. S. Shin, G. Eda, L. J. Li, K. P. Loh and H. Zhang, *Nature Chemistry*, 2013, **5**, 263-275.
10. H. J. Conley, B. Wang, J. I. Ziegler, R. F. Haglund, Jr., S. T. Pantelides and K. I. Bolotin, *Nano Letters*, 2013, **13**, 3626-3630.
11. K. F. Mak, C. Lee, J. Hone, J. Shan and T. F. Heinz, *Physical Review Letters*, 2010, **105**.
12. A. Splendiani, L. Sun, Y. Zhang, T. Li, J. Kim, C.-Y. Chim, G. Galli and F. Wang, *Nano Letters*, 2010, **10**, 1271-1275.
13. R. Kappera, D. Voiry, S. E. Yalcin, B. Branch, G. Gupta, A. D. Mohite and M. Chhowalla, *Nature Materials*, 2014, **13**, 1128-1134.
14. F. Bonaccorso, Z. Sun, T. Hasan and A. C. Ferrari, *Nat Photon*, 2010, **4**, 12.
15. Q. H. Wang, K. Kalantar-Zadeh, A. Kis, J. N. Coleman and M. S. Strano, *Nature Nanotechnology*, 2012, **7**, 699-712.
16. J.-F. Ge, Z.-L. Liu, C. Liu, C.-L. Gao, D. Qian, Q.-K. Xue, Y. Liu and J.-F. Jia, *Nature Materials*, 2015, **14**, 285-289.
17. A. N. Grigorenko, M. Polini and K. S. Novoselov, *Nature Photonics*, 2012, **6**, 749-758.
18. W. Wu, L. Wang, Y. Li, F. Zhang, L. Lin, S. Niu, D. Chenet, X. Zhang, Y. Hao, T. F. Heinz, J. Hone and Z. L. Wang, *Nature*, 2014, **514**, 470-+.
19. D. Chen, L. Tang and J. Li, *Chemical Society Reviews*, 2010, **39**, 3157-3180.
20. R. Raccichini, A. Varzi, S. Passerini and B. Scrosati, *Nature materials*, 2015, **14**, 271-279.
21. C. H. Xu, B. H. Xu, Y. Gu, Z. G. Xiong, J. Sun and X. S. Zhao, *Energy & Environmental Science*, 2013, **6**, 1388-1414.

22. S. Bae, H. Kim, Y. Lee, X. Xu, J.-S. Park, Y. Zheng, J. Balakrishnan, T. Lei, H. Ri Kim, Y. I. Song, Y.-J. Kim, K. S. Kim, B. Ozyilmaz, J.-H. Ahn, B. H. Hong and S. Iijima, *Nat Nano*, 2010, **5**, 574-578.
23. M. Chhowalla, H. S. Shin, G. Eda, L.-J. Li, K. P. Loh and H. Zhang, *Nature Chemistry*, 2013, **5**, 263-275.
24. J. Y. Wan, W. Z. Bao, Y. Liu, J. Q. Dai, F. Shen, L. H. Zhou, X. H. Cai, D. Urban, Y. Y. Li, K. Jungjohann, M. S. Fuhrer and L. B. Hu, *Advanced Energy Materials*, 2015, **5**, 7.
25. S. D. Lacey, J. Y. Wan, A. V. Cresce, S. M. Russell, J. Q. Dai, W. Z. Bao, K. Xu and L. B. Hu, *Nano Letters*, 2015, **15**, 1018-1024.
26. M. Z. Cai, D. Thorpe, D. H. Adamson and H. C. Schniepp, *Journal of Materials Chemistry*, 2012, **22**, 24992-25002.
27. X. S. Li, W. W. Cai, J. H. An, S. Kim, J. Nah, D. X. Yang, R. Piner, A. Velamakanni, I. Jung, E. Tutuc, S. K. Banerjee, L. Colombo and R. S. Ruoff, *Science*, 2009, **324**, 1312-1314.
28. S. Bae, H. Kim, Y. Lee, X. F. Xu, J. S. Park, Y. Zheng, J. Balakrishnan, T. Lei, H. R. Kim, Y. I. Song, Y. J. Kim, K. S. Kim, B. Ozyilmaz, J. H. Ahn, B. H. Hong and S. Iijima, *Nature Nanotechnology*, 2010, **5**, 574-578.
29. X. S. Li, C. W. Magnuson, A. Venugopal, R. M. Tromp, J. B. Hannon, E. M. Vogel, L. Colombo and R. S. Ruoff, *Journal of the American Chemical Society*, 2011, **133**, 2816-2819.
30. Y. Gao, W. C. Ren, T. Ma, Z. B. Liu, Y. Zhang, W. B. Liu, L. P. Ma, X. L. Ma and H. M. Cheng, *Acs Nano*, 2013, **7**, 5199-5206.
31. J. H. Park, J. C. Park, S. J. Yun, H. Kim, D. H. Luong, S. M. Kim, S. H. Choi, W. Yang, J. Kong, K. K. Kim and Y. H. Lee, *Acs Nano*, 2014, **8**, 8520-8528.
32. Y. H. Lee, X. Q. Zhang, W. J. Zhang, M. T. Chang, C. T. Lin, K. D. Chang, Y. C. Yu, J. T. W. Wang, C. S. Chang, L. J. Li and T. W. Lin, *Advanced Materials*, 2012, **24**, 2320-2325.
33. A. M. van der Zande, P. Y. Huang, D. A. Chenet, T. C. Berkelbach, Y. M. You, G. H. Lee, T. F. Heinz, D. R. Reichman, D. A. Muller and J. C. Hone, *Nature Materials*, 2013, **12**, 554-561.
34. Y. J. Zhan, Z. Liu, S. Najmaei, P. M. Ajayan and J. Lou, *Small*, 2012, **8**, 966-971.
35. X. S. Li, C. W. Magnuson, A. Venugopal, J. H. An, J. W. Suk, B. Y. Han, M. Borysiak, W. W. Cai, A. Velamakanni, Y. W. Zhu, L. F. Fu, E. M. Vogel, E. Voelkl, L. Colombo and R. S. Ruoff, *Nano Letters*, 2010, **10**, 4328-4334.
36. C. Mattevi, H. Kim and M. Chhowalla, *Journal of Materials Chemistry*, 2011, **21**, 3324-3334.
37. J. W. Suk, A. Kitt, C. W. Magnuson, Y. F. Hao, S. Ahmed, J. H. An, A. K. Swan, B. B. Goldberg and R. S. Ruoff, *Acs Nano*, 2011, **5**, 6916-6924.
38. G. Deokar, J. Avila, I. Razado-Colambo, J. L. Codron, C. Boyaval, E. Galopin, M. C. Asensio and D. Vignaud, *Carbon*, 2015, **89**, 82-92.
39. A. Reina, X. T. Jia, J. Ho, D. Nezich, H. B. Son, V. Bulovic, M. S. Dresselhaus and J. Kong, *Nano Letters*, 2009, **9**, 30-35.
40. J. N. Coleman, M. Lotya, A. O'Neill, S. D. Bergin, P. J. King, U. Khan, K. Young, A. Gaucher, S. De, R. J. Smith, I. V. Shvets, S. K. Arora, G. Stanton, H. Y. Kim, K. Lee, G. T. Kim, G. S. Duesberg, T. Hallam, J. J. Boland, J. J. Wang, J. F.

- Donegan, J. C. Grunlan, G. Moriarty, A. Shmeliov, R. J. Nicholls, J. M. Perkins, E. M. Grieverson, K. Theuwissen, D. W. McComb, P. D. Nellist and V. Nicolosi, *Science*, 2011, **331**, 568-571.
41. Y. Hernandez, V. Nicolosi, M. Lotya, F. M. Blighe, Z. Y. Sun, S. De, I. T. McGovern, B. Holland, M. Byrne, Y. K. Gun'ko, J. J. Boland, P. Niraj, G. Duesberg, S. Krishnamurthy, R. Goodhue, J. Hutchison, V. Scardaci, A. C. Ferrari and J. N. Coleman, *Nature Nanotechnology*, 2008, **3**, 563-568.
  42. U. Khan, A. O'Neill, M. Lotya, S. De and J. N. Coleman, *Small*, 2010, **6**, 864-871.
  43. V. Nicolosi, M. Chhowalla, M. G. Kanatzidis, M. S. Strano and J. N. Coleman, *Science*, 2013, **340**, 1420-+.
  44. A. O'Neill, U. Khan, P. N. Nirmalraj, J. Boland and J. N. Coleman, *Journal of Physical Chemistry C*, 2011, **115**, 5422-5428.
  45. K. R. Paton, E. Varrla, C. Backes, R. J. Smith, U. Khan, A. O'Neill, C. Boland, M. Lotya, O. M. Istrate, P. King, T. Higgins, S. Barwich, P. May, P. Puczkarski, I. Ahmed, M. Moebius, H. Pettersson, E. Long, J. Coelho, S. E. O'Brien, E. K. McGuire, B. M. Sanchez, G. S. Duesberg, N. McEvoy, T. J. Pennycook, C. Downing, A. Crossley, V. Nicolosi and J. N. Coleman, *Nature Materials*, 2014, **13**, 624-630.
  46. X. X. Liu, J. L. Liu, D. Zhan, J. X. Yan, J. Wang, D. L. Chao, L. F. Lai, M. H. Chen, J. H. Yin and Z. X. Shen, *Rsc Advances*, 2013, **3**, 11601-11606.
  47. K. G. Zhou, N. N. Mao, H. X. Wang, Y. Peng and H. L. Zhang, *Angewandte Chemie-International Edition*, 2011, **50**, 10839-10842.
  48. J. N. Coleman, *Accounts of Chemical Research*, 2013, **46**, 14-22.
  49. C. Y. Zhi, Y. Bando, C. C. Tang, H. Kuwahara and D. Golberg, *Advanced Materials*, 2009, **21**, 2889-+.
  50. D. A. Dikin, S. Stankovich, E. J. Zimney, R. D. Piner, G. H. B. Dommett, G. Evmenenko, S. T. Nguyen and R. S. Ruoff, *Nature*, 2007, **448**, 457-460.
  51. A. O'Neill, U. Khan and J. N. Coleman, *Chemistry of Materials*, 2012, **24**, 2414-2421.
  52. C. J. Shih, A. Vijayaraghavan, R. Krishnan, R. Sharma, J. H. Han, M. H. Ham, Z. Jin, S. C. Lin, G. L. C. Paulus, N. F. Reuel, Q. H. Wang, D. Blankshtein and M. S. Strano, *Nature Nanotechnology*, 2011, **6**, 439-445.
  53. X. Huang, Z. Zeng and H. Zhang, *Chemical Society Reviews*, 2013, **42**, 1934-1946.
  54. S. Park and R. S. Ruoff, *Nature Nanotechnology*, 2009, **4**, 217-224.
  55. Q. Liu, X. L. Li, Z. R. Xiao, Y. Zhou, H. P. Chen, A. Khalil, T. Xiang, J. Q. Xu, W. S. Chu, X. J. Wu, J. L. Yang, C. M. Wang, Y. J. Xiong, C. H. Jin, P. M. Ajayan and L. Song, *Advanced Materials*, 2015, **27**, 4837-4844.
  56. G. Eda, H. Yamaguchi, D. Voiry, T. Fujita, M. W. Chen and M. Chhowalla, *Nano Letters*, 2011, **11**, 5111-5116.
  57. X. L. Li, X. R. Wang, L. Zhang, S. W. Lee and H. J. Dai, *Science*, 2008, **319**, 1229-1232.
  58. Y. Gong, J. Lin, X. Wang, G. Shi, S. Lei, Z. Lin, X. Zou, G. Ye, R. Vajtai, B. I. Yakobson, H. Terrones, M. Terrones, B. K. Tay, J. Lou, S. T. Pantelides, Z. Liu, W. Zhou and P. M. Ajayan, *Nature Materials*, 2014, **13**, 1135-1142.

59. J. Zhao, Q. M. Deng, A. Bachmatiuk, G. Sandeep, A. Popov, J. Eckert and M. H. Rummeli, *Science*, 2014, **343**, 1228-1232.
60. J. Kang, S. Tongay, J. Li and J. Wu, *Journal of Applied Physics*, 2013, **113**.
61. W. Bao, J. Wan, X. Han, X. Cai, H. Zhu, D. Kim, D. Ma, Y. Xu, J. N. Munday, H. D. Drew, M. S. Fuhrer and L. Hu, *Nature communications*, 2014, **5**, 4224-4224.
62. Y. Yu, F. Yang, X. F. Lu, Y. J. Yan, Y.-H. Cho, L. Ma, X. Niu, S. Kim, Y.-W. Son, D. Feng, S. Li, S.-W. Cheong, X. H. Chen and Y. Zhang, *Nature Nanotechnology*, 2015, **10**, 270-276.
63. F. Wang, Y. Zhang, C. Tian, C. Girit, A. Zettl, M. Crommie and Y. R. Shen, *Science*, 2008, **320**, 206-209.
64. Z. Q. H. Li, E. A. Jiang, Z. Hao, Z. Martin, M. C. Kim, P. Stormer, H. L. Basov, D. N., *Nat Phys*, 2008, **4**, 13.
65. W. Bao, L. Jing, J. Velasco, Jr., Y. Lee, G. Liu, D. Tran, B. Standley, M. Aykol, S. B. Cronin, D. Smirnov, M. Koshino, E. McCann, M. Bockrath and C. N. Lau, *Nature Physics*, 2011, **7**, 948-952.
66. J. Feng, X. Qian, C.-W. Huang and J. Li, *Nature Photonics*, 2012, **6**, 865-871.
67. M. S. Dresselhaus and G. Dresselhaus, *Advances in Physics*, 2002, **51**, 1-186.
68. E. Benavente, M. A. Santa Ana, F. Mendizabal and G. Gonzalez, *Coordination Chemistry Reviews*, 2002, **224**, 87-109.
69. H. Wang, Z. Lu, S. Xu, D. Kong, J. J. Cha, G. Zheng, P.-C. Hsu, K. Yan, D. Bradshaw, F. B. Prinz and Y. Cui, *Proceedings of the National Academy of Sciences of the United States of America*, 2013, **110**, 19701-19706.
70. T. H. Bointon, I. Khrapach, R. Yakimova, A. V. Shytov, M. F. Craciun and S. Russo, *Nano Letters*, 2014, **14**, 1751-1755.
71. K. J. Koski, C. D. Wessells, B. W. Reed, J. J. Cha, D. S. Kong and Y. Cui, *Journal of the American Chemical Society*, 2012, **134**, 13773-13779.
72. H. T. Yuan, H. T. Wang and Y. Cui, *Accounts of Chemical Research*, 2015, **48**, 81-90.
73. J. P. Motter, K. J. Koski and Y. Cui, *Chemistry of Materials*, 2014, **26**, 2313-2317.
74. A. Zak, Y. Feldman, V. Lyakhovitskaya, G. Leitus, R. Popovitz-Biro, E. Wachtel, H. Cohen, S. Reich and R. Tenne, *Journal of the American Chemical Society*, 2002, **124**, 4747-4758.
75. M. Sakamoto, J. S. Speck and M. S. Dresselhaus, *Journal of Materials Research*, 1986, **1**, 685-692.
76. D. Zhan, L. Sun, Z. H. Ni, L. Liu, X. F. Fan, Y. Y. Wang, T. Yu, Y. M. Lam, W. Huang and Z. X. Shen, *Advanced Functional Materials*, 2010, **20**, 3504-3509.
77. W. J. Zhao, P. H. Tan, J. Liu and A. C. Ferrari, *Journal of the American Chemical Society*, 2011, **133**, 5941-5946.
78. I. Khrapach, F. Withers, T. H. Bointon, D. K. Polyushkin, W. L. Barnes, S. Russo and M. F. Craciun, *Advanced Materials*, 2012, **24**, 2844-2849.
79. T. Ohzuku, Y. Iwakoshi and K. Sawai, *Journal of the Electrochemical Society*, 1993, **140**, 2490-2498.
80. J. A. Seel and J. R. Dahn, *Journal of the Electrochemical Society*, 2000, **147**, 892-898.
81. C. Y. Su, A. Y. Lu, Y. P. Xu, F. R. Chen, A. N. Khlobystov and L. J. Li, *Acs Nano*, 2011, **5**, 2332-2339.

82. C. Sole, N. E. Drewett, F. Liu, A. M. Abdelkader, I. A. Kinloch and L. J. Hardwick, *Journal of Electroanalytical Chemistry*, 2015, **753**, 35-41.
83. K. Parvez, Z. S. Wu, R. J. Li, X. J. Liu, R. Graf, X. L. Feng and K. Mullen, *Journal of the American Chemical Society*, 2014, **136**, 6083-6091.
84. C. T. J. Low, F. C. Walsh, M. H. Chakrabarti, M. A. Hashim and M. A. Hussain, *Carbon*, 2013, **54**, 1-21.
85. A. M. Abdelkader, I. A. Kinloch and R. A. W. Dryfe, *Acs Applied Materials & Interfaces*, 2014, **6**, 1632-1639.
86. N. Liu, P. Kim, J. H. Kim, J. H. Ye, S. Kim and C. J. Lee, *Acs Nano*, 2014, **8**, 6902-6910.
87. C. Wan, X. Gu, F. Dang, T. Itoh, Y. Wang, H. Sasaki, M. Kondo, K. Koga, K. Yabuki, G. J. Snyder, R. Yang and K. Koumoto, *Nature Materials*, 2015, **14**, 622-627.
88. J. T. Ye, Y. J. Zhang, R. Akashi, M. S. Bahramy, R. Arita and Y. Iwasa, *Science*, 2012, **338**, 1193-1196.
89. J. Ye, M. F. Craciun, M. Koshino, S. Russo, S. Inoue, H. Yuan, H. Shimotani, A. F. Morpurgo and Y. Iwasa, *Proceedings of the National Academy of Sciences of the United States of America*, 2011, **108**, 13002-13006.
90. W. Bao, Z. Fang, J. Wan, J. Dai, H. Zhu, X. Han, X. Yang, C. Preston and L. Hu, *ACS Nano*, 2014.
91. N. Kim, K. S. Kim, N. Jung, L. Brus and P. Kim, *Nano Letters*, 2011, **11**, 860-865.
92. J. Yao, K. J. Koski, W. Luo, J. J. Cha, L. Hu, D. Kong, V. K. Narasimhan, K. Huo and Y. Cui, *Nature communications*, 2014, **5**, 5670-5670.
93. J. J. Cha, K. J. Koski, K. C. Y. Huang, K. X. Wan, W. Luo, D. Kong, Z. Yu, S. Fan, M. L. Brongersma and Y. Cui, *Nano Letters*, 2013, **13**, 5913-5918.
94. K. J. Koski, C. D. Wessells, B. W. Reed, J. J. Cha, D. Kong and Y. Cui, *Journal of the American Chemical Society*, 2012, **134**, 13773-13779.
95. K. P. Chen, F. R. Chung, M. Wang and K. J. Koski, *Journal of the American Chemical Society*, 2015, **137**, 5431-5437.
96. M. Wang and K. J. Koski, *Acs Nano*, 2015, **9**, 3226-3233.
97. C. Wan, Y. Wang, N. Wang, W. Norimatsu, M. Kusunoki and K. Koumoto, *Journal of Electronic Materials*, 2011, **40**, 1271-1280.
98. J. Cho, M. D. Losego, H. G. Zhang, H. Kim, J. Zuo, I. Petrov, D. G. Cahill and P. V. Braun, *Nature Communications*, 2014, **5**.
99. E. Morosan, H. W. Zandbergen, L. Li, M. Lee, J. G. Checkelsky, M. Heinrich, T. Siegrist, N. P. Ong and R. J. Cava, *Physical Review B*, 2007, **75**.
100. W. J. Hardy, C.-W. Chen, A. Marcinkova, H. Ji, J. Sinova, D. Natelson and E. Morosan, *Physical Review B*, 2015, **91**.
101. C. K. Chan, H. Peng, G. Liu, K. McIlwrath, X. F. Zhang, R. A. Huggins and Y. Cui, *Nat Nano*, 2008, **3**, 31-35.
102. P. Simon and Y. Gogotsi, *Nature Materials*, 2008, **7**, 845-854.
103. J. Wan, A. F. Kaplan, J. Zheng, X. Han, Y. Chen, N. J. Weadock, N. Faenza, S. Lacey, T. Li, J. Guo and L. Hu, *Journal of Materials Chemistry A*, 2014, **2**, 6051-6057.
104. M. Acerce, D. Voiry and M. Chhowalla, *Nature Nanotechnology*, 2015, **10**, 313-318.

105. M. A. Lukowski, A. S. Daniel, C. R. English, F. Meng, A. Forticaux, R. J. Hamers and S. Jin, *Energy & Environmental Science*, 2014, **7**, 2608-2613.
106. J. Kibsgaard, Z. Chen, B. N. Reinecke and T. F. Jaramillo, *Nature Materials*, 2012, **11**, 963-969.
107. D. Voiry, M. Salehi, R. Silva, T. Fujita, M. Chen, T. Asefa, V. B. Shenoy, G. Eda and M. Chhowalla, *Nano Letters*, 2013, **13**, 6222-6227.
108. D. Voiry, H. Yamaguchi, J. Li, R. Silva, D. C. B. Alves, T. Fujita, M. Chen, T. Asefa, V. B. Shenoy, G. Eda and M. Chhowalla, *Nature Materials*, 2013, **12**, 850-855.
109. M. A. Lukowski, A. S. Daniel, F. Meng, A. Forticaux, L. Li and S. Jin, *Journal of the American Chemical Society*, 2013, **135**, 10274-10277.
110. H. Wang, Z. Lu, D. Kong, J. Sun, T. M. Hymel and Y. Cui, *Acs Nano*, 2014, **8**, 4940-4947.
111. Z. Lu, H. Wang, D. Kong, K. Yan, P.-C. Hsu, G. Zheng, H. Yao, Z. Liang, X. Sun and Y. Cui, *Nature Communications*, 2014, **5**.
112. M. Armand and J. M. Tarascon, *Nature*, 2008, **451**, 652-657.
113. B. Dunn, H. Kamath and J.-M. Tarascon, *Science*, 2011, **334**, 928-935.
114. J. M. Tarascon and M. Armand, *Nature*, 2001, **414**, 359-367.
115. Y. Cao, L. Xiao, M. L. Sushko, W. Wang, B. Schwenzer, J. Xiao, Z. Nie, L. V. Saraf, Z. Yang and J. Liu, *Nano Letters*, 2012, **12**, 3783-3787.
116. L.-F. Cui, R. Ruffo, C. K. Chan, H. Peng and Y. Cui, *Nano Letters*, 2008, **9**, 491-495.
117. J. Luo, X. Zhao, J. Wu, H. D. Jang, H. H. Kung and J. Huang, *The Journal of Physical Chemistry Letters*, 2012, **3**, 1824-1829.
118. Y. Yao, N. Liu, M. T. McDowell, M. Pasta and Y. Cui, *Energy & Environmental Science*, 2012, **5**, 7927-7930.
119. M. S. Whittingham, *Science*, 1976, **192**, 1126-1127.
120. M. S. Whittingham, *Journal of The Electrochemical Society*, 1976, **123**, 315-320.
121. K. Bindumadhavan, S. K. Srivastava and S. Mahanty, *Chemical Communications*, 2013, **49**, 1823-1825.
122. T. Stephenson, Z. Li, B. Olsen and D. Mitlin, *Energy & Environmental Science*, 2014, **7**, 209-231.
123. X. H. Liu, J. W. Wang, Y. Liu, H. Zheng, A. Kushima, S. Huang, T. Zhu, S. X. Mao, J. Li, S. L. Zhang, W. Lu, J. M. Tour and J. Y. Huang, *Carbon*, 2012, **50**, 3836-3844.
124. J. R. Dahn, R. Fong and M. J. Spoon, *Physical Review B*, 1990, **42**, 6424-6432.
125. P. J. Zomer, S. P. Dash, N. Tombros and B. J. van Wees, *Applied Physics Letters*, 2011, **99**.
126. A. K. Geim and K. S. Novoselov, *Nat Mater*, 2007, **6**, 183-191.
127. S. Das Sarma, S. Adam, E. H. Hwang and E. Rossi, *Reviews of Modern Physics*, 2011, **83**, 407-470.
128. C. Lee, X. Wei, J. W. Kysar and J. Hone, *Science*, 2008, **321**, 385-388.
129. A. A. Balandin, *Nature Materials*, 2011, **10**, 569-581.
130. K. F. Mak, L. Ju, F. Wang and T. F. Heinz, *Solid State Communications*, 2012, **152**, 1341-1349.

131. F. Bonaccorso, Z. Sun, T. Hasan and A. C. Ferrari, *Nature Photonics*, 2010, **4**, 611-622.
132. K. S. Kim, Y. Zhao, H. Jang, S. Y. Lee, J. M. Kim, K. S. Kim, J.-H. Ahn, P. Kim, J.-Y. Choi and B. H. Hong, *Nature*, 2009, **457**, 706-710.
133. D. Aurbach, Y. Eineli, B. Markovsky, A. Zaban, S. Luski, Y. Carmeli and H. Yamin, *Journal of the Electrochemical Society*, 1995, **142**, 2882-2890.
134. J. Xiao, D. Choi, L. Cosimbescu, P. Koech, J. Liu and J. P. Lemmon, *Chemistry of Materials*, 2010, **22**, 4522-4524.
135. M. S. Dresselhaus and G. Dresselhaus, *Advances in Physics*, 1981, **30**, 139-326.
136. Y. Sun, Q. Wu and G. Shi, *Energy & Environmental Science*, 2011, **4**, 1113-1132.
137. J. Hwang, J. P. Carbotte, S. Tongay, A. F. Hebard and D. B. Tanner, *Physical Review B*, 2011, **84**, 041410.
138. K. Kanetani, K. Sugawara, T. Sato, R. Shimizu, K. Iwaya, T. Hitosugi and T. Takahashi, *Proceedings of the National Academy of Sciences of the United States of America*, 2012, **109**, 19610-19613.
139. G. R. Hennig, *Journal of Chemical Physics*, 1965, **43**, 1201-&.
140. Z. Q. Li, E. A. Henriksen, Z. Jiang, Z. Hao, M. C. Martin, P. Kim, H. L. Stormer and D. N. Basov, *Nature Physics*, 2008, **4**, 532-535.
141. J. Yan, Y. Zhang, P. Kim and A. Pinczuk, *Physical Review Letters*, 2007, **98**.
142. Y. Zhang, T.-T. Tang, C. Girit, Z. Hao, M. C. Martin, A. Zettl, M. F. Crommie, Y. R. Shen and F. Wang, *Nature*, 2009, **459**, 820-823.
143. D. K. Efetov and P. Kim, *Physical Review Letters*, 2010, **105**.
144. S. De and J. N. Coleman, *Acs Nano*, 2010, **4**, 2713-2720.
145. L. Pietronero, S. Strässler, H. R. Zeller and M. J. Rice, *Physical Review B*, 1980, **22**, 904-910.
146. F. Xiong, H. Wang, X. Liu, J. Sun, M. Brongersma, E. Pop and Y. Cui, *Nano Letters*, 2015, **15**, 6777-6784.
147. M. Inaba, H. Yoshida, Z. Ogumi, T. Abe, Y. Mizutani and M. Asano, *Journal of The Electrochemical Society*, 1995, **142**, 20-26.
148. L. M. Malard, M. A. Pimenta, G. Dresselhaus and M. S. Dresselhaus, *Physics Reports*, 2009, **473**, 51-87.
149. M. Inaba, H. Yoshida, Z. Ogumi, T. Abe, Y. Mizutani and M. Asano, *Journal of the Electrochemical Society*, 1995, **142**, 20-26.
150. A. M. Dimiev, G. Ceriotti, N. Behabtu, D. Zakhidov, M. Pasquali, R. Saito and J. M. Tour, *Acs Nano*, 2013, **7**, 2773-2780.
151. N. A. W. Holzwarth, S. G. Louie and S. Rabi, *Physical Review B*, 1983, **28**, 1013-1025.
152. S. Basu, C. Zeller, P. J. Flanders, C. D. Fuerst, W. D. Johnson and J. E. Fischer, *Materials Science and Engineering*, 1979, **38**, 275-283.
153. S. Wu, S. G. Kaplan, H. T. S. Lihn, H. D. Drew, S. Y. Hou, J. M. Phillips, J. C. Barbour, E. L. Venturini, Q. Li and D. B. Fenner, *Physical Review B*, 1996, **54**, 13343-13347.
154. T. Stauber, N. M. R. Peres and A. H. Castro Neto, *Physical Review B*, 2008, **78**.
155. N. M. R. Peres, *Reviews of Modern Physics*, 2010, **82**, 2673-2700.
156. J.-H. Chen, C. Jang, S. Xiao, M. Ishigami and M. S. Fuhrer, *Nature Nanotechnology*, 2008, **3**, 206-209.

157. V. C. Tung, L.-M. Chen, M. J. Allen, J. K. Wassei, K. Nelson, R. B. Kaner and Y. Yang, *Nano Letters*, 2009, **9**, 1949-1955.
158. A. R. Rathmell, N. Minh, M. Chi and B. J. Wiley, *Nano Letters*, 2012, **12**, 3193-3199.
159. J.-Y. Lee, S. T. Connor, Y. Cui and P. Peumans, *Nano Letters*, 2008, **8**, 689-692.
160. S. L. Hellstrom, M. Vosgueritchian, R. M. Stoltenberg, I. Irfan, M. Hammock, Y. B. Wang, C. Jia, X. Guo, Y. Gao and Z. Bao, *Nano Letters*, 2012, **12**.
161. D. S. Hecht, L. Hu and G. Irvin, *Advanced Materials*, 2011, **23**, 1482-1513.
162. H. Wu, D. Kong, Z. Ruan, P.-C. Hsu, S. Wang, Z. Yu, T. J. Carney, L. Hu, S. Fan and Y. Cui, *Nature Nanotechnology*, 2013, **8**, 421-425.
163. N. M. R. Peres, T. Stauber and A. H. C. Neto, *Epl*, 2008, **84**, 6.
164. L. Gomez De Arco, Y. Zhang, C. W. Schlenker, K. Ryu, M. E. Thompson and C. Zhou, *ACS Nano*, 2010, **4**, 2865-2873.
165. J. C. Kehan Yu, *Materials Matters*, 2014, **9**.
166. P. Blake, P. D. Brimicombe, R. R. Nair, T. J. Booth, D. Jiang, F. Schedin, L. A. Ponomarenko, S. V. Morozov, H. F. Gleeson, E. W. Hill, A. K. Geim and K. S. Novoselov, *Nano Letters*, 2008, **8**, 1704-1708.
167. D. Li, M. B. Mueller, S. Gilje, R. B. Kaner and G. G. Wallace, *Nature Nanotechnology*, 2008, **3**, 101-105.
168. X. Han, Y. Chen, H. Zhu, C. Preston, J. Wan, Z. Fang and L. Hu, *Nanotechnology*, 2013, **24**.
169. Y. Hernandez, V. Nicolosi, M. Lotya, F. M. Blighe, Z. Sun, S. De, I. T. McGovern, B. Holland, M. Byrne, Y. K. Gun'ko, J. J. Boland, P. Niraj, G. Duesberg, S. Krishnamurthy, R. Goodhue, J. Hutchison, V. Scardaci, A. C. Ferrari and J. N. Coleman, *Nature Nanotechnology*, 2008, **3**, 563-568.
170. A. A. Green and M. C. Hersam, *Nano Letters*, 2009, **9**, 4031-4036.
171. K. Parvez, R. Li, S. R. Puniredd, Y. Hernandez, F. Hinkel, S. Wang, X. Feng and K. Muellen, *Acs Nano*, 2013, **7**, 3598-3606.
172. H. A. Becerril, J. Mao, Z. Liu, R. M. Stoltenberg, Z. Bao and Y. Chen, *Acs Nano*, 2008, **2**, 463-470.
173. J. K. Wassei and R. B. Kaner, *Materials Today*, 2010, **13**, 52-59.
174. X. Li, G. Zhang, X. Bai, X. Sun, X. Wang, E. Wang and H. Dai, *Nature Nanotechnology*, 2008, **3**, 538-542.
175. H.-J. Shin, K. K. Kim, A. Benayad, S.-M. Yoon, H. K. Park, I.-S. Jung, M. H. Jin, H.-K. Jeong, J. M. Kim, J.-Y. Choi and Y. H. Lee, *Advanced Functional Materials*, 2009, **19**, 1987-1992.
176. C. Mattevi, G. Eda, S. Agnoli, S. Miller, K. A. Mkhoyan, O. Celik, D. Mastrogiovanni, G. Granozzi, E. Garfunkel and M. Chhowalla, *Advanced Functional Materials*, 2009, **19**, 2577-2583.
177. Y. Zhu, W. Cai, R. D. Piner, A. Velamakanni and R. S. Ruoff, *Applied Physics Letters*, 2009, **95**.
178. J. Zhao, S. Pei, W. Ren, L. Gao and H.-M. Cheng, *Acs Nano*, 2010, **4**, 5245-5252.
179. J. Wang, M. Liang, Y. Fang, T. Qiu, J. Zhang and L. Zhi, *Advanced Materials*, 2012, **24**, 2874-2878.
180. X. Wang, L. Zhi and K. Muellen, *Nano Letters*, 2008, **8**, 323-327.

181. G. Eda, Y.-Y. Lin, S. Miller, C.-W. Chen, W.-F. Su and M. Chhowalla, *Applied Physics Letters*, 2008, **92**.
182. Z. Yin, S. Sun, T. Salim, S. Wu, X. Huang, Q. He, Y. M. Lam and H. Zhang, *Acs Nano*, 2010, **4**, 5263-5268.
183. D. W. Lee, T.-K. Hong, D. Kang, J. Lee, M. Heo, J. Y. Kim, B.-S. Kim and H. S. Shin, *Journal of Materials Chemistry*, 2011, **21**, 3438-3442.
184. Y. Yang, X. Yang, W. Yang, S. Li, J. Xu and Y. Jiang, *Nanoscale Research Letters*, 2014, **9**.
185. Y. Wen, K. He, Y. Zhu, F. Han, Y. Xu, I. Matsuda, Y. Ishii, J. Cumings and C. Wang, *Nature Communications*, 2014, **5**.
186. Y. Matsuo and K. Ueda, *Journal of Power Sources*, 2014, **263**, 158-162.
187. S. Komaba, W. Murata, T. Ishikawa, N. Yabuuchi, T. Ozeki, T. Nakayama, A. Ogata, K. Gotoh and K. Fujiwara, *Advanced Functional Materials*, 2011, **21**, 3859-3867.
188. J. Wan, W. Bao, Y. Liu, J. Dai, F. Shen, L. Zhou, X. Cai, D. Urban, Y. Li, K. Jungjohann, M. S. Fuhrer and L. Hu, *Advanced Energy Materials*, 2014, n/a-n/a.
189. S. Pei and H.-M. Cheng, *Carbon*, 2012, **50**, 3210-3228.
190. N. Yabuuchi, K. Kubota, M. Dahbi and S. Komaba, *Chemical Reviews*, 2014, **114**, 11636-11682.
191. B. L. Ellis and L. F. Nazar, *Current Opinion in Solid State and Materials Science*, 2012, **16**, 168-177.
192. S.-W. Kim, D.-H. Seo, X. Ma, G. Ceder and K. Kang, *Advanced Energy Materials*, 2012, **2**, 710-721.
193. H. L. Pan, Y. S. Hu and L. Q. Chen, *Energy & Environmental Science*, 2013, **6**, 2338-2360.
194. V. Palomares, M. Casas-Cabanas, E. Castillo-Martinez, M. H. Han and T. Rojo, *Energy & Environmental Science*, 2013, **6**, 2312-2337.
195. C. Bommier and X. Ji, *Israel Journal of Chemistry*, 2015, n/a-n/a.
196. H. Zhu, Z. Jia, Y. Chen, N. Weadock, J. Wan, O. Vaaland, X. Han, T. Li and L. Hu, *Nano Letters*, 2013, **13**, 3093-3100.
197. N. Yabuuchi, M. Kajiyama, J. Iwatate, H. Nishikawa, S. Hitomi, R. Okuyama, R. Usui, Y. Yamada and S. Komaba, *Nature Materials*, 2012, **11**, 512-517.
198. B. L. Ellis and L. F. Nazar, *Current Opinion in Solid State & Materials Science*, 2012, **16**, 168-177.
199. Y. Liu, Y. Xu, X. Han, C. Pellegrinelli, Y. Zhu, H. Zhu, J. Wan, A. C. Chung, O. Vaaland, C. Wang and L. Hu, *Nano Letters*, 2012, **12**, 5664-5668.
200. L. David, R. Bhandavat and G. Singh, *ACS Nano*, 2014, **8**, 1759-1770.
201. S. Y. Lim, H. Kim, J. Chung, J. H. Lee, B. G. Kim, J.-J. Choi, K. Y. Chung, W. Cho, S.-J. Kim, W. A. Goddard, III, Y. Jung and J. W. Choi, *Proceedings of the National Academy of Sciences of the United States of America*, 2014, **111**, 599-604.
202. L. Xiao, Y. Cao, J. Xiao, W. Wang, L. Kovarik, Z. Nie and J. Liu, *Chemical Communications*, 2012, **48**, 3321-3323.
203. R. Alcantara, M. Jaraba, P. Lavela and J. L. Tirado, *Chemistry of Materials*, 2002, **14**, 2847-+.

204. Y. Jiang, M. Hu, D. Zhang, T. Yuan, W. Sun, B. Xu and M. Yan, *Nano Energy*, 2014, **5**, 60-66.
205. Y. Wang, X. Yu, S. Xu, J. Bai, R. Xiao, Y.-S. Hu, H. Li, X.-Q. Yang, L. Chen and X. Huang, *Nature Communications*, 2013, **4**.
206. J. Qian, X. Wu, Y. Cao, X. Ai and H. Yang, *Angewandte Chemie-International Edition*, 2013, **52**, 4633-4636.
207. Y. Kim, Y. Park, A. Choi, N.-S. Choi, J. Kim, J. Lee, J. H. Ryu, S. M. Oh and K. T. Lee, *Advanced Materials*, 2013, **25**, 3045-3049.
208. Y. Zhu, Y. Wen, X. Fan, T. Gao, F. Han, C. Luo, S.-C. Liou and C. Wang, *ACS nano*, 2015, **9**, 3254-3264.
209. W. Luo, M. Allen, V. Raju and X. Ji, *Advanced Energy Materials*, 2014, **4**.
210. E. M. Lotfabad, J. Ding, K. Cui, A. Kohandehghan, W. P. Kalisvaart, M. Hazelton and D. Mitlin, *Acs Nano*, 2014, **8**, 7115-7129.
211. W. Luo, C. Bommier, Z. Jian, X. Li, R. Carter, S. Vail, Y. Lu, J.-J. Lee and X. Ji, *Acs Applied Materials & Interfaces*, 2015, **7**, 2626-2631.
212. J. Wan, F. Gu, W. Bao, J. Dai, F. Shen, W. Luo, X. Han, D. Urban and L. Hu, *Nano Letters*, 2015.
213. Y.-X. Wang, S.-L. Chou, H.-K. Liu and S.-X. Dou, *Carbon*, 2013, **57**, 202-208.
214. L. David and G. Singh, *Journal of Physical Chemistry C*, 2014, **118**, 28401-28408.
215. S. S. a. J. G. a. P. V. P. a. V. G. a. A. A. M. a. V. M. N. a. J. X. Z. a. D. Y. a. H. H. Hng, *Nanotechnology*, 2012, **23**, 485601.
216. Y. Sun, X. Hu, W. Luo and Y. Huang, *Acs Nano*, 2011, **5**, 7100-7107.
217. D. C. Marcano, D. V. Kosynkin, J. M. Berlin, A. Sinitskii, Z. Sun, A. Slesarev, L. B. Alemany, W. Lu and J. M. Tour, *Acs Nano*, 2010, **4**, 4806-4814.
218. H. C. Schniepp, J. L. Li, M. J. McAllister, H. Sai, M. Herrera-Alonso, D. H. Adamson, R. K. Prud'homme, R. Car, D. A. Saville and I. A. Aksay, *Journal of Physical Chemistry B*, 2006, **110**, 8535-8539.
219. M. J. McAllister, J.-L. Li, D. H. Adamson, H. C. Schniepp, A. A. Abdala, J. Liu, M. Herrera-Alonso, D. L. Milius, R. Car, R. K. Prud'homme and I. A. Aksay, *Chemistry of Materials*, 2007, **19**, 4396-4404.
220. L. J. Cote, R. Cruz-Silva and J. Huang, *Journal of the American Chemical Society*, 2009, **131**, 11027-11032.
221. D. R. Dreyer, S. Park, C. W. Bielawski and R. S. Ruoff, *Chemical Society Reviews*, 2010, **39**, 228-240.
222. H. Nam, C. Tran Viet, M. Han, B. D. Ryu, S. Chandramohan, J. B. Park, J. H. Kang, Y.-J. Park, K. B. Ko, H. Y. Kim, H. K. Kim, J. H. Ryu, Y. S. Katharria, C.-J. Choi and C.-H. Hong, *Nature Communications*, 2013, **4**.
223. X. H. Liu, H. Zheng, L. Zhong, S. Huang, K. Karki, L. Q. Zhang, Y. Liu, A. Kushima, W. T. Liang, J. W. Wang, J.-H. Cho, E. Epstein, S. A. Dayeh, S. T. Picraux, T. Zhu, J. Li, J. P. Sullivan, J. Cumings, C. Wang, S. X. Mao, Z. Z. Ye, S. Zhang and J. Y. Huang, *Nano Letters*, 2011, **11**, 3312-3318.
224. X. H. Liu, Y. Liu, A. Kushima, S. Zhang, T. Zhu, J. Li and J. Y. Huang, *Advanced Energy Materials*, 2012, **2**, 722-741.
225. Y. Liu, X. H. Liu, B.-M. Nguyen, J. Yoo, J. P. Sullivan, S. T. Picraux, J. Y. Huang and S. A. Dayeh, *Nano Letters*, 2013, **13**, 4876-4883.

226. X.-F. Luo, C.-H. Yang and J.-K. Chang, *Journal of Materials Chemistry A*, 2015, **3**, 17282-17289.
227. X.-F. Luo, C.-H. Yang, Y.-Y. Peng, N.-W. Pu, M.-D. Ger, C.-T. Hsieh and J.-K. Chang, *Journal of Materials Chemistry A*, 2015, **3**, 10320-10326.
228. C. Bommier, T. W. Surta, M. Dolgos and X. Ji, *Nano Letters*, 2015, **15**, 5888-5892.
229. D. A. Stevens and J. R. Dahn, *Journal of the Electrochemical Society*, 2000, **147**, 4428-4431.
230. D. A. Stevens and J. R. Dahn, *Journal of the Electrochemical Society*, 2001, **148**, A803-A811.
231. F. Shen, H. Zhu, W. Luo, J. Wan, L. Zhou, J. Dai, B. Zhao, X. Han, K. Fu and L. Hu, *Acs Applied Materials & Interfaces*, 2015, **7**, 23291-23296.
232. M. Inagaki, *Journal of Materials Research*, 1989, **4**, 1560-1568.
233. K. Xu, *Chemical Reviews*, 2004, **104**, 4303-4417.
234. W. Sirisaksoontorn, A. A. Adenuga, V. T. Remcho and M. M. Lerner, *Journal of the American Chemical Society*, 2011, **133**, 12436-12438.
235. M. S. Whittingham, *Chemical Reviews*, 2004, **104**, 4271-4301.
236. D. P. Divincenzo and E. J. Mele, *Physical Review B*, 1985, **32**, 2538-2553.
237. J. Sun, H.-W. Lee, M. Pasta, H. Yuan, G. Zheng, Y. Sun, Y. Li and Y. Cui, *Nature Nanotechnology*, 2015, **10**, 980-U184.
238. T. Inoshita, K. Nakao and H. Kamimura, *Journal of the Physical Society of Japan*, 1977, **43**, 1237-1243.
239. X. Ren and Y. Wu, *Journal of the American Chemical Society*, 2013, **135**, 2923-2926.
240. Q. Zhao, Y. Hu, K. Zhang and J. Chen, *Inorganic Chemistry*, 2014, **53**, 9000-9005.
241. M. Pasta, C. D. Wessells, R. A. Huggins and Y. Cui, *Nature Communications*, 2012, **3**.
242. E. Peled, *Journal of the Electrochemical Society*, 1979, **126**, 2047-2051.
243. D. Aurbach, A. Zaban, A. Schechter, Y. Eineli, E. Zinigrad and B. Markovsky, *Journal of the Electrochemical Society*, 1995, **142**, 2873-2882.
244. D. Aurbach, B. Markovsky, A. Shechter, Y. EinEli and H. Cohen, *Journal of the Electrochemical Society*, 1996, **143**, 3809-3820.
245. M. Dion, H. Rydberg, E. Schroder, D. C. Langreth and B. I. Lundqvist, *Physical Review Letters*, 2004, **92**.
246. P. Giannozzi, S. Baroni, N. Bonini, M. Calandra, R. Car, C. Cavazzoni, D. Ceresoli, G. L. Chiarotti, M. Cococcioni, I. Dabo, A. Dal Corso, S. de Gironcoli, S. Fabris, G. Fratesi, R. Gebauer, U. Gerstmann, C. Gougoussis, A. Kokalj, M. Lazzeri, L. Martin-Samos, N. Marzari, F. Mauri, R. Mazzarello, S. Paolini, A. Pasquarello, L. Paulatto, C. Sbraccia, S. Scandolo, G. Sclauzero, A. P. Seitsonen, A. Smogunov, P. Umari and R. M. Wentzcovitch, *Journal of Physics-Condensed Matter*, 2009, **21**.
247. J. R. Dahn, *Physical Review B*, 1991, **44**, 9170-9177.
248. J. E. Fischer and H. J. Kim, *Synthetic Metals*, 1985, **12**, 137-142.
249. C. D. Wessells, S. V. Peddada, R. A. Huggins and Y. Cui, *Nano Letters*, 2011, **11**, 5421-5425.

250. P. C. Eklund, G. Dresselhaus, M. S. Dresselhaus and J. E. Fischer, *Physical Review B*, 1977, **16**, 3330-3333.
251. R. J. Nemanich, S. A. Solin and D. Guerard, *Physical Review B*, 1977, **16**, 2665-2672.
252. P. Lian, X. Zhu, S. Liang, Z. Li, W. Yang and H. Wang, *Electrochimica Acta*, 2010, **55**, 3909-3914.
253. J. Xu, M. Wang, N. P. Wickramaratne, M. Jaroniec, S. Dou and L. Dai, *Advanced Materials*, 2015, **27**, 2042-2048.
254. K. Ellmer, *Nature Photonics*, 2012, **6**, 808-816.
255. C. Uthaisar, V. Barone and J. E. Peralta, *Journal of Applied Physics*, 2009, **106**, 113715-113716.
256. A. Marini, C. Hogan, M. Gruening and D. Varsano, *Computer Physics Communications*, 2009, **180**, 1392-1403.
257. L. Hu, D. S. Hecht and G. Gruener, *Chemical Reviews*, 2010, **110**, 5790-5844.
258. S. Ye, A. R. Rathmell, Z. Chen, I. E. Stewart and B. J. Wiley, *Advanced Materials*, 2014, **26**, 6670-6687.
259. B. Han, K. Pei, Y. Huang, X. Zhang, Q. Rong, Q. Lin, Y. Guo, T. Sun, C. Guo, D. Carnahan, M. Giersig, Y. Wang, J. Gao, Z. Ren and K. Kempa, *Advanced Materials*, 2014, **26**, 873-877.
260. P.-C. Hsu, S. Wang, H. Wu, V. K. Narasimhan, D. Kong, H. R. Lee and Y. Cui, *Nature Communications*, 2013, **4**.
261. N. Kim, S. Kee, S. H. Lee, B. H. Lee, Y. H. Kahng, Y.-R. Jo, B.-J. Kim and K. Lee, *Advanced Materials*, 2014, **26**, 2268-2272.
262. L. Hu, D. S. Hecht and G. Gruner, *Nano Letters*, 2004, **4**, 2513-2517.
263. R. R. King, D. C. Law, K. M. Edmondson, C. M. Fetzer, G. S. Kinsey, H. Yoon, R. A. Sherif and N. H. Karam, *Applied Physics Letters*, 2007, **90**.
264. D. Y. Kim, T.-H. Lai, J. W. Lee, J. R. Manders and F. So, *Scientific Reports*, 2014, **4**.
265. N. Tessler, V. Medvedev, M. Kazes, S. H. Kan and U. Banin, *Science*, 2002, **295**, 1506-1508.
266. J. Bland-Hawthorn, S. C. Ellis, S. G. Leon-Saval, R. Haynes, M. M. Roth, H. G. Loehmannsroeben, A. J. Horton, J. G. Cuby, T. A. Birks, J. S. Lawrence, P. Gillingham, S. D. Ryder and C. Trinh, *Nature Communications*, 2011, **2**.
267. Q. Bao and K. P. Loh, *Acs Nano*, 2012, **6**, 3677-3694.
268. O. Balci, E. O. Polat, N. Kakenov and C. Kocabas, *Nature Communications*, 2015, **6**.
269. W. Luo, J. Wan, B. Ozdemir, W. Bao, Y. Chen, J. Dai, H. Lin, Y. Xu, F. Gu, V. Barone and L. Hu, *Nano Letters*, 2015, **15**, 7671-7677.
270. B. A. Korgel, *Nature*, 2013, **500**, 278-279.
271. L. Xiao, H. Ma, J. Liu, W. Zhao, Y. Jia, Q. Zhao, K. Liu, Y. Wu, Y. Wei, S. Fan and K. Jiang, *Nano Letters*, 2015, **15**, 8365-8370.
272. C. Uthaisar, V. Barone and B. D. Fahlman, *Carbon*, 2013, **61**, 558-567.
273. A. P. Cohn, K. Share, R. Carter, L. Oakes and C. L. Pint, *Nano Letters*, 2016, **16**, 543-548.

274. Z. C. Wu, Z. H. Chen, X. Du, J. M. Logan, J. Sippel, M. Nikolou, K. Kamaras, J. R. Reynolds, D. B. Tanner, A. F. Hebard and A. G. Rinzler, *Science*, 2004, **305**, 1273-1276.
275. N. Jung, A. C. Crowther, N. Kim, P. Kim and L. Brus, *Acs Nano*, 2010, **4**, 7005-7013.
276. M. A. Py and R. R. Haering, *Canadian Journal of Physics*, 1983, **61**, 76-84.
277. R. Dominko, D. Arcon, A. Mrzel, A. Zorko, P. Cevc, P. Venturini, M. Gaberscek, M. Remskar and D. Mihailovic, *Advanced Materials*, 2002, **14**, 1531-+.
278. K. F. Mak, K. He, J. Shan and T. F. Heinz, *Nature Nanotechnology*, 2012, **7**, 494-498.
279. H. Zeng, J. Dai, W. Yao, D. Xiao and X. Cui, *Nature Nanotechnology*, 2012, **7**, 490-493.
280. Y. Wang, J. Z. Ou, S. Balendhran, A. F. Chrimes, M. Mortazavi, D. D. Yao, M. R. Field, K. Latham, V. Bansal, J. R. Friend, S. Zhuiykov, N. V. Medhekar, M. S. Strano and K. Kalantar-zadeh, *Acs Nano*, 2013, **7**, 10083-10093.
281. Z. Zeng, Z. Yin, X. Huang, H. Li, Q. He, G. Lu, F. Boey and H. Zhang, *Angewandte Chemie-International Edition*, 2011, **50**, 11093-11097.
282. J.-Z. Wang, L. Lu, M. Lotya, J. N. Coleman, S.-L. Chou, H.-K. Liu, A. I. Minett and J. Chen, *Advanced Energy Materials*, 2013, **3**, 798-805.
283. H. Liu, D. Su, R. Zhou, B. Sun, G. Wang and S. Z. Qiao, *Advanced Energy Materials*, 2012, **2**, 970-975.
284. K. Chang, D. Geng, X. Li, J. Yang, Y. Tang, M. Cai, R. Li and X. Sun, *Advanced Energy Materials*, 2013, **3**, 839-844.
285. J. Park, J.-S. Kim, J.-W. Park, T.-H. Nam, K.-W. Kim, J.-H. Ahn, G. Wang and H.-J. Ahn, *Electrochimica Acta*, 2013, **92**, 427-432.
286. G. S. Bang, K. W. Nam, J. Y. Kim, J. Shin, J. W. Choi and S.-Y. Choi, *Acs Applied Materials & Interfaces*, 2014, **6**, 7084-7089.
287. Y. Liang, R. Feng, S. Yang, H. Ma, J. Liang and J. Chen, *Advanced Materials*, 2011, **23**, 640-+.
288. Y. Liu, L. Jiao, Q. Wu, J. Du, Y. Zhao, Y. Si, Y. Wang and H. Yuan, *Journal of Materials Chemistry A*, 2013, **1**, 5822-5826.
289. Q. Gao, M. Gu, A. Nie, F. Mashayek, C. Wang, G. M. Odegard and R. Shahbazian-Yassar, *Chemistry of Materials*, 2014, **26**, 1660-1669.
290. C.-M. Wang, W. Xu, J. Liu, J.-G. Zhang, L. V. Saraf, B. W. Arey, D. Choi, Z.-G. Yang, J. Xiao, S. Thevuthasan and D. R. Baer, *Nano Letters*, 2011, **11**, 1874-1880.
291. X. Zhou, L.-J. Wan and Y.-G. Guo, *Nanoscale*, 2012, **4**, 5868-5871.
292. F. Wang, R. Robert, N. A. Chernova, N. Pereira, F. Omenya, F. Badway, X. Hua, M. Ruotolo, R. Zhang, L. Wu, V. Volkov, D. Su, B. Key, M. S. Whittingham, C. P. Grey, G. G. Amatucci, Y. Zhu and J. Graetz, *Journal of the American Chemical Society*, 2011, **133**, 18828-18836.
293. K. E. Gregorczyk, Y. Liu, J. P. Sullivan and G. W. Rubloff, *Acs Nano*, 2013, **7**, 6354-6360.
294. F. Lin, D. Nordlund, T.-C. Weng, Y. Zhu, C. Ban, R. M. Richards and H. L. Xin, *Nature Communications*, 2014, **5**.
295. U. Halim, C. R. Zheng, Y. Chen, Z. Lin, S. Jiang, R. Cheng, Y. Huang and X. Duan, *Nature Communications*, 2013, **4**.

296. K. Wang, J. Wang, J. Fan, M. Lotya, A. O'Neill, D. Fox, Y. Feng, X. Zhang, B. Jiang, Q. Zhao, H. Zhang, J. N. Coleman, L. Zhang and W. J. Blau, *Acs Nano*, 2013, **7**, 9260-9267.
297. M. T. Armand, J.-M., *Nature*, 2008, **451**.
298. B. Kang and G. Ceder, *Nature*, 2009, **458**, 190-193.
299. I. Kovalenko, B. Zdyrko, A. Magasinski, B. Hertzberg, Z. Milicev, R. Burtovyy, I. Luzinov and G. Yushin, *Science*, 2011, **334**, 75-79.
300. X. Ji, K. T. Lee and L. F. Nazar, *Nat Mater*, 2009, **8**, 500-506.
301. J. B. Goodenough and Y. Kim, *Chemistry of Materials*, 2009, **22**, 587-603.
302. M. Whittingham, *Journal*, 2008, **33**, 411-419.
303. A. Magasinski, P. Dixon, B. Hertzberg, A. Kvit, J. Ayala and G. Yushin, *Nat Mater*, **9**, 353-358.
304. Y. Yao, K. Huo, L. Hu, N. Liu, J. J. Cha, M. T. McDowell, P. K. Chu and Y. Cui, *ACS Nano*, **5**, 8346-8351.
305. H. Kim and J. Cho, *Nano Letters*, 2008, **8**, 3688-3691.
306. L.-F. Cui, Y. Yang, C.-M. Hsu and Y. Cui, *Nano Letters*, 2009, **9**, 3370-3374.
307. T. H. Hwang, Y. M. Lee, B.-S. Kong, J.-S. Seo and J. W. Choi, *Nano Letters*, 2011, **12**, 802-807.
308. H. Wu, G. Chan, J. W. Choi, I. Ryu, Y. Yao, M. T. McDowell, S. W. Lee, A. Jackson, Y. Yang, L. Hu and Y. Cui, *Nat Nano*, **7**, 310-315.
309. M.-H. Park, M. G. Kim, J. Joo, K. Kim, J. Kim, S. Ahn, Y. Cui and J. Cho, *Nano Letters*, 2009, **9**, 3844-3847.
310. H. Kim, B. Han, J. Choo and J. Cho, *Angewandte Chemie*, 2008, **120**, 10305-10308.
311. C. K. Chan, R. Ruffo, S. S. Hong, R. A. Huggins and Y. Cui, *Journal of Power Sources*, 2009, **189**, 34-39.
312. X. H. Liu, H. Zheng, L. Zhong, S. Huang, K. Karki, L. Q. Zhang, Y. Liu, A. Kushima, W. T. Liang, J. W. Wang, J.-H. Cho, E. Epstein, S. A. Dayeh, S. T. Picraux, T. Zhu, J. Li, J. P. Sullivan, J. Cumings, C. Wang, S. X. Mao, Z. Z. Ye, S. Zhang and J. Y. Huang, *Nano Letters*, **11**, 3312-3318.
313. H. Yang, S. Huang, X. Huang, F. Fan, W. Liang, X. H. Liu, L.-Q. Chen, J. Y. Huang, J. Li, T. Zhu and S. Zhang, *Nano Letters*, **12**, 1953-1958.
314. I. Ryu, J. W. Choi, Y. Cui and W. D. Nix, *Journal of the Mechanics and Physics of Solids*, 2011, **59**, 1717-1730.
315. H. Wu, G. Zheng, N. Liu, T. J. Carney, Y. Yang and Y. Cui, *Nano Letters*, **12**, 904-909.
316. Y. He, B. Yang, K. Yang, C. Brown, R. Ramasamy, H. Wang, C. Lundgren and Y. Zhao, *Journal of Materials Chemistry*, 2012, **22**, 8294-8303.
317. B. Varghese, M. V. Reddy, Z. Yanwu, C. S. Lit, T. C. Hoong, G. V. Subba Rao, B. V. R. Chowdari, A. T. S. Wee, C. T. Lim and C.-H. Sow, *Chemistry of Materials*, 2008, **20**, 3360-3367.
318. J. Wang, Z. Li, N. Singh and S. Lee, *Opt. Express*, 2011, **19**, 23078-23084.
319. S. Kurita, A. Yoshimura, H. Kawamoto, T. Uchida, K. Kojima, M. Tachibana, P. Molina-Morales and H. Nakai, *Journal of Applied Physics*, 2005, **97**.
320. S. H. Ahn and L. J. Guo, *Advanced Materials*, 2008, **20**, 2044-2049.

321. V. L. Pushparaj, M. M. Shaijumon, A. Kumar, S. Murugesan, L. Ci, R. Vajtai, R. J. Linhardt, O. Nalamasu and P. M. Ajayan, *Proceedings of the National Academy of Sciences of the United States of America*, 2007, **104**, 13574-13577.
322. K.-H. Choi, S.-H. Kim, H.-J. Ha, E.-H. Kil, C. K. Lee, S. B. Lee, J. K. Shim and S.-Y. Lee, *Journal of Materials Chemistry A*, 2013, **1**, 5224-5231.
323. L. J. Guo, *Advanced Materials*, 2007, **19**, 495-513.
324. M. M. Brewster, M.-Y. Lu, S. K. Lim, M. J. Smith, X. Zhou and S. Gradečak, *The Journal of Physical Chemistry Letters*, 2011, **2**, 1940-1945.
325. P. H. L. Notten, F. Roozeboom, R. A. H. Niessen and L. Baggetto, *Advanced Materials*, 2007, **19**, 4564-4567.
326. C. Trompoukis, O. El Daif, V. Depauw, I. Gordon and J. Poortmans, *Applied Physics Letters*, 2012, **101**, 103901-103904.
327. A. F. Kaplan, T. Xu and L. J. Guo, *Applied Physics Letters*, 2011, **99**, 143111-143113.
328. M.-G. Kang, H. Joon Park, S. Hyun Ahn and L. Jay Guo, *Solar Energy Materials and Solar Cells*, 2010, **94**, 1179-1184.
329. Y. Yang, K. Mielczarek, M. Aryal, A. Zakhidov and W. Hu, *ACS Nano*, 2012, **6**, 2877-2892.
330. T. Ling, S.-L. Chen and L. J. Guo, *Opt. Express*, 2011, **19**, 861-869.
331. P. Mukherjee, A. Bruccoleri, R. K. Heilmann, M. L. Schattenburg, A. F. Kaplan and L. J. Guo, 2010.
332. Y. Yao, K. Huo, L. Hu, N. Liu, J. J. Cha, M. T. McDowell, P. K. Chu and Y. Cui, *ACS Nano*, 2011, **5**, 8346-8351.
333. R. Demir Cakan, M.-M. Titirici, M. Antonietti, G. Cui, J. Maier and Y.-S. Hu, *Chemical Communications*, 2008, **0**, 3759-3761.
334. Y. He, X. Yu, Y. Wang, H. Li and X. Huang, *Advanced Materials*, 2011, **23**, 4938-4941.
335. K. Zhao, M. Pharr, S. Cai, J. J. Vlassak and Z. Suo, *Journal of the American Ceramic Society*, 2011, **94**, s226-s235.
336. K. Zhao, M. Pharr, Q. Wan, W. L. Wang, E. Kaxiras, J. J. Vlassak and Z. Suo, *Journal of The Electrochemical Society*, 2012, **159**, A238-A243.
337. N. Weadock, N. Varongchayakul, J. Wan, S. Lee, J. Seog and L. Hu, *Nano Energy*, 2013, **2**, 713-719.
338. S. D. Lacey, J. Wan, A. v. W. Cresce, S. M. Russell, J. Dai, W. Bao, K. Xu and L. Hu, *Nano Letters*, 2015, **15**, 1018-1024.